SITE-DIRECTED FLUORESCENCE SPECTROSCOPY: NEW APPROACHES FOR STUDYING PROTEIN STRUCTURE AND OLIGOMERIZATION

by

Steven Elias Mansoor

A DISSERTATION

Presented to the Department of Biochemistry and Molecular Biology
and the Oregon Health & Science University School of Medicine
in partial fulfillment of the requirements for the degree of
Doctor of Philosophy

June 2007

School of Medicine
Oregon Health & Science University

CERTIFICATE OF APPROVAL

This is to certify that the Ph.D. Dissertation of

Steven Elias Mansoor

has been approved by the following:

Dr. David L. Farrens, mentor

Dr. James R. Lundblad, committee chair

Dr. Hans Peter Bächinger, committee member

Dr. Svetlana Lutsenko, committee member

Dr. Peter Rotwein, committee member

TABLE OF CONTENTS

Chapter 1 Introduction

Chapter 2 Mapping Proximity within Proteins Using Fluorescence Spectroscopy. A Study of T4 Lysozyme Showing that Tryptophan Residues Quench Bimane Fluorescence

Chapter 3 High-Throughput Protein Structural Analysis Using Site-Directed Fluorescence Labeling and the Bimane Derivative (2-Pyridyl)dithiobimane

Chapter 4 Rhodopsin Self-Associates in Asolectin Liposomes

Chapter 5 Summary and Conclusions

Appendix 1 Tryptophan Fluorescence Quenching of Four Different Fluorophores: A Calibration Study

Appendix 2 Luminescence Resonance Energy Transfer: A Distance Calibration Using Double Cysteine Mutants in T4 Lysozyme

LIST OF TABLES

LIST OF FIGURES

LIST OF ABBREVIATIONS

α	alpha
α_1	Pre-exponential factor for τ_1 in a lifetime decay fit
α_2	Pre-exponential factor for τ_2 in a lifetime decay fit
α_{GTP}	GTP-bound alpha subunit of the heterotrimeric G-protein
A (amino acid)	alanine
Å	Angstrom
Abs	absorption
AFM	atomic force microscopy
Arg	arginine
Asn	asparagine
Asp	aspartic acid
Asp-N	proteinase
-Atto	Atto-655 attached to a cysteine residue on a protein
A.U.	arbitrary units
B_1	mBBr attached to a cysteine residue on a protein
B_2	PDT-Bimane attached to a cysteine residue on a protein
B_3	qBBr attached to a cysteine residue on a protein
β	beta
Bim	bimane
BRET	bioluminescence resonance energy transfer

-By	Bodipy 507/535 attached to a cysteine residue on a protein
C-1	cytoplasmic loop 1 of rhodopsin
C-2	cytoplasmic loop 2 of rhodopsin
C-3	cytoplasmic loop 3 of rhodopsin
C (amino acid)	cysteine
C-	carboxyl-
°C	degrees Celsius
Ca	calcium
C_A	reduced acceptor surface density
cal	calories
cAMP	cyclic adenosine monophosphate
CD	circular dichroism
CHAPS	3-[(3-cholamidopropyl)dimethyl-ammonio]-1-propanesulfonate
χ^2	chi-square, which describes the deviance of the residuals to a fit
Cl	chlorine
cm	centimeter
cps	counts per second
CS124-DTPA-EMCH•Tb^{3+}	diethylenetriaminepentaacetate chelate covalently joined through one amide bond to carbosytril 124 chromophore, and through a second amide bond to a maleimide group
Cu^{+2}	copper

CY3	carboxymethylindocyanine dye 3.18
CY5	carboxymethylindocyanine dye 5.18
Cys	cysteine
δ	delta
Δ	delta, or the difference between two values
D (amino acid)	aspartic acid
D2	dopamine receptor, subtype 2
Da	Dalton, unit of atomic mass
ΔG	change in Gibbs free energy
ΔH	change in enthalpy
ΔS	change in entropy
DDM	n-dodecyl-β-D-maltoside
DMSO	dimethylsulfoxide
DNA	deoxyribonucleic acid
DPTA	diethylenetriaminepentaacetate
DTT	dithiothreitol
ε (absorbance)	extinction coefficient
ε (solvent)	dielectric
E (amino acid)	glutamic acid
E-1	extracellular loop 1 of rhodopsin
E-2	extracellular loop 2 of rhodopsin
E-3	extracellular loop 3 of rhodopsin
EDTA	ethylenediamine-tetraacetic acid

EM	electron microscopy
EPR	electron paramagnetic resonance
E_{random}	amount of energy transfer expected due to random association and receptor crowding
ESM	exponential series method
ET	electron transfer
et al.	*et alii* (Latin), “and others”
eV	electron volt
F (amino acid)	phenylalanine
F_0	fluorescence intensity in the absence of quencher (Trp residue)
F1	V8 proteolytic fragment of rhodopsin (~ 27 kDa)
F2	V8 proteolytic fragment of rhodopsin (~ 15 kDa)
F_D	fluorescence intensity of the donor in the absence of an acceptor (or quencher)
F_{DA}	fluorescence intensity of the donor in the presence of an acceptor
FRET	fluorescence resonance energy transfer
F_W	fluorescence intensity in the presence of a Trp residue
fwhm	full width at half max
γ	gamma
g (mass)	gram
g	acceleration due to gravity

G	G-factor in an anisotropy experiment that corrects for monochromator bias in transmitting parallel *versus* perpendicularly polarized light
G (amino acid)	glycine
$G\alpha_T$	alpha subunit of the G-protein transducin
G_α	alpha subunit of the heterotrimeric G-protein
$G_{\beta\gamma}$	beta and gamma subunits of the heterotrimeric G-protein
G_s	Stimulatory G-protein subtype that activates adenylate cyclase
GABA	γ-aminobutyric acid
GDP	guanosine diphosphate
Glu	glutamic acid
GRK	G-protein coupled receptor kinase
GPCR	G-protein coupled receptor
G-protein	guanine nucleotide-binding regulatory protein
GTP	guanosine triphosphate
h	hours
H (atom)	hydrogen
H (amino acid)	histidine
HDM	n-hexadecyl-β-D-maltoside
HIV	human immunodeficiency virus
$h\nu$	light
$h\upsilon_A$	absorption of a photon

I^-	free Iodide
$I_{\parallel}$	intensity of fluorescence emission parallel to the plane of excitation light
$I_{\perp}$	intensity of fluorescence emission perpendicular to the plane of excitation light
I-1	intracellular loop 1 of rhodopsin
I-2	intracellular loop 2 of rhodopsin
I-3	intracellular loop 3 of rhodopsin
I (amino acid)	isoleucine
IPTG	isopropyl β-thiogalactoside
IRF	instrument response function
$J(\lambda)$	overlap integral for a FRET donor/acceptor pair
κ^2	orientation factor in a FRET/LRET experiment
k	rate constant
K (atom)	potassium
K (amino acid)	lysine
kDa	kilodalton
kcal	kilocalories
k_{EC}	rate of external conversion
k_{ET}	rate of electron transfer
k_F	rate of fluorescence
k_P	rate of phosphorescence
k_{RET}	rate of resonance energy transfer

k_q	bimolecular quenching constant (collisions/second)
kV	kilovolt
λ_{max}	wavelength of maximum absorbance or emission
L (amino acid)	leucine
LED	light emitting diode
LRET	luminescence resonance energy transfer
Lys	lysine
-LY	lucifer yellow attached to a cysteine residue on a protein
M	molar
M (amino acid)	methionine
max	maximum
Met	methionine
Mg	magnesium
mGluR	metabotropic glutamate receptor
MW	molecular weight
μg	microgram
mg	milligram
min	minute
μl	microliter
ml	milliliter
μM	micromolar
mM	millimolar
mol	mole

MOPS	3-(*N*-morpholino)-propanesulfonic acid
μs	microsecond
ms	millisecond
mBBr	monobromobimane
n	refractive index
N	normal
N (amino acid)	asparagine
N (atom)	nitrogen
N-	amino-
Na	sodium
NBD	nitrobenzoxadiazole
NBD-PS	phosphatidylserine lipid covalently modified with a nitrobenzoxadiazole fluorescent group.
nm	nanometer
NMR	nuclear magnetic resonance
ns	nanosecond
O (atom)	oxygen
OD	optical density
OG	1-O-n-octyl-β-glucoside
P (amino acid)	proline
P (atom)	phosphate
PCR	polymerase chain reaction
PDT-Bimane	(2-pyridyl)dithiobimane

PET	photo-induced electron transfer
pH	potential of hydrogen
Phe	phenylalanine
Φ	quantum yield
pKa	acid dissociation constant
pmol	picomole
PS	phosphatidylserine
PTI	Photon Technology International
PyMPO	1-(2-maleimidylethyl)-4-(5-(4-methoxyphenyl)oxazol-2-yl)-pyridinium methanesulfonate
Q (amino acid)	glutamine
[Q]	concentration of quencher
qBBr	monobromo(trimethylammonio)bimane
r (mobility)	anisotropy
r (energy transfer)	distance
R (amino acid)	arginine
Rh	rhodopsin
R_0	Förster distance, defined for each donor/acceptor pair as the distance at which the energy transfer efficiency equals 50%
ROS	rod outer segment
S_0	electronic ground state
S_1	first electronic excited state
s	second

S (amino acid)	serine
S (atom)	sulfur
SCE	standard calomel electrode
SDL	site-directed labeling
SDFL	site-directed fluorescence labeling
SDS	sodium dodecyl sulfate
SDSL	site-directed spin labeling
SDS PAGE	SDS polyacrylamide gel electrophoresis
SEM	standard error of the mean
Ser	serine
T4L	T4 lysozyme
T (amino acid)	threonine
τ	fluorescence decay lifetime
$<\tau>$	amplitude-weighted average fluorescence lifetime, defined by $<\tau> = \alpha_1*\tau_1 + \alpha_2*\tau_2$
$\tau_{1/2}$	half-life
τ_{AD}	sensitized luminescence lifetime of acceptor in an LRET experiment
τ_D	fluorescence lifetime of donor in the absence of acceptor
τ_{DA}	fluorescence lifetime of donor in the presence of acceptor
Tb^{3+}	terbium
T_m	melting temperature
τ_W	fluorescence lifetime in the presence of a Trp residue

TCA	trichloroacetic acid
TCEP	tris(2-carboxyethyl)phosphine
TDM	n-tetradecyl-β-D-maltoside
TM	transmembrane
Tris	2-amino-2-(hydroxymethyl)-1,3-propanediol
Trp	tryptophan
UV	ultraviolet
V (amino acid)	valine
V_2	Vasopressin receptor
V8	protease from *Staphylococcus aureus* strain V8 that cleaves the carboxyl side of Asp and Glu residues
Vis	visible
W (amino acid)	tryptophan
WT	wild type
Y (amino acid)	tyrosine

ACKNOWLEDGEMENTS

Most importantly, I wish to thank my advisor and mentor, Dr. David L. Farrens for providing me with leadership and direction during my graduate studies here at OHSU - my growth as a scientist, a writer, and a critical thinker has flourished through our daily interactions. But more than that, I have grown as a person. I have known Dr. Farrens for more than 10 years now and during this time, he has been like a big brother watching over me. I am truly going to miss our discussions/arguments, whether they be about science, philosophy, religion, politics, or computers. Thanks for all the help, Dave.

I would also like to thank members of the Farrens' lab, past and present, for making the lab environment social and productive: Dr. Brian Nauert, Dr. Jay Janz, Dr. Martha Sommer, Jonathan Fay, Tom Dunham, Abhinov Sinev, Mark DeWitt, Emily Weimer, and Loren Brown. Thanks for putting up with “Aggroman” for all these years. Shields down! I wish to extend a special thanks to Jon Fay, my baymate and lunch partner, for all the good memories in and out of the lab.

I would also like to thank my collaborators, Dr. Hassane Mchaourab at Vanderbilt University and Dr. Krzysztof Palczewski at Case Western Reserve University, for making much of this work possible. Hassane's assistance and support have been there from the first time I stepped foot in the Farrens lab. I thank the members of my research advisory committee – Dr. Hans Peter Bächinger, Dr. James Lundblad, Dr. Svetlana Lutsenko, and Dr. Peter Rotwein - for their guidance and helpful comments. Additional gratitude is extended to Dr. Hans Peter Bächinger for insighful discussions regarding the thermodynamic analyses performed in Chapter 2 and Chapter 3. I wish to thank Dr. Arthur Glasfeld for reading parts of this document as well as for, along with Dr. Richard

Brennan and Dr. Maria Schumacher, helping me learn some crystallography during graduate school. I also wish to thank Dr. Peter Rotwein for his dedication and commitment to the MD/PhD program.

Finally, I wish to thank my family. I thank my parents, Edward and Salma, for providing me with the opportunity for an education and for always being there when I needed anything. I certainly would not be where I am today without their love, support and encouragement. I thank my brothers and sisters – Sherri, David, Aimee, Lori, and André – for the phone calls, text messages, fun e-mails, food packages and support during many of my late-night sessions during graduate school.

This thesis dissertation is dedicated to my mom who always encouraged me to follow my ambition for a career in science and medicine.

If it can only be done once, it is but a trick.

When it can be done more than once, it becomes a method.

The Mansoorian Method

ABSTRACT

A protein’s structure and oligomerization state dictates its function. Unfortunately, for many proteins, especially membrane-bound proteins like G-protein coupled receptors (GPCRs), elucidating the dynamic conformational changes required for activation is often not possible using traditional structural methodologies. As a result, new methodologies are needed for the study of these receptors.

This dissertation discusses three things. First, it presents the development of a novel site-directed fluorescence labeling (SDFL) methodology that can be used to determine protein secondary structure at the level of the backbone fold and provide protein tertiary structural constraints of ~ 5 – 15 Å. This method, which exploits the distance-dependent quenching of bimane fluorescence by proximal tryptophan residues, is generally useful for studying protein/protein interactions as well as measuring real-time conformational changes in membrane proteins.

Second, a way to automate and increase the speed with which SDFL methods can be undertaken is presented. The thiol-cleavable fluorophore, PDT-Bimane, shows solvent-sensitive characteristics to its fluorescence, as well as susceptibility to quenching by proximal tryptophan residues. Together, these properties enable its use for studying both protein secondary and tertiary structure. Furthermore, the reducible nature of PDT-Bimane resolves problems often faced in SDFL experiments: ensuring specific labeling of cysteine residues, determining the extent of free label contamination, and accurately determining labeling efficiency even at low sample concentrations. Thus, the ability to cleave PDT-Bimane off the protein enables automated, rapid determination of these

parameters, and positions it as an ideal fluorophore for high-throughput SDFL structural studies.

Finally, a spectroscopic approach is described for studying the oligomerization state of visual rhodopsin, the model GPCR. This approach uses a novel combination of SDFL and resonance energy transfer methodologies to determine that visual rhodopsin, when reconstituted into a membrane environment, prefers to self-associate into higher order oligomers. In fact, greater than 90% of the receptors were found to associate both in the dark and following light-activation.

In summary, this dissertation both develops novel SDFL methods to assess protein/protein interactions and conformational changes, as well as demonstrates how to assess oligomerization states in difficult to study membrane proteins.

Chapter 1

Introduction

There are a limited number of ways to study protein dynamics and protein oligomerization in solution. This is especially true for G-protein coupled receptors (GPCRs), the largest known superfamily of cell-surface receptors. Elucidation of the dynamic conformational changes required for activation of these membrane proteins has proven difficult to achieve using traditional structural methods such as nuclear magnetic resonance (NMR) spectroscopy and X-ray crystallography, and as of Spring 2007, the structure of only one GPCR, visual rhodopsin, is available [1-3]. As a result, new methodologies need to be developed to study these receptors.

The over-arching goals in this dissertation are two-fold: (1) to develop novel fluorescence methodologies for studying the structure and conformational dynamics of GPCR activation, and (2) to use a fluorescence spectroscopic approach to study the oligomerization state of visual rhodopsin, the model GPCR.

The first part of the introductory chapter will provide a general background on G-protein coupled receptor activation and signaling. It will also review traditional methods as well as newly emerging spectroscopic methods used to study membrane protein structure/function and conformational dynamics. This chapter will then discuss current literature regarding the oligomerization state of GPCRs and its significance to receptor function and pharmaceutical therapeutics. Finally, I will discuss the structural data on visual rhodopsin, with a summary on the controversy surrounding the oligomerization state of this receptor. A dissertation overview is presented at the end of this chapter.

* * *

1. 1: G-PROTEIN COUPLED RECEPTORS

Genome analysis has shown that a large superfamily of membrane proteins, called G-protein coupled receptors (GPCRs), encompass approximately 950 genes in the human genome [4,5]. This superfamily is involved in a wide variety of physiological processes, and mutations in these receptors have been implicated in numerous diseases [6]. Currently, GPCRs form the largest class of therapeutic targets [7-9], comprising more than 50% of drug targets [10,11]. Two pressing questions in the GPCR field involve understanding how receptor structural dynamics and oligomerization state affect function and signaling.

1. 1. 1: Historical Background on G-Protein Coupled Receptors.

Experiments on “receptive substances”, performed more than 100 years ago, are now known to have involved ligand-binding G-protein coupled receptors. Many of today’s essential concepts in pharmacology, such as binding sites, receptor theory, the definitions of agonists and antagonists, affinity, efficacy, as well as the use of radioligands for binding site and receptor quantification, emerged from these early studies of GPCRs. Many of the important elements of the signaling cascade were discovered in the 1960s and 1970s, before the molecular identity of the receptors was identified [12,13]. Major discoveries include the identification of cyclic adenosine monophosphate (cAMP) as the first characterized second messenger molecule [14], the identification of the enzyme adenylate cyclase as responsible for the synthesis of cAMP, and the heterotrimeric G-proteins as the transducers of the signal.

The first GPCR identified and purified was visual rhodopsin (reviewed in [15]). Rhodopsin is the only GPCR naturally present in high abundance in biological tissue.

After methods were developed to isolate rod outer segment (ROS) disk membranes, the purification of rhodopsin on an affinity column in detergent was reported [16], and rhodopsin became a model for early studies on membrane proteins. Several years later, the first ligand-binding GPCR, the β_2-adrenergic receptor, was purified [17]. Interestingly, at this time, no connection was made between rhodopsin and the ligand-binding GPCRs.

It was not until the mid 1980s when advances in molecular biology techniques revealed the sequence similarities and obvious homology between visual rhodopsin and the β_2-adrenergic receptor. Studies on the mechanisms of visual rhodopsin function had identified its association with the G-protein transducin [18], and the functional analogies between rhodopsin/transducin and β_2-adrenergic/G_s were finally appreciated [19,20]. Thus, based on both the sequence and signaling mechanism similarities between visual rhodopsin and the β_2-adrenergic receptor, it was established that rhodopsin, because of the ease by which it is obtained from bovine retina preparations, would provide a useful and convenient model system for GPCRs. Years of cloning have subsequently identified a large number of GPCRs, all showing the characteristic seven transmembrane signatures in hydrophobicity plot analysis. To this day, both visual rhodopsin and the β_2-adrenergic receptor remain the best understood model systems for studying GPCR structure and function.

1. 1. 2: Diverse Biological Processes Through a Conserved Structure.

The majority of transmembrane signal transduction events that respond to hormones and neurotransmitters are mediated through GPCRs [21]. These receptors play important roles in multiple systems including, but not limited to, vision, olfaction, feeding and satiety, regulation of the immune system and inflammation, behavior and mood regulation, as well as autonomic nervous system transmission. In each of these systems, however, the receptors play the same functional role: they provide the molecular link that communicates extracellular signals across the cell membrane to trigger intracellular response pathways.

Because GPCRs are involved in such a wide variety of sensory and physiological responses, it is not surprising that there is tremendous variability in the types of GPCR ligands, ranging from photons and ions to small molecules and peptides. However, despite the vast diversity in the sizes and shapes of the ligands, these receptors have evolved to arrive at a conserved molecular structure [22]. GPCRs are characterized structurally by an amino-terminal extracellular domain, a carboxy-terminal intracellular domain, and a core domain made of seven hydrophobic transmembrane α-helices. GPCRs can further be divided into five family subtypes based on more significant sequence homology [23]. The type “A” subfamily (rhodopsin-like subfamily) is the largest of these five subfamilies and includes visual rhodopsin and the β_2-adrenergic receptor [22,24]. Figure 1. 1A shows a two-dimensional model of visual rhodopsin highlighting some of the key features shared by type A GPCRs. The overall three-dimensional fold of GPCRs is demonstrated with the structure of visual rhodopsin in Figure 1. 1B.

In the GPCR system, the heterotrimeric guanine nucleotide-binding regulatory proteins (G-proteins) are the signal transducers which relay the information from the membrane-bound receptor to the various effector systems. The G-protein consists of three subunits: α, β, and γ. Additionally, each subunit can be further divided into multiple subtypes generating an additional layer of diversity [25-27]. This greatly increases the number of signal transduction pathways in which G-proteins can participate, as each subtype can regulate the activity of different effector proteins. The tremendous variability observed in the GPCR system, both at the level of the ligand, as well as the level of the G-protein, explains why these receptors can control so many different biological systems [28].

1. 1. 3: GPCR Signaling Activation.

Figure 1. 2A provides an overview of GPCR signaling. The interaction of the ligand or "agonist" with the GPCR binding pocket, found either within the hydrophobic core of the α-helices or within the amino-terminal domain of the receptor, begins the signal transduction cascade. Following ligand binding, the activated receptor binds to, and induces conformational changes in, its cognate G-protein α-subunit. This stimulates the exchange of GDP for GTP on the α-subunit, inducing the GTP-bound α-subunit to release from its β/γ partners as well as from the active receptor [29-31]. For all G-proteins, the GDP- and GTP-bound complexes define the inactive and active states, respectively. The released α_{GTP} and β/γ subunits then modulate downstream signaling pathways through interaction with various effector proteins such as adenylate cyclases, phospholipases, various channel proteins and second messenger systems [25,26,32] (Figure 1. 2A). It is now generally established that the β/γ complex mediates as many functions as the α_{GTP} subunit [25].

One of the most important and powerful aspects of the GPCR system is the signal amplification that occurs through the catalytic activity of the receptors. That is, the binding of one ligand to activate one receptor can induce the GDP/GTP exchange in multiple G-proteins. In turn, each G-protein subunit can subsequently modulate the activity of multiple second messengers and multiple effector proteins. The resulting signal transduction cascade serves two important roles. First, it amplifies the original signal, ensuring a cellular response even from, in the case of visual rhodopsin, the absorption of as little as a single photon of light [33,34]. Second, it ensures a prompt cellular response time.

1. 1. 4: GPCR Signaling Attenuation.

Nearly all GPCRs are tightly regulated through a common desensitizing mechanism [35,36]. The α-subunit remains active until the bound GTP is hydrolyzed back to GDP, using the intrinsic GTPase activity of the α-subunit [32]. Receptor inactivation, however, requires a number of steps and involves the activities of two families of proteins. First, the G-protein coupled receptor kinases (GRKs) phosphorylate the C-terminus of the receptor [35,37]. Next, the action of the arrestin family of proteins recognize and bind to phosphorylated receptor to prevent coupling to G-proteins [35-37]. A summary of the steps involved in GPCR attenuation can be seen in Figure 1. 2B. In addition to blocking receptor/G-protein coupling, the arrestins also play a role in receptor internalization by acting as adapters to recruit the internalization machinery [35]. Following internalization, the GPCRs are either recycled back to the plasma membrane in the case of type “A” GPCRs or degraded in the case of type “B” GPCRs [38].

1. 1. 5: GPCR Activation Involves Receptor Dynamic Conformational Changes.

How does the binding of a ligand on the extracellular domain of the receptor trigger events on the inside of the cell? One theory is that ligand binding provides the energy used to overcome the interactions that stabilize the inactive receptor [21,39] and induces a conformational change through the receptor's transmembrane domain [40-42]. This conformational change opens up cytoplasmic binding sites allowing the receptor to activate the G-proteins, leading to a physiological response inside the cell [21,43-45].

It is hypothesized that an "ionic lock", formed between an Asp(Glu)-Arg residue pair at the cytoplasmic loop of transmembrane domain III (forming the highly conserved D(E)RY motif in type "A" GPCRs; see Figure 1. 1) and a Glu residue (conserved in amine and opsin receptors) at the cystoplasmic end of transmembrane domain VI (TM VI), maintains GPCRs in the resting state [46-48]. Evidence for light-induced conformational changes in visual rhodopsin that may disrupt the "ionic lock" to trigger receptor activation has been reported in a series of biophysical studies. Specifically, proximity experiments using electron paramagnetic resonance spectroscopy (EPR) showed that photo-activation of rhodopsin involves a rotation and tilting of TM VI relative to TM III. Preventing this movement by cross-linking the helices together precludes G-protein activation [41]. Consistent with this type of movement, cysteine residues on the inner face of TM VI are protected from modification with a bulky cysteine-specific fluorescent probe in the dark state but are susceptible to modification immediately following light activation [42]. Furthermore, fluorescence measurements indicate that a small fluorophore attached to a cysteine residue on the inner face of helix VI detected changes in the polarity of its environment following light-activation, consistent with a movement that exposes the fluorophore to solvent [42] (see Figure 1. 3A). These results are important because they were among the earliest data to suggest that specific conformational changes are important for GPCR activation and signaling.

However, they do not resolve the exact nature of the movement or rule out concomitant movements in surrounding helices.

A single conformational change might not be sufficient to fully activate a GPCR. Recent reports from the Kobilka laboratory have demonstrated, using fluorescence techniques, that GPCR activation is a conformationally complex phenomenon, with different ligands (agonists, partial agonists, and antagonists) inducing distinct, ligand-specific, conformational states [40,49,50]. This has led to the proposal of the sequential binding model in which an unliganded receptor exists in a dynamic and relatively flexible state and binding of the ligand occurs through multiple, kinetically distinguishable steps leading to discrete, intermediate conformational states [51] (Figure 1. 3B). It is clear that a mechanistic understanding of how GPCRs become activated will ultimately require an understanding of each of these distinct conformational changes at the molecular level.

The majority of data in the literature agrees that some type of conformational change is involved in GPCR activation. Recently, however, the crystal structure of a light-activated form of rhodopsin was determined [1]. Interestingly, the structure shows no evidence of transmembrane domain movements relative to the dark state crystal structure of rhodopsin [3], leading the authors to suggest that changes in receptor structure upon photo-activation are smaller than previously predicted. According to their model, activation may simply involve receptor relaxation to a somewhat less rigid structure rather than a distinct conformational change [1]. Clearly, more research needs to be performed as to the extent and location of the structural changes involved in GPCR activation.

The first two chapters of this dissertation describe my development of new techniques which can be used to measure the type of dynamic, real-time changes in protein structure that are proposed to occur during GPCR activation. These methods (described in Chapter 2 and Chapter 3) have been successfully used to identify a clear conformational change between TM III and TM VI in rhodopsin [52] and in the β_2-adrenergic receptor [40]. To place the significance of the new fluorescence techniques developed in this dissertation into context, the next section will discuss the limitations in traditional structural methods as well as newly emerging spectroscopic methods to study membrane protein structure/function and conformational dynamics.

1. 2: TECHNIQUES USED TO STUDY GPCR STRUCTURE AND DYNAMICS

1. 2. 1: Limitations of Traditional Methodologies to Study GPCR Structure.

Both X-ray crystallography and nuclear magnetic resonance (NMR) spectroscopy can produce atomic resolution structures of proteins. However, to date, there is only one structure described for a GPCR, the visual receptor rhodopsin. The striking disparity between the importance of GPCRs relative to the limited high-resolution data available reflects the inherent difficulty involved in their structural characterization.

Part of the difficulty in studying GPCR structure by X-ray crystallography is the requirement of large amounts of pure, homogenous sample. Additionally, the detergents used to solubilize the membrane proteins out of the lipid environment often produces samples too heterogeneous to easily crystallize. Finally, the dynamic structure of many membrane proteins with flexible regions reduces the number of possible crystal contacts and makes structure determination that much more difficult [53]. Even after obtaining the dark state crystal structure of rhodopsin, the static picture provided by X-ray crystallography cannot provide insight into any dynamic events and mechanisms involved in GPCR activation.

Although NMR spectroscopy can be used to measure protein structural dynamics [54,55], it is not sensitive – large amounts of sample are required at high protein concentrations. Additionally, solution NMR is typically limited to solving the structures of small and medium-sized molecules in the ~ 25 - 35 kDa range [56], although it may soon be possible to tackle proteins as large as 100 kDa [57,58]. Researchers have found ways to obtain enough sample to study rhodopsin dynamics using NMR by specifically labeling cysteine, tyrosine and/or lysine residues [59-62], but there are currently no NMR structures of full-length GPCRs.

1. 2. 2: New Site-Directed Labeling Methodologies.

Because of the shortcomings of X-ray crystallography and NMR spectroscopy described above, researchers have sought to develop new techniques to study membrane protein structure and dynamics. Recently, in combination with site-directed mutagenesis, site-directed probing methods have emerged as a unique and flexible tool for approaching these questions with structural resolution at the level of the backbone fold [63,64]. These methodologies include site-directed spin labeling (SDSL) for electron paramagnetic resonance spectroscopy (EPR) and site-directed fluorescence labeling (SDFL) for fluorescence spectroscopy. The probing methods involve first introducing cysteine residues systematically into a defined region of a protein, then attaching spectroscopic probes to the cysteines. The probes are used to glean information about the local environment around each probe molecule. Combining the array of data generated from a scan of such probes through a region allows deduction of the solvent-accessibility and secondary structure of the region being studied.

Site-Directed Labeling. The general strategy of SDL is to systematically introduce cysteine residues, one at a time, into defined regions of a protein. To each cysteine residue, some type of spectroscopic probe, for example a nitroxide spin label (for SDSL) or a fluorescent reporter group (for SDFL), is then attached, and the mobility and solvent accessibility of the labels are determined from analysis of the EPR data or the fluorescence data, respectively. Through the combination of scanning each side-chain position through a domain of a protein sequence and distance measurements between reporter groups, movements between regions of a protein can be detected and three-dimensional models can be generated. A key feature to this approach is the fact that introduction of the reporter probe usually does not result in large changes to the structure of the protein at the level of the backbone fold. For reviews of the SDSL technique, see [63,65-68]. SDSL will not be discussed further in this Dissertation. Rather, I will focus on SDFL, its background and uses.

Note - the rest of this section will describe the basic principles of fluorescence spectroscopy and how, in combination with site-directed fluorescence labeling, it can be used to study protein structure and conformational changes. Since examples of these types of analyses are present in Chapter 2, Chapter 3, and Chapter 4, a brief description of the theory behind the methods is given below.

Fluorescence Spectroscopy. Fluorescence is a spectroscopic technique that follows the absorption and emission of photons in molecules from a photo-induced excited state back to the ground state. These basic processes are outlined in the Jabłoński diagram shown in Figure 1. 4. For a molecule to absorb a photon, the energy of the incident photon must match the energy difference between the ground state and one of the excited state energy levels of the molecule. When the incident photon is in the visible spectrum, electrons are promoted from the ground state to a higher vibrational energy level within either the first or second electronic excited states, S_1 or S_2. If the electron is promoted to an electronic level higher than S_1, it is almost always the case that, in solution, it will immediately (10^{-12} seconds or less) [69] relax back to the lowest vibrational state in S_1 through processes known as internal conversion and vibrational relaxation. Once in the first electronic excited state, electrons can return to the ground state by a number of processes, only one of which results in a fluorescence emission signal. These include: (1) external conversion from non-specific collisional deactivation, (2) intersystem crossing resulting in a phosphorescence signal, (3) energy transfer to an acceptor fluorophore, (4) specific quenching processes by small molecules or ions, including electron transfer, and (5) fluorescence emission (refer to the Jabłoński diagram in Figure 1. 4). These processes are briefly described below.

External Conversion. Perhaps least interesting to the spectroscopist, a molecule in the excited-state may collide with other molecules and lose its excited state energy through non-specific collision called external conversion (k_{EC}). The molecules that lose their energy in this manner do not contribute to the fluorescence emission signal and this type of emission is non-radiative (k_{NR}).

Intersystem Crossing. Intersystem crossing involves an electron undergoing a spin flip and transition to a triplet state, T_1. Relaxation down to the ground state from the T_1

triplet state is referred to as phosphorescence, which can be measured in the visible spectrum with lifetimes on the order of hundreds of microseconds to several milliseconds. Transitions from $S_1 \rightarrow T_1$ are somewhat rare because they result in a spin flip which is considered forbidden, resulting in rate constants for phosphorescence that are many orders of magnitude smaller than for fluorescence ($k_P << k_F$). Additionally, the triplet state is of lower energy than the singlet state, and the phosphorescent emission is almost exclusively at longer wavelength than the fluorescent emission.

Fluorescence Resonance Energy Transfer (FRET). FRET is yet another process in which an excited state can be depopulated. This can occur when the emission spectrum of the excited-state fluorophore, called the donor, overlaps with the absorbance spectrum of another molecule, called the acceptor, which may or may not be fluorescent. An example of this spectral overlap for a donor/acceptor pair can be seen in Figure 4. 3B. Energy transfer does not involve emission of light by the donor and there is no intermediate photon; the donor and acceptor are coupled by a dipole-dipole interaction [69]. This dipole interaction depopulates the excited-state of the donor, thereby decreasing the probability that fluorescence will occur from the donor.

Quenching. A wide variety of small molecules and ions can depopulate an excited-state by colliding with the fluorophore, returning the electrons to the ground state in a radiationless manner. These small molecules act as quenching agents because they decrease the overall fluorescence emission intensity. This type of quenching is dependent on the number of collisions per second (k_q) as well as the concentration of quenching agent ([Q]) and the rate is described by k_q*[Q]. A sub-type of quenching referred to as electron transfer can also occur. In this type of quenching, the excited state fluorophore acts as an electron donor or electron acceptor when interacting with a ground-state species.

Fluorescence Emission. Finally, if energy is not lost through any of the above processes, following internal conversion and vibrational relaxation down to the lowest vibrational sub-state in the first electronic excited state, an electron may relax from S_1 to its electronic ground state S_0 in the process known as fluorescence. In doing so, it emits light of the wavelength corresponding to the energy gap between S_1 and S_0.

Fluorescence Quantum Yield and Lifetime. The fluorescence quantum yield (Q) of a fluorophore is a term used to describe how fluorescent a molecule is, reflected by the ratio of the number of photons emitted to the number absorbed. Mathematically, this can be expressed by the fraction of fluorophores which decay through fluorescence emission compared to the sum of all the ways that an excited state can be depopulated (refer to Figure 1. 4):

$$Q = \frac{k_F}{k_F + k_P + k_{EC} + k_{RET} + k_q[Q]} = \frac{k_F}{k_F + k_{NR}} \qquad \text{[Eq. 1. 1]}$$

where k_F is the fluorescence radiative rate and k_{NR} is the non-emissive radiative rate, composed of all the processes from Figure 1. 4 that do not result in fluorescence emission yet still depopulate the excited state. The quantum yield is close to unity when the non-emissive radiation rates are much smaller than the emissive radiation rates, $k_{NR} << k_F$.

The lifetime of the excited state, τ, is the average period of time the fluorophore remains in the excited state [69] and can be represented by:

$$\tau = \frac{1}{k_F + k_{NR}} \qquad \text{[Eq. 1. 2]}$$

Thus, the value of τ is inversely proportional to the rate of relaxation from $S_1 \rightarrow S_0$. Typical fluorescence lifetimes are on the order of nanoseconds.

The usefulness of fluorescence spectroscopy emerges because changes in the fluorescence signal reveals information about the environment around the probe.

The Fluorescence Signal Can Reveal Protein Structural Information. Figure 1. 5 highlights three categories of fluorescence measurements that can be performed to obtain protein secondary structural information as well as tertiary structural constraints: *(i)* accessibility of the fluorophore to external quenching agents or to solvent, *(ii)* mobility of the fluorophore, and *(iii)* proximity between two fluorophores. These are described in further detail below.

(i) Accessibility Studies. Fluorescence quenching can be used to provide insight into the dynamic nature of protein structure [70,71]. Whether a fluorophore attached to a cysteine residue on a protein backbone is buried or exposed can be determined by measuring its rate of collision with an external quenching agent such as I^- or acrylamide. A greater rate of collision correlates with greater accessibility whereas lower rates of collision indicate that the label is buried inside the protein's three-dimensional fold. Collision rates are assessed by measuring the fluorescence intensity in the presence of increasing concentrations of external quencher. The greater the decrease in fluorescence intensity at any given quencher concentration suggests a more exposed fluorophore. This type of study is called a Stern-Volmer quenching analysis and can be used to directly determine how exposed the fluorophore is [69].

The accessibility of probes sensitive to solvent polarity can also be assessed simply by measuring the emission λ_{max} of the fluorophore at each site of attachment. The dependence of the emission λ_{max} for these solvent sensitive probes results from a re-orientation of the solvent shell around the chromophore when it is excited [72]. Fluorescent groups that have a higher dipole moment in the excited state compared to the ground state show this effect. Consequently, the emission is shifted toward the red (lower energy) in polar environments and toward the blue (higher energy) in nonpolar environments. Thus, attachment of the fluorophore at a solvent accessible site in a protein fold results in a relatively red-shifted emission spectra while attachment of the fluorophore at a buried site results in relatively blue-shifted emission spectra. Comparison between different sites on a protein, then, will allow relative assignments of “buried” or “exposed”.

The power of accessibility studies emerges when used in conjunction with a scanning approach. Using these techniques, a systematic scan through sequential residues in a short peptide [73], in a full-length soluble protein [64], or a membrane protein [74-76] can reflect periodic repeats in secondary structure and identify membrane/water interfaces.

(ii) *Mobility Studies*. The mobility of a fluorophore attached to a protein can be determined by measuring its anisotropy. In these types of studies, the light used in excitation is plane polarized and the amount of polarization that remains in the emitted light is assessed. The technique of anisotropy is possible because both the absorption and the emission of molecules contain transition moments that lie along specific directions within a fluorophore’s structure [69]. When free in solution, the ground state absorption transition moments of a molecule are homogenous and randomly oriented. However, once exposed to plane polarized light, only those fluorophores which have their absorption dipoles oriented along the electric vector of the excitation light become preferentially excited. In this manner, randomly oriented ground-state molecules can be selectively oriented in the excited-state. Measuring the anisotropy of a molecule then involves monitoring how the emission dipole properties of the selectively oriented excited-state changes relative to the absorption dipole.

For moieties that are freely mobile (ie., a fluorophore on the surface of the protein), the emission will lose its polarization due to the scrambling of the absorption dipole and will display a low anisotropy. However, for groups that are not freely mobile and thus have not moved or rotated significantly between excitation and emission (ie., a fluorophore buried inside a protein fold), the emission will retain the same polarization dipole used to excite it and will thus display a high anisotropy [69]. It has been found that fluorescent labels at buried sites exhibit a higher anisotropy than labels at exposed sites, indicating that the dense packing of residues at buried sites restricts the rotational mobility of the probe. Just as with the accessibility studies, systematically labeling sequential residues in a short peptide [73] or a full-length protein [64], and measuring the resultant anisotropy, can reveal periodic repeats in secondary structure.

(iii) Proximity Studies. In 1967, Stryer demonstrated that fluorescence resonance energy transfer (FRET) can be readily used as a spectroscopic ruler to determine distances of ~ 20 – 100 Å in proteins [72,77,78]. As discussed in the previous section, FRET measurements are based on the observations that energy absorbed by a chromophore (donor) can be transmitted to another chromophore (acceptor) through space in a distance-dependent manner. The rate of energy transfer (k_{RET}) is governed by:

$$k_{RET} = \frac{1}{\tau_D}\left(\frac{R_0}{r}\right)^6 \qquad \text{[Eq. 1. 3]}$$

where τ_D is the lifetime of the donor in the absence of acceptor, R_0 is called the Förster distance which reflects the distance at which the energy transfer efficiency is 50%, and r is the distance between the donor and acceptor.

The rate of energy transfer is also related to efficiency of energy transfer, (E), defined as the fraction of photons absorbed by the donor that are transferred to the acceptor:

$$E = \frac{R_0^6}{R_0^6 + r^6} \qquad \text{[Eq. 1.4]}$$

For energy transfer to occur between two molecules, a number of criteria must be satisfied. First, the emission spectrum of the donor fluorophore must overlap with the absorbance spectrum of the acceptor fluorophore. The greater the overlap integral, called $J(\lambda)$, the greater the value of R_0, and the faster the rate of energy transfer. Additionally, the quantum yield of the donor and the relative orientation between the donor and the acceptor can affect the rate. Finally, implicit in Eq. 1. 3 and Eq. 1. 4, the rate and efficiency of energy transfer are highly dependent on the distance between the donor and acceptor – the closer the distance, the greater the energy transfer efficiency. Using Eq. 1. 4, determining the efficiency of energy transfer in any given FRET experiment can predict distances between sites in a protein since the value of R_0 is constant for any given donor/acceptor pair.

There are four ways to determine energy transfer efficiency in an experiment. The most reliable method is from the excitation spectrum of the energy donor. In such an experiment, the emission of the acceptor is monitored while the excitation spectrum of the donor is scanned. In this manner, the efficiency of energy transfer is calculated according to:

$$E = \left[\frac{G(\lambda_2)}{G(\lambda_1)} - \frac{\varepsilon_A(\lambda_2)}{\varepsilon_A(\lambda_1)}\right] * \left(\frac{\varepsilon_A(\lambda_1)}{\varepsilon_D(\lambda_2)}\right) \qquad \text{[Eq. 1. 5]}$$

where G(λ) is the magnitude of the corrected excitation spectrum of the energy acceptor at wavelength λ, and ε_A and ε_D are the extinction coefficients of the energy acceptor and donor at wavelengths λ_1 and λ_2. The wavelengths λ_1 and λ_2 should be chosen such that at λ_1, the donor has minimal absorption and at λ_2, the extinction coefficient of the donor is large compared to that of the acceptor.

Another way to measure the efficiency of energy transfer is by monitoring the relative fluorescence intensity and fluorescence lifetime of the donor fluorophore:

$$E = 1 - \frac{F_{DA}}{F_D} \qquad \text{[Eq. 1. 6]}$$

where F_D is the relative fluorescence intensity of the donor in the absence of acceptor and F_{DA} is the relative fluorescence intensity of the donor in the presence of acceptor.

$$E = 1 - \frac{\tau_{DA}}{\tau_D} \qquad \text{[Eq. 1. 7]}$$

where τ_D is the lifetime of the donor is the absence of acceptor and τ_{DA} is the lifetime of the donor in the presence of acceptor. Although this method can produce highly accurate efficiency values, care must be taken to ensure that energy transfer, and not some other quenching phenomenon, is the cause of the decrease in donor intensity and lifetime.

Finally, the efficiency of energy transfer can be determined by measuring the size of the enhanced acceptor fluorescence:

$$E = \left(\frac{\varepsilon_A(\lambda_D^{ex})}{\varepsilon_D(\lambda_D^{ex})}\right) * \left[\frac{F_{AD}(\lambda_A^{em})}{F_A(\lambda_A^{em})} - 1\right]\left(\frac{1}{f_D}\right) \qquad \text{[Eq. 1. 8]}$$

where ε is the extinction coefficient, F_{AD} is the fluorescence intensity of the acceptor in the presence of donor, F_A is the fluorescence intensity of the acceptor in the absence of donor, and f_D is the labeling ratio of the donor. Furthermore, λ_D^{ex} represents the wavelength at which the donor is excited and λ_A^{em} represents the wavelength of the enhanced acceptor fluorescence. This equation assumes that the donor does not contribute intensity at the wavelength of enhanced acceptor emission. Because this is often not true, this is the least accurate method for calculating FRET efficiency [69].

Derivations of FRET, called luminescence resonance energy transfer (LRET) and bioluminescence resonance energy transfer (BRET), have been developed (for reviews see [79-81]). The principles of LRET are discussed in detail in Appendix 2. Very recently, a manuscript demonstrated that steady-state anisotropy can also be used to determine distances between two identical fluorophores using fluorescence homotransfer [82].

Chapter 2 and Chapter 3 of this dissertation describe my development of a method, complementary to FRET, that can measure short-range distances within proteins from 5 – 15 Å. This technique involves the distance-dependent quenching of a bimane fluorophore by tryptophan residues, presumably through a photo-induced electron transfer mechanism. My initial discovery of the distance-dependent quenching of bimane fluorescence by proximal Trp residues emerged from an SDFL calibration of the bimane fluorophore, briefly described below.

1. 2. 3: Example of SDFL: Protein Secondary Structure Determination – A Calibration Study.

Earlier, I was involved in a comprehensive study to calibrate the SDFL technique. Our goal was to determine which fluorescence parameters accurately and reliably reflect secondary structure in a full-length protein [64]. The results of this study are briefly covered below as they set the stage for the first two chapters of this dissertation. The study involved an analysis of twenty-one mutants of T4 lysozyme (T4L) in which consecutive cysteine residues were introduced in the protein traversing a helix-turn-helix motif, labeled with the fluorescence probe monobromobimane (mBBr), and the fluorescent properties of each bimane labeled site recorded (Figure 1. 6). The study allowed a direct comparison of the SDFL fluorescence data with the known structure of T4 lysozyme to determine which fluorescence parameters (fluorescence excitation spectra, emission spectra, lifetime, quantum yield, and steady-state anisotropy) best reflected the protein secondary structure [64].

Introduction of the mBBr Label Does not Dramatically Alter Protein Structure. Monobromobimane was used, in part, because it is a relatively small fluorescent probe (molecular volume of bimane is 158 $Å^3$ compared to 128 $Å^3$ for a tryptophan residue). Thermodynamic analysis of the mBBr-labeled samples indicate the probe did not dramatically alter the protein fold unless introduced at largely buried residues. Introduction of the fluorescent label into sites with greater than 40 $Å^2$ solvent accessible surface area resulted in destabilizations that were less than 1.5 kcal/mole.

Monobromobimane Exhibits Solvent Sensitive Fluorescence Properties. The spectral properties of mBBr-labeled mutants vary at different sites on the protein, indicating mBBr is a solvent-sensitive probe (Figure 1. 7). For example, addition of a bimane label to an exposed cysteine residue at site E128C on T4 lysozyme (referred to as E128B$_1$) has red shifted spectral properties relative to placement of a bimane label at a buried site (L133B$_1$). Calibration of these spectral shifts (performed in various mixtures of dioxane/water) enable one to convert the wavelength shifts to an apparent polarity (insets of Figure 1. 7).

Apparent Polarity and Steady-State Anisotropy Best Reflected the Solvent Surface Accessibility in a Full-Length Protein. Of all the fluorescence parameters assayed, the fluorescence emission λ_{max} values and the steady-state anisotropy values of the mBBr-labeled mutants best reflected the T4L protein structure. Specifically, they best reflected the solvent-accessible surface area of residues 115 - 135 in T4L (Figure 1. 8). Figure 1. 8A shows the calculated solvent surface accessibility at each residue compared to the apparent polarity at each residue versus the residue number. Figure 1. 8B compares the fluorescence anisotropy as a function of residue number. Notice how both these parameters visually reflect the periodic nature of the helix-turn-helix motif.

Conclusions of the Calibration Study. Analysis of the results from the SDFL study established that a cysteine scan coupled to labeling with the fluorescence probe monobromobimane (mBBr) can be used to determine the solvent accessible surface of the protein, from which the protein's secondary structure could be inferred.

In Chapter 2 and Chapter 3 of my Dissertation, I demonstrate that an SDFL approach with bimane can also provide additional information regarding protein structure. Chapter 2 describes my discovery that bimane can also be used to obtain distance constraints within a protein structure, providing tertiary structural information.

Chapter 3 shows how an SDFL scan, coupled with the determination of distance constraints, can be rapidly performed using a bimane derivative, enabling a “high-throughput” approach. Both of these types of analyses becomes very important for studies of protein folding or for the dynamic, real-time monitoring of conformational changes within proteins.

Finally, in Chapter 4 of this Dissertation, I describe my use of fluorescence resonance energy transfer methods (FRET and LRET) to assess the oligomerization state of visual rhodopsin in a membrane environment. I demonstrate how SDFL methods can be employed to study oligomerization states of membrane proteins in solution, an experiment that is difficult to perform using traditional structural methodologies. Importantly, the results from these studies provide compelling evidence that rhodopsin self-associates in a membrane environment.

1. 3: OLIGOMERIZATION OF GPCRs

Classically, GPCRs have been assumed to exist and function in membranes as monomers. Because of this, the paradigm of GPCR ligand binding and signal transduction was based on the 1 : 1 : 1 hypothesis: one ligand binds to one receptor, and in turn, the ligand/receptor complex activates one G-protein at a time. However, a growing body of evidence suggests this view is too simplistic, as some GPCRs appear to form both homodimers and even heterodimers.

A few of the key lines of evidence leading to the belief that GPCRs exist as functional oligomers are reviewed below. Note - the majority of studies on GPCR dimerization do not make a distinction between dimers or higher order oligomers and the term “dimer” is often used by default, interchangeably with the terms oligomer and multimer. At the moment, there is no conclusive evidence to indicate the extent of oligomerization in GPCRs, ie. exactly how “large” the oligomers of GPCRs are.

1. 3. 1: Evidence that GPCRs Form Homodimers and Heterodimers.

Early pharmacological observations suggested GPCRs may function as dimers or higher order oligomers. Complex binding curves for ligands of the β-adrenergic receptor and the muscarinic receptor were interpreted as evidence of negative cooperativity or allosterism in the ligand binding site between receptors [83-85], leading some authors to suggest that “…muscarinic receptors normally exist in the membranes as dimers” [85]. Further support for dimers of the muscarinic receptor was provided by experiments demonstrating the amino- and carboxy-termini of muscarinic receptors fold as independent units [86], while chimeric proteins of the adrenergic and muscarinic receptors in which the C-terminal portions were exchanged required expression of both chimeras to retain functionality [87].

Immunoprecipitation studies using differential epitope tagging has also been employed to demonstrate oligomers of a number of GPCRs including $GABA_B$ [88-90], mGluR5 [91], δ-opioid [92], calcium [93], M3 muscarinic [94], and serotonin receptors [95]. However, these types of studies are fraught with potential artifacts. GPCRs are hydrophobic membrane proteins and incomplete solubilization in the immunoprecipitation and cross-linking studies could easily result in non-specific aggregation making it difficult to discriminate true protein-protein interactions from nonspecific aggregates formed during the extraction procedure [96,97]. Because of these problems, several groups turned to functional assays and biophysical fluorescence assays to look for the existence of GPCR dimers in living cells – these approaches and results are discussed below.

The first widely accepted and most compelling demonstration of GPCR heterodimerization was performed on the $GABA_B$ receptors by functional complementation [98,99]. Neither the first $GABA_B$ receptor cloned ($GABA_BR1$) [100], nor a subsequent $GABA_B$ receptor with high homology to $GABA_BR1$ ($GABA_BR2$) [88-90,101-103], could be expressed or functionally characterized [104]. However, when co-expressed together, $GABA_BR1$ and $GABA_BR2$ were found to assemble into a functional $GABA_B$ receptor hetero-dimer that trafficks efficiently to the cell surface [98]. This set of experiments demonstrated that receptor heterodimerization between $GABA_BR1$ and $GABA_BR2$ is essential for $GABA_B$ function. Co-immunoprecipitation studies provided physical evidence supporting the functional evidence [88,89,101].

Functional heterodimerization between the histamine H1 receptor and the α_{1b}-adrenergic receptor was demonstrated in an interesting approach from Milligan’s laboratory [105]. The authors generated and analyzed fusion proteins between either wild type GPCRs or mutant GPCRs unable to activate G-proteins and wild type or mutant G-proteins unable to be activated by GPCRs. The authors showed that co-expression of pairs of these non-functional mutant fusion proteins is complementary, producing functional dimers. Fusion proteins in which the α-subunit of the G-protein is linked to the C-terminus of a GPCR have been previously shown to be a useful tool to study the GPCR/G-protein interaction [106,107]. The authors concluded that dimers of these receptors could only function via trans-activation of associated G-proteins. If true, this has interesting functional consequences, especially when considering GPCR heterodimerization.

Multiple groups have moved to assess GPCR oligomerization in living cells using biophysical, instead of functional, assays [108-116]. These studies are based on fluorescence resonance energy transfer (FRET) and bioluminescence resonance energy transfer (BRET) techniques. Both of these techniques measure the transfer of energy from a donor molecule to an acceptor molecule only when they are roughly 20 – 100 Å apart [79,81].

These energy transfer techniques were originally employed to demonstrate homodimerization of the β_2-adrenergic receptor [110] and the yeast α-mating factor [112]. Since then, dimerization of the δ-opioid receptor [113], the dopamine receptor [113], and the luteinizing hormone receptor [116] have also been confirmed in whole cells using energy transfer. By performing BRET experiments in cells, the influence of β-adrenergic receptor density on the size of the energy transfer signal allowed a quantitative assessment of β_1- and β_2- receptor homo- and heterodimerization, where it was concluded that the proportion of adrenergic receptors forming dimers is > 80% [108]. Dimerization of GPCRs selectively measured at the cell surface has been performed using hydrophilic BRET agonists that cannot cross the cell membrane [110,113] or by using modified FRET with fluorescent antibodies directed to the extracellular region of the receptors [114,115]. However, the concern that positive FRET signals in these heterologous expression systems may simply be due to over-expression and receptor crowding, and not specific protein/protein interactions, have led some to challenge the validity of these studies [117]. Work still needs to be done to determine whether all, or just a small subset of GPCRs exist in the membrane as dimers.

1. 3. 2: Significance of GPCR Dimers.

The possibility of GPCR/GPCR interactions has not only resulted in the revision of traditional models of ligand/receptor structure and function, it has also created new paradigms in signal transduction. The idea that GPCRs exist in the membrane as dimers or higher order oligomers has a profound impact for both science and medicine.

GPCR Dimerization Challenges Traditional Signal Transduction Paradigms. It is becoming clear the model that ligand, receptor, and G-protein operate in a 1: 1: 1 stoichiometry needs revision. If receptors exist as dimers, how many ligands bind to the receptor dimers? How might a dimer affect coupling to G-proteins? What is the stoichiometry between receptor and G-protein - does the receptor dimer activate one G-protein at a time or multiple G-proteins? In a monomeric model of the rhodopsin/transducin interaction, the interface surface area of visual rhodopsin is too small to cover all of the regions of transducin known to be critical for interaction with the receptor. Modeling studies suggest the surface area of one transducin molecule is large enough to accommodate the docking of <u>four</u> rhodopsin molecules [118]. Clearly, the stoichiometry involved in GPCR signal transduction is not yet defined.

As mentioned earlier, one of the most powerful aspects of GPCR signaling is the signal amplification that occurs inside the cell. Traditionally, this amplification has been thought to only occur at the level of the G-protein. However, if the binding of a single agonist to a single receptor might activate <u>neighboring</u> receptors with which the agonist-bound receptor is oligomerized [119], it would imply that signal amplification may even occur at the level of the receptor – yet another paradigm shift in GPCR signal transduction.

GPCR Dimerization May Be Physiologically Important and Medically Relevant. Truncated receptors generated by alternative splicing or genetic mutation may play a previously unappreciated physiological role through receptor dimerization. For example, a prevalent truncation mutant of the human CCR5 receptor can actually inhibit CCR5-receptor-mediated human immunodeficiency virus (HIV) infection in individuals who are heterozygous for the mutant GPCR [120], perhaps because heterodimerization between mutant receptor and wild-type receptor prevents virus transport. Additionally, nephrogenic diabetes insipidus has been shown to be present in individuals heterozygous for a truncated vasopressin (V_2) receptor that interacts with wild type receptor, inhibiting its function [121].

From a physiology perspective, one of the most exciting aspects of GPCR dimerization is the observation that hetero-oligomerization can result in receptor complexes that have ligand and signaling properties that are distinct from the constituent receptors. For example, the κ- and δ-opioid receptors form a heterodimeric complex where the heterodimer shows no significant activity for either κ- or δ-opioid receptor-selective agonists or antagonists but showed significantly higher affinity for partially selective agonists [92].

For years, positive and negative downstream interactions between GPCRs, referred to as receptor crosstalk, have been observed [122-124]. This has made it quite clear that GPCR signaling is not a result of sequential activation of a linear pathway, but rather, is the result of an elaborate, branched signaling scheme. However, unrecognized

GPCR heterodimerization can generate signaling phenotypes interpreted as downstream pathway crosstalk. Thus, heterodimerization could be responsible for much of the physiological crosstalk observed for many different GPCRs.

Finally, since GPCRs are currently the largest target for therapeutic drug intervention [7-9], whether or not GPCRs homo- or heterodimerize is very relevant for both drug administration and drug screening, as different drugs will most certainly have altered efficacies and potencies depending on whether the target GPCR is heterodimerized. The use of dimeric or bivalent ligands to selectively modulate hetero-oligomers or increase potency and selectivity of monovalent ligands for dimeric receptors has great potential as a means to develop and improve candidate drugs [119].

1. 4: VISUAL RHODOPSIN: STRUCTURE AND OLIGOMERIZATION STATE

Chapter 4 of this dissertation examines the oligomerization state of visual rhodopsin in a membrane environment, a subject that is currently under intense investigation with conclusions that, as of Spring 2007, are still under debate. Rhodopsin is the only GPCR whose three-dimensional structure has been solved by X-ray crystallography [3,125,126]. Further, it is the only GPCR whose native oligomeric arrangement has been visualized using atomic force microscopy (AFM) [127,128], although the validity of the data has been questioned [129]. Based on these structural studies of visual rhodopsin, an atomic model for the putative rhodopsin oligomeric interaction has been proposed [118,128].

The following three sections will briefly review the first structure of rhodopsin, then touch on the controversy surrounding its oligomerization state, as well as the putative model for visual rhodopsin oligomerization.

1. 4. 1: Rhodopsin Structure.

Below a brief overview of the dark state structure of rhodopsin is presented as a reference to understand the oligomerization models of visual rhodopsin, discussed later.

The sequence of rhodopsin exhibits key features found in most GPCRs (refer to Figure 1. 1), and it shows behavior consistent with the experimental data available for other receptors in the GPCR family [3]. Because of these similarities, the data on visual rhodopsin is used as the template for the structure and function of all GPCRs [130].

These similar features include palmitoylation of cysteine residues near the C-terminal tail at residues Cys-322 and Cys-323 [131,132], a conserved disulfide bond between cysteines in extracellular loops one and two (between Cys-110 and Cys-187), and glycosylation at the N-terminus (at residues Asn-2 and Asn-15) [2,133]. A ribbon model of the rhodopsin structure is presented in Figure 1. 1B and each of the major domains, extracellular, transmembrane, retinal binding pocket and intracellular, are briefly discussed below.

Extracellular Domain. The extracellular domain is a compact structure formed by the N-terminal tail and three extracellular loops (E-1, E-2, and E-3) [3]. The crystal structure confirmed that Cys-187 forms a disulfide bond with Cys-110. This disulfide is conserved in most GPCRs [3]. Previous mutagenesis studies suggested the importance of the extracellular domain in the folding and stability of rhodopsin [134-138] but the degree of structural complexity was not expected. It is now thought that this structural complexity is required to form a lid over the retinal-binding site that acts to stabilize dark state rhodopsin [139-141].

Transmembrane Domain. The membrane-embedded domain consists of seven α-helical TM segments that form a tight bundle in which the 11-*cis*-retinal chromophore is shielded from the aqueous and lipid environments [3,130,133,142]. Interestingly, most of the helices in visual rhodopsin are not regular α-helices. Several of these helices are bent or contain segments with partial 3_{10}- or π–helical conformations. For most of these distortions, proline residues are associated with the bends [130]. It is hypothesized that the bends in the helices, and the twists associated with them, might be important hinge-points for conformational changes associated with receptor activation [130,142-144].

Retinal Binding Pocket. The 11-*cis*-retinal ligand is covalently attached to Lys-296 in transmembrane helix VII [3], through a Schiff base linkage. Due to its high pK_a, this Schiff base linkage is protonated in the dark state, and the positive charge is stabilized by a negatively charged counter-ion from Glu-113 in helix III [145]. Interestingly, this salt-bridge, which neutralizes the charged residue in rhodopsin, corresponds to the binding of the cationic moiety in the diffusible ligands of a number of other rhodopsin-like receptors [50,51,146] and is a critical determinant of activity.

Cytoplasmic Domain. The cytoplasmic domain of rhodopsin is comprised of three intracellular loops (I-1, I-2, and I-3), the C-terminal tail, and a short amphipathic α-helix (helix VIII) which lays parallel to the membrane [2,3,125]. Activation of rhodopsin likely involves a conformational change that exposes a previously buried hydrophobic cleft in loop I-3, to which the C-terminal tail of the transducin G_α subunit binds to become activated [45].

1. 4. 2: Controversy Surrounding the Oligomerization State of Visual Rhodopsin.

Visual rhodopsin was one of the first intrinsic membrane proteins to be purified to homogeneity in detergent. Early studies found the dark-state rhodopsin/detergent complex corresponded exactly to that of a single rhodopsin monomer [147,148]. Interestingly, in these studies it was reported that light-activation of rhodopsin induced, on the time-scale of minutes, a doubling of the scattering intensity in the small-angle neutron analysis studies, characteristic of protein dimerization [148]. From these results, the authors concluded that the slow kinetics of this apparent dimerization excluded the possibility that the rhodopsin dimer could have a role in visual signal transduction (which occurs on a subsecond time scale). They attributed the result to protein denaturation upon photo-activation in the detergent. Further, using the same technique of small-angle neutron diffraction [149], dimerization and oligomerization of rhodopsin upon illumination was never observed in the native membrane in the absence of detergent.

Additionally, early measurements on the diffusion rates of visual rhodopsin in the membrane indicated it was near the upper limit (10^{-9} cm^2/s) of membrane protein mobility [149-153]. Finally, near-infrared light scattering studies determined the kinetics and stoichiometry of the rhodopsin/transducin interaction in native membranes as 1 : 1 [154]. These studies arrived at similar conclusions as the detergent studies – rhodopsin exists in the membrane as a monomer. In fact, until relatively recently, the monomeric status of rhodopsin was universally accepted [155].

However, this paradigm was challenged in 2003, when an atomic force microscopy (AFM) study from the Palczewski laboratory was published [127]. This work, visualizing mouse disk membranes, reopened the debate regarding the oligomerization state of visual rhodopsin [127,128,155]. The AFM images showed individual rhodopsin molecules form distinct, densely packed double rows of rhodopsin dimers in the rod outer segment (ROS) and demonstrated the putative dimeric nature of native rhodopsin in ROS [127] (Figure 1. 9).

The visual evidence of rhodopsin dimerization demonstrated in the AFM study has been challenged by Dr. Marc Chabre's group in France. In a brief communication to *Nature*, Dr. Chabre contends that these rows of dimers are in fact long, double rows of equally spaced protein monomers, packed in partially ordered micro-crystalline arrays - an artifact of the mica membrane preparation required for AFM [129]. Further, because rhodopsin is packed so tightly in the membrane at concentrations as high as 3 mM [156], Dr. Chabre postulated the AFM studies cannot discriminate crowded receptor monomers from specific, protein-protein interactions.

The Palczewski laboratory addressed this criticism by varying the material used to prepare the samples for visualization [128]. They reported that the native disk membranes adsorbed similarly to EM grids and mica, with both preparations revealing paracrystalline packing of rhodopsin. From this additional study, they concluded the paracrystalline packing was independent of the support used for sample preparation. Also, the samples were studied at room temperature, precluding the possible induction of paracrystals by lipid phase transitions [128].

Following the AFM results, a number of additional studies revisited the oligomerization state of rhodopsin in detergent. For example, Medina *et al*. [157] investigated the oligomeric state of rhodopsin using cross-linking techniques. In both retinal rod outer segment membranes and after purification in dodecyl maltoside (DDM), dimers, trimers, and higher-order oligomers were detected by SDS-PAGE after cross-linking. However, the monomer remained the major species, and there was not a single (but multiple) oligomeric species, making the cross-linking results inconclusive.

A second experimental approach in the same manuscript also suggested that DDM-solubilized rhodopsin is dimeric. Calibrated gel permeation column chromatography and sedimentation velocity each indicated that DDM-solubilized rhodopsin was dimeric. However, the results of these experiments were also challenged by Dr. Chabre [155]. Chabre contends that the Medina *et al*. study [157] is flawed by a number of conceptual mistakes that make the conclusions invalid. First, the gel filtration column was calibrated in terms of molecular mass using soluble proteins, a procedure reported to be unreliable with membrane proteins [155,158,159]. Further, the mass of a pure DDM micelle (50 kDa) was subtracted from the apparent mass (126 kDa) to obtain the mass of the protein (76 kDa), which corresponds approximately to dimeric rhodopsin. However, Chabre points out [155] that this procedure cannot always be used to determine the mass of membrane proteins of this size, since the mass of the bound detergent is not necessarily equivalent to the micellar mass [160,161].

An additional study by Jastrzebska *et al.* [162] used cross-linking to examine the oligomerization state of rhodopsin in varying DDM/protein ratios. At a high DDM/protein ratio, rhodopsin could not be cross-linked, a strong indication that it is monomeric when disperse in DDM. However, at a low DDM/protein ratio, i.e., near the critical micellar concentration of DDM (or in the absence of any detergent), cross-linking induced dimer, trimer, and higher-order oligomer formation. Cross-linking was not complete, however, and monomeric rhodopsin was still the major species. As before, the validity of these data was challenged with the argument that even a monomeric rhodopsin would be cross-linked within retinal rod outer segments because of its very high concentration (3 mM) within the membrane [155].

To explain the monomeric species of rhodopsin observed at high DDM detergent concentrations, Jastrzebska *et al*. [162] suggested that rhodopsin dimers exist natively within the membrane but are destroyed by high detergent concentrations. This hypothesis originated because they observed a higher proportion of rhodopsin oligomers in the detergent 3-[(3-cholamidopropyl)dimethyl-ammonio]-1-propanesulfonate (CHAPS) than in DDM [162]. They speculated that CHAPS, because of its higher critical micelle concentration, likely extracts larger amounts of lipid associated with rhodopsin [163], thereby preserving the original architecture of the rod outer segment.

To test the hypothesis that extracting more ROS phospholipids preserves the natural oligomeric state of rhodopsin, Jastrzebska *et al.* isolated rhodopsin using gel filtration techniques in different detergents, n-dodecyl-β-D-maltoside (DDM), n-tetradecyl-β-D-maltoside (TDM), and n-hexadecyl-β-D-maltoside (HDM), quantified the phospholipid content in each sample using each detergent, and examined the resulting quaternary structure of rhodopsin using transmission electron microscopy [164]. This study found that, of the three detergents, HDM best preserved the oligomeric structure of rhodopsin – in HDM, most of the particles were present in tightly packed rows of dimers. DDM preserved the oligomeric structure the least with a predominant mixture of monomers over dimers while TDM resultant in an intermediate mixture of monomers and dimers. The transmission electron microscopy images can be seen in Figure 1. 9. Further, quantitative phospholipid analysis indicated that, consistent with the hypothesis, the rhodopsin extracted with HDM had twice the amount of phospholipid (44.0 ± 8 phospholipids/rhodopsin) as the sample extracted with DDM (22.0 ± 3 phospholipids/rhodopsin) [164]. Interestingly, activation of transducin was significantly faster in HDM than in DDM, with TDM showing an intermediate activity rate. The latter result implies that oligomerization may have a substantial impact on rhodopsin signaling.

1. 4. 3: Proposed Model for Rhodopsin Oligomerization.

The dimer interface is not likely the same for every homo- and heterodimer and there may be no universal mechanism for GPCR oligomerization. Given the divergence across all GPCR family members, this is not unexpected. However, in general, the molecular determinants for GPCR oligomeric interactions have been described to fall into three categories, shown in Figure 1. 10: disulfide bonds, intracellular and extracellular domain interactions, and transmembrane domain interactions.

The most recent atomic model proposed for oligomeric rhodopsin [165] was constructed by the Palczewski laboratory using both the high resolution structures of rhodopsin [3,125,126,164] and the native oligomeric arrangement visualized using AFM [127,128]. The model possesses intradimeric contacts that involve TM IV and TM V, whereas contacts between TM I and TM II and the cytoplasmic loop connecting TM V and TM VI (I-3) facilitate the formation of rows of rhodopsin dimers [165] (Figure 1. 11A).

According to this model, the weakest interaction is between dimers in a given row, resulting from contact at the extracellular ends of TM I (Figure 1. 11A; contact 3). The rows of protein were observed to accommodate 10 - 30 dimers and the extended contact between rhodopsin dimers across a given row provides a relatively strong interaction (Figure 1. 11A; contact 2). The strongest interaction is between monomers of rhodopsin in the dimer pair and primarily involves interactions between TM IV and TM V (Figure 1. 11A; contact 1).

A rather extensive cross-linking study using an amino-specific homo-bifunctional cross-linker found that a number of lysine residues (see Figure 1. 11A) have the capacity to covalently stabilize a rhodopsin dimer. Additionally, a hetero-bifunctional, thiol-specific cross-linker can stabilize a crosslink between Lys-66 and Cys-140 [166]. These cross-linking results are reflected in the model via the interdimeric contact 2 of Figure 1. 11A.

Currently, there is no high resolution experimental data on rhodopsin assessing the putative TM IV – TM V interface between monomers. However, site-directed cysteine mutants created in TM IV of rhodopsin most rapidly formed dimers in the presence of Cu^{2+}-phenanthroline, suggesting that residues in this helix are located in the dimer interface [167]. Additionally, TM IV was identified as part of the dimer interface for another type “A” GPCR, the dopamine D2 receptor, using Cu^{2+}-phenanthroline [168]. Another study on the D2 receptor revealed functional crosstalk across the dimer interface formed by TM IV [169]. Inverse agonists slowed cross-linking across sets of cysteines in TM IV while agonists accelerated cross-linking and locked the receptor in an active state, suggesting that a conformational change around the TM IV dimer interface may be part of the receptor activation mechanism. Finally, further support for the model comes from cross-linking studies of cysteine residues in TM V of the D2 receptor [169]. The key residues involved in the putative dimer interface in TM IV and TM V are shown in Figure 1. 11B.

As discussed above, the growing evidence suggesting rhodopsin exists in the membrane and in detergent as a dimer or higher order oligomer is not universally accepted in the vision field [129,155]. Addressing this question was the goal of my work presented in Chapter 4.

1. 5: DISSERTATION OVERVIEW

The overall objectives of this thesis project were two-fold: (1) to develop new fluorescence-based techniques that allow the study of dynamic conformational changes associated with G-protein coupled receptor activation and (2) to determine the oligomerization state of visual rhodopsin in a membrane environment. The first part of this dissertation discusses a novel technique developed that uses bimane fluorophores to assess both protein secondary structure as well as proximity (~ 5 – 15 Å) within proteins. The dissertation ends with a fluorescence based method to assess the oligomerization state of visual rhodopsin when reconstituted into lipid vessicles. Below, I have outlined how these results are presented in the remaining chapters of this dissertation.

Chapter 2, first published in *Biochemistry* in 2002, describes the development of a novel technique to measure short-range proximity in proteins. The method exploits the quenching of the fluorescent label monobromobimane by nearby Trp residues through a photo-induced electron transfer mechanism. In Chapter 2, the quenching effect is shown to be distance dependent and orientation specific. Thus, by using the intrinsic tryptophans in a protein or by selectively introducing tryptophans, three dimensional insight into the spatial orientation of the protein fold can be obtained. This method can be used to monitor local (~ 5 – 15 Å) conformational changes in proteins upon activation and/or study protein-protein interactions. Since my manuscript calibrating the technique [170], a number of studies have used the method to: measure short-range molecular rearrangements in an ion channel [171], study how a chaperone binds its target [172,173], assess protein/protein interactions by mapping transducin's binding pocket in rhodopsin [45], and measure the dynamic mechanisms involved in β_2-adrenergic receptor activation [40].

Chapter 3, first published in *Biochemistry* in 2004, examines the use of a thiol-cleavable bimane derivative, (2-pyridyl)dithiobimane (PDT-Bimane) for high-throughput SDFL structural studies. The reducible nature of PDT-Bimane can be exploited to resolve problems often faced in SDFL studies: ensuring specific labeling of cysteine residues, determining the extent of free label contamination, and accurately determining labeling efficiency even at low concentrations. Additionally, the ability to cleave PDT-Bimane off the protein enables rapid determination of these parameters, and positions it as an ideal fluorophore for automated, high-throughput SDFL structural studies of protein folding, the detection of protein-protein interactions, and the monitoring of real-time conformational changes. Chapter 3 ends with an outline of how SDFL studies could be automated using PDT-Bimane.

Chapter 4, first published in the *Proceedings of the National Academy of Sciences* in 2006, describes the use of fluorescence spectroscopy and biochemical approaches to assess the oligomerization state of visual rhodopsin. An experimental approach was undertaken to ensure true, specific protein-protein interactions and not artificial interactions due to receptor crowding were assessed (this is critical as rhodopsin is found in very high concentrations in the membrane). To do this, rhodopsin was purified from its native membrane environment, reconstituted into liposomes at low receptor densities, and assessed whether the receptor associates into higher order oligomers using energy transfer approaches. By attaching combinations of fluorophores to specific residues in the protein, the average distance between the fluorophores was measured using luminescence resonance energy transfer (LRET). The fluorescently labeled rhodopsin was fully functional when reconstituted into the liposomes and the energy transfer measurements revealed that the receptors were within 47-50 Å of each, consistent with the current dimer/oligomer model for visual rhodopsin. Further, the strength of the energy transfer signal suggested that > 90% of the proteins were self-associated as oligomers.

Finally, the appendices of this dissertation present experimental results related to this dissertation project. Appendix 1 reports studies to identify and calibrate additional fluorophores, with properties unique and distinct from bimane, that are also quenched by Trp residues. Appendix 2 shows the results of a calibration study for the luminescence resonance energy transfer (LRET) technique performed on a double-cysteine mutant of T4 lysozyme and demonstrates the accuracy of the LRET technique. This calibration was done to ensure a reliable determination of the rhodopsin/rhodopsin distances reported in Chapter 4.

Figure 1. 1: Two-dimensional cartoon and three-dimensional structural model of rhodopsin in the dark state. (A) Two-dimensional model of rhodopsin. The transmembrane domains of rhodopsin cross the membrane seven times. C-I, C-II, and C-III correspond to the cytoplasmic loops, and E-I, E-II, and E-III correspond to the extracellular loops. The transmembrane segment is α-helical (yellow cylinders), although the helices are highly distorted and tilted. The stability of the helical segment is increased by the Cys-110/Cys-187 bridge (depicted in dark yellow), conserved among many GPCRs. The chromophore, 11-cis-retinal is attached to Lys-296 (dark red) via a protonated Schiff base. The positive charge of the base is neutralized by counterion Glu-113 (blue). Asn-2 and Asn-15 (red) are sites of glycosylation and Met-1 (orange) is acetylated. Cys-322 and Cys-323 (light green) are palmitoylated, whereas two other Cys residues, Cys-140 and Cys-316 (brown), are reactive to many chemical probes and are used to explore rhodopsin’s structure. Rhodopsin, when exposed to light, is phosphorylated by rhodopsin kinase at sites Ser-334, Ser-338, and Ser-343 (green). The highly conserved domains among GPCRs, D(E)RY in helix 3 and NPXXY in helix VII (gray), are important for receptor activation. Figure taken from Palczewski, K. (2006) *Annu. Rev. Biochem*. 75: 743 – 767. **(B)** Ribbon model of the dark state rhodopsin crystal structure. The model illustrates the location of the cytoplasmic, transmembrane and extracellular domains. It shows the retinal chromophore, in blue, residing within the TM helical bundle, attached to Lys-296 via a protonated Schiff base linkage. The location of cytoplasmic and extracellular loops are also denoted. Figure taken from Klein-Seetharaman, J. *et al.* (2004) *Proc. Natl. Acad. Sci.* 101: 3409 – 3413.

(A)

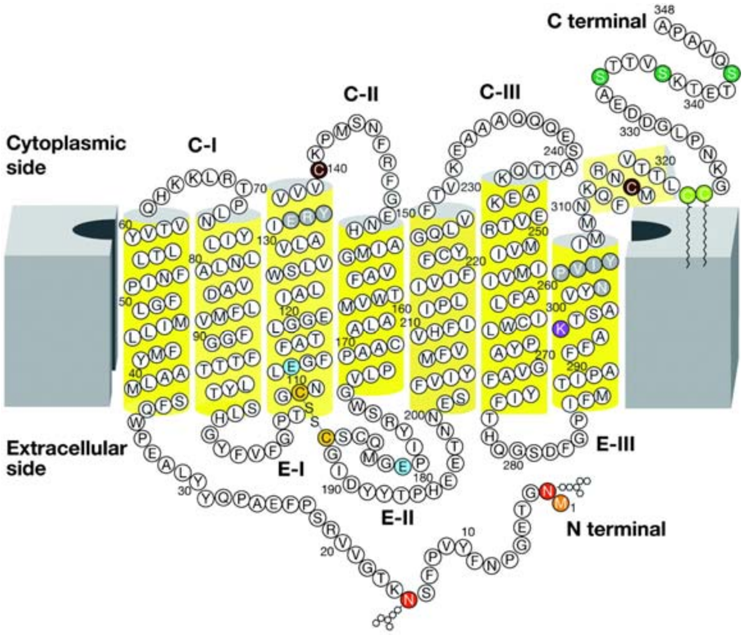
C terminal
Cytoplasmic side
C-I
C-II
C-III
Extracellular side
E-I
E-II
E-III
N terminal

(B)

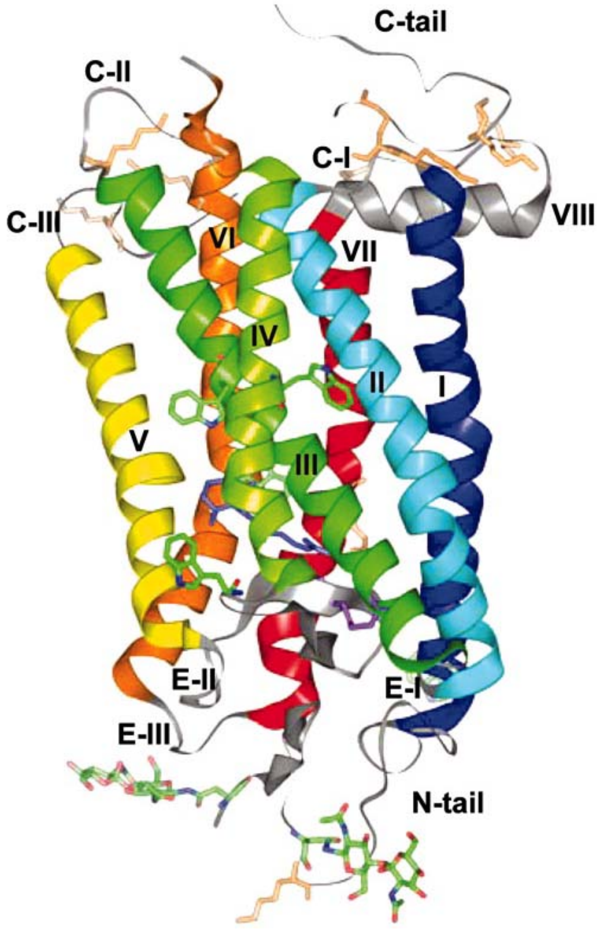
C-tail
C-II
C-I
VIII
C-III
VI
VII
IV
II
I
V
III
E-II
E-I
E-III
N-tail

Figure 1. 2: G-protein coupled receptor mediated signal transduction and attenuation. **(A)** GPCRs have a conserved structure composed of seven transmembrane α-helices with an extracellular N-terminus and an intracellular C-terminus, leading to three intracellular (I-1, I-2, I-3) and three extracellular (E-1, E-2, E-3) loops. Despite the universal topology, GPCRs respond to a wide variety of ligands including photons, ions, small molecules, and peptides. Binding of the ligand is thought to induce a conserved conformational change in the receptor causing it to become “active.” The “active” receptor initiates a cellular signal transduction cascade by binding to its cognate heterotrimeric G-proteins, inducing the exchange of GDP for GTP in the α-subunit and the dissociation of α_{GTP} from the β/γ complex. Thus activated, these subunits interact with their respective effector proteins, ultimately resulting in an intracellular response to the extracellular stimulus. G-proteins can interact with multiple downstream effectors leading to a signal amplification. Figure taken from Bockaert, J., and Pin, J.P. (1999) *Embo. J*. 18: 1723 – 1729. **(B)** GPCR signaling is attenuated through the actions of both the G-protein-coupled receptor kinases (GRKs) and the β-arrestins (visual arrestin for rhodopsin). Activation of the receptor allows it to couple to and activate the heterotrimeric G-proteins, catalyzing its dissociation into G_α and $G_{\beta\gamma}$. Free $G_{\beta\gamma}$ subunits recruit the GRKs to the membrane, where they phosphorylate the C-terminal tail of the receptor [174,175]. β-arrestins recognize and bind to activated, phosphorylated receptor sterically hindering additional G-protein coupling. β-arrestins also target some GPCRs to clathrin-coated pits for internalization. Figure taken from Pierce, K.L. *et al*. (2002) *Nat. Rev. Mol. Cell Biol*. 3: 639 – 650.

(A)

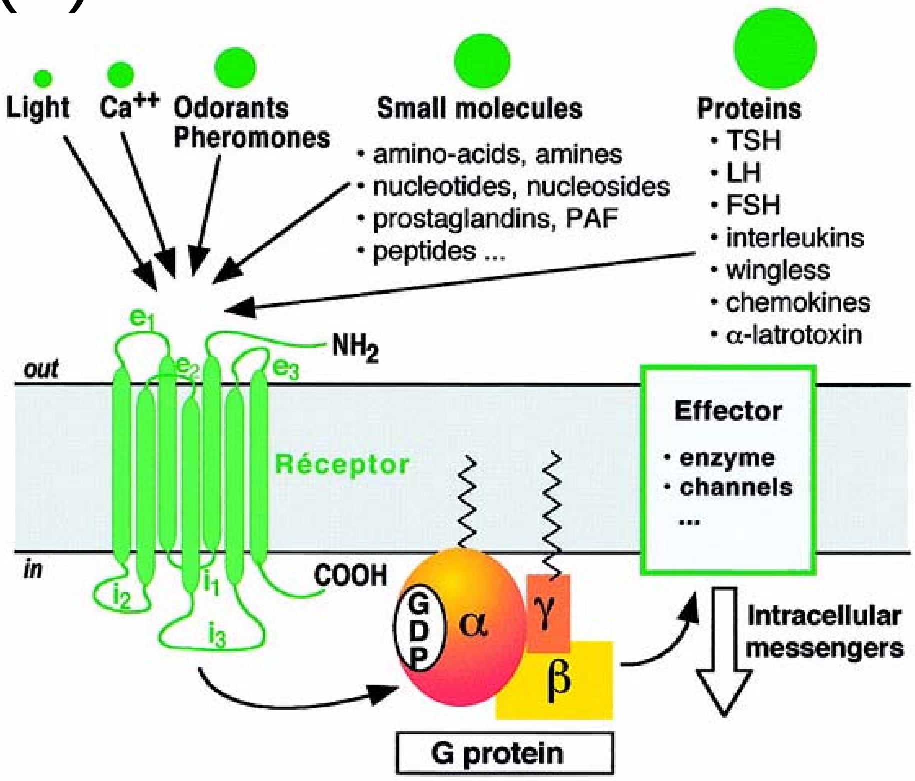
Light
Ca++
Odorants
Pheromones
Small molecules
• amino-acids, amines
• nucleotides, nucleosides
• prostaglandins, PAF
• peptides ...
Proteins
• TSH
• LH
• FSH
• interleukins
• wingless
• chemokines
• α-latrotoxin
e1
e2
e3
NH2
out
in
Réceptor
i1
i2
i3
COOH
GDP
α
γ
β
G protein
Effector
• enzyme
• channels
...
Intracellular messengers

(B)

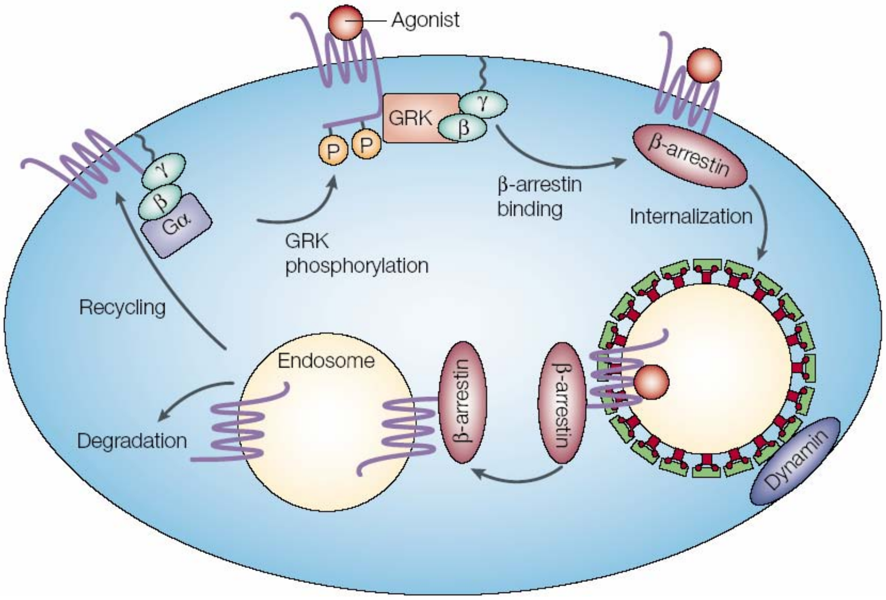
Agonist
GRK
γ
β
P
P
GRK phosphorylation
β-arrestin binding
β-arrestin
Internalization
γ
β
Gα
Recycling
Endosome
Degradation
β-arrestin
β-arrestin
Dynamin

Figure 1. 3: GPCR activation is proposed to involve receptor dynamic conformational changes with multiple, discrete structural intermediates. (A) A model viewed from the intracellular surface showing the putative conformational change that occurs in TM VI of visual rhodopsin during photo-activation first predicted from EPR studies [41]. This movement is consistent with other data which found that light-activation results in a cysteine residue V250C (shown) to be more accessible to modification with PyMPO-maleimide. Light-activation also increased the accessibility of an attached fluorescent label at V250C to quenching agents [42]. However, at this stage the data cannot yet distinguish between a helix rotation or tilt. Figure taken from Dunham, T. D. and Farrens, D. L., (1999) *J. Biol. Chem.* 274: 1683 – 1690. **(B)** The sequential binding model of GPCR activation. The arrangement of the agonist binding TM domains (TM III, TM V, and TM VI) of the β_2-Adrenergic receptor as viewed from the extracellular surface. In the absence of ligand, the receptor **R** is conformationally flexible. Conformational state $\mathbf{R^1}$ is stabilized by interactions between TMs V and VI and the catechol ring of the agonist, norepinephrine. A rapid transition to state $\mathbf{R^2}$ occurs when Asp-113 in TM III binds the amine nitrogen of the agonist. The slow transition from $\mathbf{R^2}$ to $\mathbf{R^3}$ involves interactions between the chiral β-hydroxyl and Asn-293 on TM VI. The model suggests that different conformational changes occur in the receptor to produce multiple, discrete receptor conformational states. Figure taken from Swaminath, G. *et al.*, (2004) *J. Biol. Chem.* 279: 686 – 691.

(A)

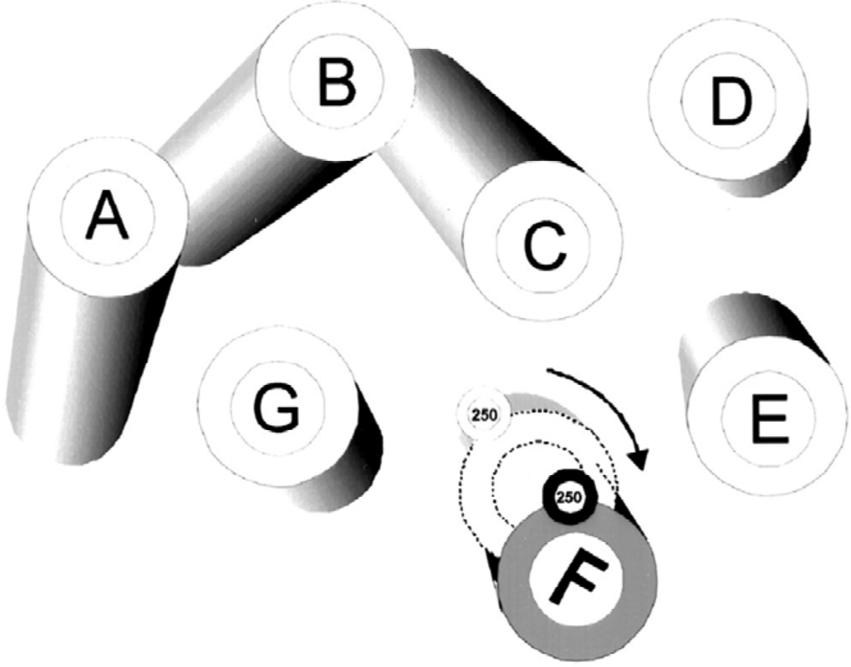
B
D
A
C
G
250
E
250
F

(B)

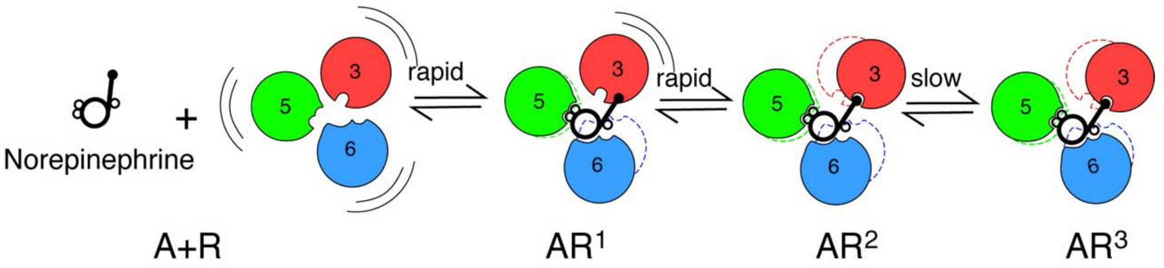
Norepinephrine
+
5
3
6
rapid
rapid
slow
A+R
AR^{1}
AR^{2}
AR^{3}

Figure 1. 4: A Jabłoński diagram representing the processes involved in absorption and emission. Upon absorption of photons, a molecule's electrons are excited from the ground state, S_0, to some higher vibrational energy level within either the first or second electronic excited states, S_1 or S_2. If the electron goes to an electronic level higher than S_1, it will relax back to the lowest vibrational state in S_1 through processes known as internal conversion and vibrational relaxation. The resulting excited electron can subsequently return to the electronic ground state through: external conversion by collisional deactivation (k_{EC}), intersystem crossing resulting in phosphorescence (k_P), transferring the excited-state energy to another molecule through resonance energy transfer (k_{RET}), specific collision with a quenching molecule ($k_q[Q]$, where [Q] is the concentration of quenching agent and k_q is the number of collisions per second), or the emission of fluorescent light (k_F). Fluorescence always occurs out of the lowest vibrational state in the first electronic excited state. Thus, the emission of light is at a wavelength corresponding to the energy gap between S_1 and S_0. The light is emitted with a lifetime, τ, which can be thought of as the average period of time the fluorophore remains in the excited state. Figure adapted from Lakowicz, J. R. (1999) *Principles of fluorescence spectroscopy* (Kluwer Academic/Plenum, New York).

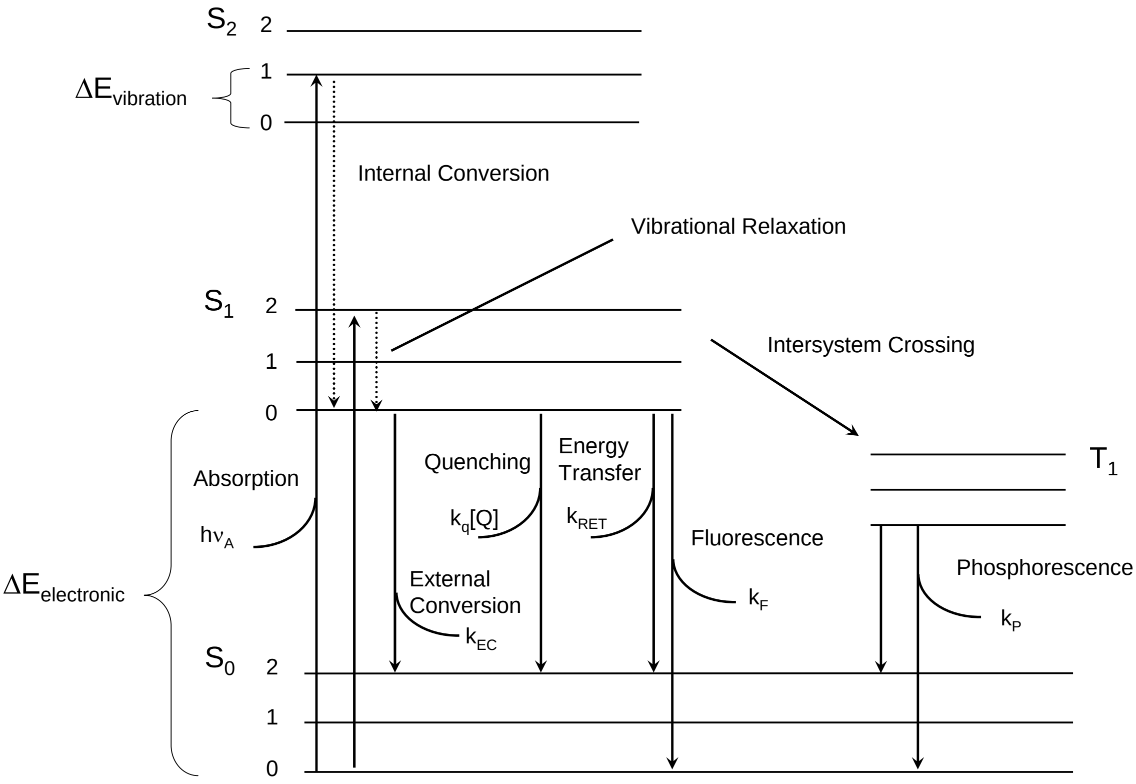

S2
2
1
0
ΔEvibration
Internal Conversion
Vibrational Relaxation
S1
2
1
0
Intersystem Crossing
T1
Absorption
hνA
Quenching
kq[Q]
Energy Transfer
kRET
Fluorescence
kF
Phosphorescence
kP
External Conversion
kEC
ΔEelectronic
S0
2
1
0

Figure 1. 5: Types of structural data that can be learned by fluorescence spectroscopy. ***Fluorophore Accessibility.*** Whether a fluorophore is exposed or buried in a protein fold can be ascertained by measuring its accessibility, either to an external quenching agent or to solvent. An experiment to determine accessibility to an external quenching agent is a Stern-Volmer quenching analysis. A greater rate of collision, resulting in a decrease in fluorescence intensity as a function of increasing quencher concentration, correlates with greater accessibility of the fluorophore, whereas a lower rate of collision suggests the label is buried. Alternatively, for solvent-sensitive fluorophores, accessibility to solvent can be assessed by the shifts in the fluorescence emission λ_{max} values. Red-shifted emission λ_{max} values suggest the label is exposed to solvent while blue-shifted values suggest the label is buried inside the protein fold, protected from solvent. ***Fluorophore Mobility***. The mobility of a fluorophore attached to a protein can be determined by measuring its anisotropy. Molecules that are freely mobile (ie., a fluorophore on the surface of the protein) will display a low anisotropy. However, molecules that are at buried sites exhibit a higher anisotropy indicating that the dense packing at buried sites restricts the rotational mobility of the probe. ***Fluorophore Proximity.*** Distances of ~ 20 – 100 Å can be readily measured between two fluorophores in a protein using traditional fluorescence resonance energy transfer (FRET) methods. As developed in this dissertation, shorter-range distances (~ 5 – 15 Å) can be assessed using photo-induced electron transfer techniques. Figure adapted from Farrens, D. L. (1999) in *Structure-Function Analysis of G Protein-Coupled Receptors.*, ed. Wess, J. (Wiley-Liss, Inc., New York), pp. 289-314.

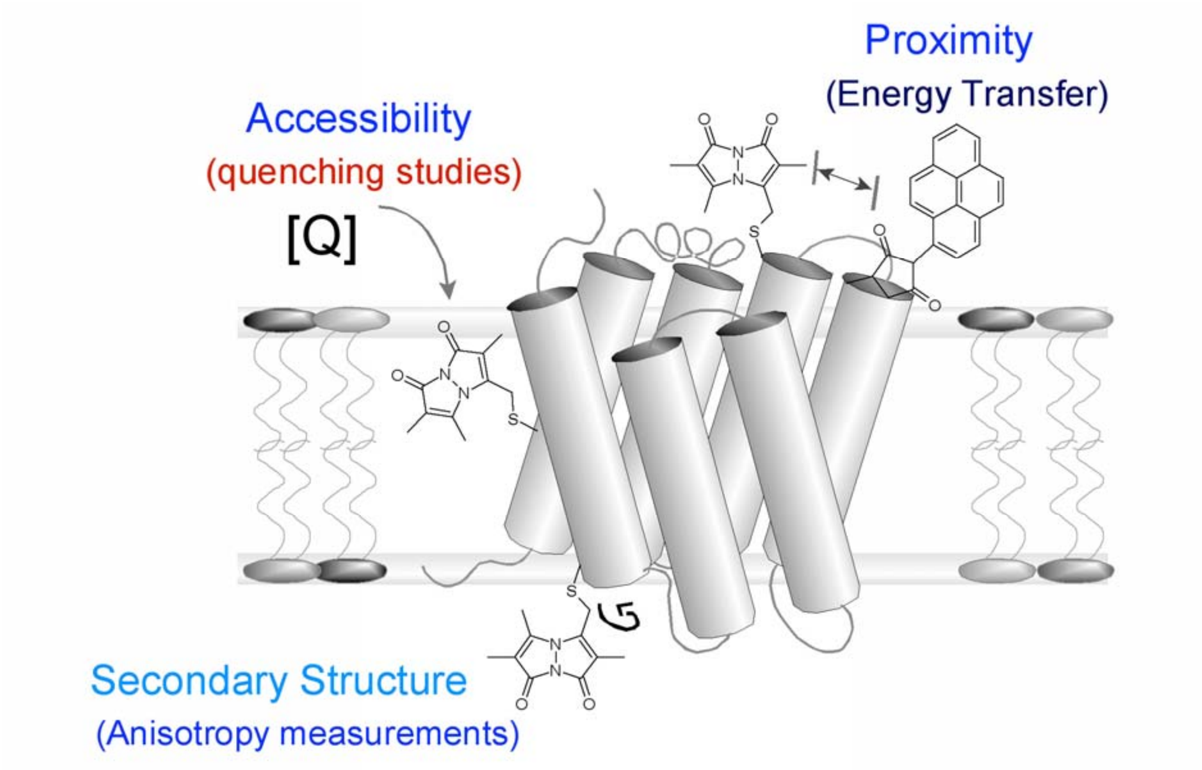

Proximity
(Energy Transfer)
Accessibility
(quenching studies)
[Q]
Secondary Structure
(Anisotropy measurements)

Figure 1. 6: Calibration of SDFL methods for determining protein secondary structure using T4 lysozyme and the fluorescent probe monobromobimane. (A) Model of cysteine-less T4 lysozyme based on the crystal structure showing the location of the cysteine mutants that were labeled with monobromobimane. The black balls show the relative positions of each α-carbon. **(B)** Reaction of the monobromobimane (mBBr) label with a cysteine residue to produce an –S-bimane side chain. Figure taken from Mansoor, SE., Mchaourab, H.S., and Farrens, D.L. (1999) *Biochemistry* 38: 16383 – 16393.

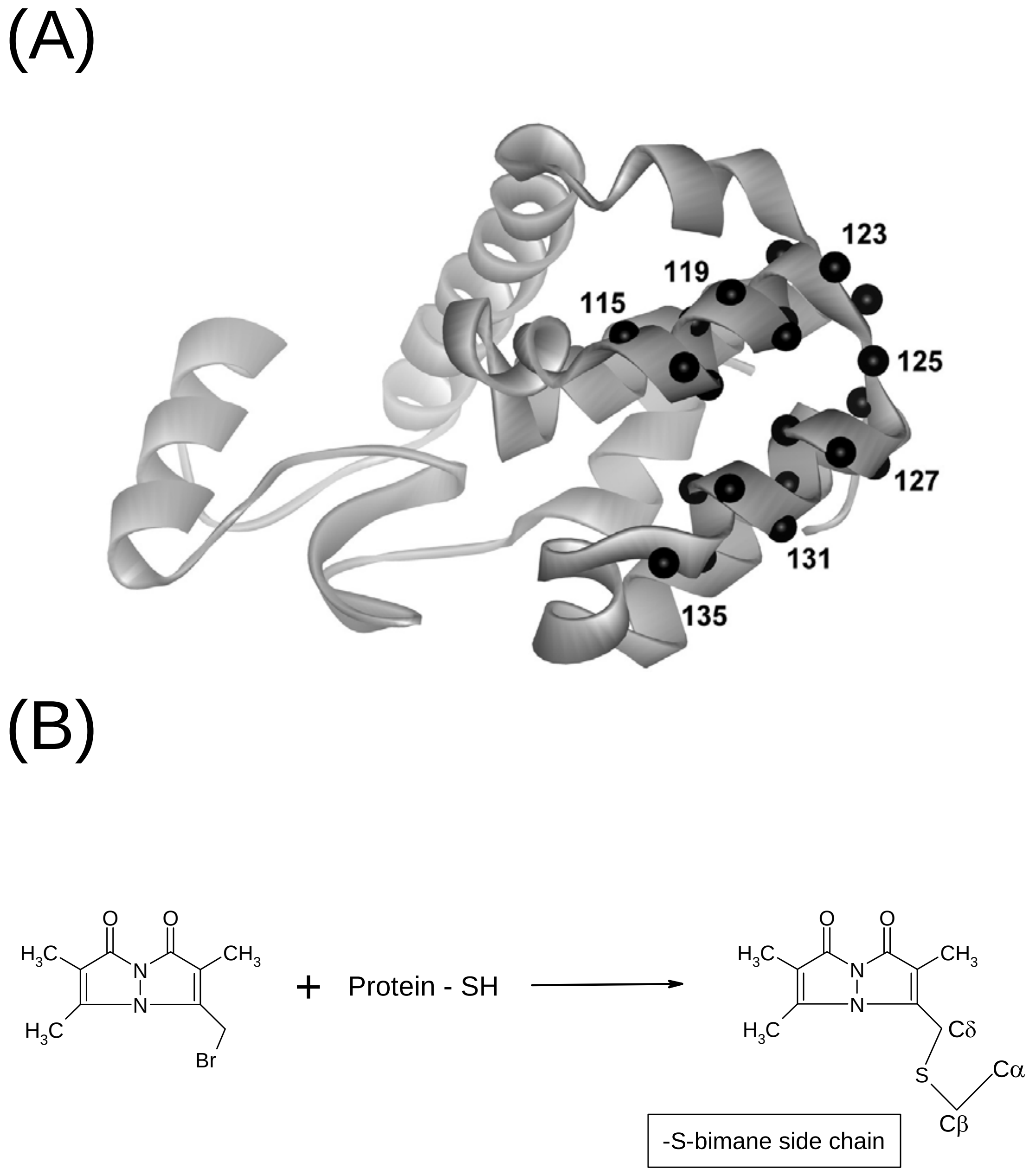
(A)
123
119
115
125
127
131
135
(B)
O
O
H$_3$C
CH$_3$
N
N
H$_3$C
Br
+
Protein - SH
O
O
H$_3$C
CH$_3$
N
N
H$_3$C
Cδ
S
Cα
Cβ
-S-bimane side chain

Figure 1. 7: Monobromobimane labeled samples are solvent sensitive. The examples show mBBr on an exposed site of T4L (E128B_1, black line) and at a buried site (L133B_1, ○). The inset of each panel shows the linear dependence of mBBr-Cys on the solvent polarity, achieved by varying the dielectric of the solvent. **(A)** Solvent sensitivity of the absorbance spectra. **(B)** Solvent sensitivity of the fluorescence excitation spectra. **(C)** Solvent sensitivity of the fluorescence emission spectra. In each case, the fluorescence characteristics of the exposed site (E128B_1) are red-shifted while those of the buried site (L133B_1) are blue-shifted. Figure taken from Mansoor, SE., Mchaourab, H.S., and Farrens, D.L. (1999) *Biochemistry* 38: 16383 – 16393.

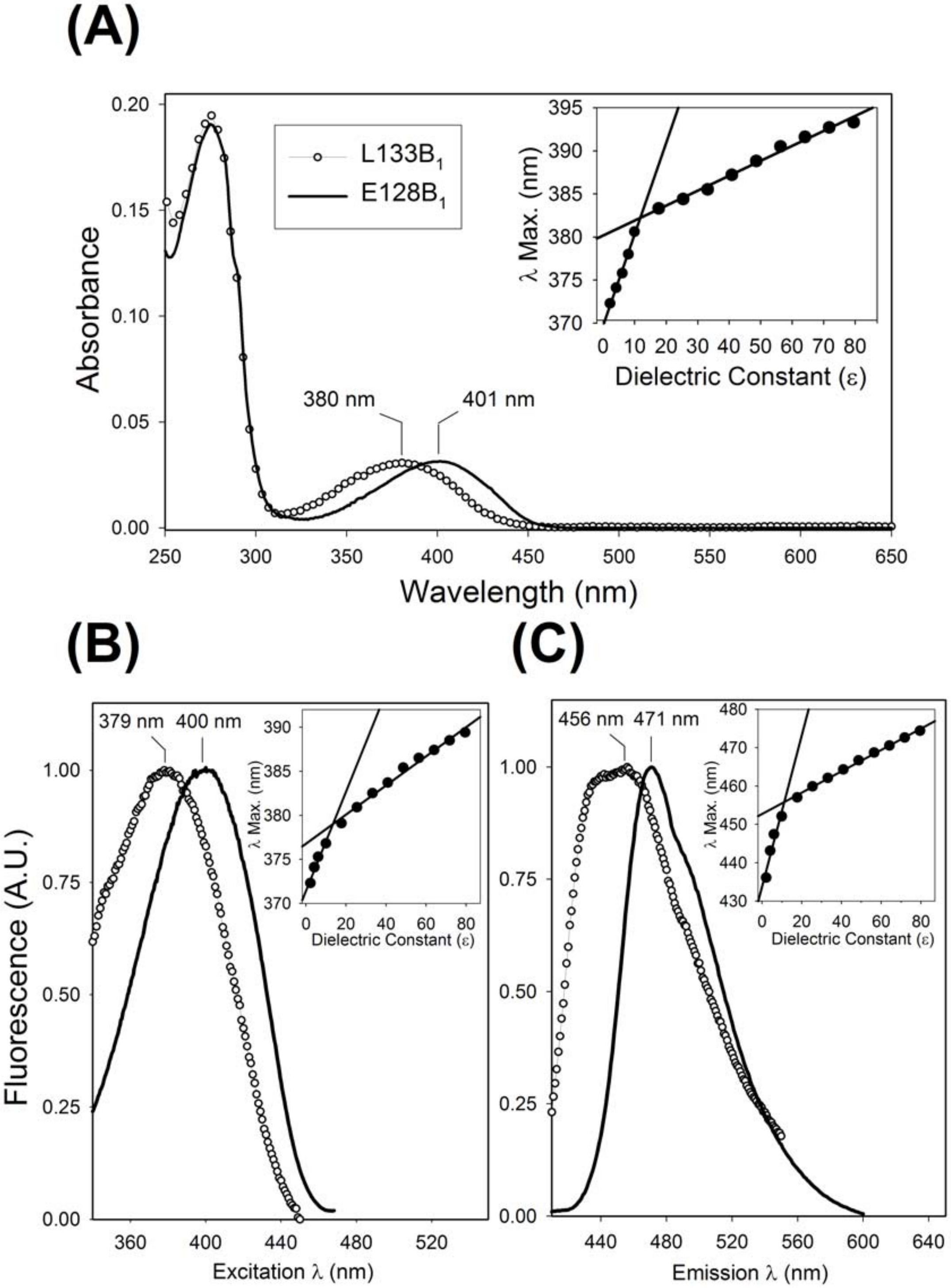
(A)
Absorbance
Wavelength (nm)
L133B$_1$
E128B$_1$
380 nm
401 nm
λ Max. (nm)
Dielectric Constant (ε)
(B)
Fluorescence (A.U.)
Excitation λ (nm)
379 nm
400 nm
λ Max. (nm)
Dielectric Constant (ε)
(C)
Emission λ (nm)
456 nm
471 nm
λ Max. (nm)
Dielectric Constant (ε)

Figure 1. 8: Comparison of the calculated residue solvent accessibility with the apparent polarity and steady-state anisotropy (mobility) at each cysteine substitution site. (A) Fluorescence emission polarity values at each mBBr-labeled site (●) compared with the residue solvent accessibility (○). **(B)** Inverted steady-state fluorescence anisotropy values (●) compared with the residue solvent accessibility (○). Measurements were performed in triplicate and the standard errors in the mean values are shown by the error bars. The solid black and dotted lines represent a cubic-spline fit of the data. The steady-state anisotropy values are inverted to allow a direct comparison with the solvent accessibility. Figure taken from Mansoor, SE., Mchaourab, H.S., and Farrens, D.L. (1999) *Biochemistry* 38: 16383 – 16393.

(A)

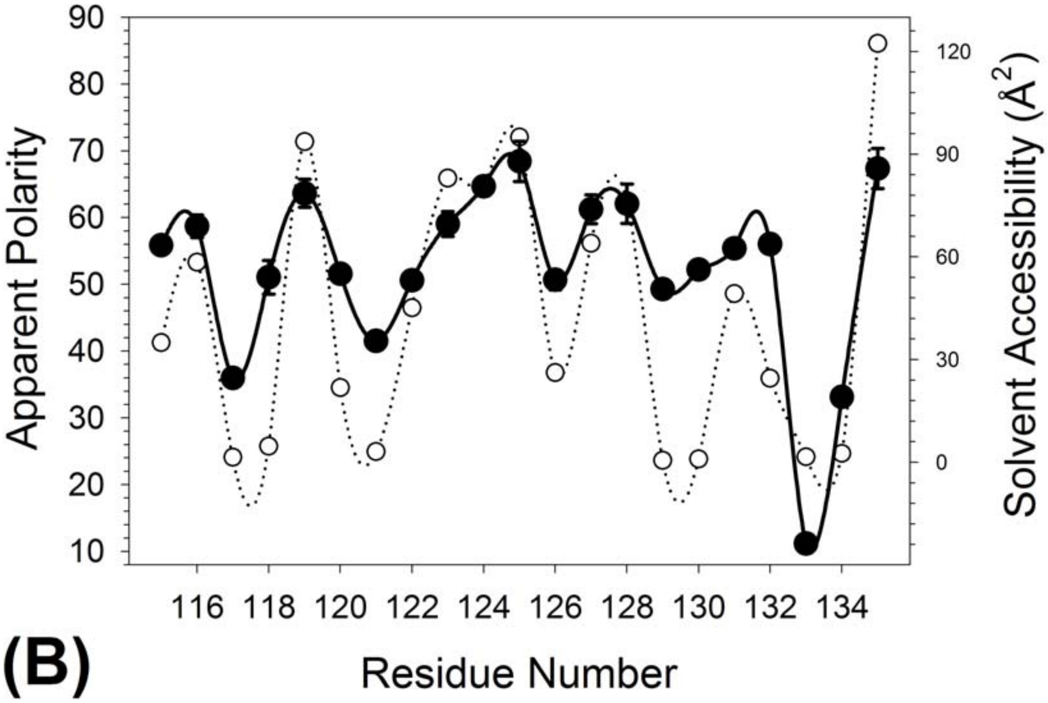
Apparent Polarity
90
80
70
60
50
40
30
20
10
Solvent Accessibility ($\AA^2$)
120
90
60
30
0
116
118
120
122
124
126
128
130
132
134
Residue Number

(B)

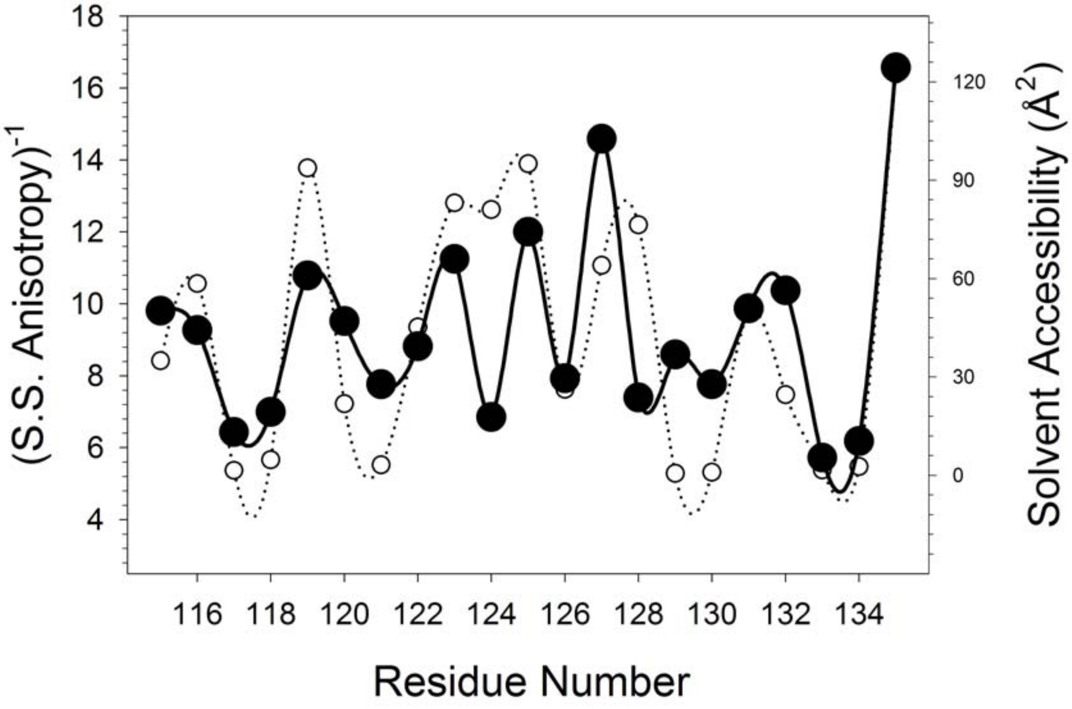
(S.S. Anisotropy)$^{-1}$
18
16
14
12
10
8
6
4
Solvent Accessibility ($\AA^2$)
120
90
60
30
0
116
118
120
122
124
126
128
130
132
134
Residue Number

Figure 1. 9: Paracrystalline array of rhodopsin dimers visualized by atomic force microscopy. (A) Organization and topography of the cytoplasmic surface of rhodopsin showing rows of rhodopsin dimers, as well as individual dimers (inside dashed ellipse). An occasional rhodopsin monomer (arrowheads) can be observed. Figure taken from Fotiadis, D. *et al.* (2003) *Nature* 421: 127 – 128. **Transmission electron microscopy images of negatively stained rhodopsin solubilized in (B) DDM, (C) TDM, and (D) HDM and purified by gel filtration.** In DDM, the images showed particles which did not reveal a distinct substructure and exhibited dimensions compatible with monomeric rhodopsin. In TDM, although the sample was not fully homogeneous, two significant populations of particles were discerned with wormlike structures present as well. In HDM the sample was not homogeneous either, but most of the particles were significantly bigger than those observed in TDM and displayed a significantly larger proportion of worm-like structures. The inset in the top right corner of (D) represents the atomic force microscopy topography of a native disk membrane. Figure taken from Jastrzebska, B. *et al.* (2006) *J. Biol. Chem.* 281: 11917 – 11922.

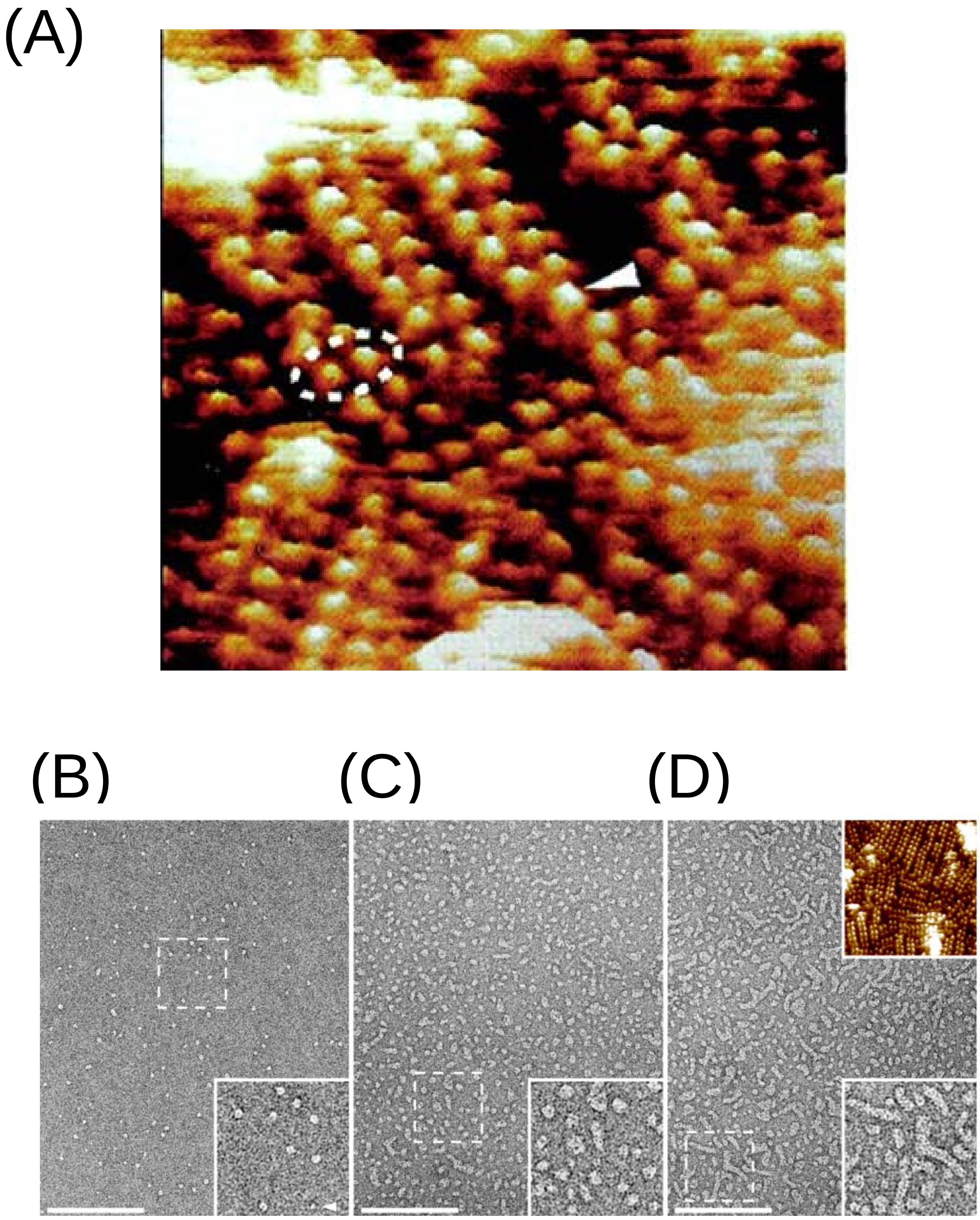
(A)
(B)
(C)
(D)

Figure 1. 10: Molecular determinants of GPCR dimerization. There does not appear to be a universal architecture for GPCR dimerization. Three general categories of interactions have been identified. Covalent disulfide bonds have been found to be important for the dimerization of the calcium-sensing and metabotropic glutamate receptors. A carboxy-tail coiled-coil interaction was shown to be involved in formation of the $GABA_B$ heterodimer. Finally, interactions between transmembrane helices have been proposed for the type “A” GPCRs. Figure taken from Bouvier, M. (2001) *Nat Rev Neurosci.* 2: 274 – 286.

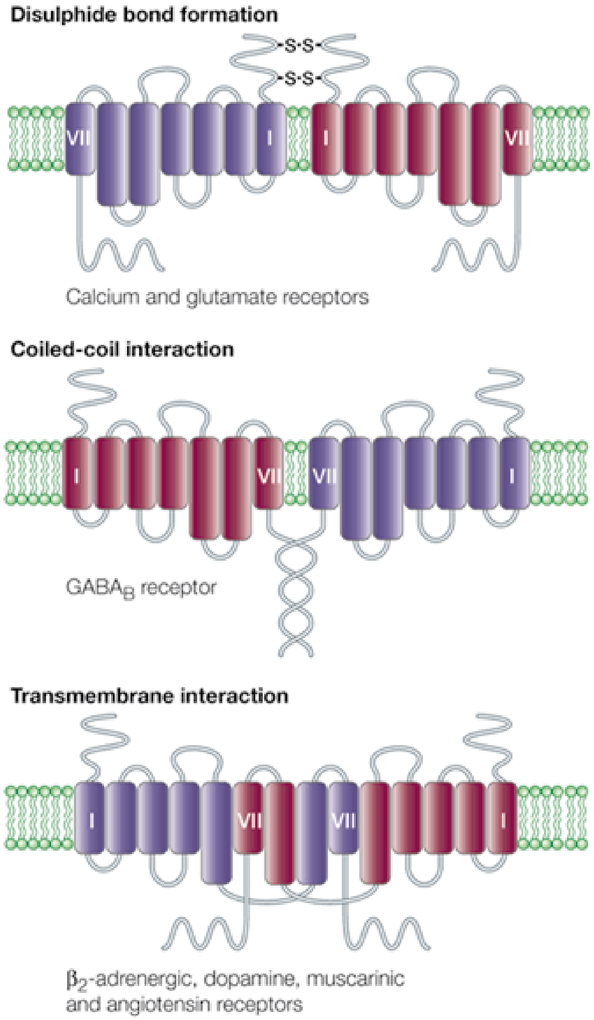

Disulphide bond formation

Calcium and glutamate receptors

Coiled-coil interaction

GABA$_B$ receptor

Transmembrane interaction

β_2-adrenergic, dopamine, muscarinic and angiotensin receptors

Figure 1. 11: Proposed rhodopsin dimer/oligomer model showing the putative dimeric interface. (A) Model of the packing arrangement of rhodopsin molecules within the paracrystalline arrays in the native disk membrane. The intradimeric (contact 1), interdimeric (contact 2) and row–row (contact 3) contacts that form the higher-order structure are highlighted. Additionally, the amino acids shown to be involved in the cross-link products from [166] are labeled: amino acid residues K66, K245, K248 and C140. The cross-links formed by the homo-bifunctional cross-linker DSP are marked by the red line while the cross-links formed by the hetero-bifunctional cross-linker LC-SPDP are marked by the black lines. **(B)** The putative intradimeric interface of rhodopsin formed by TM IV and TM V. The α- and β-carbon atoms (orange spheres) mark the location of the amino acid residues in rhodopsin that correspond to the amino acid residues found at the dimer interface of dopamine D2R, as identified by site-directed cysteine mutagenesis and cross-linking [168]. The models are visualized from the cytoplasmic side of the membrane. Figure taken from Fotiadis, D. *et al.* (2006) *Curr. Opin. Struct. Biol.* 16: 252 – 259.

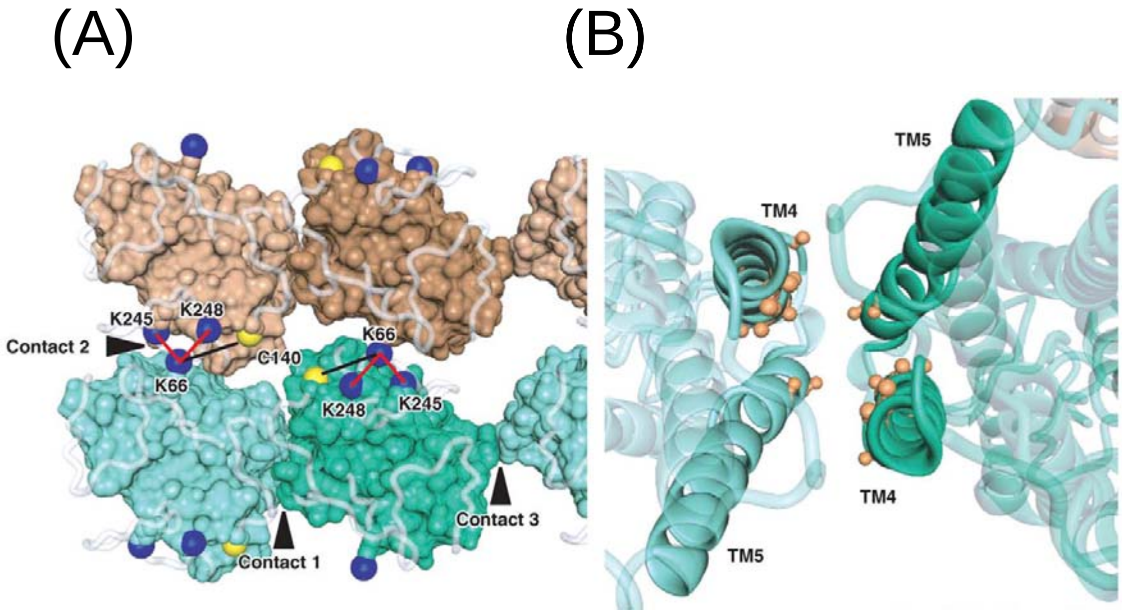
(A)
(B)
K245
K248
Contact 2
C140
K66
K66
K248
K245
Contact 3
Contact 1
TM4
TM5
TM4
TM5

Chapter 2

Mapping Proximity within Proteins Using Fluorescence Spectroscopy. A Study of T4 Lysozyme Showing that Tryptophan Residues Quench Bimane Fluorescence

Steven E. Mansoor[‡], Hassane S. Mchaourab[§] and David L. Farrens[‡]

[‡] Department of Biochemistry and Molecular Biology, Oregon Health and Science
University, Portland, Oregon 97239-3098, USA

[§] Department of Molecular Physiology and Biophysics, Vanderbilt University,
Nashville, Tennessee 37232, USA

Running Title: Proximity within Proteins Measured by Bimane Labeling

2. 1: SUMMARY

We present a novel method for mapping proximity within proteins. The method exploits the quenching of the fluorescent label bimane by nearby tryptophan residues. In studies of T4 lysozyme we show that this effect appears to be distance dependent and orientation specific. Specifically, we show that a proximal tryptophan residue can reduce bimane fluorescence intensity by up to 500% and induce complicated fluorescence decay kinetics. Replacing the neighboring tryptophan residue with phenylalanine removes these spectral perturbations. The advantages of using the tryptophan quenching of bimane fluorescence for protein structural studies include the low amount of protein required and the substantial simplification of labeling strategies. We anticipate this method will prove suitable for a wide array of high-throughput protein studies such as protein folding, the detection of protein-protein interactions, and, most importantly, the dynamic monitoring of conformational changes.

All experiments and data analysis reported in this chapter were performed by the author of this dissertation. The DNA plasmid constructs used to express the protein samples were supplied by Dr. Hassane S. Mchaourab. The data presented in this chapter has been previously published in Mansoor, S.E., Mchaourab, H.S., and Farrens, D. L. (2002) *Biochemistry* **41**, 2475-2484 and presented as a platform talk at the 46th Annual Biophysical Society Meeting, San Francisco, CA, 2002.

2. 2: INTRODUCTION

Site-directed labeling methods (SDL) are unique and powerful ways to study protein structure and dynamics. Generally, these methods involve introducing cysteine residues into defined regions of a protein and then attaching spectroscopic probes to the cysteines to obtain information about the local environment around each probe molecule. This approach generates an array of data from which the solvent accessibility and secondary structure of the region can be inferred [67,68,176,177].

One of these methods uses nitroxide spin labeling and EPR spectroscopy. This approach, called site-directed spin labeling (SDSL), can determine conformational changes and local secondary structure in proteins [67]. In general, fluorescence-based strategies can be used to provide similar information [42,64,74,178-185].

However, the larger question of determining protein structure is a more formidable challenge with SDL methods. In addition to sequence-specific secondary structure, geometric information is required to establish the overall packing of pairs of secondary structure elements. With the spin labeling method, this problem can be overcome by measuring spin-spin interactions between two nitroxide spin labels [41,186-189].

Fluorescence-based SDL strategies for measuring distances are not as straightforward. The classical approach has been to measure fluorescence resonance energy transfer (FRET) between two fluorescent probes on different parts of the protein [182-184]. Although powerful, the FRET approach is usually complicated by the need to label with two different, spectrally overlapping probes and by the orientation factor required for data analysis. Also, the linear range of distances that can be determined by

FRET (usually 20 - 100 Å) is often too large to be useful for determining very close packing between secondary structure elements in proteins, since the size of the probes often used is larger than 10 Å.

We report in this chapter a new, simple way to obtain short-range distance constraints in proteins by fluorescence spectroscopy. Conceptually, our approach is similar to recent methods which selectively introduce fluorescence quenching groups into proteins [190,191]. The method we describe here exploits the ability of tryptophan to quench the fluorescence of the cysteine-specific probe, bimane. Because this approach eliminates the need for the use of two different fluorescent probes and operates over much shorter ranges (essentially collision or contact distance), it complements the longer range FRET methods for protein structure and dynamics studies. Furthermore, because the Trp quencher is built into the protein sequence, the labeling strategies are substantially simplified.

We recently deduced that Trp quenches bimane fluorescence upon further analysis of our previous SDFL work on T4 lysozyme (T4L) [64]. In that work we found that bimane fluorescence was unusually low at several sites on the protein and showed complicated decay kinetics. Intriguingly, the location of these sites did not follow any obvious pattern with respect to their topological or secondary structure location.

Upon closer examination of the crystal structure of T4L, we noticed that these anomalous sites are within ~ 6 Å of one of the Trp residues in the native protein, as illustrated in Figure 2. 1. Four of the sites, 121, 124, 129, and 133, showed abnormally low fluorescence quantum yields, as well as complex fluorescence decays (see Figure 4 in ref [64]). We hypothesized that these Trp residues may be interacting with and influencing the fluorescence properties of neighboring bimane residues. The physical basis of this effect has previously been established by Kosower and colleagues, who found that Trp strongly quenches the fluorescence of bimane free in solution and when attached to small peptides (3-4 amino acids in length) [192].

In this chapter we present results showing that proximal Trp residues cause quenching of bimane in proteins, thus explaining the unusual fluorescence observed in our previous work [64]. Further, we show that this property is distance-dependent and can be used to map distances between Trp and bimane probes introduced at strategic sites in a protein. We discuss future uses of Trp/bimane quenching for SDFL studies in the context of protein fold determination, detection of protein-protein interactions, and resolving protein conformational changes.

2. 3: EXPERIMENTAL PROCEDURES

2. 3. 1: Materials.

The reagents (fluorescent label, etc.) and the equipment (filters, cuvettes, etc.) used were identical to those described previously [64]. The cysteine-free pseudo-wild-type lysozyme gene containing the substitutions C54T and C97A [193,194] was kindly provided by F. W. Dahlquist (University of Oregon). Hereafter, this mutant will be called the “wildtype” or T4L.

2. 3. 2: Buffers.

The buffers used were as follows: buffer A, 50 mM MOPS, 50 mM Tris, and 1 mM EDTA, pH 7.6; buffer B, 20 mM Tris, 20 mM MOPS, 0.02% sodium azide, 1 mM

EDTA, and 1 mM DTT, pH 7.6; buffer C, 20 mM KH_2PO4 and 25 mM KCl, pH 3.0; buffer D, 50 mM MOPS, 50 mM Tris, 1 mM EDTA, pH 7.6, and 3 M guanidine hydrochloride.

2. 3. 3: Construction of T4L Mutants.

Site-directed mutagenesis was carried out using polymerase chain reaction (PCR) methods [195]. To facilitate this work, two new restriction sites, *Sph*I and *Xba*I, were introduced into the previously described plasmid using the overlap extension method. Oligonucleotides containing the X to cysteine substitution and overlapping either of the restriction sites were used to generate PCR fragments. The PCR fragments were then digested and ligated into the appropriate cloning vector, and the mutant constructs were confirmed by DNA sequencing.

2. 3. 4: Nomenclature.

Throughout this chapter, mutants are named by specifying the original residue, the number of the residue, and the new residue, in that order. For example, the code K124C indicates that the native lysine residue at the 124th amino acid position was mutated to a cysteine. Similarly, N116W indicates the native asparagine was mutated to a tryptophan. Mutants labeled with mBBr are named by specifying the original residue, the number of the residue, and the suffix B_1, indicating the monobromobimane label. For example, the code $K124B_1$ indicates that the native lysine residue at the 124th amino acid position has been mutated to a cysteine and reacted with the mBBr label.

2. 3. 5: Expression and Purification of T4L Mutants.

Expression of mutant proteins was as described previously [64,196]. Briefly, K38 *Escherichia coli* cells were transformed with the T4L cysteine mutant plasmid [197], and protein production was induced in log phase cultures (OD_{595nm} = 1.2). After 90-120 min of shaking at room temperature, the cells were harvested, and the cell pellet was resuspended in 30 mL of buffer B, lysed, and clarified by centrifugation followed by filtration. DTT was added to the filtered cell solution to 20 mM, and after 30 min, the solution was loaded onto a cation-exchange column (Pharmacia Biotech HiTrap, 1 mL SP) equilibrated with buffer A. The samples were eluted with an increasing salt gradient from 0 to 1 M NaCl. The purity of the proteins was assessed by SDS-PAGE and judged to be at least 90% pure for all samples studied.

2. 3. 6: Fluorescence Labeling of T4L Mutants.

Labeling of each lysozyme mutant was carried out by using a 10× molar excess of the fluorescent label in buffer D at 4 °C overnight. Free label was separated from the labeled protein by gel filtration on a desalting column (Pharmacia Biotech HiTrap, 5 mL) equilibrated with buffer A. Absorption spectra (measured using a Shimadzu UV 1601) were used to calculate the labeling efficiency for each mutant. Concentrations were calculated using extinction coefficients of $\varepsilon_{280} = 23327$ L cm^{-1} mol^{-1} for T4 lysozyme and $\varepsilon_{380} = 5000$ L cm^{-1} mol^{-1} for mBBr. To correct for mutants in which a Trp residue was either introduced or removed, an extinction coefficient value of $\varepsilon_{280} = 5600$ L cm^{-1} mol^{-1} was either added or subtracted to the WT T4 lysozyme extinction coefficient. (Note that a mutation from a tryptophan to a phenylalanine resulted in an extinction coefficient of $\varepsilon_{280} = 18027$ L cm^{-1} mol^{-1}.) The contribution from mBBr at 280 nm was subtracted before the protein concentrations were calculated. Control experiments using the cysteine-less WT protein showed that background labeling was less than 3% (as judged by absorption and fluorescence spectroscopy).

2. 3. 7: Thermodynamic Stability

Analysis of thermal unfolding properties was used to assess the stability of each mBBr-labeled mutant [198,199]. This analysis was carried out by monitoring the tryptophan fluorescence emission intensity at 320 and 350 nm as a function of temperature [64]. At the point of thermal denaturation, the emission intensities at each of these wavelengths change due to the solvent-sensitive property of tryptophan fluorescence [199,200].

The details of the measurements were as previously described [64]. Briefly, 2 μM labeled protein (dialyzed against buffer C) were measured using the PTI steady-state fluorescence spectrophotometer in a T-format. Samples were excited at 280 nm and monitored at 350 and 320 nm. The melts involved ramping the temperature from 6 to 80 °C at a rate of 2°/min, after which the samples were cooled to 6 °C, to determine the extent of protein refolding, and melted again. The mutants showed greater than 75% refolding, as judged by the extent to which the ratio returned to its starting value (except L133B_1/W138F). The melts were done in duplicate, and the reported T_m values are the average of the two melts. Analysis of the thermal melt data was performed assuming an equilibrium of a two-state model (native folded state and totally denatured state) [198,199].

With the assumptions made by Becktel and Schellman that $\Delta S_{mutant} \approx \Delta S_{wt}$ [201], $\Delta\Delta G$ values for each mBBr-labeled T4 lysozyme mutant were calculated using the approximation:

$$\Delta\Delta G = \Delta T_m \Delta S_{wt} \qquad \text{[Eq. 2. 1]}$$

where ΔT_m is the difference in melting temperatures between the mutant and the wild type and the ΔS_{wt} value is the change in entropy between the folded and denatured states of the wild-type protein. For more details, see refs [64] and [201].

2. 3. 8: Steady-State Fluorescence.

Unless noted otherwise, the steady-state fluorescence measurements of mBBr-labeled mutants were carried out at 22 °C, using 2 μM to 10 μM sample in buffer A and the PTI fluorometer. The fluorescence emission spectra were measured from 395 to 600 nm (1 nm slits) while being excited at 381 nm (2 nm slits).

2. 3. 9: Quantum Yield Measurements.

The quantum yield for each mBBr-labeled mutant was measured as described previously [64] using quinine sulfate (quantum yield equal to 0.55 in 1 N H_2SO_4) as the standard. Emission spectra were taken using 360 nm excitation (3 nm slit width) from 370 to 700 nm (1 nm slits). Measurements were at 22° C using ~ 2 μM to 10 μM bimane-labeled lysozyme mutants and for the quinine sulfate standard.

2. 3. 10: Fluorescence Lifetime Measurements.

The fluorescence lifetimes of the mBBr mutants were measured as previously described [64]. Briefly, the measurements were carried out at 22 °C using a PTI Laserstrobe fluorescence lifetime instrument on 250 μL of a 2-10 μM sample placed in a 4 mm black-jacketed cuvette. The samples were excited at 381 nm (pulses of fwhm ~ 1.5 ns), and fluorescence emission was monitored through two long-pass filters (>470 nm). Each data point on a lifetime decay curve represents two averages of five laser flashes, and each decay represents 150 of these data points spaced out over the collection time interval.

Data were acquired using an arithmetic data collection method and analyzed using the commercial PTI software. Both the exponential series method (ESM) and a two-exponential decay model were used in the analysis [202-204]. In brief, the ESM analysis fits the decay data using a series of exponentials with fixed, logarithmically spaced lifetimes and variable pre-exponentials. In the present ESM analysis, the fluorescence decays were fit allowing 100 discrete lifetimes of varying amplitude from 0.1 to 30 ns until the χ^2 value was minimized. Plots of ESM analysis are included because they provide a graphical way to differentiate between continuous lifetime distributions and discrete, multiexponential decays. Thus, analysis of the ESM plots provides a rapid way to qualitatively assess the proximity between a bimane label and a Trp residue. The decay data were also fit to a two-exponential decay model, and these values were used to calculate weighted lifetime values.

2. 3. 11: Calculation of the Driving Force for Photoinduced Electron Transfer Rates (PET).

The driving force (ΔG_{el}) for the PET was calculated using a form of the Rehm-Weller equation [205-207]:

$$\Delta G_{el} = e[E_{ox}(D) - E_{red}(A)] - \Delta G_{oo} - w_p \qquad \text{[Eq. 2. 2]}$$

The above variables are defined as follows: *e* is the conversion factor from eV to kcal/mol (1 eV = 23.061 kcal/mol). E_{ox} and E_{red} are the donor (D, Trp) and acceptor (A, bimane) redox values [E_{red} = -1.38 V vs SCE for bimane [208] and E_{ox} = 1.00 V vs SCE for Trp [209]]. The ΔG_{oo} term is the energy for the bimane excited state (at 381 nm ΔG_{oo}

= 75 kcal/mol, or 3.25 eV). Finally, the w_p term represents the “work” term for the Coulombic attraction felt by the transiently charged species. For the present work we approximated w_p = -1.3 kcal/mol assuming a center to center distance between the bimane and Trp of 7 Å [206]. Using the above relationships, the driving force for the electron transfer was calculated to be ΔG_{el} = -18.8 kcal/mol (or -0.816 eV), suggesting an exergonic photoinduced electron transfer.

2. 3. 12: Calculation of Photoinduced Electron Transfer Rates (PET).

Electron transfer rates were calculated from the weighted fluorescence lifetimes [$<\tau> = f_1\tau_1 + f_2\tau_2$, where $f_1 = \alpha_1/(\alpha_1 + \alpha_2)$ and $f_2 = \alpha_2/(\alpha_1 + \alpha_2)$] by using the relationship $k_{ET}^{\tau} = 1/\tau - 1/\tau_{ref}$ [210]. In this analysis, the lifetime of the bimane-labeled sample in the presence of the proximal Trp residue (τ_w) was used for τ, and the lifetime of the samples lacking the Trp residue (τ_0) was used for τ_{ref}. Similarly, the steady-state fluorescence data were used to calculate electron-transfer rates using the relationship $k_{ET}^{F} = (F_0/F_w - 1)/\tau_0$, where F_w and F_0 represent the integrated fluorescence intensity (from 410 to 600 nm, with excitation at 381 nm) of the bimane-labeled samples with and without the proximal Trp residue, respectively. τ_0 represents the lifetime value as defined above.

2. 4: RESULTS

2. 4. 1: Construction and Characterization of Mutants K124B$_1$/W126F and L133B$_1$/W138F.

As discussed in the introduction, a prior SDFL scan of T4 lysozyme showed perturbed fluorescence from bimane labels at several sites on the protein, especially sites

124 and 133 (see Figure 1 and Figure 4 in ref [64]). To determine if these perturbations were due to neighboring tryptophan residues, we substituted the “suspect” neighboring Trp residues to phenylalanines (W126F to test site 124 and W138F to test site 133). Both mutants could incorporate the bimane label with similar efficiency (Table 2.1). Neither Trp substitution resulted in a dramatic destabilization of the bimane-labeled cysteine mutant protein beyond that reported previously, indicating the overall fold of the protein was not significantly altered (Table 2.1) [211]. The ΔT_m and $\Delta\Delta G$ values for mutants L133B$_1$ and L133B$_1$/W138F are larger than the values for the other mutants. However, such a result is not unexpected and, in fact, would be predicted. Residue 133 is the most buried (least solvent exposed) of the residues in the present study, and it has been previously found that destabilization is larger for substitutions at completely buried sites [64,211]. Thus, because mutations at site 133 result in large $\Delta\Delta G$ values, it is possible that both mutants L133B$_1$ and L133B$_1$/W138F contain a small fraction of sample that is not fully folded under the experimental conditions. Note that, for all of the data reported below, the samples were matched, by absorbance, to have the same bimane concentration during the measurements.

2. 4. 2: Mutating the Neighboring Tryptophan Residue to Phenylalanine Causes an Increase in Bimane Fluorescence Intensity and Lifetime at Sites 124 and 133.

Figures 2.2 and 2.3 show the results of making the W126F and W138F substitutions on the fluorescence of bimane labels attached to sites K124C and L133C, respectively. Figure 2.2A shows the location of K124 and W126 on the T4L structure. Figure 2.2B and Table 2.1 show how the fluorescence increases approximately 5-fold upon the W126F mutation, with a concomitant increase in the fluorescence lifetime (Figure 2.2C, Table 2.2). Simplification of the decay kinetics is also seen, as reflected in the two-exponential (Table 2.2) and ESM analysis (Figure 2.2D). Similarly, the W → F mutation at site 138 (Figure 2.3A) results in an approximate 5-fold increase in fluorescence intensity (quantum yield) from the bimane label at site 133 (Figure 2.3B, Table 2.1). The W138F mutation also results in an increased fluorescence lifetime (Figure 2.3C, Table 2.2) and simplified decay kinetics in the ESM analysis (Figure 2.3D). Interestingly, for both mutants, removing the neighboring tryptophan changes the complicated lifetime distribution (Figures 2.2D and 2.3D, top half) to essentially one lifetime (Figures 2.2D and 2.3D, bottom half).

With the exception of position 133, an overlap of the (normalized) fluorescence emission spectrum from each sample demonstrates that the $\lambda_{\max}$ of fluorescence emission does not show significant changes due to the Trp → Phe substitution (Table 2.1). This latter result indicates that the difference in intensity is not due to a repacking/change in hydrophobicity of the bimane label.

2. 4. 3: Construction and Characterization of Mutants D72B$_1$ and D72B$_1$/R76W.

To investigate if a Trp can be introduced to alter the fluorescence of a neighboring bimane residue, we introduced a Trp at site 76, one turn away from a bimane label attached at site 72. We chose this pair of sites because the 72/76 pair is on the exposed surface of the long helix in T4L and substitutions are unlikely to disturb the structure (Figure 2.4A). Furthermore, the $i + 4$ residue where the Trp is introduced is located away from termini, allowing a better estimation of the distance separation between the Trp and the bimane side chains. Both mutants could be labeled with bimane to unity. Neither the introduction and labeling of the cysteine residue at site 72 nor the $D72B_1/R76W$ mutation had much effect on the thermodynamic properties of the protein (Table 2.1).

Introducing the Trp at site 76 caused a dramatic decrease in intensity (Figure 2.4B, Table 2.1) and shortened and complicated the fluorescence decay properties (Figure 2.4C,D, Table 2.2).

2. 4. 4: Construction of N116W Mutants To Measure Distance Dependencies of Bimane Quenching by Trp.

We next tested if tryptophan quenching of bimane can be used to obtain proximity information between secondary structure elements in proteins. A reference Trp was introduced at site 116 at the N-terminus of helix G, and the bimane probe was introduced on selected surface-exposed residues on helix H, a neighboring helix in the structure. The location of the mutation, N116W, and the four sites are shown in Figure 2.5A. The neighboring bimane attachment sites predicted to be potentially affected by the Trp residue (sites 123, 128, 132, 135) are in various distances from this Trp site. The sites encompass an $i + 8$ as well as several different interhelix distances, thus allowing for a qualitative assessment of the distance dependence of the Trp → bimane quenching phenomena. The Trp substitutions at N116 did not appear to affect the protein stability compared to the previous single cysteine mutants (see Table 2.1). Note that the four sites in lysozyme being tested were previously shown [64] to have normal bimane fluorescence characteristics [i.e., quantum yields of ~ 0.2 or greater (see Figure 2.1B) and monoexponential fluorescence decay properties].

2. 4. 5: The Fluorescence Properties of the N116W Mutants Depend on the Distance of Bimane from N116W.

The site-specific effects of N116W on the neighboring bimane fluorescence intensity depend on the relative proximity to the bimane side chain (Table 2.1, left panels Figure 2.5B-E). What is more important, the distance dependence is in qualitative agreement with the crystal structure. For instance, the bimane label at site 132 shows the largest quenching, consistent with it being closest to the tryptophan at site 116 based on the structure. In contrast, bimane at site 135 is the farthest and shows the least quenching.

In addition to quenching the steady-state fluorescence intensity, the Trp residue introduced at N116W causes dramatic effects on the decay properties of some of the neighboring bimane labels. For example, the presence of the Trp residue at site 116 increases the fluorescence decay rates (shortens the fluorescence lifetime) for the bimane labels at sites 128 and 132 (Table 2.2). Not only are the decay rates faster but they are also more complicated, as can be seen graphically from analysis of the decay data using the ESM method for measuring lifetime distributions (right panels, Figure 2.5C,D). As found for the previous mutants, the ESM analysis of the bimane-labeled mutants without the Trp residue is essentially monoexponential (Figure 2.5B-E, top half of each panel on the right). However, the introduction of the Trp residue results in multiexponential decay characteristics for most of the sites, which is reflected in the distribution of lifetimes observed in the ESM analysis (Figure 2.5B-E, bottom half of each panel on the right).

2. 5 DISCUSSION

The fluorescent probe monobromobimane is an excellent reporter group for protein structural studies. As a probe, it has a relatively small molar volume, and thus introduces minimal structural perturbation, and shows a defined solvent-dependent shift in its emission spectra [42,64].

However, we recently noticed several unusual aspects of bimane fluorescence during an SDFL study of T4 lysozyme: at a number of attachment sites on the protein, the bimane fluorescence intensity was abnormally low and the decay kinetics were complex [64]. What was the cause of these anomalies? Closer analysis of the T4L crystal structure revealed that all of the anomalous bimane sites were close to a Trp residue, suggesting the tryptophans might be causing the abnormal bimane fluorescence. A search of the literature supported this theory; in a study of small, bimane-labeled peptides, Kosower and colleagues found that only Trp (and to a much lesser extent tyrosine) affected the bimane fluorescence [192].

Thus, we tested two of the affected sites (K124 and L133) to determine the effect of mutating the proximal tryptophan residues to a phenylalanine. In both cases the substitution caused an increase in bimane fluorescence intensity and a simplification of the fluorescence decay kinetics (Tables 2.1 and 2.2, Figures 2.2 and 2.3). Further, we found the reverse to be true: introducing a Trp residue (at site 76) caused quenching of a nearby bimane label (at site 72) one turn away on the same helix (Tables 2.1 and 2.2, Figure 2.4).

These observations are important for two reasons: they highlight an interesting property of bimane fluorescence, and they suggest a possible use of this phenomenon in protein structure-function studies. Although SDFL scans can yield information about secondary structural elements and the solvent-accessible surfaces of proteins, determining the three-dimensional arrangement (packing) of these elements is more difficult. The distance constraints provided by the Trp quenching of bimane might provide tertiary structure (packing) information to complement secondary structural information obtained from an SDFL scan.

With this goal in mind, we tested whether Trp quenching of bimane could be used to measure distance separations between sites in a protein, such as between two helices. We introduced the Trp residue at a location (site 116) that should cause different amounts of quenching of bimane labels attached to neighboring sites. As expected, the Trp mutation at site 116 caused variations in the fluorescence intensity/quantum yields from bimane labels at neighboring sites 123, 128, 132, and 135. The extent of the quenching was in qualitative agreement with the distance between the Trp residue and these sites on the T4L structure (compare Figure 2.5 with the data in Tables 2.1 and 2.2).

2. 5. 1: Probable Mechanism for Trp Quenching of Bimane Fluorescence.

Why do the proximal Trp residues cause such dramatic quenching of bimane fluorescence? The probable cause of the quenching is through photoinduced electron transfer (PET) from Trp to the excited-state bimane. Bimane is sensitive to quenching by electron-donating groups [208,212], and the Trp quenching of bimane on peptides was proposed to occur by the Trp donating an electron to the excited-state bimane [192]. We calculated the possible driving force for a PET process from Trp to bimane (using their E_{ox} and E_{red} values) and found it to be ΔG_{el} = -0.816 eV, indicating an exergonic and thus likely process (see Experimental Procedures, Section 2. 3. 11). According to the PET fluorescence quenching hypothesis, after electron transfer from the Trp to the proximal bimane, the resulting radical ion pair, Trp (+·): Bim(–·), would undergo reverse electron transfer to return the bimane to the ground state (S_0) in a radiationless manner.

Similarly, excited-state electron transfer has been ascribed to be the cause of tryptophan fluorescence and phosphorescence quenching [213,214] and be the cause of the complicated, multiexponential decay properties often observed for the tryptophan fluorescence in many proteins [193,215]. The fluorescence decay data also support a PET fluorescence quenching mechanism. In every case tested, bimane residues most able to come within contact distance of a Trp residue showed shorter lifetimes in the two-exponential analysis and multiple lifetime species in the ESM analysis, whereas removing the neighboring Trp caused an increase in the lifetimes and a simplification of the ESM decay analysis.

Assuming a PET quenching mechanism, we calculated rate constants for the electron transfer from Trp to bimane (k_{ET}) for each of the mutants. These rates were calculated as described in Experimental Procedures (Section 2. 3. 12) and are given in Table 2.3. The calculated k_{ET} rates (maximum value ~5×10^8 s^{-1}) are in reasonable agreement with a PET mechanism. Note that both the changes in fluorescence lifetime and the changes in fluorescence intensity were used to calculate the k_{ET} rates. This approach avoids the possibility of missing very rapid PET occurring from proximal conformers that would be too fast to detect with our lifetime instrumentation, as it would still appear as a decrease in steady-state fluorescence intensity. Several instances where $k_{ET}^{F} > k_{ET}^{\tau}$ can be seen in Table 2.3.

In principle, it should be possible to use these k_{ET} rates, combined with the driving force for the PET, to determine distances between the Trp donor and bimane acceptor. Unfortunately, to accurately assess distances between the Trp and bimane pairs using the calculated k_{ET} rates is beyond the scope of the present work. Unknown variables in such calculations include uncertainty in the solvent polarity on protein surfaces [216], as well as distance, steric, and stereochemical factors [217] such as the shape and relative orientation of the two molecule pairs [218]. Thus, instead of approximating distances from the k_{ET} rates, we propose a more simple, qualitative way to assess the proximity of Trp and bimane residues directly from the fluorescence data, described below.

2. 5. 2: Simple, Qualitative Way To Classify the Different Types of Trp/Bimane Quenching.

We propose that comparing the steady-state and fluorescence lifetime data provides a qualitative yet reliable assessment of the proximity of the Trp/bimane pair. In this approach, one first determines the ratio of the fluorescence intensity without (F_0) and with (F_w) the presence of the tryptophan residue (F_0/F_w) and then compares this value to the ratio obtained from the weighted fluorescence lifetime data without and with the Trp residue (τ_0/τ_w). Note that the weighted fluorescence lifetime data are proportional to the steady-state fluorescence intensity [69].

These ratios are then used to assess whether the Trp/bimane pair is “not close” (>15 Å), “close” (~10-15 Å), or “very close” (5-10 Å). Not close pairs are defined as those in which no effect of Trp on the bimane fluorescence is observed. Close pairs are those showing significant dynamic fluorescence quenching, i.e., quenching that occurs because the two species are able to collide during the lifetime of the bimane excited state.

Dynamic quenching is indicated when both the steady-state fluorescence intensity and fluorescence lifetimes decrease by roughly the same amount (i.e., $F_0/F_w > 1$, $\tau_0/\tau_w > 1$, and $F_0/F_w \approx \tau_0/\tau_w$) [219].

We are defining very close Trp/bimane pairs to be pairs for which static fluorescence quenching is observed. Static quenching is indicated when the fluorescence intensity decreases but the fluorescence lifetimes do not change (i.e., $F_0/F_w > 1$, but $\tau_0/\tau_w \approx 1$) [219]. Static quenching can occur only when two molecules are initially very close (i.e., within contact distance) at the moment of fluorophore excitation. At these close distances, the quenching occurs because the two molecules have either formed a ground-state, nonfluorescent complex or alternatively because they undergo a "dynamic" quenching process so rapid that it cannot be detected by the fluorescence lifetime instrumentation [220].

The different intensity and lifetime ratios for the Trp/bimane mutants are given in Table 2.3. An example of dynamic vs static quenching for the T4L mutants is shown in Figure 2.6. Figure 2.6A shows the effect of the quenching phenomenon on the fluorescence lifetime decays, with the decay intensity plotted on a log scale. Note the rapid, sharp component to the decay of K124B_1 compared to K124B_1/W126F, indicating a dynamic quenching mechanism. In contrast, no such rapid component is observed in the decay of mutant N116W/N132B_1; rather the two decays are seen to be nearly parallel. These results suggest that at least some fraction of the Trp/bimane pair in N116W/N132B_1 is very close, forming a nonfluorescent ground-state complex or, alternatively, the PET-induced quenching is too fast to be resolved by our instrumentation.

Similarly, the bar graphs in Figure 2.6B compare the quenching ratios of the steady-state fluorescence intensity (F_0/F_w) with the quenching ratios determined from the weighted fluorescence lifetimes (τ_0/τ_w). As can be seen, the bimane at 124 shows dynamic quenching ($F_0/F_w \approx \tau_0/\tau_w$), whereas the bimane at 132 shows substantial static quenching ($F_0/F_w >> \tau_0/\tau_w$), suggesting that the bimane at site 132 is very close to N116W and thus is being quenched by a static process. Note also that the absorption spectrum is altered for mutant N116W/N132B_1 compared to mutant N132B_1, also suggestive of a ground-state complex for the former mutant (Figure 2.6C). Note further that the same conclusions can be reached by comparing the ratio of the k_{ET}^F and k_{ET}^τ rates for each mutant.

2. 5. 3: Conclusion.

We have shown that Trp quenching of bimane fluorescence can be used to measure proximity within proteins. The amount of quenching depends on the distance between the two molecules as well as on their ability to come within contact, and thus these constraints limit the number of Trp/bimane pairs that are able to show quenching. However, these limitations are also a strength of this method, since it is only sensitive to local, short-range interactions that are difficult to measure using longer range FRET methods. Another advantage of this method is that these short-range interactions can be measured using widely available fluorescence instrumentation and requires only minimal amounts of sample. More quantitative interpretations of distance constraints await further studies, including analysis of crystal structures of bimane-labeled samples combined with molecular modeling and analysis of the time-resolved data using the distance-dependent quenching model of Zelent *et al.* [221]. Work of this type is currently underway in our laboratory. Because the Trp quenching of bimane fluorescence is easily detected, we anticipate this phenomenon will be useful in protein folding studies, the detection of protein-protein interactions, and the monitoring of protein conformational changes.

2. 6: ACKNOWLEDGEMENTS

We thank Dr. A. Beth for critical reading of the manuscript.

Table 2. 1: Characterization of Bimane-Labeled Mutants

Mutant	Mol of[a] label per mol of T4L	ΔT_m[b,c] (^{0}C)	$\Delta\Delta G$[b,c] (kcal/ mole)	Abs.[e] λ_{max} (nm)	Emm. λ_{max} (nm)	Quantum[f] yield (Φ)
K124B$_1$	0.9	-2.5 ± 0.2[c]	-0.7[c]	392	472.4 ± 0.6	0.036 ± 0.005
K124B$_1$/W126F	0.9	-4.0 ± 0.3	-1.2	391	472.3 ± 0.1	0.185 ± 0.009
L133B$_1$	1.2	-19.5 ± 1.0[c]	-5.5[c]	380	456.9 ± 0.6	0.096 ± 0.016
L133B$_1$/W138F	1.0	-20.4 ± 1.0	-6.0[d]	382	452.3 ± 2.8	0.573 ± 0.017
D72B$_1$	0.9	-0.9 ± 0.1	-0.3	385	463.8 ± 0.4	0.294 ± 0.043
D72B$_1$/R76W	1.1	-2.1 ± 0.2	-0.6	387	465.3 ± 0.5	0.057 ± 0.006
Q123B$_1$	0.9	+0.3 ± 0.5[c]	+0.1[c]	388	468.9 ± 0.4	0.220 ± 0.017
N116W/Q123B$_1$	1.0	-4.0 ± 0.3	-1.2	390	469.1 ± 0.8	0.135 ± 0.004
E128B$_1$	1.0	-1.8 ± 0.3[c]	-0.5[c]	401	469.5 ± 0.5	0.182 ± 0.001
N116W/E128B$_1$	1.0	-7.0 ± 0.5	-2.1	397	469.7 ± 0.5	0.043 ± 0.003
N132B$_1$	0.9	+1.8 ± 0.2[c]	+0.5[c]	386	466.8 ± 0.1	0.201 ± 0.004
N116W/N132B$_1$	0.9	+3.1 ± 0.8	+0.9	394	468.9 ± 0.4	0.047 ± 0.004
K135B$_1$	0.9	-0.6 ± 0.2[c]	-0.2[c]	391	472.0 ± 0.7	0.146 ± 0.023
N116W/K135B$_1$	1.0	-4.0 ± 0.2	-1.2	390	471.0 ± 0.3	0.118 ± 0.022

[a] Represent an average of two independent labeling experiments; the standard error of the mean on all mutants < ± 0.1.

[b] Values are in comparison to cysteine-less "wild-type" T4 lysozyme, $T_m = 53.0\ ^oC$, and $\Delta S_{wt} = 292.8$ cal*mol^{-1}K^{-1}; $\Delta\Delta G$ calculated using the approximation that $\Delta\Delta G = \Delta T_m * \Delta S_{wt}$.

[c] ΔT_m and $\Delta\Delta G$ values for the indicated mutants are from [64], and are provided for comparison purposes.

[d] Apparent $\Delta\Delta G$ value as this mutant did not appear to be fully reversible.

[e] Represent an average of two values; all values have a standard error of < ± 1 nm.

[f] Quantum yields were measured by integrating fluorescence intensity from 370 nm to 700 nm with 360 nm excitation using Quinine Sulfate in 1N H_2SO_4 as the standard.

Table 2. 2: Two-Exponential Lifetime Analysis of the Fluorescence Decay Measurements.[a]

Mutant	τ_1 (ns)	f_1	τ_2 (ns)	f_2	$\chi 2$	$<\tau>$[b] (ns)
K124B$_1$	4.9 4.4	0.2 0.2	1.4 1.3	0.8 0.8	1.0 1.0	2.1 ± $1.3e^{-2}$
K124B$_1$/W126F	9.5 9.4	1.0 1.0	--- ---	--- ---	1.1 0.9	9.4 ± $3.8e^{-2}$
L133B$_1$	7.0 7.2	0.3 0.3	1.0 1.3	0.7 0.7	1.0 1.4	3.1 ± 0.1
L133B$_1$/W138F	8.6 8.9	0.7 0.8	0.7 0.9	0.3 0.2	1.1 1.0	6.8 ± 0.2
D72B$_1$	9.7 9.9	1.0 1.0	--- ---	--- ---	0.9 1.0	9.8 ± 0.1
D72B$_1$/R76W	6.6 6.6	0.5 0.6	0.7 0.9	0.5 0.4	0.7 1.0	4.1 ± 0.1
Q123B$_1$	9.8 9.9	1.0 0.8	$2.4e^{-3}$ $2.2e^{-2}$	$1.9e^{-2}$ 0.2	1.1 1.4	8.9 ± 0.4
N116W/Q123B$_1$	7.2 7.4	0.7 0.8	0.5 1.0	0.3 0.2	1.1 0.8	5.6 ± 0.3
E128B$_1$	8.7 8.7	1.0 0.9	0.9 0.8	$4.5e^{-3}$ 0.1	0.8 0.9	8.5 ± 0.1
N116W/E128B$_1$	4.9 4.9	0.3 0.3	0.9 0.9	0.7 0.7	0.9 0.9	2.1 ± $6.9e^{-3}$
N132B$_1$	11.8 12.3	0.9 0.9	0.3 1.2	0.1 0.1	1.0 0.9	10.9 ± 0.4
N116W/N132B$_1$	8.3 9.4	0.6 0.7	0.7 2.1	0.4 0.3	0.8 0.9	6.2 ± 0.6
K135B$_1$	8.9 8.7	0.6 0.8	0.6 1.1	0.4 0.2	0.7 0.9	6.5 ± 0.3
N116W/K135B$_1$	6.0 6.1	0.8 0.7	0.7 0.7	0.2 0.3	1.0 0.8	4.8 ± $3.2e^{-2}$

[a] Excitation wavelength 381 nm; emission collected using two > 470 nm longpass filters. Two sets of the lifetime data are reported for comparison purposes.

τ_1, τ_2 - fluorescence lifetimes in nanoseconds; f_1, f_2 - fractional amplitude of each lifetime; $f_1 = \alpha_1/\Sigma\alpha_i$ and $f_2 = \alpha_2/\Sigma\alpha_i$, where α_1 and α_2 are the pre-exponential factors for τ_1 and τ_2, respectively; χ^2 - chi squared value of the fit.

[b] $<\tau> = f_1*\tau_1 + f_2*\tau_2$, the lifetime amplitude weighted quantum yield. The $<\tau>$ values represent the average of the two reported sets of lifetimes ± the standard error of the mean.

Table 2. 3: Electron Transfer Rates and Intensity and Lifetime Ratios Calculated from Trp Quenching of Bimane-Labeled Samples.

Bimane Attachment Site	k_{ET}^{τ} [a] ($\times 10^8$ s^{-1})	k_{ET}^{F} [a] ($\times 10^8$ s^{-1})	Ratio τ_0/τ_W [a,b]	Ratio F_0/F_W [b]
124	3.8	4.8	4.5	5.5
133	1.7	4.8	2.2	4.2
72	1.4	3.3	2.4	4.2
123	0.7	0.5	1.6	1.5
128	3.7	3.1	4.0	3.7
132	0.7	4.0	1.8	5.3
135	0.6	0.3	1.4	1.2

[a] Electron transfer rates (k_{ET}) calculated as described in Experimental Procedures (Section 2. 3. 12) using the fluorescence intensity (k_{ET}^{F}) and lifetime (k_{ET}^{τ}) measured with and without the proximal Trp residue. The lifetime values (τ) used were the amplitude weighted lifetimes assuming a bi-exponential distribution, defined by $f_1\tau_1 + f_2\tau_2$, where $f_1 = \alpha_1/(\alpha_1+\alpha_2)$ and $f_2 = \alpha_2/(\alpha_1+\alpha_2)$.

[b] The ratio of the fluorescence values (intensity, F, and weighted lifetime, τ) without (F_0 and τ_0) and with (F_W and τ_W) the presence of the neighboring Trp residue, measured with 381 nm excitation, as described in Experimental Procedures.

Figure 2. 1: Location and quantum yields of bimane-labeled T4 lysozyme. (A) Model of T4 lysozyme based on the crystal structure. The model indicates the location of two of the Trp residues in T4 lysozyme, as well as the α-carbons for the 21 cysteine substitutions labeled with monobromobimane described previously [64]. **(B)** Relative quantum yields of mBBr labels attached to the 21 cysteine sites. Notice that sites 121, 124, 129 and 133 all show dramatically lower quantum yields. These residues also lay close to the two Trp residues shown in (A) above.

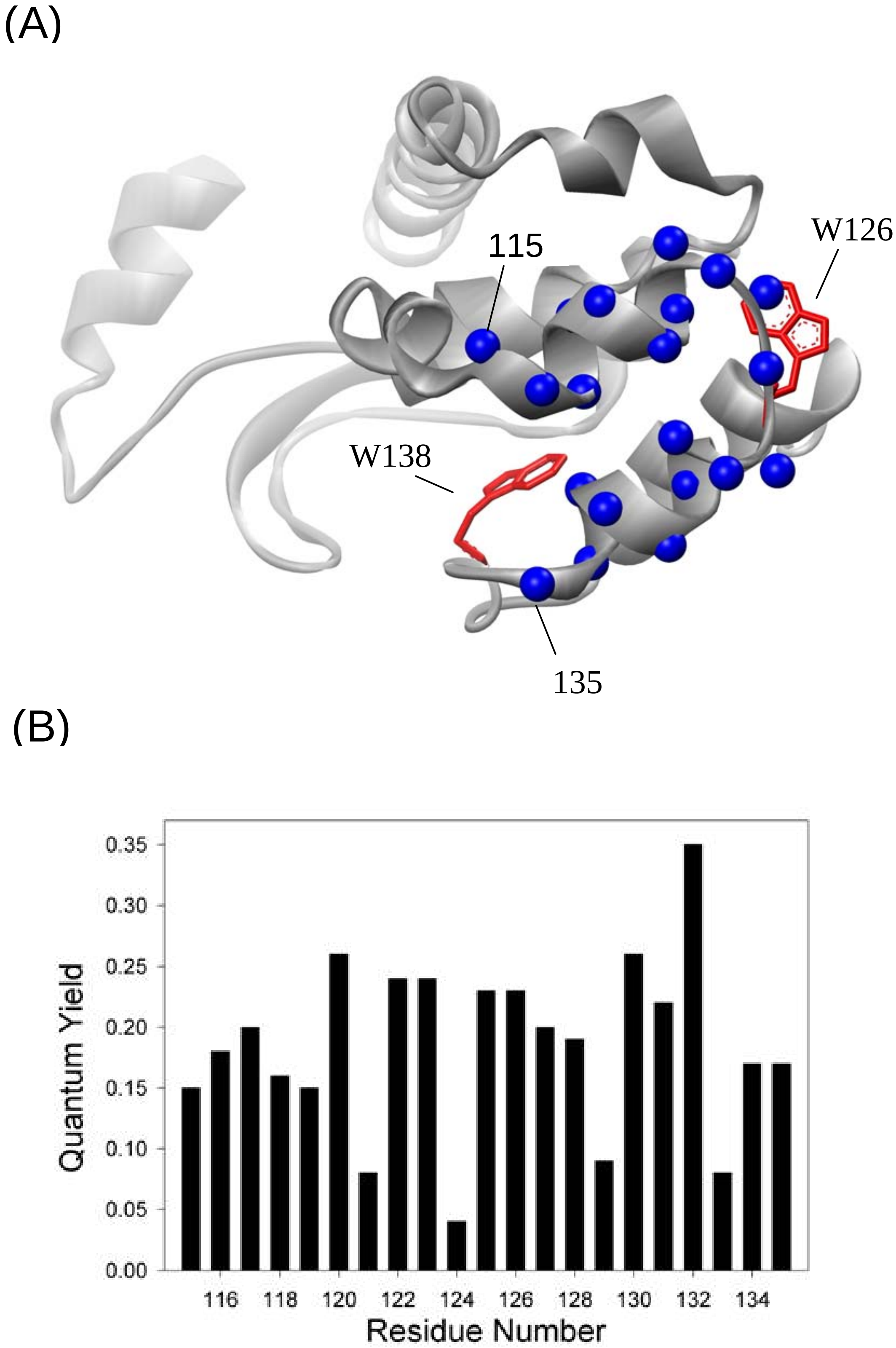
(A)
115
W126
W138
135
(B)
0.35
0.30
0.25
0.20
0.15
0.10
0.05
0.00
Quantum Yield
116
118
120
122
124
126
128
130
132
134
Residue Number

Figure 2. 2: Location and fluorescence properties of bimane labels at site 124 before and after mutating the neighboring Trp residue at site 126. (A) Model of T4 lysozyme indicating α-carbon for sites $K124B_1$ and W126. **(B)** Fluorescence emission spectrum of $K124B_1$ and $K124B_1$/W126F. Notice the ~ 5X difference in fluorescence intensity between the samples, even though the samples contained identical amounts of bimane label. **(C)** Fluorescence decay of $K124B_1$ and $K124B_1$/W126F. **(D)** ESM analysis of mutants $K124B_1$ and $K124B_1$/W126F. Notice that the complex ESM pattern observed for the sample containing the neighboring Trp residue is replaced by a pattern showing only one apparent lifetime upon converting the Trp residues to Phe.

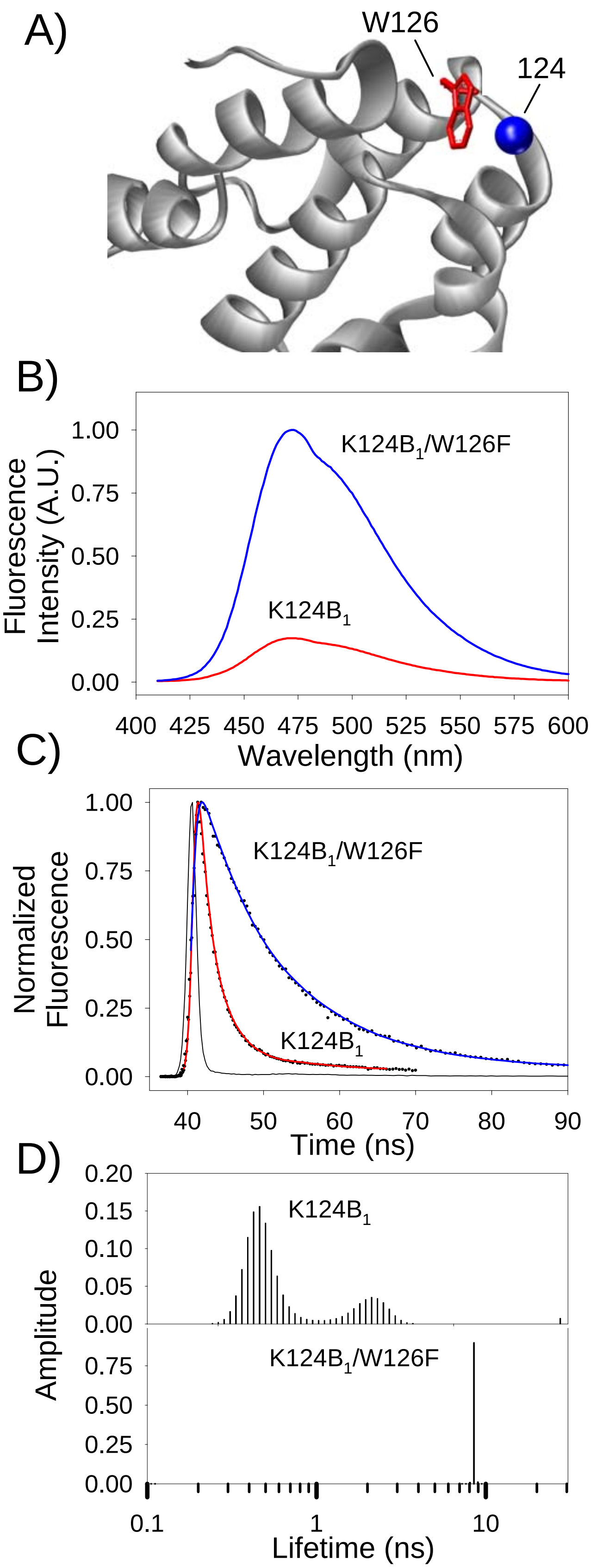
A)
W126
124
B)
Fluorescence Intensity (A.U.)
1.00
0.75
0.50
0.25
0.00
K124B$_1$/W126F
K124B$_1$
400
425
450
475
500
525
550
575
600
Wavelength (nm)
C)
Normalized Fluorescence
1.00
0.75
0.50
0.25
0.00
K124B$_1$/W126F
K124B$_1$
40
50
60
70
80
90
Time (ns)
D)
Amplitude
0.20
0.15
0.10
0.05
0.00
K124B$_1$
0.75
0.50
0.25
0.00
K124B$_1$/W126F
0.1
1
10
Lifetime (ns)

Figure 2. 3: Location and fluorescence properties of bimane labels at site 133 before and after mutating the neighboring Trp residue at site 138. (A) Model of T4 lysozyme indicating α-carbon for sites L133B_1 and W138. **(B)** Fluorescence emission spectrum of L133B_1 and L133B_1/W138F. Notice the ~ 5X difference in fluorescence intensity between the samples containing identical amounts of bimane label. **(C)** Fluorescence decay of L133B_1 and L133B_1/W138F. **(D)** ESM analysis of mutants L133B_1 and L133B_1/W138F. Notice that the complex ESM pattern observed for the sample containing the neighboring Trp residue is replaced by a pattern showing only a low number of apparent lifetimes upon converting the Trp residues to Phe.

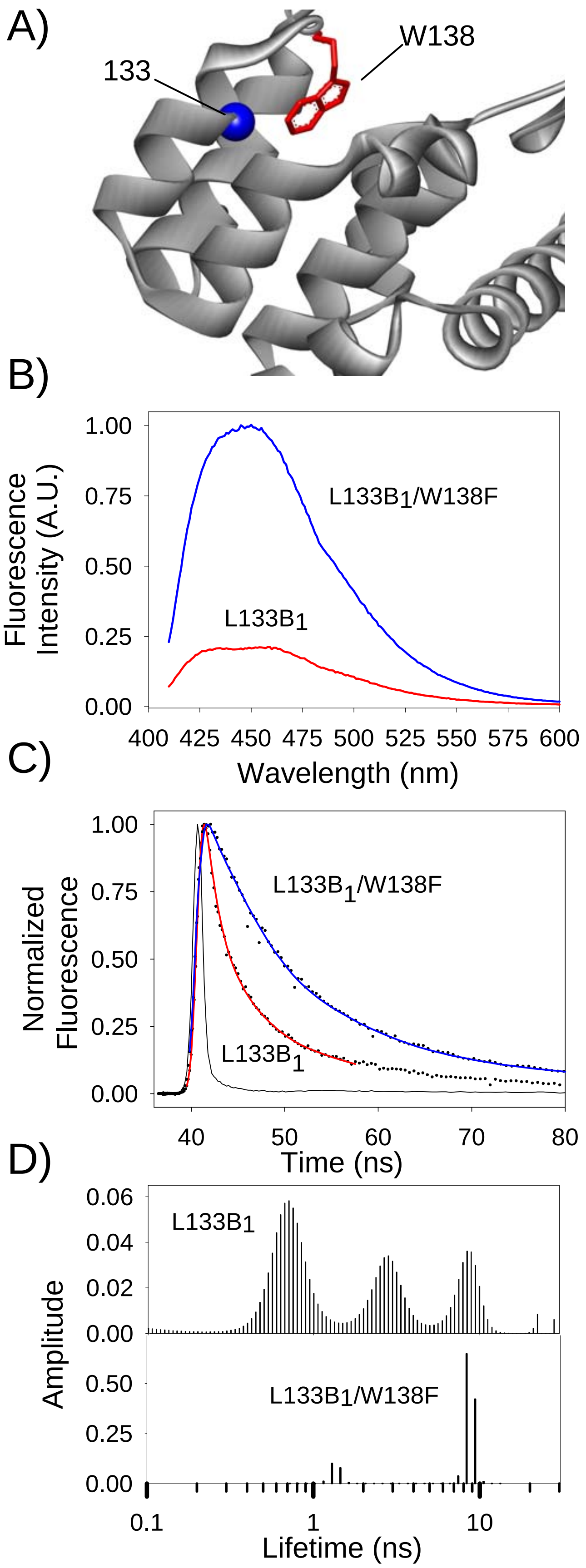
A)
133
W138
B)
1.00
0.75
0.50
0.25
0.00
Fluorescence Intensity (A.U.)
L133B1/W138F
L133B1
400 425 450 475 500 525 550 575 600
Wavelength (nm)
C)
1.00
0.75
0.50
0.25
0.00
Normalized Fluorescence
L133B1/W138F
L133B1
40 50 60 70 80
Time (ns)
D)
0.06
0.04
0.02
0.00
L133B1
Amplitude
0.50
0.25
0.00
L133B1/W138F
0.1 1 10
Lifetime (ns)

Figure 2. 4: Location and fluorescence properties of bimane labels at site 72 before and after introducing a Trp residue one turn away at site 76. (A) Model of T4 lysozyme indicating α-carbon for sites D72B$_1$ and R76W. **(B)** Fluorescence emission spectrum of D72B$_1$ and D72B$_1$/R76W. Notice the ~ 4X decrease in bimane fluorescence for the label at site 72 after a Trp residue is introduced at site 76. **(C)** Fluorescence decay of D72B$_1$ and D72B$_1$/R76W. **(D)** ESM analysis of mutants D72B$_1$ and D72B$_1$/R76W. Notice that the single lifetime for mutant D72B$_1$ is converted to a complex ESM pattern upon introducing the Trp residue at site 76.

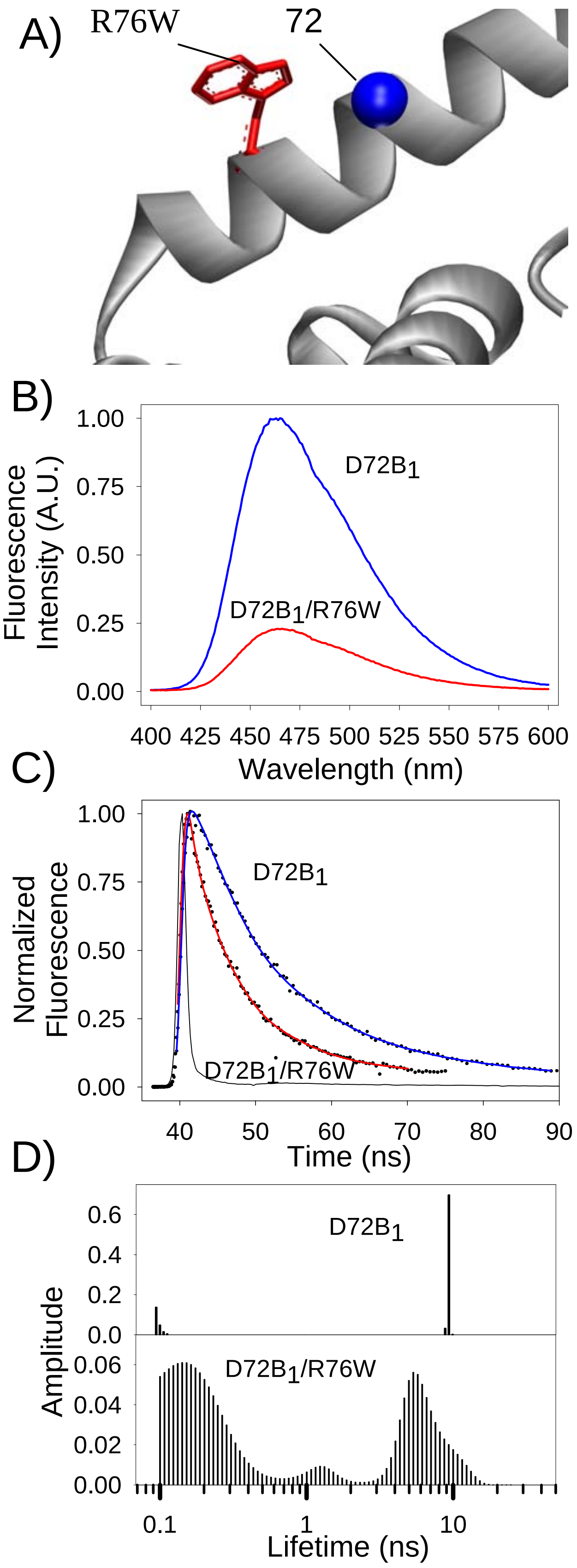
A)
R76W
72
B)
1.00
0.75
0.50
0.25
0.00
Fluorescence Intensity (A.U.)
D72B$_1$
D72B$_1$/R76W
400 425 450 475 500 525 550 575 600
Wavelength (nm)
C)
1.00
0.75
0.50
0.25
0.00
Normalized Fluorescence
D72B$_1$
D72B$_1$/R76W
40 50 60 70 80 90
Time (ns)
D)
0.6
0.4
0.2
0.0
D72B$_1$
Amplitude
0.06
0.04
0.02
0.00
D72B$_1$/R76W
0.1
1
10
Lifetime (ns)

Figure 2. 5: Trp quenching of bimane fluorescence is distance-dependent. (A) Model of T4 lysozyme indicating the α-carbon site for each cysteine substitution and the location of the tryptophan residue introduced in this region (N116W). **(Left panels, B-E)** Steady-state fluorescence intensity measurements of mBBr-labeled cysteine mutants with and without the Trp residue introduced at site 116. Notice the decrease in fluorescence intensity, especially at sites 128 and 132, upon introduction of the Trp residue. **(Right panels, B-E)** ESM analyses of proteins in the presence and absence of the Trp residue at 116. Note the low number of apparent lifetimes in the absence of the N116W residue (top half of each panel on the right side of the figure). This is in sharp contrast to the multiple species seen in the ESM decay analysis data for the same labeling sites containing the Trp residue at site 116 (bottom half of each panel on the right side of the figure).

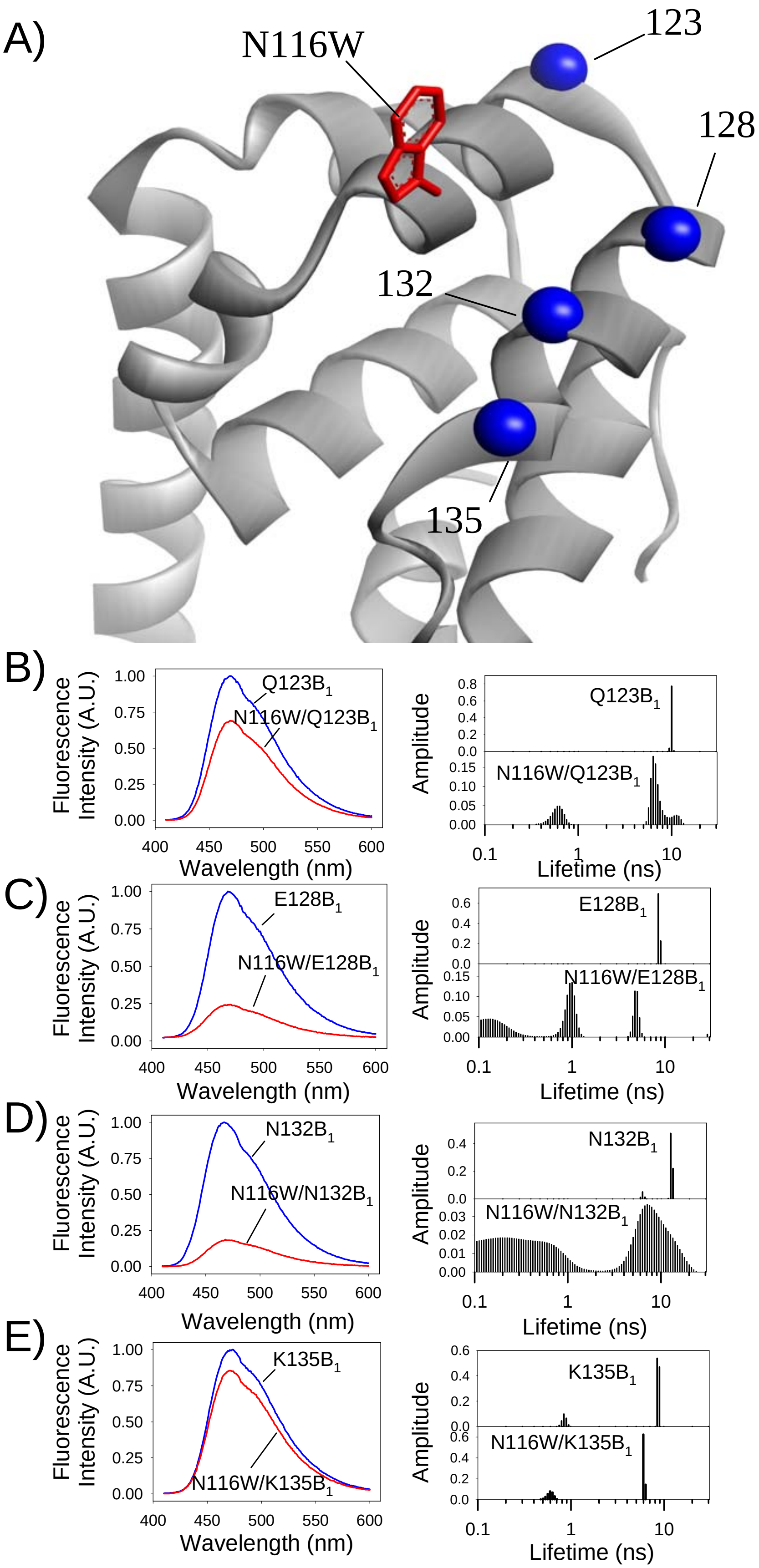
A)
N116W
123
128
132
135
B)
Fluorescence Intensity (A.U.)
1.00
0.75
0.50
0.25
0.00
400
450
500
550
600
Wavelength (nm)
Q123B$_1$
N116W/Q123B$_1$
Amplitude
0.8
0.6
0.4
0.2
0.0
0.15
0.10
0.05
0.00
0.1
1
10
Lifetime (ns)
C)
Fluorescence Intensity (A.U.)
1.00
0.75
0.50
0.25
0.00
400
450
500
550
600
Wavelength (nm)
E128B$_1$
N116W/E128B$_1$
Amplitude
0.6
0.4
0.2
0.0
0.15
0.10
0.05
0.00
0.1
1
10
Lifetime (ns)
D)
Fluorescence Intensity (A.U.)
1.00
0.75
0.50
0.25
0.00
400
450
500
550
600
Wavelength (nm)
N132B$_1$
N116W/N132B$_1$
Amplitude
0.4
0.2
0.0
0.03
0.02
0.01
0.00
0.1
1
10
Lifetime (ns)
E)
Fluorescence Intensity (A.U.)
1.00
0.75
0.50
0.25
0.00
400
450
500
550
600
Wavelength (nm)
K135B$_1$
N116W/K135B$_1$
Amplitude
0.6
0.4
0.2
0.0
0.6
0.4
0.2
0.0
0.1
1
10
Lifetime (ns)

Figure 2. 6: Fluorescence decay profiles and steady state intensities indicate that some T4L mutants show dynamic quenching and others static quenching. (A) Fluorescence decay profiles of bimane at sites 124 and 132. The profiles are shown as log fluorescence intensity to more easily allow comparison. Notice that the decay at site 124 changes sharply in the presence of the Trp residue (suggesting a dynamic quenching mechanism), whereas the decays at site 132 show very similar rates (indicating the quenching occurs through a static-like mechanism). **(B)** Graph comparing the ratio of steady-state intensities (F_0/F_w) and fluorescence lifetimes (τ_0/τ_w). **(C)** Absorption spectra of bimane labels attached at sites 124 and 132 with (dashed line) and without (solid line) the presence of the neighboring Trp residue. Notice the change in the absorption spectra at site 132, suggesting a ground-state complex for mutant N116W/N132B_1.

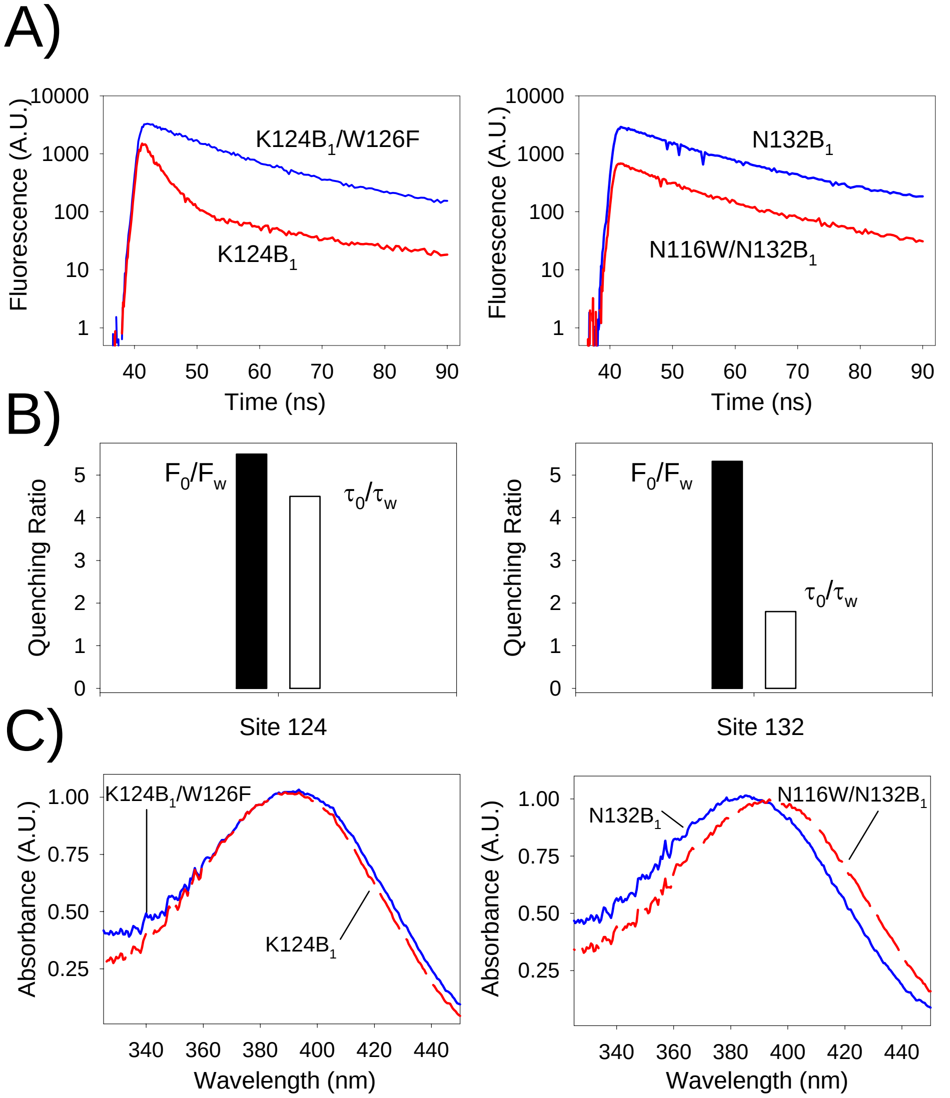
A)
Fluorescence (A.U.)
10000
1000
100
10
1
K124B$_1$/W126F
K124B$_1$
40
50
60
70
80
90
Time (ns)
Fluorescence (A.U.)
10000
1000
100
10
1
N132B$_1$
N116W/N132B$_1$
40
50
60
70
80
90
Time (ns)
B)
Quenching Ratio
0
1
2
3
4
5
F$_0$/F$_w$
τ$_0$/τ$_w$
Site 124
Quenching Ratio
0
1
2
3
4
5
F$_0$/F$_w$
τ$_0$/τ$_w$
Site 132
C)
Absorbance (A.U.)
1.00
0.75
0.50
0.25
K124B$_1$/W126F
K124B$_1$
340
360
380
400
420
440
Wavelength (nm)
Absorbance (A.U.)
1.00
0.75
0.50
0.25
N132B$_1$
N116W/N132B$_1$
340
360
380
400
420
440
Wavelength (nm)

Chapter 3

High-Throughput Protein Structural Analysis Using Site-Directed Fluorescence Labeling and the Bimane Derivative (2-Pyridyl)dithiobimane

Steven E. Mansoor[‡] **and David L. Farrens**[‡]

[‡] Department of Biochemistry and Molecular Biology, Oregon Health and Science University, Portland, Oregon 97239-3098, USA

Running Title: High-Throughput Site-Directed Fluorescence Labeling

3. 1 SUMMARY

We present a site-directed fluorescence labeling (SDFL) study of 25 different T4 lysozyme protein samples labeled with the thiol-cleavable fluorophore, (2-pyridyl)dithiobimane (PDT-Bimane). Our results demonstrate PDT-Bimane can be used in cysteine-scanning studies to detect protein secondary structure, and to map proximity between sites in proteins by monitoring tryptophan quenching of bimane fluorescence. In addition, the reducible nature of PDT-Bimane can be exploited to resolve problems often faced in SDFL studies: ensuring specific labeling of cysteine residues, determining the extent of free label contamination, and accurately determining labeling efficiency even at low concentrations. The ability to cleave PDT-Bimane off the protein enables rapid determination of these parameters, and positions it as an ideal fluorophore for automated, high-throughput structural studies of protein folding, the detection of protein-protein interactions, and the monitoring of real-time conformational changes.

All experiments and data analysis reported in this chapter were performed by the author of this dissertation. The DNA plasmid constructs used to express the protein samples were supplied by Dr. Hassane S. Mchaourab. The data presented in this chapter has been previously published in Mansoor, S.E. and Farrens, D. L. (2004) *Biochemistry* **43**, 9426-9438, which received the 2005 Oregon Health & Science University Outstanding Student Journal Article of the Year Award. The data was also presented as a poster at the 49th Annual Biophysical Society Meeting, Long Beach, CA, 2005.

3. 2 INTRODUCTION

The ability to carry out site-directed fluorescence labeling (SDFL) has dramatically advanced the type of questions biochemists can address using fluorescence spectroscopy [42,64,81,170,181,183,184,191,222-225]. In brief, SDFL involves introducing unique cysteine residues at defined sites in a protein, then attaching fluorescent labels to these sites to act as local reporter groups. The information these probes report on their local environment (for example, buried vs solvent exposed) is then used to assess the structure and monitor dynamic changes in the protein. By systematically scanning through a protein region, SDFL can be used to obtain localized secondary structure information [64], map proximity in proteins [170], study protein folding [226], assess conformational changes in a protein's structure [42,227] determine membrane protein topology and insertion [74], and monitor protein-protein interactions [228]. Similar information can be obtained using other site-directed methods, such as site-directed tryptophan fluorescence [73,75,215,229] or site-directed spin labeling (SDSL) [66,67,188,230-237].

Although powerful, SDFL is an immature structural technique still under development. To help standardize and improve our SDFL methods, we have been carrying out a series of scanning SDFL studies on the protein T4 lysozyme (T4L) [64,170], inspired by previous studies using SDSL [65,177,186,238-240]. Our work has focused on using the small fluorescent probe monobromobimane (mBBr; Figure 3.1A) with the goal of defining exactly what structural information can be obtained in SDFL studies using this probe, and assessing the effect of introducing this fluorescent reporter group on the protein's structure and stability.

In the present chapter, we report that our SDFL studies can be substantially improved and simplified by using a new bimane derivative, (2-pyridyl)dithiobimane (PDT-Bimane; Figure 3.1B). PDT-Bimane is small, and its unique properties provide key features that should allow automation of SDFL procedures. We demonstrate from scanning SDFL studies of 25 different T4L mutants (Figure 3.1C) that PDT-Bimane can be used to map solvent accessibility and determine local regions of protein secondary structure (by assessing shifts in the probe's emission λ_{max} values and changes in the steady-state anisotropy values). Further, we find PDT-Bimane fluorescence is dramatically quenched by proximal tryptophan residues, and this distance-dependent quenching can be used to obtain localized tertiary structure information.

A major goal of this chapter is to develop procedures that substantially simplify SDFL studies of protein structure. We ultimately hope to combine these methods with the recently developed automated protein expression and purification systems [241], thus enabling automated, high-throughput studies of protein structure by SDFL methods.

We find that along with the well-established properties of bimane fluorescence, PDT-Bimane provides a key advantage for automating SDFL studies - it attaches to proteins through a reversible disulfide linkage. We find the nature of this linkage can be used to overcome a number of practical difficulties: ensuring label specificity and quantitating the amount of specific label incorporation into samples at low concentrations. Furthermore, the cleavable nature of PDT-Bimane can be exploited to dramatically simplify SDFL studies: by simply comparing spectra of labeled samples before and after reduction, one can rapidly assess the solvent accessibility (and thus secondary structure) of the region under study, and detect the proximity of the site to Trp residues.

In summary, the unique spectral properties of PDT-Bimane coupled with its ability to be reduced off proteins make it an ideal probe for automated, high-throughput SDFL studies of protein structure and function, for mapping protein-protein interactions, and for monitoring real-time conformational changes in proteins.

3. 3: EXPERIMENTAL PROCEDURES

3. 3. 1: Materials.

(2-Pyridyl)dithiobimane (PDT-Bimane or suffix-B_2) was purchased from Toronto Research Biochemicals. TCEP-HCl was purchased from Pierce. Quinine sulfate monohydrate was purchased from Aldrich Chemical Co. Neutral density filters, long-pass filters, and interference filters were from Oriel Corporation. All cuvettes were from Uvonics. All buffer components were purchased from Fisher- Biotech and GibcoBRL. The cysteine-free lysozyme gene (containing the substitutions C54T and C97A) was kindly provided by F. W. Dahlquist (University of Oregon). This will hereafter be called the “wild type” or T4L.

3. 3. 2: Buffers.

The buffers used were as follows: buffer A, 50 mM MOPS, 50 mM Tris, 1 mM EDTA, pH 7.6. Buffer B, 0.1 M Tris-HCl, 0.1 M Na_2EDTA. Buffer C, 20 mM Tris-HCl, 1 mM $CaCl_2$, pH 8.0. Buffer D, 20 mM Tris, 20 mM MOPS, 0.02% sodium azide, 1 mM EDTA, 1 mM DTT, pH 7.6. Buffer E, 20 mM KH_2PO4, 25 mM KCl, pH 3.0. Buffer F, 50 mM MOPS, 50 mM Tris, 1 mM EDTA, pH 7.6, 3 M guanidine hydrochloride.

3. 3. 3: Construction, Expression and Purification of Mutants.

The construction and expression of the cysteine mutants used in the present work has been previously described in detail [64,170]. Briefly, K38 *Escherichia coli* cells were transformed with the T4L cysteine-mutant plasmid, and protein production was induced in log-phase cultures, harvested, lysed in buffer D by French press, and clarified by centrifugation. Following centrifugation, the cell solution was filtered and DTT was added to 20 mM. After 30 min, the solution was loaded onto a Pharmacia Biotech HiTrap cation exchange column equilibrated with buffer A. The samples were eluted with a salt gradient (ramped from 0 to 1 M in 20 min). The purity of the proteins was assessed by SDS-PAGE and judged to be at least 90% pure for all samples studied.

3. 3. 4: Fluorescence Labeling.

Labeling of each lysozyme mutant was carried out essentially as described previously [64,170] using a 5-10x molar excess of the fluorescent label in buffer F at 4 °C overnight. Free label was separated from labeled protein using gel filtration on a Pharmacia Biotech HiTrap desalting column previously equilibrated with buffer A and the labeling efficiency for each mutant was calculated from the absorption spectrum (using a Shimadzu UV 1601 UV-Vis spectrophotometer). Protein concentrations were calculated using an extinction coefficient of ε_{280} = 23 327 L cm^{-1} $mole^{-1}$ for T4 lysozyme. A value of 5000 L cm^{-1} mol^{-1} was used for the PDT-Bimane label. Note that this value is based on the value of mBBr. A value of ε_{280} = 5600 L cm^{-1} mol^{-1} was either added or subtracted to the WT T4 lysozyme extinction coefficient to correct for mutants that had a tryptophan introduced or removed, respectively. The contribution from the PDT-Bimane label at 280 nm was subtracted before calculating the protein concentrations. Control experiments using the cysteine-less WT protein showed that background labeling was less than 3% for PDT-Bimane (as judged by absorbance).

3. 3. 5: Monitoring Reaction Rate of PDT-Bimane.

Reaction rates for PDT-Bimane can be determined by monitoring the formation of pyridine-2-thione (absorbance extinction coefficient ε_{343} = 8080 L cm^{-1} mol^{-1}), the leaving group in the reaction of PDT-Bimane with a cysteine (see Figure 3.1B;[242]). The relative stability of the PDT-Bimane label in solution was assessed by monitoring the absorbance increase at 343 nm (as a function of time) from a 30 μM sample in buffer A (pH 7.6) and room temperature using a Shimadzu UV 1601 UV-Vis spectrophotometer. The resulting curve was fit to a single-exponential rise to maximum function in Sigma Plot 8.0 to give the rate of spontaneous hydrolysis.

The reaction rate of PDT-Bimane to a protein sample was performed by adding 12 μM of sample K124C (500 μL in buffer A) to a cuvette to which 5x molar PDT-Bimane was rapidly mixed and monitored at room temperature for the formation of the pyridine-2-thione product (343 nm absorbance). The resulting curve was fit to a double exponential rise to maximum function with one of the rates being fixed at the rate obtained from the spontaneous hydrolysis experiment (k = 4.4 x 10^{-5} s^{-1}).

3. 3. 6: Nomenclature.

The nomenclature for identifying the various mutations and bimane labeled T4 lysozyme derivatives follows the same formula as before [64,170]. The samples are named by specifying the original residue, the number of the residue, and the new residue, in that order. For example, the code T115C indicates that the native threonine residue at the 115th amino acid position was mutated to a cysteine. Hereafter, protein samples labeled with a bimane fluorophore are indicated with the suffix -B_1 for mBBr, and -B_2 for PDT-Bimane. For example, the code T115B_2 indicates that the native threonine residue at the 115th amino acid position has been mutated to a cysteine and reacted with the PDT-Bimane label.

3. 3. 7: Protein Activity Assays.

The enzymatic activity of each PDT-Bimane labeled mutant was measured by monitoring changes in light scattering due to the fluorescently labeled T4L digesting a suspension of peptidoglycan. As previously reported [64], the assay measured changes in light intensity at 365 nm (5-nm band-pass) from a 358 nm (1-nm bandpass) excitation beam using a Photon Technology International (PTI) steady-state fluorescence spectrophotometer. Reactions were initiated by adding 5 μL of PDT-Bimane labeled lysozyme mutants (2 μM in buffer A) to 350 μL of peptidoglycan solution, and the activity rates were determined from the initial slope of a plot of change in light intensity versus time. The mutants' activities thus determined are reported as a percentage of the wild type's activity. All measurements were performed in triplicate at 20 °C and the average values are reported.

3. 3. 8: Assessment of Thermodynamic Stability.

A fluorescence assay (as previously described in refs [64] and [170]) was used to assess the thermodynamic stability and analyze the thermal unfolding properties of the PDT-Bimane labeled samples. Briefly, these measurements used 2 μM labeled protein (dialyzed against buffer E) and were measured using the PTI fluorometer in a T-format. Samples were excited at 280 nm and the fluorescence emission was monitored at 350 and 320 nm while the temperature was increased from 6 to 80 °C at a rate of 2 deg/min. At the end of each run, the samples were cooled back to 6 °C, to determine the extent of protein refolding, and melted again. Except for samples A130B_2, L133B_2, and A134B_2, the mutants showed greater than 75% refolding, as judged by the extent to which the ratio returned to its starting value. The reported T_m values are the average of the two melts thus measured and were calculated assuming a two-state model (native folded state and totally denatured state) in equilibrium. The $\Delta\Delta G$ values for each mutant were calculated using the approximation that $\Delta\Delta G = \Delta T_m \Delta S_{WT}$ [201] and the magnitude of these values were taken to reflect the amount of perturbation induced in the protein structure by the presence of the label. For more details, see ref [64].

3. 3. 9: Solvent Sensitivity of Model Bimane Compounds.

The sensitivity of PDT-Bimane fluorescence to solvent polarity was assessed by reacting PDT-Bimane with L-cysteine (5x excess) to create a model compound referred to as Cys-B_2. The Cys-B_2 model compound was then used to measure fluorescence emission spectra in dioxane/water mixtures ranging from 0 ($\varepsilon = 79.5$) to 100% ($\varepsilon = 2.2$) dioxane (v/v) at 22 °C. Wavelength maxima were determined from the first derivative of the spectra. The emission λ_{max} values thus obtained were used to generate a standard curve reflecting emission λ_{max} as a function of solvent dielectric (ε). This standard curve was subsequently used to assess the solvent polarity for each one of the PDT-Bimane labeled samples from T115-K135, based on their measured emission λ_{max} values. For more details, see ref [64].

3. 3. 10: Steady-State Fluorescence and Anisotropy Measurements.

All steady-state fluorescence excitation, emission, and anisotropy measurements were carried out using a PTI fluorescence spectrometer essentially as described previously [64,170]. The fluorescence excitation measurements were carried out at 22 °C on 2 μM sample in buffer A and were measured from 300 to 450 nm using an integration time of 1 s, a step size of 1 nm, and a corrected emission signal at 490 nm. Excitation slits were 1-nm band-pass and emission slits were set at 15-nm band-pass. Fluorescence emission measurements to determine the emission λ_{max} values of the PDT-Bimane labeled mutants were taken at 22 °C, using 2 μM sample in buffer A and measured from 395 to 600 nm with excitation at 381 nm, using an integration time of 1 s, a step size of 1 nm, and a corrected emission signal. Excitation and emission slits were 10- and 1-nm band-pass, respectively.

All other emission measurements (i.e., for comparing fluorescence intensities of PDT-Bimane labeled samples with and without Trp residues) used samples at 5 μM in buffer A. These emission spectra were measured from 395 to 600 nm (1-nm band-pass) with excitation at 381 nm (3-nm bandpass), a 1-nm step size, and a 1 s integration time.

Anisotropy measurements were carried out at 15 °C using each PDT-Bimane labeled sample (2 μM) in buffer A. Excitation was at 381 nm (4-nm slits) and emission was collected at 475 nm (5-nm slits) with the samples lightly stirred. The measurements were performed in triplicate and the average steady-state anisotropy was obtained.

3. 3. 11: Quantum Yield Measurements.

The quantum yields for the PDT-Bimane labeled mutants, as well as for PDT-Bimane, free in solution at pH 4.0, were measured using a Quinine Sulfate standard (quantum yield equal to 0.55 in 1 N H_2SO4), as described previously [64,170]. The quantum yields of 5 μM PDT-Bimane labeled protein samples in buffer A were measured using 360 nm excitation (3-nm band-pass) while monitoring emission from 370 to 700 nm (1-nm band-pass) and compared to the quinine sulfate standard measured under identical conditions. The buffer intensity was subtracted from all samples before integration from 370 to 625 nm. The quantum yield of the PDT-Bimane label, free in solution, was measured by first reacting a stock solution of the label with 15x TCEP-HCl (to remove the pyridyl group from the bimane moiety). The TCEP-reacted stock PDT-Bimane sample was then aliquoted into a 400 mM sodium acetate (pH 4.0) buffer to 5 μM, and emission scans were taken as described above. Using these conditions, the quantum yield of reduced PDT-Bimane at pH 4.0 was established to be 0.27.

3. 3. 12: Lifetime Measurements.

All fluorescence lifetimes were measured at 22 °C using a PTI Laserstrobe fluorescence lifetime instrument on 250 μL of 5 μM samples [64,170,243]. Measurements used 381 nm excitation passed through a 298-435 nm band-pass filter, and emission was monitored through two long-pass filters (>470 nm). The instrument response function (IRF ~ 1.5 ns) was determined using a solution of Ludox. Each lifetime decay was measured using two averages of five shots per point, collected randomly in time over 150 channels. Data were acquired using an arithmetic data collection method, and analyzed using the commercial PTI T-Master software with either single exponential or double exponential fits. Goodness of fit was evaluated by χ^2 values (acceptable values between 0.8 and 1.2) and visual inspection of the residuals.

For data requiring a two-exponential analysis, the amplitude-weighted fluorescence lifetime, $\langle\tau\rangle = \alpha_1 * \tau_1 + \alpha_2 * \tau_2$, where α_1 and α_2 are the preexponential factors ($\alpha_1 + \alpha_2 = 1.0$) for τ_1 and τ_2, respectively, was used to represent the “average” lifetime for the sample. The value of the amplitude-weighted fluorescence lifetime represents the area under the decay curve and is thus proportional to the steady-state intensity (i.e., quantum yield) [69,220,244-246]. This is easily shown in the following derivation, adapted from ref [220].

The fluorescence decay is represented by the following sum of exponentials:

$$E(t) = \sum_{i=1}^{N} \alpha_i e^{-t/\tau_i} \qquad \text{[Eq. 3. 1]}$$

where the sum of α_i is normalized to unity. The steady-state fluorescence intensity, (I), is proportional to the integral of $E(t)$:

$$I \propto \sum_{i=1}^{N} \alpha_i \int_0^{\infty} e^{-t/\tau_i} dt = \sum_{i=1}^{N} \alpha_i \tau_i \qquad \text{[Eq. 3. 2]}$$

Thus, the steady-state intensity is proportional to the amplitude-weighted fluorescence lifetime. Deviations from this proportionality, for example, when changes in steady-state intensity are not reflected by comparable changes in the fluorescence decay, suggest underlying static quenching mechanisms are affecting the fluorescence of the fluorophore [219,245]. In the discussion section, we show how identifying the type of quenching (i.e., dynamic quenching vs static quenching) can be used to determine the distance between the PDT-Bimane label and the Trp residue.

3. 3. 13: Calculation of Solvent Accessible Surface Area.

The solvent-accessible surface area for each residue between T115-K135 was calculated with the program ICM Lite [247] using a probe radius of 1.4 Å (radius of a water molecule) and the crystal structure coordinates of a cysteine-less WT T4 lysozyme mutant (PDB file 1L63; [248]).

3. 3. 14: Reduction and pH-Dependent Fluorescence Properties of Free, Reduced PDT-Bimane Label.

To assess the pH dependence of the free, reduced fluorophore, PDT-Bimane (0.5 mM in buffer A) was reacted with the reducing agent TCEP (5x molar excess) for 20 min to produce -S-Bimane and pyridine-2-thione (see Figure 3.1B). This reaction mixture was then aliquoted to a 5 μM final concentration in sodium phosphate buffer varying from pH = 3.0 to pH = 10.0 to assess the pH-dependent titration of the remaining thiol on this bimane derivative. The fluorescence intensities of these reduced bimane samples were measured in the steady-state fluorometer by taking emission scans from 395 to 600 nm (1-nm band-pass) while exciting at 381 nm (3-nm band-pass).

3. 3. 15: Effect of Reducing PDT-Bimane Labeled Protein Samples on Fluorescence Intensities.

The effect of reducing the PDT-Bimane label off the protein was assessed by adding 10 μL from a 100 mM TCEP-HCl stock to 200 μL of a 5 μM PDT-Bimane labeled sample in buffer A (absorbance of samples matched at 380 nm). Although it is not necessary to do so, the TCEP-HCl stocks were made up fresh before each set of experiments and used immediately. It has been shown that TCEP-HCl, in the absence of phosphate buffers (such as the buffers we used when reducing the label), is resistant to oxidation (<20%) at millimolar concentrations for periods up to 3 weeks, with no change in concentration detected after 24 h at room temperature [249]. This reaction was allowed to proceed for 5 min and then 30 μL of 2.5 M sodium acetate (pH 4.0) was added to lower the pH to 4.0. Fluorescence emission scans were recorded before and after fluorophore reduction to monitor fluorescence intensity changes by exciting at 381 nm

(3-nm band-pass) and averaging 2 emission scans from 395 to 700 nm (1-nm bandpass). The fluorescence intensity values obtained for each PDT-Bimane labeled sample were determined by the fraction of its integrated intensity from 370 to 700 nm as compared to the same sample with the fluorophore reduced (pH 4.0). Before integrating the total intensity from 370 to 700 nm, the dilution factors were accounted for and the buffer intensity was subtracted.

3. 3. 16: TCEP Reduction Method to Determine the Extent of PDT-Bimane Labeling and Extent of Free Label Contamination.

A protocol for determining the amount of free label was developed that involves comparing the fluorescence intensities of the labeled protein samples before and after protein precipitation with TCA. The procedure was as follows. Two tubes containing 100 μL of sample at identical concentrations were first prepared. To tube I, 100 μL of 10% TCA was added. To tube 2, 100 μL of 100 mM TCEP was added. Both tubes were allowed to incubate at room temperature for 5 min and then spun for 5 min on a tabletop centrifuge. After centrifugation of the sample, 100 μL from each tube was removed and placed into fresh eppendorf tubes. To tube I, 100 μL of 100 mM TCEP was added and to tube II, 100 μL of 10% TCA was added. The fluorescence of each tube was then measured and compared using excitation at 381 nm (3-nm band-pass) and monitoring the fluorescence emission intensity from 395 to 600 nm (1-nm band-pass). Note that this protocol results in tube I and tube II receiving identical treatment but in a different order (see Figure 3.4A). Finally, note that the TCA precipitation protocol does not result in the precipitation of free PDT-Bimane label (data not shown).

To quantitate the total amount of label present on a protein sample, a standard curve of fluorescence intensity as a function of PDT-Bimane concentration was generated. Briefly, this first involved making PDT-Bimane stock solutions from 50 nM to 40 μM in 0.4 M sodium acetate (pH 4.0). To 200 μL each of these stock PDT-Bimane solutions, 10 μL of 100 mM TCEP was added (5-min incubation), followed by 190 μL of 10% TCA. The fluorescence intensity of each sample was measured using 381 nm excitation (3-nm band-pass) while collecting emission from 395 to 600 nm (1-nm band-pass). This generated a plot of fluorescence intensity as a function of PDT-Bimane concentration. Following generation of the standard curve, 200 μL of a labeled protein sample was subjected to the same protocol (10 μL of 100 mM TCEP was added, followed by 190 μL of 10% TCA). The fluorescence intensity produced by the sample, following buffer subtraction, was compared to the standard curve to yield the concentration of bimane in the labeled protein sample.

3. 4: RESULTS

3. 4. 1: Characterization of PDT-Bimane and Labeled Mutants.

Table 3.1 reports the labeling efficiency of the mutants used in this study. This region of T4L was chosen since it possesses two significant stretches of secondary structure (a helix-turn-helix motif; see Figure 3.1C) and was previously studied with mBBr [64]. Most of the samples could be labeled with efficiencies between 0.7 and 0.9, although interestingly, two of the sites, R119B_2 and L133B_2, displayed lower labeling efficiencies (0.4 and 0.3, respectively), even though the labeling was carried out on guanidine-denatured samples. We anticipate PDT-Bimane to be more selective for cysteine residues than other derivative bimane probes (such as monobromobimane and monochlorobimane) because it attaches to cysteines via a disulfide exchange reaction. In contrast, the monobromo- and monochlorobimanes attach to the most reactive nucleophile available through an S_N2 reaction usually, but not always, a cysteine at pH 7.4.

3. 4. 2: Stability of PDT-Bimane Free in Solution and Reaction Rate With Protein Samples.

We find the spontaneous hydrolysis of a 30 μM solution of PDT-Bimane in buffer A (pH 7.6) is slow, but not insignificant, and occurs with a $\tau_{1/2}$ of about 4.5 h. In contrast, the rate of labeling of 12 μM mutant K124C in buffer A, using 60 μM PDT-Bimane, occurs with a $\tau_{1/2}$ of ~ 12 min. Thus, under these conditions, the rate of labeling the protein sample is >20x faster than the rate of spontaneous hydrolysis (data not shown).

3. 4. 3: Functional and Thermodynamic Assessments.

Our functional studies showed that all the PDT-Bimane labeled samples retained some enzymatic activity, measured by their ability to breakdown a preparation of *E. coli* cell walls. In general, mutants where the label is incorporated at buried sites show substantially reduced activity, although this is not always the case (Table 3.1). Similarly, the thermodynamic stabilities of the PDT-Bimane labeled mutants (Table 3.1) indicate protein stability is generally impaired only for mutants whose labeled site is buried in the protein structure. We feel the thermodynamic stability data better reflect global structural perturbation due to the bimane label than do enzyme activity assays, since some residues may play a functional role as well as a structural one.

3. 4. 4: Spectral Properties of PDT-Bimane Reflect Solvent Accessibility at the Site of Attachment.

The fluorescence of PDT-Bimane is solvent sensitive (Figure 3.2A), thus emission spectra of the PDT-Bimane labels attached to the protein at exposed sites (i.e., K135B$_2$) are more red-shifted than when attached at buried sites (i.e., L133B$_2$). We calibrated this sensitivity by reacting PDT-Bimane with L-cysteine and then measuring the fluorescence of this compound (Cys-B$_2$) in different mixtures of dioxane (dielectric, $\varepsilon = 2.2$) and water (dielectric, $\varepsilon = 79.5$). These measurements allowed us to generate an "apparent polarity" scale, which we used to compare with the PDT-Bimane labeled T4L samples. The advantage of this approach is that it provides an instrument-independent way to compare results. i.e., any systematic error in wavelength accuracy for a particular instrument is removed by measuring an apparent polarity scale using model compounds on the same instrument [64]. Note that the "apparent polarity" thus determined for each site compares well with the solvent-accessible surface calculated from the crystal structure (Figure 3.2B).

As seen in the inset of Figure 3.2A, the emission λ_{max} values for Cys-B$_2$ vary as a function of the "apparent polarity". Two linear regions are observed, one from $\varepsilon \sim 2$ to 10, and a second from $\varepsilon \sim 18$ to 80. Fits to these linear regions yield the following relationships: $W = 2.02(\text{nm}/\varepsilon)D + 432.7$ nm (for $\varepsilon = 2$ to 10) and $W = 0.28(\text{nm}/\varepsilon)D + 451.6$ nm (for $\varepsilon = 18$ to 80), where W is the absorbance wavelength in nanometers and D is the dielectric constant (ε). Comparing these results with this region of the T4L structure (Figure 3.1C) indicates that emission λ_{max} values for the PDT-Bimane labeled samples reflect the solvent surface accessibilities of the residues from 115 to 135, as calculated from the crystal structure (Figure 3.2B).

3. 4. 5: Measurement of PDT Fluorophore Mobility.

The steady-state fluorescence anisotropy values of PDT-Bimane labeled samples also reflect the solvent accessibility of the probes at the points of attachment. As expected, labels at buried sites reveal a higher steady-state anisotropy since their rotational mobility is restricted. There are, however, some outliers that may be related to differences in fluorescence lifetimes or because of local interactions between the label and the protein, both of which will affect the apparent steady-state anisotropy. The absolute values are given in Table 3.2 (to facilitate comparison with the solvent-accessible surface, the inverse of these anisotropy values are plotted in Figure 3.2C).

3. 4. 6: Power Series Calculation of SDFL Data Can Be Used to Assess Protein Secondary Structure.

To provide a more quantitative comparison of the PDT-Bimane data with the solvent-accessible surface of T4L, we carried out a power series analysis of the periodicity in the emission λ_{max} data combined with the fluorescence anisotropy data (shown in Figure 3.2D). Note that the data shows good agreement with that expected for a region that is α-helical, exhibiting primarily periodicity of ~ 96°. Further details on the power series calculation are given in ref [64].

3. 4. 7: Fluorescence Intensity of Reduced PDT-Bimane is pH Dependent, but PDT-Bimane Attached to the Protein is Not.

The PDT-Bimane label can be reduced off T4L, using TCEP as a reducing agent (see Figure 3.3A). However, when carrying out these studies, we found the fluorescence intensity of the resulting -S-Bimane increases as the pH is lowered (Figure 3.3B), presumably as the resulting free thiol group becomes protonated. Titration of this effect shows an inflection point at approximately pH 6.5, a value within the range of possible p*K*a's observed for thiol groups (Figure 3.3C). Identical results were obtained using β-mercaptoethanol as the reducing agent, indicating this effect is not TCEP dependent (data not shown). The fluorescence lifetime of TCEP reduced PDT-Bimane is also increased from τ = 6.2 ns (pH 10.0) to τ = 10.4 ns (pH 3.0) at the lower pH values (Figure 3.3D), consistent with an increase in quantum yield. Importantly, we find PDT-Bimane fluorescence is *not* pH dependent when attached to the protein (Figure 3.3E).

The fluorescence lifetime of PDT-Bimane is not monoexponential, thus in this paper we report the amplitude-weighted fluorescence lifetime, $<\tau>$, described by the formula $<\tau> = \alpha_1\tau_1 + \alpha_2\tau_2$, where α_1 and α_2 are the normalized preexponential factors (i.e., $\alpha_1 + \alpha_2 = 1.0$) for each lifetime, τ_1 and τ_2, respectively. The amplitude-weighted fluorescence $<\tau>$ lifetime is used here because it represents the area under the decay curve and thus, in the absence of static quenching phenomena, is proportional to the steady-state intensity (see Experimental Procedures for details).

3. 4. 8: Labeling Efficiency and Specificity can be Determined using a Protocol Combining TCEP Reduction and TCA Protein Precipitation.

We find TCEP reduction of PDT-Bimane can be used to determine both the total amount of bimane label and the amount of free, unattached label present in the sample. Importantly, this approach can even be used at low sample concentrations, which cannot be determined from absorbance spectra.

The protocol is as follows. The protein samples are first treated with TCA to precipitate the protein. Any fluorescence signal remaining in the supernatant after centrifugation is assumed to be free, unattached label. To determine the *total* amount of PDT-Bimane label present, the samples are first reduced with TCEP (as described above) *prior* to TCA precipitation and centrifugation. Finally, these two values are compared to standard curves of PDT-Bimane (generated by the same protocol as the samples) to determine the molar amounts of label present, from which the extent of specific protein labeling can then be calculated.

Figure 3.4 shows an example of this analysis carried out on sample N132B_2. Note that, after TCA precipitation, very little (<2.5%) of the total signal remains, indicating minimal free label contamination (Figure 3.4B). The labeling efficiency of this sample was next determined by subjecting the sample at concentration 1.2 μM (determined by absorbance) to the protocol described above. The results in Figure 3.4C show that a value of 1.1 μM PDT-Bimane was obtained from the standard curve, indicating this procedure can be used to reliably determine labeling efficiency.

3. 4. 9: PDT-Bimane Displays Distance Dependent Quenching by Proximal Tryptophan Residues, and the Quenching is Removed Upon Reduction with TCEP.

To test if proximal Trp residues quench PDT-Bimane fluorescence (as they do for mBBr) [170], we introduced a Trp residue at site 116 in T4L, and measured its effect on a PDT-Bimane probe introduced on nearby sites 123, 128, 132, and 135 (see Figure 3.5A). As expected, the Trp residue affects the fluorescence intensity of the PDT-Bimane labeled sites in a manner consistent with their relative proximity. For example, the bimane label at site 132, closest to W116, shows the largest amount of quenching (compare N132B_2 with N116W/N132B_2). In contrast, the bimane labels farthest away from site 116 (sites 123 and 135) show the least amount of quenching. The tryptophan-induced quenching is observed as an effect on both the steady-state fluorescence intensity (Figure 3.5B) and the fluorescence lifetimes (Table 3.3). Furthermore, we carried out an independent test of the Trp/bimane quenching hypothesis by measuring the effect of reducing the samples with TCEP. As seen in Figure 3.5C, addition of TCEP to reduce the PDT-Bimane off the samples is accompanied by an increase in fluorescence, the magnitude of which depends on proximity to the Trp residue. These results are further analyzed in Discussion.

3. 5: DISCUSSION

3. 5. 1: Overview

We set out to explore whether a new bimane derivative, PDT-Bimane, might prove advantageous for use in SDFL studies of protein structure. Our hope was this label could be used to determine localized regions of secondary structure and short-range distances within proteins, while also providing a unique ability to overcome problems that plague SDFL studies: (i) concern about labeling of noncysteine residues, (ii) problems with determining the molar labeling efficiency and extent of free label contamination, and (iii) circumventing the need to carry out the labor-intensive procedures such as matching sample concentrations for comparative studies. As discussed below, we find PDT-Bimane can be used to address all of these issues, and can greatly simplify the process of carrying out SDFL studies, potentially allowing for automation and high-throughput proteomic studies.

3. 5. 2: Advantages of PDT-Bimane for Preserving Protein Function and Stability and for Determining Labeling Efficiency.

The function and thermodynamic stability of T4L are mainly affected only when the PDT-Bimane is introduced at buried sites (Table 3.1). We previously observed a similar result for mBBr, but the PDT-Bimane appears to be slightly less destabilizing than mBBr. One explanation may be the disulfide bond in PDT-Bimane allows additional degrees of rotational freedom, thus enabling the protein to undergo structural dynamics necessary for function and stability. This conclusion is consistent with previous analysis of EPR spin-label probes on T4L, which found nitroxide spin labels attached through a disulfide linkage increased the tolerance to the exogenous probe [177], because the disulfide bond allows the probe to alter its conformations to minimize steric clash at buried sites [239].

Another advantage of PDT-Bimane is that the ability to cleave it off the protein and compare it to standards provides a simple way to quantitate both labeling efficiency and the extent of free label contamination. This approach is very useful for samples with concentrations in the nanomolar range, which cannot be accurately measured on an absorbance spectrometer. Finally, because PDT-Bimane attaches to proteins through a disulfide bond, it specifically reacts with cysteine residues, as opposed to mBBr, which has the potential to label other amino acid residues under unusual circumstances [250].

3. 5. 3: PDT-Bimane Can be Used in Scanning SDFL Studies to Map the Solvent-Accessible Surface of a Protein and thus Determine Secondary Structure.

Our results indicate that, in general, the emission λ_{max} and steady-state anisotropy values of PDT-Bimane labeled protein samples reliably report on the local environment around the probe. Thus, PDT-Bimane can be used in an SDFL scan to map the solvent-accessible surface of a protein by assessing the “apparent polarity” at each site and the mobility of the attached probe. Although visual inspection of these data (Figure 3.2B,C) can be used to glean the probable secondary structure of the region under study, a more quantitative result can be obtained by analyzing the results using a power series analysis that calculates periodicity in the data. For example, a strong periodic peak at ~ 96° indicates the region of the protein is an α-helix (Figure 3.2D), as would be expected.

3. 5. 4: PDT-Bimane Can be Used to Map Proximity Within Protein Through Monitoring Trp Quenching of Bimane Fluorescence.

As we previously found for mBBr, proximal Trp residues dramatically affect PDT-Bimane fluorescence in a distance-dependent manner. This effect is clearly seen in Figure 3.5, where the Trp residue at site 116 affects the fluorescence intensities of the neighboring PDT-Bimane labels depending on its relative proximity (Table 3.3, Figure 3.5B). These observations are consistent with our hypothesis that the Trp quenching is due to photoinduced electron transfer (PET) from Trp to the excited-state bimane [208,212], since PET is sharply dependent on distance. Formally, it should be possible to calculate distances between Trp/bimane pairs based on PET transfer rates. However, PET is a complex phenomenon that depends on factors such as solvent polarity [216], steric and stereochemical factors [217], and the relative orientation between the molecule pair [218]. Thus, quantitative interpretations of distance would require taking these factors into account while also carrying out molecular modeling and analysis of the time-resolved data using a distance-dependent quenching model by Zelent *et al*. [221]. Thus, rather than trying to determine distance from PET quenching rates, we have developed a more simple and robust method to assess proximity directly from the fluorescence data, as discussed below.

The degree of Trp/bimane proximity can be determined by assessing the nature of the fluorescence quenching at a given site, by comparing the fluorescence intensity data to the fluorescence lifetime data. Specifically, one compares the ratio of the steady-state fluorescence intensity without and with the presence of the tryptophan residue (F_0/F_w) to the ratio of the weighted fluorescence lifetime data (τ_0/τ_w). From these results, one can determine whether the Trp/bimane pair is "close" and in near contact distance (~ 10-15 Å) or "very close" and within contact distance (~ 5-10 Å) based on the type of quenching observed; i.e., whether the quenching is dynamic or static in nature.

The rationale for this analysis is as follows: if the Trp/bimane pair is "close", then the quenching can occur through dynamic or collisional mechanisms during the lifetime of the bimane excited state. Such quenching will cause the steady-state fluorescence intensities and the fluorescence lifetimes to decrease by roughly the same amount (thus $F_0/F_w > 1$, $\tau_0/\tau_w > 1$, and $F_0/F_w \approx \tau_0/\tau_w$ [219]). In contrast, a special situation is observed for Trp/bimane pairs that are "very close", or within contact distance (~ 5-10 Å) at the moment of excitation. For such "very close" pairs, static quenching will occur through the formation of a non-fluorescent ground-state complex and be observed as a drop in fluorescence intensity that is greater than the change seen in the fluorescence lifetime (thus, $F_0/F_w >> \tau_0/\tau_w$ [219]). Note that this type of quenching could also be observed if the quenching occurs faster than the time resolution of our lifetime instrument.

Figure 3.6 shows an example of how this type of analysis can further resolve Trp/bimane proximity. The data compare the PDT-Bimane labeled sites shown in Figure

3.5 (123, 128, 132, and 135) with and without the tryptophan residue at site 116. Note that the N116W/E128B$_2$ pair shows substantial steady-state quenching, yet the F_0/F_w and τ_0/τ_w ratios are similar (Figure 3.6A), indicating the quenching is primarily dynamic, classifying this pair as "close" (~10-15 Å). In contrast, the lifetime and steady-state ratios do *not* match for mutant N116W/N132B$_2$ (Figure 3.6A), indicating substantial static quenching, and thus this Trp/bimane pair must be "very close" (~ 5-10 Å). These conclusions are consistent with the T4L crystal structure (Figure 3.5A), and are further supported from an analysis of the absorption spectra, which shows the absorption spectrum for N116W/N132B$_2$ is altered by 6 nm compared to mutant N132B$_2$ alone, further suggesting the Trp residue and bimane label in this pair form a ground-state complex (Figure 3.6B).

3. 5. 5: TCEP Reduction Provides a Simple Way to Assess Trp/PDT-Bimane Proximity.

Identifying Trp proximity can be determined by comparing quantum yields and fluorescence intensity measurements between carefully matched protein samples (see Figure 3.5B). However, this process is laborious, and requires measurements be repeated on samples in which the suspected "offending" Trp residue has been mutated to a phenylalanine to relieve the quenching. A similar process is required when using mBBr.

However, the ability to reduce the PDT-Bimane label off the protein dramatically simplifies this process by eliminating the need for precisely matching sample concentration or mutating Trp residues. Using PDT-Bimane, the proximity to a nearby tryptophan residue can simply be determined by reducing the label off the protein and assessing the amount of fluorescence increase. Figure 3.5C shows an example of this approach. Note that some increase in PDT-Bimane fluorescence occurs upon reduction even in the absence of a neighboring Trp residue (possibly due to lesser quenching from other amino acids), and this change explains the limited discrepancy between the data in Figure 3.5B and Figure 3.5C. However, as shown in our control experiments in Figure 3.7, this increase is small compared to the change observed in the presence of a proximal Trp. Reduction of samples not containing neighboring Trp residues (Q123B_2, E128B_2, N132B_2, and K135B_2) results in an average 70 ± 20% increase in fluorescence (Figure 3.7A), possibly due to relief of quenching by proximal tyrosine residues, which can also quench bimane fluorescence but do so with ~ 4-fold less efficiency [192]. In contrast, the fluorescence intensity increase observed after reducing samples that contain a proximal Trp residue are an order of magnitude larger. For example, there is a 600% increase observed for N116W/E128B_2 and a 3700% increase for N116W/N132B_2 (Figure 3.7B). When the inherent ~ 70% increase in fluorescence intensity caused by TCEP reduction is taken into account, almost identical results are obtained to those using the much more laborious approach of measuring and comparing the quantum yields of samples with and without the Trp residue; compare Figure 3.7, panel C to D.

These results also suggest the PDT-Bimane reduction method can be used to assess Trp/bimane distances, independent of sample concentration and labeling efficiency. While other powerful methods exist for measuring distances in macromolecules (fluorescence resonance energy transfer [81,183,184,251] or spin-spin interactions [41,186,252]), these can sometimes be affected by labeling efficiency and usually require equal concentrations of donor and acceptor. Like these other labeling methods, however, the PDT-Bimane reduction method is sensitive to the amount of contaminating free label, and this must be determined using the methods outlined here.

3. 5. 6: PDT-Bimane Enables a High Throughput Approach For Assessing Protein Structure and Dynamics.

In Figure 3.8, we outline how PDT-Bimane could be used to simplify and automate SDFL studies. In brief, one would first generate single cysteine protein mutants, label these samples with PDT-Bimane, and determine the amount of labeling and the percent free label in each sample using the TCEP/TCA precipitation protocol. Next, one would determine the extent of solvent exposure at each site by comparing the “apparent polarity” of each bimane label (determined from the emission λ_{max} shifts) before and after TCEP reduction, and use the periodicity in these data to determine the secondary structure of the region under study (in this analysis, sites which do not label would be considered as buried). Finally, the proximity to any Trp residues would be determined by comparing fluorescence intensities before and after TCEP reduction.

At this stage of the analysis, one could deduce both the secondary structure motif of the region being scanned, and which sites are close to Trp residues. However, in proteins of unknown structure, such data would not identify precisely *which* tryptophans are next to which bimane labeled sites. To identify these, systematic Trp mutations would still need to be performed, although only for those sites already identified to be affected by Trp residues. Finally, one would classify how close each Trp/bimane pair is by determining if the type of quenching is “dynamic” (10-15 Å) or “static” (5-10 Å), by comparing the fluorescence intensity ratios (F_0/F_w) to the weighted fluorescence lifetime ratios (τ_0/τ_w).

3. 5. 7: Conclusions.

We have shown PDT-Bimane, like mBBr, can be used in a scanning SDFL approach to determine structural information at the level of the backbone fold and to measure proximity within proteins by the distance-dependent tryptophan quenching method [64,170]. In addition, we demonstrated the ability to reduce PDT-Bimane off the protein can be exploited to (i) quickly and easily quantitate the extent of label incorporation and free label contamination, (ii) assess the extent of solvent exposure of the probe, and (iii) assess label proximity to tryptophan residues. These features of PDT-Bimane make it ideal for use in automated, high-throughput proteomic studies of protein structure and folding, the detection of protein-protein interactions, and the monitoring of protein conformational changes. We also anticipate the unique properties of PDT-Bimane will prove useful for technically challenging studies such as assessing real-time conformational changes in receptors and ion channels in natural membrane environments.

3. 6: ACKNOWLEDGEMENTS

We would like to thank our long-standing friend and collaborator at Vanderbilt University, Dr. Hassane McHaourab, for many helpful discussions and a critical reading of this manuscript.

Table 3. 1: Characterization of PDT-Bimane Labeled T4 Lysozyme Mutants at Residues 115-135.

Mutant Number	Mol label/ mol protein	Activity (%WT)	ΔT_m[a] (°C)	$\Delta\Delta G$[b] (kcal/mole)
$T115B_2$	0.9	121	-3.4	-1.0
$N116B_2$	0.9	161	-1.6	-0.5
$S117B_2$	0.6	46	-1.0	-0.3
$L118B_2$	0.9	69	-8.9	-2.5
$R119B_2$	0.4	150	-3.9	-1.1
$M120B_2$	0.7	62	-5.8	-1.7
$L121B_2$	0.9	41	-14.1	-4.0
$Q122B_2$	0.6	100	-2.8	-0.8
$Q123B_2$	0.8	93	-3.5	-1.0
$K124B_2$	0.8	72	-4.7	-1.3
$R125B_2$	0.8	98	-3.5	-1.0
$W126B_2$	1.1	109	-13.8	-3.9
$D127B_2$	0.7	41	-4.3	-1.2
$E128B_2$	0.7	42	-3.4	-1.0
$A129B_2$	0.7	36	-11.3	-3.2
$A130B_2$	0.7	119	-6.4	-1.8
$V131B_2$	0.6	100	-1.5	-0.4
$N132B_2$	0.8	120	-0.2	-0.1
$L133B_2$	0.3	57	-10.4	-3.0
$A134B_2$	0.6	72	-0.2	-0.1
$K135B_2$	0.7	91	-4.7	-1.3

[a] T_m for wild-type T4L = 52.4 °C.

[b] $\Delta\Delta G = \Delta T_m \Delta S_{wt}$ (ΔS_{wt} = 284.6 cal mol^{-1} K^{-1})

Table 3. 2: Spectral Characterization of PDT-Bimane Labeled T4 Lysozyme Mutants at Residues 115-135.

Mutant Number	Absorbance λ_{max} (nm)	Excitation[a] λ_{max} (nm)	Emission[b] λ_{max} (nm)	Steady-state anisotropy[c] (x 10^{-3})
T115B$_2$	386.7	389.0 ± 0.6	470.3 ± 0.2	114.1 ± 0.8
N116B$_2$	385.2	389.1 ± 1.0	470.8 ± 0.1	101.9 ± 0.5
S117B$_2$	382.0	388.5 ± 0.2	468.5 ± 0.2	137.8 ± 4.7
L118B$_2$	384.1	387.1 ± 0.2	466.9 ± 0.1	131.4 ± 3.6
R119B$_2$	387.6	388.5 ± 0.2	471.4 ± 0.2	93.5 ± 2.5
M120B$_2$	389.5	388.3 ± 0.6	469.6 ± 0.1	114.5 ± 11.1
L121B$_2$	389.3	388.4 ± 0.4	466.6 ± 0.6	132.9 ± 2.8
Q122B$_2$	391.3	388.2 ± 0.7	468.6 ± 0.1	121.4 ± 2.0
Q123B$_2$	394.7	389.8 ± 0.4	470.4 ± 0.1	86.3 ± 1.9
K124B$_2$	394.1	390.5 ± 0.3	470.1 ± 0.3	128.1 ± 6.8
R125B$_2$	391.6	383.9 ± 0.3	472.1 ± 0.2	107.4 ± 1.8
W126B$_2$	389.5	388.8 ± 0.6	468.2 ± 0.1	142.6 ± 2.9
D127B$_2$	387.8	389.0 ± 0.4	469.6 ± 0.1	93.0 ± 0.3
E128B$_2$	391.6	396.4 ± 0.1	470.8 ± 0.5	118.9 ± 0.8
A129B$_2$	384.2	387.5 ± 0.5	465.6 ± 0.1	128.0 ± 2.0
A130B$_2$	385.3	385.0 ± 0.4	468.0 ± 0.2	136.5 ± 2.4
V131B$_2$	374.3	382.6 ± 1.2	468.9 ± 0.1	99.1 ± 4.0
N132B$_2$	384.6	387.6 ± 0.1	469.1 ± 0.2	121.4 ± 3.6
L133B$_2$	383.7	383.4 ± 0.3	459.9 ± 0.1	183.0 ± 7.4
A134B$_2$	383.6	381.8 ± 1.2	462.7 ± 0.7	157.5 ± 5.8
K135B$_2$	391.0	391.4 ± 1.0	472.4 ± 0.3	80.6 ± 1.5

[a] Emission collected at 490 nm.

[b] Excitation at 381 nm.

[c] The uncertainty represents the SEM of three measurements.

Table 3. 3: Quantum Yields and Lifetime Analysis of the Fluorescence Decay Measurements.[a]

Mutant	Θ[b]	τ_1 (ns)	α_1	τ_2 (ns)	α_2	χ^2	$<\tau>$[c] (ns)
Q123B_2	0.097 ± 0.004	6.7 ± 0.3	0.8 ± 0.1	1.4 ± 0.5	0.2 ± 0.1	1.0 ± 0.1	5.6 ± 0.1
N116W/Q123B_2	0.059 ± 0.007	5.7 ± 0.2	0.6 ± 0.1	1.3 ± 0.2	0.4 ± 0.1	0.9 ± 0.1	3.9 ± 0.1
E128B_2	0.102 ± 0.008	8.5 ± 0.5	0.8 ± 0.1	1.6 ± 0.6	0.2 ± 0.1	0.9 ± 0.1	7.2 ± 0.2
N116W/E128B_2	0.019 ± 0.005	5.5 ± 0.1	0.3 ± 0.1	1.0 ± 0.1	0.7 ± 0.1	0.9 ± 0.1	2.5 ± 0.2
N132B_2	0.100 ± 0.005	7.0 ± 0.7	0.7 ± 0.1	1.8 ± 0.7	0.3 ± 0.1	1.0 ± 0.1	5.4 ± 0.2
N116W/N132B_2	0.006 ± 0.003	6.9 ± 0.2	0.2 ± 0.1	0.5 ± 0.1	0.8 ± 0.1	1.0 ± 0.1	1.7 ± 0.3
K135B_2	0.082 ± 0.009	6.2 ± 0.3	0.8 ± 0.1	0.8 ± 0.4	0.2 ± 0.1	1.1 ± 0.1	5.2 ± 0.2
N116W/K135B_2	0.059 ± 0.005	5.2 ± 0.2	0.7 ± 0.1	1.3 ± 0.1	0.3 ± 0.1	1.0 ± 0.1	3.9 ± 0.1

[a] Excitation wavelength was 381 nm and emission was collected using two > 470 nm long-pass filters. The average of six lifetime measurements ± the standard error of the mean are reported. Abbreviations: τ_1, τ_2, fluorescence lifetimes in nanoseconds; α_1, α_2, normalized pre-exponential factors such that $\alpha_1 + \alpha_2 = 1.0$; χ^2, chi-squared value of the fit.

[b] The uncertainty reported is the standard deviation from two separate quantum yield measurements.

[c] $<\tau> = \alpha_1\tau_1 + \alpha_2\tau_2$, the amplitude-weighted fluorescence lifetime. The $<\tau>$ values reported in this table represent the average of six sets of lifetimes ± the standard error of the mean.

Figure 3. 1: Reaction schemes for two bimane derivatives with sulfhydryl groups. (A) Reaction of the monobromobimane (mBBr) label with a sulfhydryl group to produce an -S-Bimane side chain (-B_1). **(B)** Reaction of the (2-Pyridyl)dithiobimane (PDT-Bimane) label with a sulfhydryl group to produce an -S-S-Bimane side chain (-B_2). The latter reaction also results in the release of pyridyl-2-thione, which can be spectroscopically monitored at 343 nm [242]. **(C)** Model of T4 lysozyme indicating sites of cysteine substitutions for the SDFL studies using PDT-Bimane. The black balls show the relative positions of each α-carbon substituted with a cysteine.

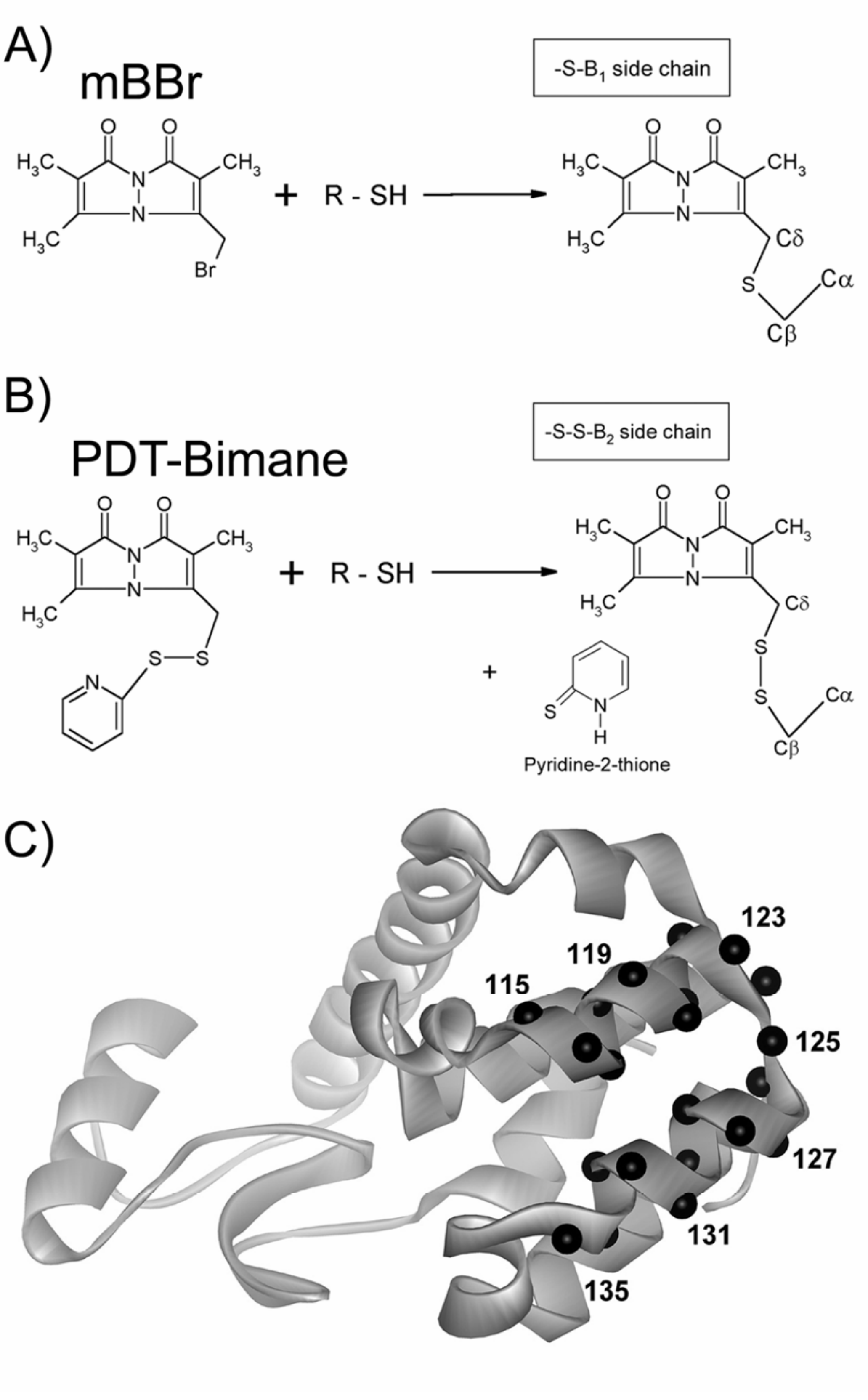
A)
mBBr
-S-B$_1$ side chain
H_3C
CH_3
O
N
Br
+ R - SH
Cδ
S
Cα
Cβ
B)
PDT-Bimane
-S-S-B$_2$ side chain
+
Pyridine-2-thione
C)
115
119
123
125
127
131
135

Figure 3. 2: Scanning SDFL studies using PDT-Bimane can be used to map solvent accessibility and protein secondary structure. (A) The spectral properties of PDT-Bimane reflect the surrounding solvent polarity. The probe shows a blue-shift in fluorescence emission when attached to a buried site (L133B_2, open circles) in comparison to an exposed site (K135B_2, black line). The inset shows the emission λ_{max} of PDT-Bimane reacted with cysteine measured in solvents of different polarity. **(B)** Comparison of the apparent polarity determined for PDT-Bimane at each attachment site (black circles) with the solvent accessibility calculated from the T4 Lysozyme crystal structure (open circles). **(C)** Comparison of the inverted steady-state fluorescence anisotropy values (black circles) with the calculated solvent accessibility (open circles). The fluorescence data in panels B and C represent measurements carried out in triplicate (note that the error bars in most cases are hidden by the symbols). In panels B and C, the solid black and dashed lines represent a cubic-spline fit of the respective data. **(D)** Fourier transform spectral density analysis of the normalized fluorescence emission apparent polarity values averaged with the normalized steady-state anisotropy values. Note the large peak at 96^{o}, indicating the presence of an α-helix.

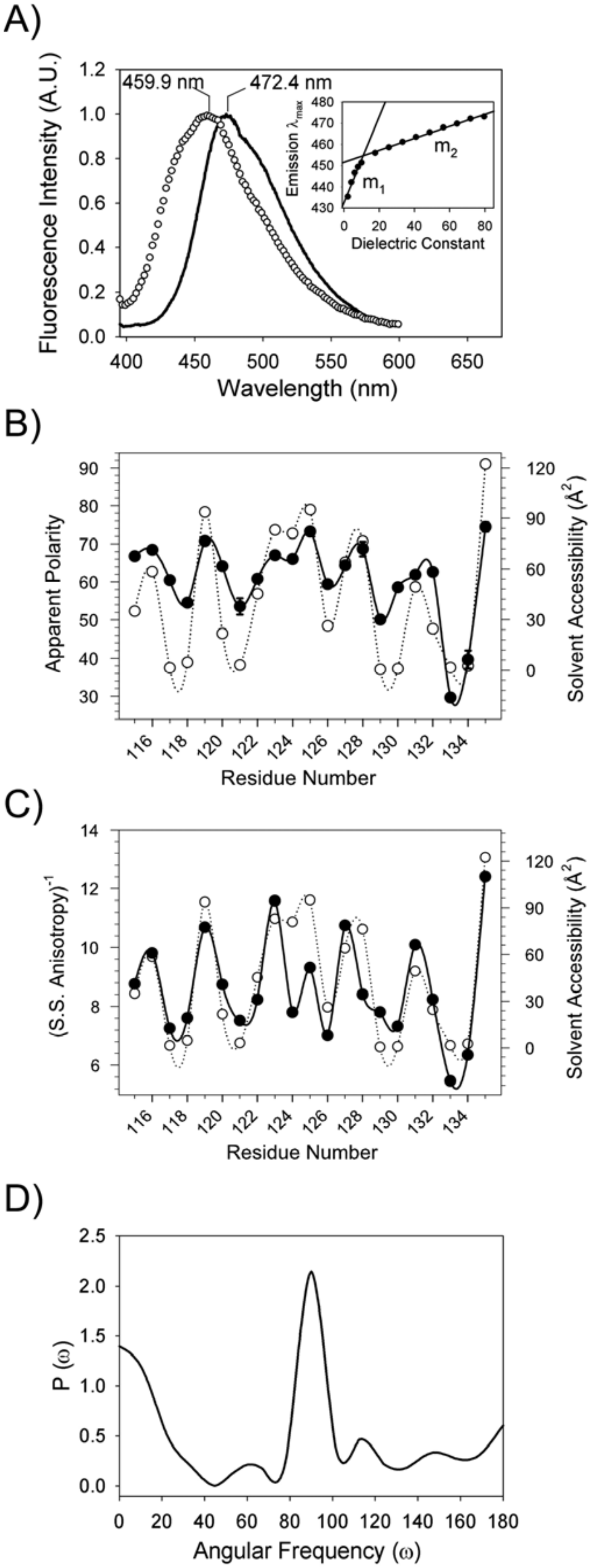
A)
459.9 nm
472.4 nm
Fluorescence Intensity (A.U.)
Wavelength (nm)
1.2
1.0
0.8
0.6
0.4
0.2
0.0
400
450
500
550
600
650
Emission λ_{max}
Dielectric Constant
m_1
m_2
480
470
460
450
440
430
0
20
40
60
80
B)
Apparent Polarity
Solvent Accessibility (Å^2)
Residue Number
90
80
70
60
50
40
30
120
90
60
30
0
116
118
120
122
124
126
128
130
132
134
C)
(S.S. Anisotropy)$^{-1}$
Solvent Accessibility (Å^2)
Residue Number
14
12
10
8
6
120
90
60
30
0
116
118
120
122
124
126
128
130
132
134
D)
P (ω)
Angular Frequency (ω)
2.5
2.0
1.5
1.0
0.5
0.0
0
20
40
60
80
100
120
140
160
180

Figure 3. 3: Reduced PDT-Bimane exhibits a strong pH dependence of fluorescence intensity. (A) The proposed chemical scheme for the Tris[2-carboxyethyl]-phosphine (TCEP) reduction of an R–S-S-B_2 labeled sample. Note that in this scheme, the reduced label can exist either as $^{-}$S-B_2 or HS-B_2, depending on the pH of the buffer. **(B)** Emission scans of TCEP reduced PDT-Bimane across the pH range 3.0 to 10.0. **(C)** Plot of maximum fluorescence intensity from panel B as a function of pH. Note the inflection point at pH 6.5, consistent with the protonation of the free thiol group produced by cleaving the disulfide. **(D)** Fluorescence lifetime decay curves of TCEP reduced PDT-Bimane exhibit an increase in fluorescence lifetime at pH 3.0 ($<\tau>$ = 10.4 ns) vs. pH 10.0 ($<\tau>$ = 6.2 ns). **(E)** Emission scans of PDT-Bimane labeled protein samples at pH 3.0 vs. pH 10.0. Note that the PDT-Bimane fluorescence is <u>not</u> sensitive to pH when the label is attached to a protein sample.

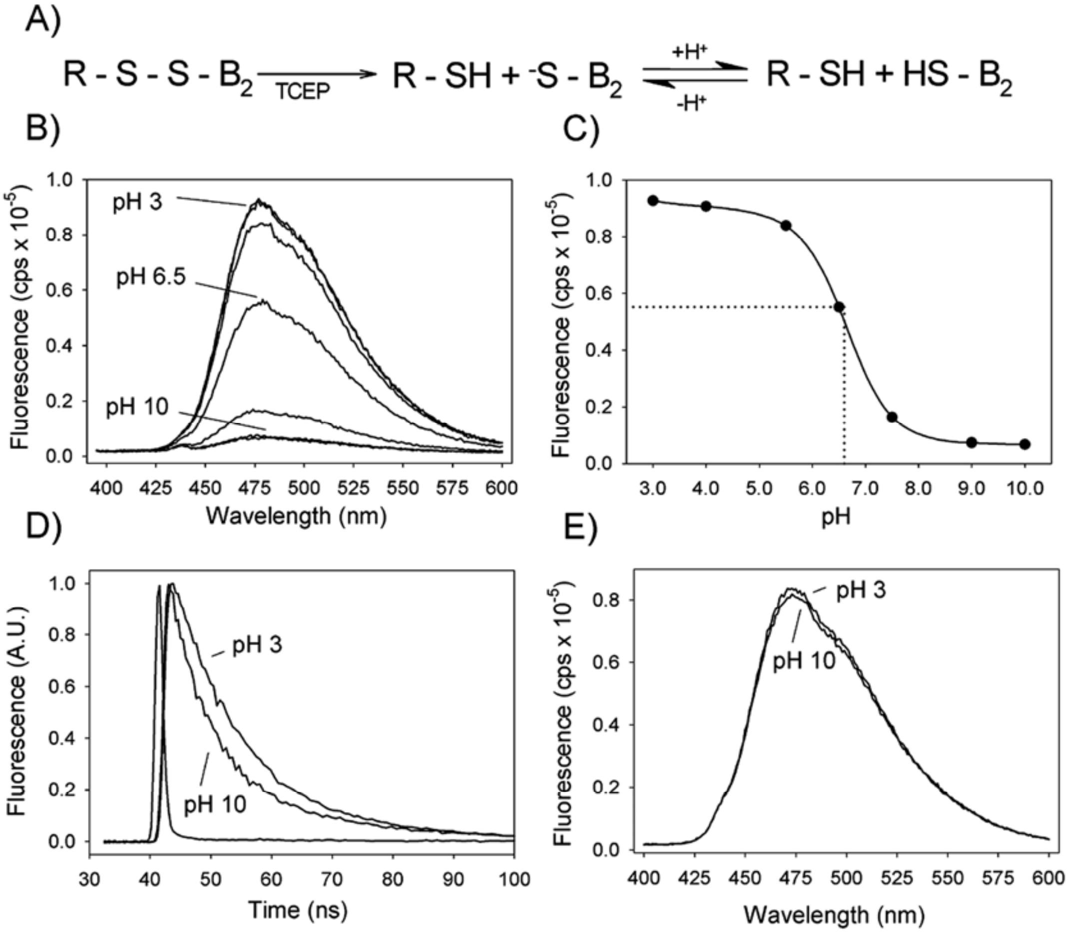
A)
R - S - S - B2 → TCEP → R - SH + -S - B2 ⇌ (+H+ / -H+) R - SH + HS - B2
B)
pH 3
pH 6.5
pH 10
Fluorescence (cps x 10-5)
Wavelength (nm)
0.0 0.2 0.4 0.6 0.8 1.0
400 425 450 475 500 525 550 575 600
C)
Fluorescence (cps x 10-5)
pH
0.0 0.2 0.4 0.6 0.8 1.0
3.0 4.0 5.0 6.0 7.0 8.0 9.0 10.0
D)
pH 3
pH 10
Fluorescence (A.U.)
Time (ns)
0.0 0.2 0.4 0.6 0.8 1.0
30 40 50 60 70 80 90 100
E)
pH 3
pH 10
Fluorescence (cps x 10-5)
Wavelength (nm)
0.0 0.2 0.4 0.6 0.8
400 425 450 475 500 525 550 575 600

Figure 3. 4: A protocol combining TCA precipitation and TCEP reduction can be used to reveal the presence of unreacted, free label in samples and to determine total labeling efficiency. (A) Protocol for determining presence of free, unreacted label (Tube I), and for determining total labeling efficiency (Tube II). **(B)** Spectrum I shows that TCA precipitation of samples followed by centrifugation and TCEP treatment results in essentially no fluorescence compared to the same sample that is first treated with TCEP before TCA precipitation and centrifugation (Spectrum II), indicating there is no unattached, free label in the sample. **(C)** Example of determining labeling efficiency by comparing TCEP reduced samples to a standard curve of PDT-Bimane. The plot shows a sample of concentration 1.2 μM (determined by absorbance) subjected to the TCA/TCEP precipitation protocol, and compared to the standard curve. Notice that a value of 1.1 μM PDT-Bimane was obtained, indicating this procedure can be used to reliably determine labeling efficiency.

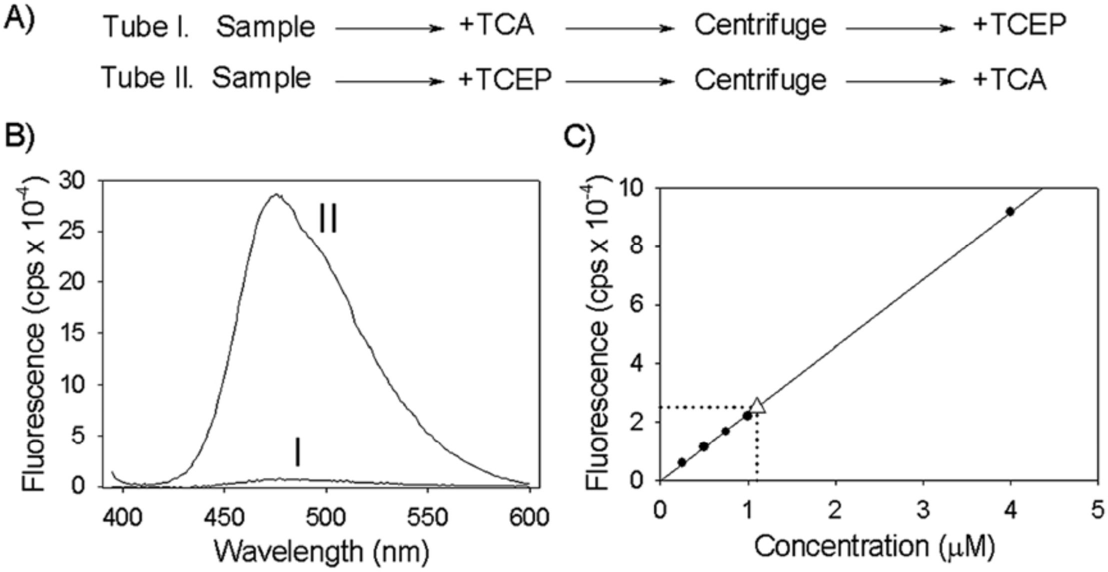
A)
Tube I. Sample → +TCA → Centrifuge → +TCEP
Tube II. Sample → +TCEP → Centrifuge → +TCA
B)
Fluorescence (cps x 10^{-4})
30
25
20
15
10
5
0
400
450
500
550
600
Wavelength (nm)
II
I
C)
Fluorescence (cps x 10^{-4})
10
8
6
4
2
0
0
1
2
3
4
5
Concentration (μM)

Figure 3. 5: PDT-Bimane shows distance-dependent quenching by proximal Trp residues. (A) Model of T4 lysozyme indicating the location of the tryptophan residue and the site of each PDT-Bimane attachment site (the α-carbon sites for each cysteine substitution are shown as blue spheres) **(B, left column)** Steady-state fluorescence intensity measurements of PDT-Bimane labeled cysteine mutants with (red) and without (blue) the Trp residue at site 116. Notice that introducing the Trp residue at 116 causes a dramatic decrease in fluorescence intensity for labels at sites 128 and 132. **(C, right column)** Comparison of PDT-Bimane labeled sites with the Trp residue at site 116 before (red) and after (blue) TCEP reduction. Notice that essentially the same results are obtained as in panel B.

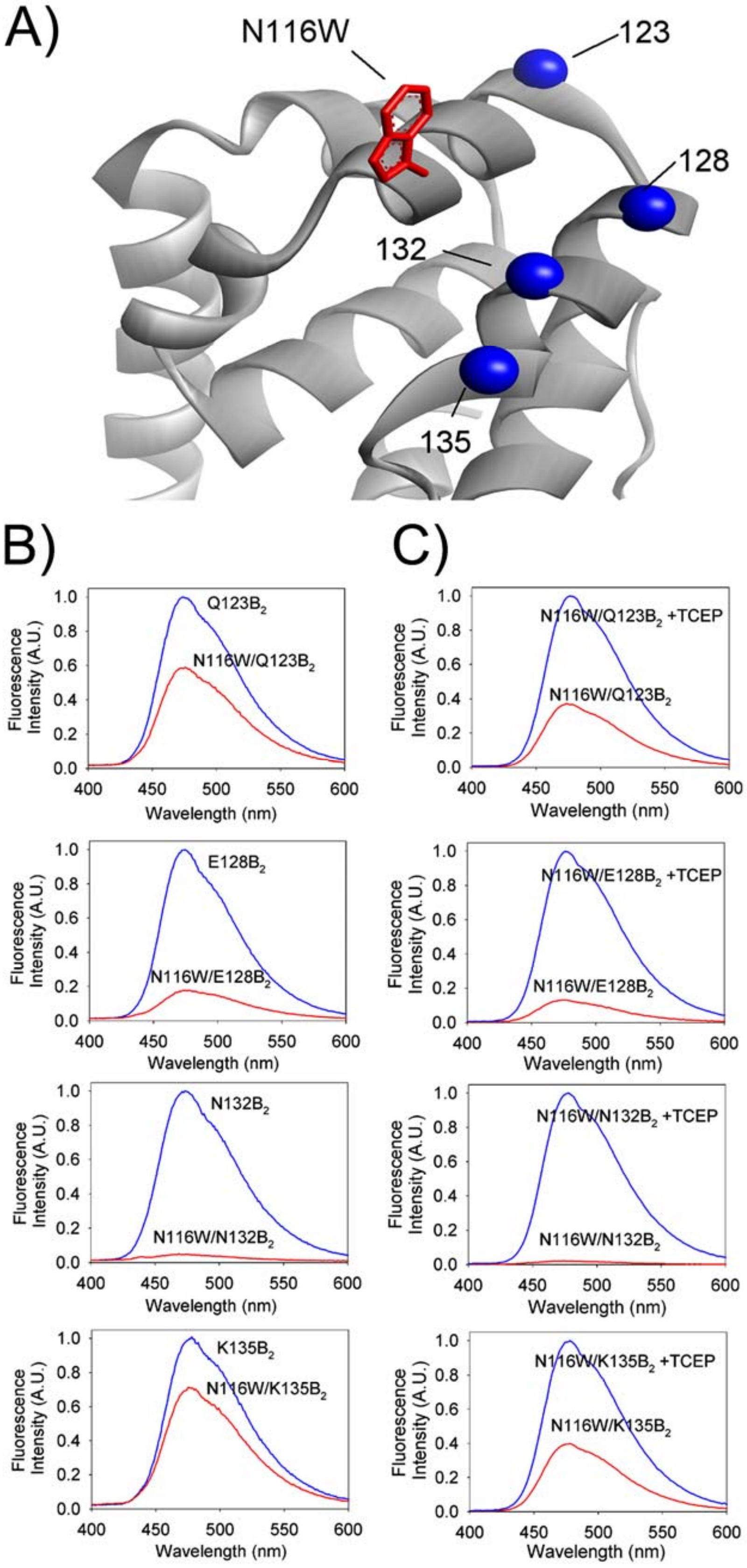
A)
N116W
123
128
132
135
B)
C)
Q123B$_2$
N116W/Q123B$_2$
E128B$_2$
N116W/E128B$_2$
N132B$_2$
N116W/N132B$_2$
K135B$_2$
N116W/K135B$_2$
N116W/Q123B$_2$ +TCEP
N116W/E128B$_2$ +TCEP
N116W/N132B$_2$ +TCEP
N116W/K135B$_2$ +TCEP
Fluorescence Intensity (A.U.)
Wavelength (nm)
0.0
0.2
0.4
0.6
0.8
1.0
400
450
500
550
600

Figure 3. 6: Proximity between Trp/bimane pairs can be further resolved by comparing the fluorescence intensities and lifetimes with (F_w; τ_w) and without (F_0; τ_0) a Trp residue. (A) The large difference in the steady-state fluorescence intensity ratio (F_0/F_w) compared to the weighted fluorescence lifetime ratio (τ_0/τ_w) reveals the Trp/bimane pair at N116W/N132B$_2$ undergoes primarily static quenching and thus is “very close” (~ 5-10 Å), whereas N116W/E128B$_2$ undergoes primarily dynamic quenching and thus is “close” (~ 10-15 Å). The uncertainty reported is the standard error of the mean from four measurements. **(B)** Absorption spectra of PDT-Bimane labels at sites 128 and 132 with (dashed line) and without (solid line) the neighboring Trp residue at site 116. The change in the absorption spectra at site 132 suggests a ground-state complex forms for mutant N116W/N132B$_2$, consistent with the static quenching detected in panel A.

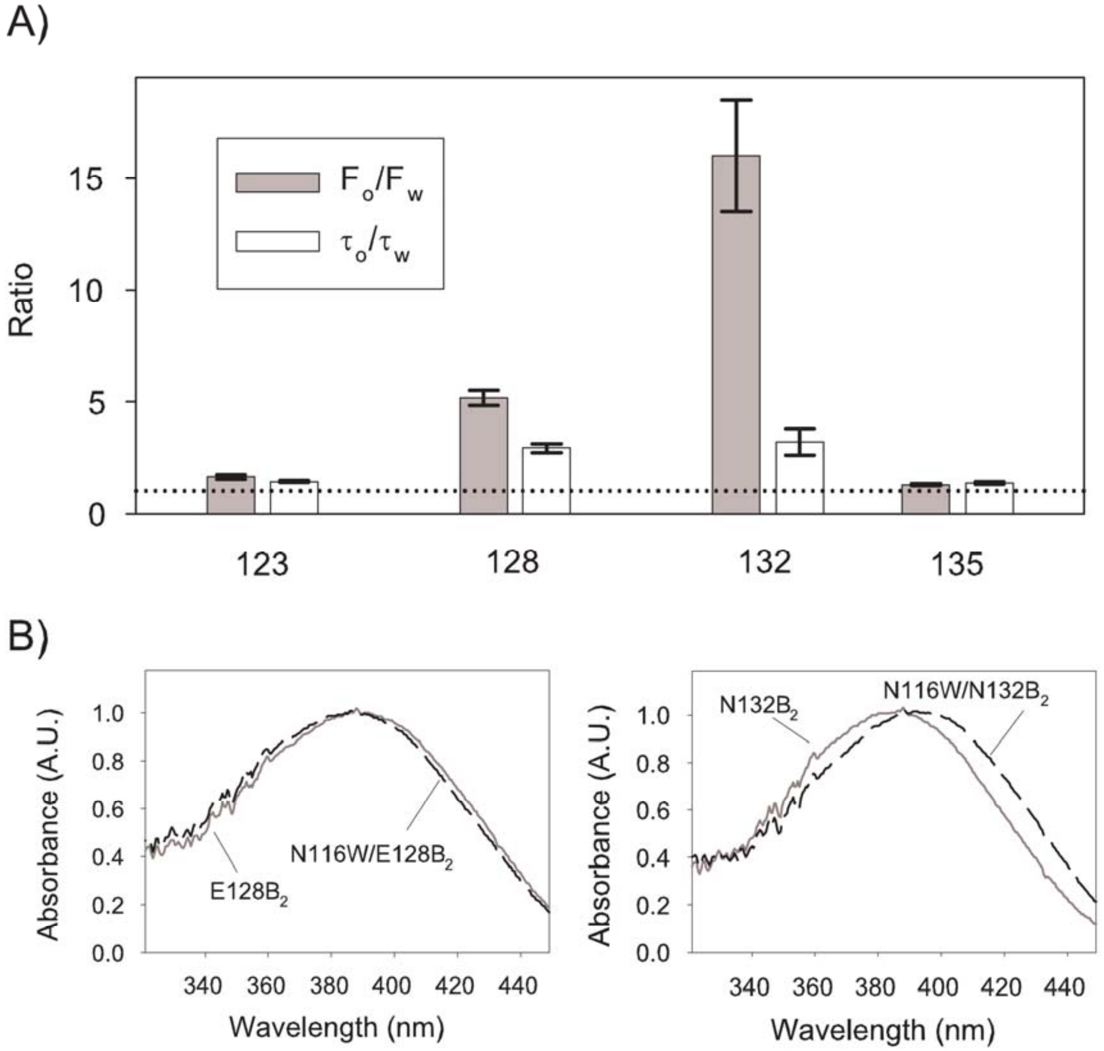
A)
15
10
5
0
Ratio
F_o/F_w
τ_o/τ_w
123
128
132
135
B)
Absorbance (A.U.)
1.0
0.8
0.6
0.4
0.2
0.0
340
360
380
400
420
440
Wavelength (nm)
E128B₂
N116W/E128B₂
N132B₂
N116W/N132B₂

Figure 3. 7: Proximity of PDT-Bimane to Trp residues can be determined by simply comparing fluorescence intensity values before and after TCEP reduction. (A) Relative fluorescence intensities of samples Q123B$_2$, E128B$_2$, N132B$_2$, and K135B$_2$ before and after reducing the PDT-Bimane label off of the protein with TCEP. Note the inherent increase in bimane fluorescence intensity (~ 70%) for these samples that do not contain the proximal Trp residue at site 116. **(B)** The fluorescence intensity increases dramatically upon TCEP reduction of sites with a proximal Trp residue at site 116. **(C)** Relative fluorescence intensities of samples from panel B after correction for the 70% increase seen in panel A. **(D)** Quantum yield values of matched concentrations (by absorbance) of the PDT-Bimane labeled samples both with and without the presence of the tryptophan residue at site 116. Note that the data from panel C provides nearly identical values relative to those seen in panel D, yet the TCEP reduction does not require mutating away the Trp residue at site 116 or carefully matching sample concentrations. The uncertainty reported in this figure represent the mean and range of two measurements.

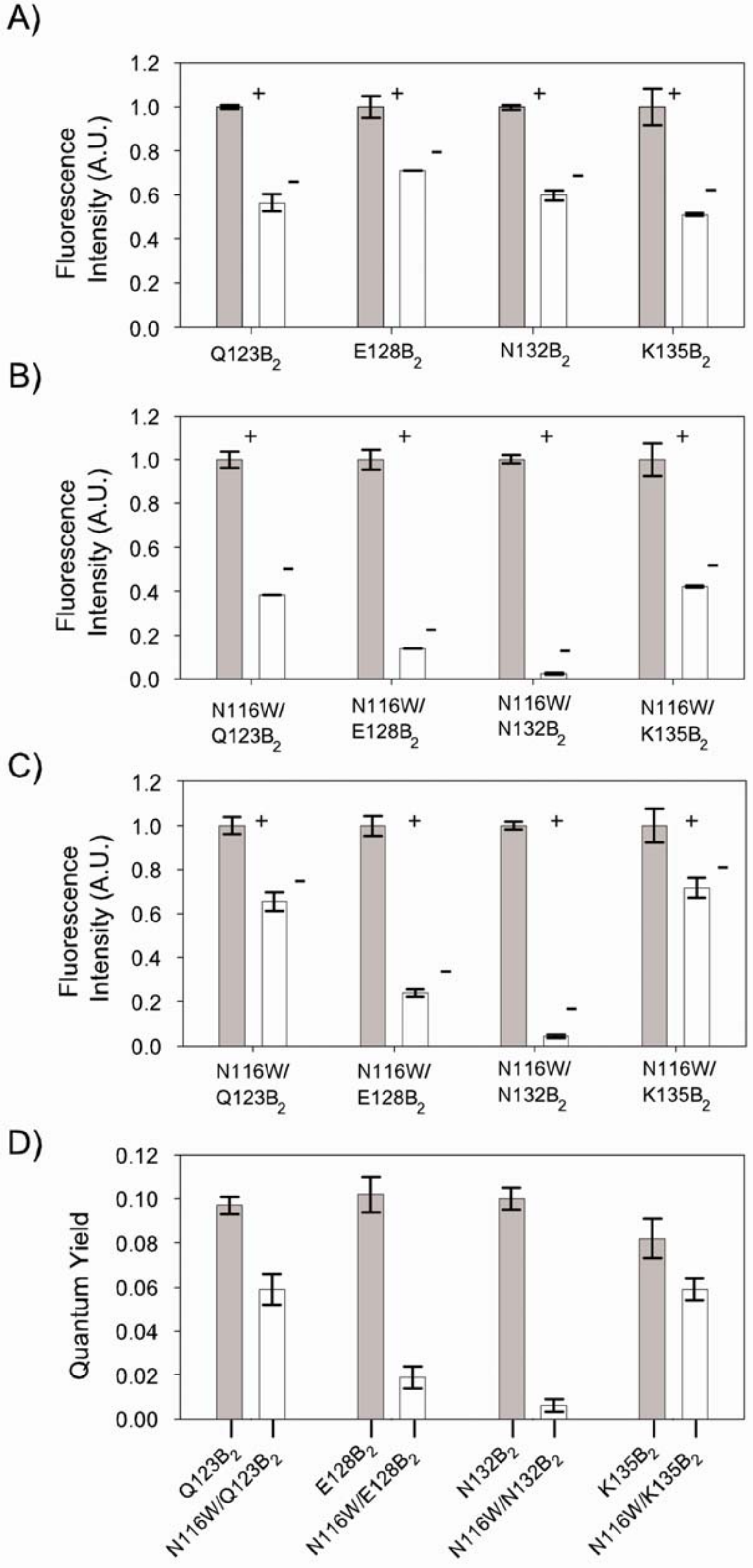
A)
Fluorescence Intensity (A.U.)
1.2
1.0
0.8
0.6
0.4
0.2
0.0
+
−
$Q123B_2$
$E128B_2$
$N132B_2$
$K135B_2$
B)
Fluorescence Intensity (A.U.)
$N116W/Q123B_2$
$N116W/E128B_2$
$N116W/N132B_2$
$N116W/K135B_2$
C)
Fluorescence Intensity (A.U.)
$N116W/Q123B_2$
$N116W/E128B_2$
$N116W/N132B_2$
$N116W/K135B_2$
D)
Quantum Yield
0.12
0.10
0.08
0.06
0.04
0.02
0.00
$Q123B_2$
$N116W/Q123B_2$
$E128B_2$
$N116W/E128B_2$
$N132B_2$
$N116W/N132B_2$
$K135B_2$
$N116W/K135B_2$

Figure 3. 8: Proposed scheme for carrying out high-throughput SDFL studies of protein structure using PDT-Bimane. Briefly, one would label samples with PDT-Bimane and measure fluorescence emission scans with and without TCEP to reduce the label off of the protein sample. Comparison of the differences in emission λ_{max} values would reflect the solvent surface accessibility, and thus secondary structure, and the differences in fluorescence intensity values would reflect proximity to tryptophan residues and thus tertiary structure. This approach would lend itself to automation and the use of a fluorescence plate reader, and thus should prove useful for high throughput protein structural studies.

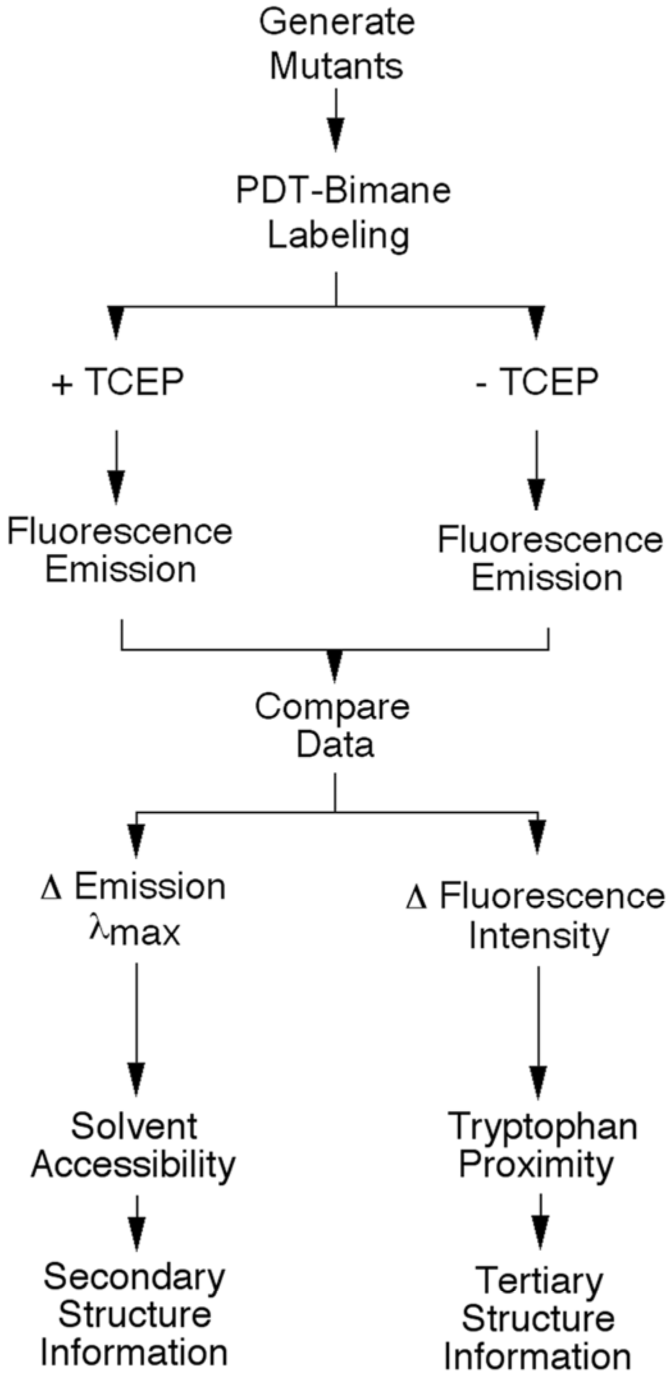
Generate Mutants
PDT-Bimane Labeling
+ TCEP
- TCEP
Fluorescence Emission
Fluorescence Emission
Compare Data
Δ Emission λmax
Δ Fluorescence Intensity
Solvent Accessibility
Tryptophan Proximity
Secondary Structure Information
Tertiary Structure Information

Chapter 4

Rhodopsin Self-Associates in Asolectin Liposomes

Steven E. Mansoor[§], Krzysztof Palczewski[◊], and David L. Farrens[§]

§ Department of Biochemistry and Molecular Biology, Oregon Health & Science University, 3181 S.W. Sam Jackson Park Road, Portland, OR 97239-3098.

◊ Department of Pharmacology, Case Western Reserve University, 10900 Euclid Avenue, Cleveland, OH 44106-4965.

4. 1: SUMMARY

We show that the photoreceptor rhodopsin (Rh) can exist in the membrane as a dimer or multimer using luminescence resonance energy transfer (LRET) and fluorescence resonance energy transfer (FRET) methods. Our approach looked for interactions between Rh molecules reconstituted into asolectin liposomes. The low receptor density used in the measurements ensured minimal receptor crowding and artifactual association. The fluorescently labeled Rh molecules were fully functional, as measured by their ability to activate the G-protein transducin. The luminescence resonance energy transfer measurements revealed a distance of 47-50 Å between Rh molecules. The measured efficiency of FRET between receptors was close to the theoretical maximum possible, indicating nearly quantitative Rh-Rh association. Together, these results provide compelling evidence that Rh spontaneously self-associates in membranes.

All experiments and data analysis reported in this chapter were performed by the author of this dissertation. The data presented in this chapter has been previously published in Mansoor, S.E., Palczewski, K., and Farrens, D. L. (2006) *Proc. Natl. Acad. Sci.* **103**, 3060-3065 and presented as a platform talk at the 50th Annual Biophysical Society Meeting, Salt Lake City, UT, 2006.

4. 2: INTRODUCTION

G-protein coupled receptors (GPCRs) are involved in diverse physiological processes and represent the single largest family of signaling molecules in the human genome. Until recently, GPCRs were assumed to exist in the membrane as monomeric proteins that are activated by the binding of one ligand to one receptor. However, a wealth of data indicates these receptors frequently form dimers or higher order oligomeric species [94,97,109,169,253]. In fact, some GPCRs may even function as hetero-oligomers [105].

The possibility that Rhodopsin (Rh) self-associates was first indicated by atomic force microscopy (AFM) measurements, which showed Rh molecules can form distinct, densely packed double rows in the rod outer segment (ROS) membranes of mouse retina [127]. Other studies carried out on detergent-solubilized protein suggest some Rh is present as dimers [157,162]. Furthermore, opsin forms dimers when expressed in COS1 cells [167]. However, the conclusion that Rh is dimeric challenges previous work that concluded Rh to be a monomer randomly distributed in the plane of the membrane [149,254-257].

In this chapter, we asked whether Rh molecules associate when reconstituted into lipid vesicles. Our approach was to use luminescence and fluorescence resonance energy transfer (LRET and FRET) techniques to assess the apparent distance between Rh molecules reconstituted in asolectin liposomes at low receptor densities. Our studies indicate that nearly all of the Rh self-associates into dimers or oligomers[1], providing further independent evidence that Rh is present in the membrane in a multimeric state.

4. 3: EXPERIMENTAL PROCEDURES

4. 3. 1: Materials.

The origin of the materials used can be found in the Supplemental section **4. 7. 1** at the end of this chapter.

4. 3. 2: Buffers.

The following buffers were used: buffer A: 137 mM NaCl, 8 mM Na_2HPO_4, 2.7 mM KCl, 1.5 mM KH_2PO_4, pH 7.2; buffer B: 137 mM NaCl, 8 mM Na_2HPO_4, 2.7 mM KCl, 1.5 mM KH_2PO_4, 4% 1-O-n- octyl-β-glucoside (OG), 0.1% asolectin, pH 7.2; buffer C: 137 mM NaCl, 8 mM Na_2HPO_4, 2.7 mM KCl, 1.5 mM KH_2PO_4, 1.46% OG, 0.1% asolectin, pH 7.2; buffer D: 137 mM NaCl, 8 mM Na_2HPO_4, 2.7 mM KCl, 1.5 mM KH_2PO_4, 1.46% OG, 0.1% asolectin, 0.3 M Methyl α-D-Mannopyranoside, pH 7.2; Transducin Assay Buffer: 10 mM Tris·HCl (pH 7.5), 0.1 M NaCl, 5 mM $MgCl_2$, 1 mM EDTA.

4. 3. 3: Nomenclature.

Here, rhodopsin is abbreviated as Rh. Abbreviations for rhodopsin derivatives are identified by Rh, followed by the fluorophore used in the labeling. For example, Rh-CY5 stands for Rh labeled with CY5-maleimide and Rh-Tb stands for Rh labeled with the Tb^{3+} chelator.

---

[1] For simplicity, we have limited our interpretation to a dimeric interaction, as suggested by others [126,156,161,166,258], but formally, our data cannot discriminate between Rh dimers and other higher order oligomers.

4. 3. 4: Purification and Fluorescent Labeling of Rh.

Rh was purified from rod outer segment (ROS) membranes and modified with the appropriate fluorophore. V8 proteolysis was used to assess the sites of fluorescent labeling. Specific details on these procedures are provided in the Supplemental sections **4. 7. 2**, **4. 7. 3** and **4. 7. 4** at the end of this chapter.

4. 3. 5: Reconstitution of Purified, Fluorescently Labeled Rh.

Reconstitution of fluorescently labeled Rh into asolectin liposomes was performed in the dark under dim red light, as described [259]. Different receptor densities were achieved by reconstituting samples with varying molar ratios of asolectin and Rh. The lipid/Rh ratios, 250:1, 2000:1, or 10,000:1, should theoretically produce receptor densities of ≈ 800, 100, and 20 Rh protein molecules per liposome, respectively. More details are provided in the Supplemental section **4. 7. 5** at the end of this chapter.

4. 3. 6: Analysis of Rh-Reconstituted Proteolipsomes Using Electron Microscopy, Asp-N Proteolysis, and Transducin Activation Assays.

After reconstitution, the size of the proteoliposomes was determined by Electron Microscopy (EM). Asp-N proteolysis was used to determine the relative orientation of Rh in the liposomes [259]. The effect of the fluorescent labels on Rh function was measured by performing transducin activation assays [260]. For details, see the Supplemental sections **4. 7. 6**, **4. 7. 7** and **4. 7. 9** at the end of this chapter.

4. 3. 7: Determination of the Quantum Yield of Rh-CY3 Donor and R_0 Value for CY3-CY5 FRET Pair.

The quantum yield for Rh-CY3 reconstituted into liposomes was measured and used to determine the overlap integral (R_0) for the Rh-CY3 and Rh-CY5 FRET pair. Details are given in the Supplemental section **4. 7. 8** following the end of this chapter.

4. 3. 8: Isopycnic Density Centrifugation.

Isopycnic density centrifugation analysis was carried out on Rh-CY3 and Rh-CY5 reconstituted into asolectin liposomes. The liposomes were supplemented with NBD-labeled phosphatidyl serine (0.4% of the total lipid content) to enable independent fluorescent monitoring of the lipid fractions. The proteoliposomes were subjected to discontinuous flotation gradients [261], and fractions were analyzed for Rh and lipid content. See the Supplemental section **4. 7. 10** for more details.

4. 3. 9: Predicted Receptor Density.

The number of Rh molecules per liposome was calculated as follows. The average radius of the asolectin liposomes was ≈ 75 nm (see our EM data, Figure 4. 1B, and reference [262]), thus producing a liposome surface area of ≈ 7,000,000 Å^2. Assuming the surface area of one lipid molecule to be 70 Å^2, and the vesicle membranes is a bilayer, yields approximately 200,000 lipids/vesicle. If equally distributed, the number of Rh molecules per liposome is:

$$\# Rh/liposome = \left(\frac{\# Lipids}{Liposome}\right) \times \left(\frac{Rh}{Lipid} Ratio\right) \qquad \text{[Eq. 4. 1]}$$

where Rh/Lipid Ratio is the inverse of the lipid/Rh ratio used during the reconstitution.

4. 3. 10: Calculation of Reduced Acceptor Surface Density (C_A).

The reduced acceptor surface density (C_A) is equal to the R_0^2 of the FRET pair multiplied by the surface density of acceptor-labeled proteins [263]. For the CY3-CY5 FRET pair on Rh, we measured an R_0 of ≈ 52 Å in the dark state and 56 Å following light activation. These values are similar to those published in references [264] and [265]. We then calculated the C_A at each lipid/Rh ratio, using the following relationship [263]:

$$C_A = (\mathrm{R}_0)^2 \times \frac{\#\,Acceptors}{LiposomeSurfaceArea, \text{Å}^2} \qquad \text{[Eq. 4. 2]}$$

$$= (56.1\text{Å})^2 \times \frac{10}{7{,}000{,}000\text{Å}^2} = 0.0045$$

Note that the change in the R_0 value between dark- and light-activated Rh-CY3 and Rh-CY5 requires the C_A values to be calculated for each state.

4. 3. 11: Calculation of Expected Random Energy Transfer (E_{random}) Based on the Reduced Acceptor Surface Density (C_A).

The C_A values (described above) were used to assess the amount of random "background" energy transfer expected under the different reconstitution conditions, as follows [263,266,267]:

$$E_{random} = 1 - \left\{ 1 + \left[\frac{\pi \times C_A}{2} \times \left(\frac{R_0}{r} \right)^4 \right] \right\}^{-1} \qquad \text{[Eq. 4. 3]}$$

where E_{random} is the amount of random energy transfer expected, C_A is the reduced acceptor surface density, and r is the distance of closest approach of the donors and acceptors (which can be approximated by the protein diameter) [263,266-271]. The value of r for rhodopsin was approximated to be ≈ 48 Å, the diameter across the face of an ellipsoid shape observed for rhodopsin from the crystal structure [3].

4. 3. 12: Measurement of the Rate of LRET Between Labeled Rh Samples in Asolectin Proteoliposomes.

LRET studies were made using a PTI LaserStrobe phosphorescence lifetime system. The Rh-Tb samples were excited with a 337 nm laser pulse, and the emission was monitored at 545 nm to obtain the lifetime of the Rh-Tb donor alone (τ_D), and at 570 nm, when Rh-Tb and Rh-CY3 were reconstituted together, to obtain the sensitized emission lifetime (τ_{AD}) from Rh-CY3. For further details, see the Supplemental section **4. 7. 11** at the end of this chapter.

4. 3. 13: Determination of Distance from LRET Measurements.

The lifetime of Rh-Tb luminescence (τ_D) and the Rh-CY3 sensitized emission (τ_{AD}) were used to calculate the efficiency of energy transfer (E):

$$E = 1 - \frac{\tau_{AD}}{\tau_D} \qquad \text{[Eq. 4. 4]}$$

This efficiency was then used to calculate the distance between the two probes [77,78]:

$$R^6 = \frac{R_0^6(1-E)}{E} \qquad \text{[Eq. 4. 5]}$$

where E is the efficiency of energy transfer, R is the distance between the probes, and R_0 is the distance at which the energy transfer is 50%. Equation 4. 4 and Equation 4. 5 were used to plot τ_{AD} as a function of R. This plot yields the appropriate distance for any experimentally measured τ_{AD} (see Figure 4. 2D). An R_0 = 61.2 Å was used for the Rh-Tb and Rh-CY3 pair [272].

To assess the maximum possible error in the LRET measurements due to uncertainties in the orientation factor (κ^2), the steady-state anisotropies of Rh-CY3 and Rh-CY5 in the liposomes were measured. Details are given in the Supplemental sections **4. 7. 14** and **4. 7. 15**.

4. 3. 14: FRET Steady-State and Lifetime Measurements.

The steady-state fluorescence measurements were carried out on Rh-CY3 and Rh-CY5 samples reconstituted individually and together. FRET was measured in two ways, first by measuring the emission spectrum of the acceptor while exciting the donor and then by measuring the excitation spectrum of the donor while collecting emission from the acceptor. Fluorescence lifetimes were measured on the samples reconstituted at the lowest receptor density. Further details are given in the Supplemental sections **4. 7. 12** and **4. 7. 13**.

4. 3. 15: FRET Efficiency Calculated From Steady-State Fluorescence Intensity and Fluorescence Lifetimes.

FRET efficiency was determined by measuring the sensitized emission from steady-state excitation spectra using standard analysis procedures [78,273]. The FRET efficiency was also determined from the fluorescence lifetimes of the donor (Rh-CY3) in the presence and absence of the acceptor (Rh-CY5) [78]. See the Supplemental section **4. 7. 16** for details.

4. 4: RESULTS

4. 4. 1: Overview.

We looked for evidence of Rh-Rh interactions using a quantitative FRET based approach. Our strategy (outlined in Figure 4. S1 of Supplemental section) was to look for Rh-Rh interactions under conditions in which the Rh molecules were given ample opportunity to not interact. Thus, we reconstituted Rh into liposomes at low receptor densities, to maximize the amount of positive FRET signal from Rh molecules truly involved in dimeric or higher order interactions. After reconstitution, we first measured the average distance between Rh receptors using LRET. Next, we measured FRET between Rh samples and correlated the amount of the energy transfer with the proportion of total receptors at the measured interaction distance. Our main postulate is that if the amount of measured FRET equals the maximum FRET possible, most of the Rh molecules must be self-associating.

4. 4. 2: Preparation and Characterization of Rh Samples.

Rh was labeled in the cytoplasmic face, as described in the Supplemental section **4. 7. 3**. The labeling occurred at the uniquely reactive cysteine residues, C140 and C316 [224,274-277]. The LRET studies used the label CS124-DTPA-EMCH•Tb^{3+} as the donor and CY3-maleimide as the acceptor. The FRET studies used CY3-maleimide as the donor and CY5-maleimide as the acceptor. These Cys-reactive fluorophores are well characterized [264,265,272], and their spectra are significantly red-shifted, resulting in minimal spectral overlap with the retinal chromophore in Rh (see Figure 4. 3B).

Rh was labeled with approximately 1.0 label per protein (data not shown). The C140 and C316 Cys residues labeled with roughly similar efficiencies, as assessed by V8 proteolysis and SDS-PAGE analysis [41], which produced two fragments (F1 and F2) with similar fluorescence intensity (Figure 4. 1A). Scanning electron microscopy indicated that the reconstituted Rh proteoliposomes ranged in size from 100 nm to 200 nm in diameter, with an approximate average diameter of 150 nm (Figure 4. 1B), consistent with previous measurements of asolectin liposomes [262].

4. 4. 3: The Labeled and Reconstituted Rh is Preferentially Oriented Inside-Out and Is Fully Functional.

Treatment with Asp-N protease increased the electrophoretic mobility of all liposome-bound Rh, as efficiently as for a detergent solubilized Rh control (Figure 4. 1C). This result indicates the Rh is oriented inside-out in the liposomes [259], with the C-terminal tail of rhodopsin exposed to the Asp-N protease [278]. Both labeled and unlabeled liposome-bound Rh samples showed essentially identical abilities to activate $G\alpha_T$ (initial activation rates ≈ 1.3 pmol/min/pmol rhodopsin), demonstrating that the attached fluorophores do not affect rhodopsin function (Figure 4. 1D).

4. 4. 4: The Quantum Yield of Rh-CY3 Increases Upon Light Activation of Rhodopsin, Resulting in an Increase in the R_0 Value Between Rh-CY3 and Rh-CY5.

The quantum yield of reconstituted Rh-CY3 rose from 0.13 ± 0.01 in the dark state to 0.20 ± 0.01 after light activation of Rh, presumably because energy transfer from the CY3 label to the retinal chromophore was abolished. It is important to note this increase in Rh-CY3 quantum yield changes the R_0 value for the Rh-CY3/Rh-CY5 FRET pair from 52 Å in the dark state to 56 Å when light activated.

4. 4. 5: LRET Measurements Show a Rh-Rh Distance of 47-50 Å in Liposomes.

The LRET approach is illustrated in Figure 4.2A. We first used the LRET method because it can accurately determine distances between two proteins, even in the presence of some labeled but non-interacting proteins (the latter are spectrally silent in LRET). Furthermore, LRET is not complicated by the false positives that often complicate FRET studies [81,272,279-282]. Most importantly, we could use the distances we obtained independently by LRET to quantitate the percentage of the total Rh proteins participating in the subsequent FRET studies.

Details on the LRET studies are given in the Supplemental section **4. 7. 11**. Briefly, they involved exciting the Rh-Tb (donor) at 337 nm with a laser pulse and then measuring energy transfer to Rh-CY3 (the acceptor), as indicated by the "sensitized emission" given off from Rh-CY3 at 570 nm (Figure 4.2B). The rate of transfer, k, is reflected in the lifetime of the sensitized emission (τ_{AD}), since $k = 1/\tau_{AD}$. We used the τ_{AD} value thus obtained, and Equation 4. 4, to determine the efficiency of luminescence resonance energy transfer. From this efficiency, we calculated the donor-acceptor distance using Equation 4. 5.

A representative result is shown in Figure 4. 2C. The data, measured from dark-state Rh reconstituted at the lowest receptor density (10,000 lipids/Rh), shows the decay of Rh-Tb donor alone (τ_D; blue curve) and the "sensitized emission" decay of Rh-CY3 (τ_{AD}; green curve). Two lifetime components were required to fit both the τ_D and τ_{AD} data, most likely because energy transfer from Rh-Tb to the retinal contributes to a short decay component. The quality of the data did not warrant a complex analysis; thus, we combined these values to calculate an "average" or amplitude-weighted lifetime, $<\tau> =$

$\alpha_1\tau_1 + \alpha_2\tau_2$, where α_1 and α_2 are the pre-exponential factors ($\alpha_1+\alpha_2 = 1.0$) for τ_1 and τ_2, respectively. The complete set of amplitude-weighted LRET lifetimes, $<\tau_D>$ and $<\tau_{AD}>$, thus measured, are reported in Table 4. 1.

These $<\tau_D>$ and $<\tau_{AD}>$ values yield a distance of 50 Å between Rh-Tb and Rh-CY3 in the dark state (Figure 4. 2D). Similar measurements were made for the samples immediately and 30 min following light activation (see Table 4. 1). In each case, the distance between Rh proteins undergoing LRET was between 47-50 Å. Interestingly, this value is in good agreement with an expected Rh-Rh distance based on the known diameter of Rh [3].

4. 4. 6: FRET Measurements Show Substantial Energy Transfer Between Rh Samples in Liposomes.

To determine the proportion of Rh protein molecules that are close enough to interact, we used quantitative FRET measurements using CY3 as the energy transfer donor and CY5 as the acceptor (Figure 4. 3A and 4. 3B).

In these experiments, we reconstituted Rh-CY3 and Rh-CY5, both together, and separately as a control (in the latter case with equimolar amounts of unlabeled Rh). We ensured that each reconstitution resulted in an identical amount of Rh in the liposomes. The results from these studies, shown in Figure 4. 3C, reveal substantial FRET, but only when the samples were combined and reconstituted together (green curves). The control samples show no FRET (red curves). The amount of FRET appears to increase immediately upon light activation of Rh and continues to increase over time (Figure 4. 3C, left panel), although we suspect this increase is mainly due to the inherent increase in the quantum yield for Rh-CY3 upon bleaching.

We quantified the amount of FRET observed in these excitation spectra using standard approaches [78,273]. Our results showed a FRET efficiency of 32% in the dark, which increased to 38% efficiency immediately after light activation and up to 46%, 30 min after light activation. Importantly, these donor- and acceptor-labeled ROS samples were prepared separately, their concentrations were determined and matched, and only then were the samples mixed for reconstitution. These stringent conditions ensured that a positive FRET signal unequivocally reflects inter-molecular FRET occurring between at least two different receptors. We stress that the data in Figure 4. 3C are raw data that, aside from buffer subtraction, have not been normalized or manipulated in any other way.

Substantial FRET is also apparent in the emission spectra and fluorescence lifetimes. For example, the sensitized acceptor emission spectra (Figure 4. 3C, right panel) show both a decrease in fluorescence intensity of Rh-CY3 emission at 570 nm and a concomitant increase in the sensitized Rh-CY5 emission at 670 nm (again, the FRET signal in the dark state appears to increase after light activation). Similarly, a high FRET efficiency is observed by measuring the fluorescence lifetime of the donor, Rh-CY3, in the absence (τ_D) and presence (τ_{DA}) of the acceptor, Rh-CY5. These measurements indicate FRET efficiencies ranging from 25% in the dark state to 32% at 30 min after light activation (Table 4. 2). These values are in qualitative agreement with the steady-state FRET efficiencies. Imperfect correlation with the steady-state data are most likely due to the short lifetimes of the donor fluorophore and to the limitations of our instrumental set-up.

To assess possible error in the LRET and FRET results, we measured the steady-state anisotropy of the samples to determine the degree of fluorophore mobility (Table 4.

S1 in Supplemental section). These results indicate the maximum possible error associated with the LRET distances (Table 4. 1), due to changes in κ^2, are < 8% in both the dark state and light-activated states, whereas the maximum error in the FRET efficiency is between 20 and 30%. Note that the actual errors are likely much less significant than these absolute possible extremes [184].

4. 4. 7: FRET Efficiency at Different Receptor Densities.

We determined the amount of non-specific "background FRET" (due to receptor crowding) by measuring FRET for samples reconstituted at varying molar lipid/Rh ratios (10,000:1, 2000:1, and 250:1). These conditions should theoretically produce receptor densities of ≈ 20, ≈ 100, and ≈ 800 proteins per vesicle, respectively. We used these receptor densities, along with the concept of a reduced acceptor surface density (C_A), to calculate the amount of background FRET expected at each lipid/Rh concentration. The FRET results, and the "background FRET" expected for the different concentrations, are shown in Figure 4. 4A. Notice that the measured FRET signal is strongly dependent on the receptor density, and appears to be superimposed on the predicted background FRET at each concentration.

4. 4. 8: Experimentally Determined Receptor Density.

The above calculation assumes a random distribution of Rh among the liposomes. We tested this assumption at the lowest Rh/lipid ratio (one Rh per 10,000 lipid molecules) by carrying out isopycnic density centrifugation analysis [261]. These studies showed that Rh, in these preparations, is not uniformly distributed (Figure 4. 4B). Instead, ≈ 90% of the Rh appears to be present in ≈ 11% of the available vesicles. This interesting result (which may suggest Rh is forming higher order oligomers) indicates that in most vesicles containing Rh, the “true” receptor density is actually ≈ 10x higher than predicted (≈ 200 rhodopsin molecules per liposome). The correct C_A values are thus 0.039 in the dark state and 0.045 following light activation, yielding a more accurate assessment of the “background FRET” at this lipid/Rh ratio of ≈ 8% in the dark and ≈ 11% following light activation (see dotted curve in Figure 4. 4A).

4. 4. 9: The Measured FRET Efficiencies Are Near the Theoretical Maximum Possible, Suggesting That the Majority of Rh Molecules Interact.

Our main postulate in this work is the following: quantitative Rh-Rh self-association is indicated if the measured FRET efficiencies equal the theoretically maximum FRET possible at the Rh-Rh distances measured from the LRET studies (Figure 4. 2D and Table 4. 1).

We estimated the total amount of interacting Rh proteins as follows. We analyzed the excitation FRET spectra [78,273] to determine the percentage of FRET in each sample (see Table 4. 2). We then compared this value to the maximal FRET possible under these conditions. To calculate the theoretical maximum FRET, we had to take into account two factors. First, only half of the labeled Rh can form donor-acceptor pairs (see Figure 4. 5A). Second, the R_0 values for a specific donor-acceptor pair must be used. When these factors are accounted for, the following theoretically maximum FRET efficiencies are predicted: 28% for the Rh-CY3-Rh-CY5 pair in the dark state (distance = 50 Å), and 37% for the Rh-CY3-Rh-CY5 pair in the light-activated state (distance = 47 Å) (Figure 4. 5B).

Importantly, as shown in Figure 4. 5C, these predicted maximum possible FRET values are nearly identical to the measured FRET efficiencies (once the expected background FRET is subtracted; Figure 4. 4A). We conclude that, for this result to be possible, almost all the Rh molecules must be within interacting distance.

4. 5: DISCUSSION

4. 5. 1: Implications of Rh-Rh Association.

Although the idea that visual Rh may self-associate in the membrane has been debated [129], our results clearly favor Rh dimerization and are consistent with evidence found for other GPCRs [94,97,109,169]. In fact, our studies found no evidence for a substantial amount of monomeric Rh. Because Rh constitutes the majority of volume of the membrane in ROS, with a concentration as high as 3 mM [118], and only ≈ 65 phospholipids solvating each Rh molecule [118], an interesting question may be "what could prevent Rh from interacting with itself?" The complete absence of any protein-protein interactions at such high concentrations would seem to require an extremely low affinity between Rh molecules, a possibility that is not supported by our present work, or the work of Kota *et. al* [167].

Thinking about Rh as a dimer, instead of a monomer, is compelling when examining the architecture of various downstream signaling components in the visual pathway. For example, the interface surface area of Rh in a monomeric model of the Rh-transducin interaction is too small to cover all the regions of transducin known to be critical for interaction with the receptor. However, subsequent modeling studies have demonstrated that the surface area of one transducin molecule is large enough to accommodate the docking of four rhodopsin molecules [118].

Similarly, the concept of a multimeric Rh may help explain Rh desensitization by visual arrestin. Arrestin acts by binding to activated, phosphorylated Rh, thus blocking further signaling [283]. Interestingly, crystal structures of arrestin show a bilobed protein with two concave surfaces [284,285]. Both concave surfaces have been demonstrated by mutagenesis studies to be involved in Rh-arrestin interactions [286]. Like transducin, the putative Rh-interaction surface on visual arrestin is highly striking: the two concave grooves can physically accommodate two molecules of rhodopsin [253]. Although the specific reasons why Rh may function as a dimer remain to be established, it is clear a dimeric state may have a profound impact on the kinetics of Rh activation, signaling through transducin, and desensitization through arrestin.

4. 5. 2: Summary and Conclusions.

We have found that Rh molecules in reconstituted asolectin liposomes are ≈ 47-50 Å apart. Further, the energy transfer between donor and acceptor-modified Rh is close to the theoretically possible maximum FRET efficiency, showing that most of the Rh molecules are in a dimeric state (if not higher-order oligomers). Finally, we anticipate the approach described here may prove generally useful for quantitatively studying GPCR self-association in membranes.

4. 6: ACKNOWLEDGEMENTS

We thank Mr. J. Fay for technical assistance on the transducin activation assays, Dr. E. Barklis for performing the electron microscopy analysis, and Dr. T. Huber for suggesting the isopycnic density centrifugation analysis. We thank Dr. T. Heyduk for providing lanthanide reagents for initial LRET trials, and Dr. T. Heyduk and Dr. S.

Lutsenko for valuable comments on the manuscript. Finally, we thank Dr. I. Sokal and Dr. G. Jang for help in initiating this project.

Table 4. 1: LRET Lifetime Data Indicate Distances of ≈ 47 - 50 Å Between Rh Molecules Reconstituted into Asolectin Liposomes.[a]

Rh-Tb + Rh-CY3 Sample	$<\tau_D>$ Lifetime (μsec)	$<\tau_{AD}>$ Lifetime (μsec)	Rh-Rh Distance (Å)
Dark State	870 ± 14	196 ± 12	50 ± 1
+hυ, 0 min.	970 ± 20	185 ± 1	48 ± 1
+hυ, 30 min.	982 ± 29	171 ± 14	47 ± 1

[a] Measurements were carried out as described in Experimental Procedures of this chapter. Note that due to the long luminescent lifetimes of Rh-Tb, we cannot completely rule out some contributions to the measured LRET distance caused by simple diffusion bringing two Rh proteins together. See Supplemental section **4. 7** for more details.

Table 4. 2: FRET Efficiencies Calculated Using Steady-State Excitation Spectra and Fluorescence Lifetime Decays of Rh Reconstituted into Liposomes.[a]

Rh-CY3 + Rh-CY5 Sample	**FRET Efficiency (%) Steady-State Excitation Data**	**FRET Efficiency (%) Lifetime Data**
Dark State	32 ± 1	25 ± 2
+hυ, 0 min.	38 ± 1	21 ± 1
+hυ, 30 min.	46 ± 1	32 ± 2

[a] Measurements were carried out as described in Experimental Procedures of this chapter. See Supplemental section **4. 7** for more details.

Figure 4. 1: Preparation and Functional Characterization of Labeled Rh Samples. **(A)** SDS-PAGE analysis of V8 digested CY3-labeled Rh samples shows roughly equal distribution of labels on C140 and C316. **(B)** Electron microscopy reveals that asolectin liposomes reconstituted with Rh have an average radius of ≈ 75 nm. **(C)** Asp-N proteolysis indicates Rh-CY3 and Rh-CY5 are preferentially oriented inside-out in the liposomes. Because Asp-N cleaves Rh at the C-terminus, a shift in protein mobility indicates the C-terminus is located outside the liposome, and is accessible to the protease. ***(Upper)*** Imaging of CY3 fluorescence. ***(Lower)*** Coomassie stain. The individually labeled, reconstituted samples are indicated. Det. refers to a detergent solubilized control. The imaging instrument was not sensitive to CY5 fluorescence. **(D)** The fluorescent labels do not alter the ability of Rh, reconstituted into liposomes, to activate transducin ($G\alpha_T$). The initial activation rates were ≈ 1.3 pmol/min/pmol Rh for both the unlabeled (open circles) and labeled (open triangles), reconstituted Rh samples. The activation rates were determined by linear regression through the data points converging 3 minutes after addition of guanosine 5'-[γ-thio]triphosphate. The filled circles show the dark state control.

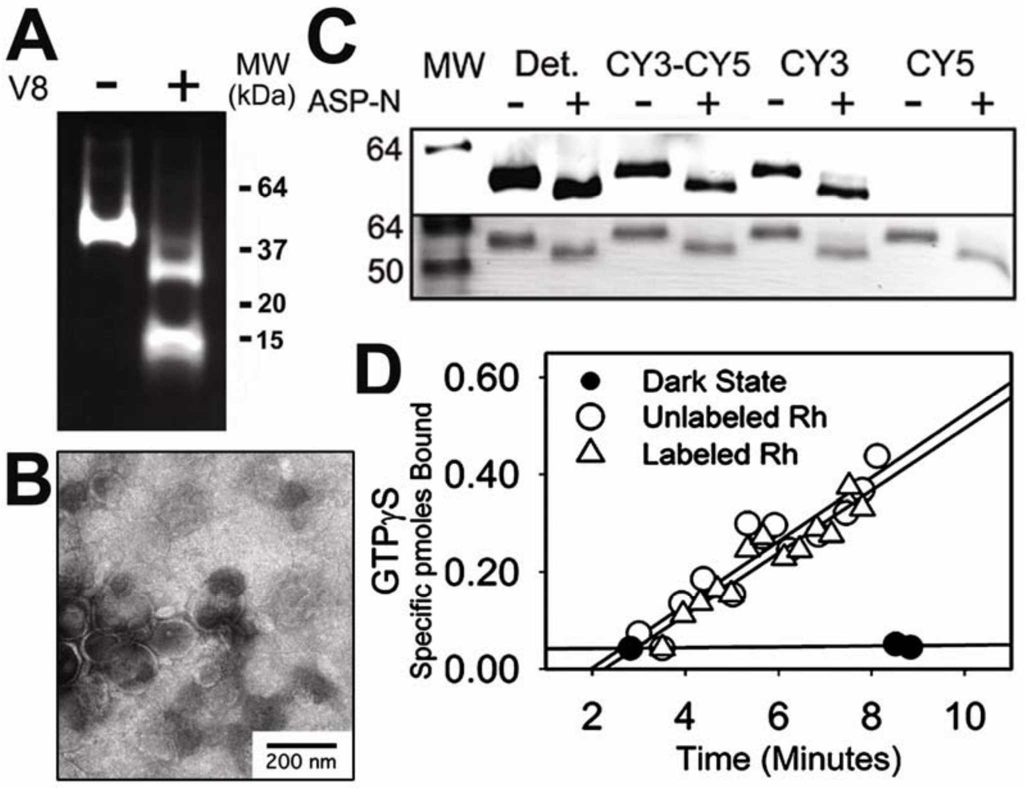
A
V8
-
+
MW
(kDa)
64
37
20
15
B
200 nm
C
MW
Det.
CY3-CY5
CY3
CY5
ASP-N
-
+
-
+
-
+
-
+
64
64
50
D
Dark State
Unlabeled Rh
Labeled Rh
GTPγS
Specific pmoles Bound
0.60
0.40
0.20
0.00
2
4
6
8
10
Time (Minutes)

Figure 4. 2: LRET Measurements Show Labeled Rh Samples are 47- 50 Å Apart. **A)** Cartoon scheme of LRET experiments. Excited Rh-Tb (donor) will transfer energy to Rh-CY3 (acceptor), with an efficiency proportional to the distance between the two proteins (see Equation 4. 4 and Equation 4. 5). **(B)** Spectral overlap of Rh-Tb and Rh-CY3. The LRET experiments involve exciting Rh-Tb at 337 nm and collecting the sensitized emission from Rh-CY3 at 570 nm. **(C)** LRET decay data obtained from a dark state mixture of Rh-Tb and Rh-CY3. Exciting the Rh-Tb results in a strong sensitized emission signal from Rh-CY3 (green decay curve), which decays with an average lifetime $<\tau_{AD}> \approx 200$ µs. The average lifetime of Rh-Tb alone yields a $<\tau_D> \approx 870$ µs (blue decay curve). **(D)** Predicted sensitized LRET lifetimes (τ_{AD}) as a function of distance between Rh-Tb and Rh-CY3. The plot indicates the ≈ 200 µs τ_{AD} measured above corresponds to an Rh-Tb to Rh-CY3 distance of ≈ 50 Å (red line). After light activation, the Rh-Rh distance decreased slightly to 47 Å (See Table 4. 1).

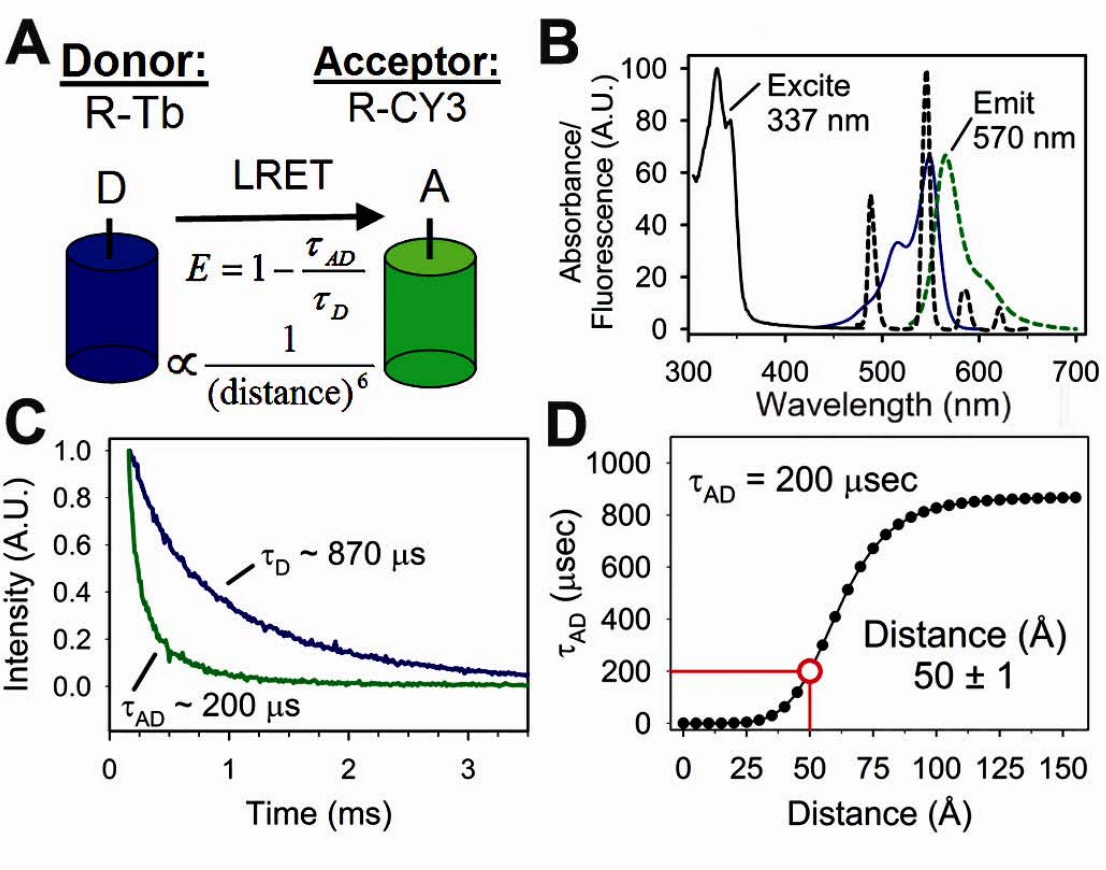A
Donor:
R-Tb
Acceptor:
R-CY3
D
LRET
A
$E = 1 - \frac{\tau_{AD}}{\tau_D}$
$\propto \frac{1}{(\text{distance})^6}$
B
Absorbance/ Fluorescence (A.U.)
Excite 337 nm
Emit 570 nm
Wavelength (nm)
300
400
500
600
700
0
20
40
60
80
100
C
Intensity (A.U.)
τ_D ~ 870 μs
τ_{AD} ~ 200 μs
Time (ms)
0
1
2
3
0.0
0.2
0.4
0.6
0.8
1.0
D
τ_{AD} = 200 μsec
τ_{AD} (μsec)
Distance (Å)
50 ± 1
Distance (Å)
0
25
50
75
100
125
150
0
200
400
600
800
1000

Figure 4. 3: FRET Studies Show Strong Rh-Rh Energy Transfer in Liposomes. (A) Cartoon Scheme of FRET studies. Excitation of Rh-CY3 (donor) will transfer energy to Rh-CY5 (acceptor) with an efficiency proportional to the distance between them (see Equation 4. 5). **(B)** Spectral overlap of CY3 and CY5. The amount of overlap, J(λ), is indicated in dark gray and results in a calculated R_0 for this FRET pair of 52 Å in the dark state and 56 Å after light activation of rhodopsin. **(C)** The arrows indicate the strong FRET observed between Rh-CY3 and Rh-CY5 when reconstituted together into asolectin liposomes (green curve). The control (red curve) shows no FRET signal for a summation of individually labeled and reconstituted Rh-CY3 and Rh-CY5 measured at identical concentrations and conditions. In this example, reconstitution used 10,000 moles of asolectin lipids per mole of Rh. Except for buffer subtraction, the data have not been manipulated or normalized in any way.

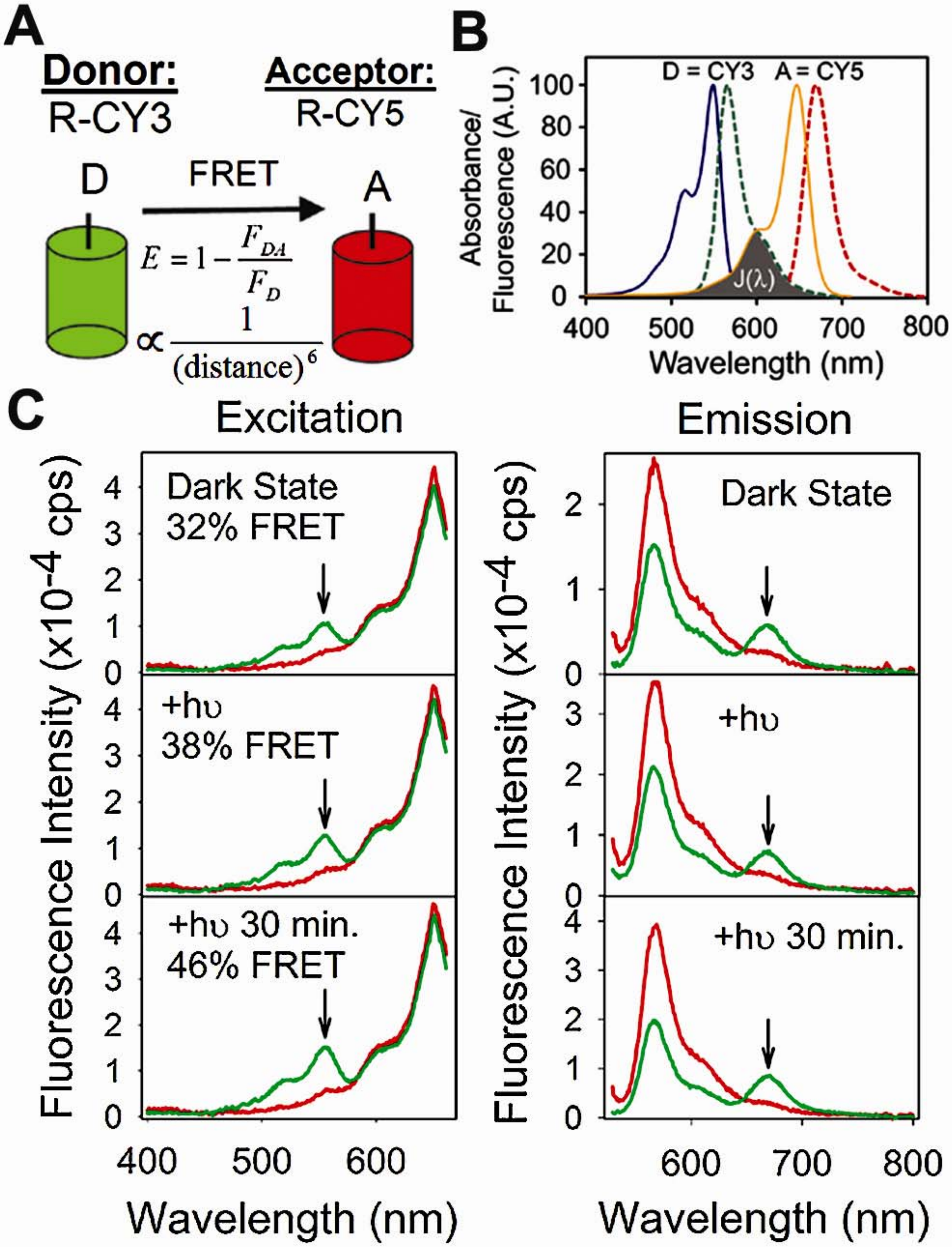
A
Donor:
R-CY3
Acceptor:
R-CY5
D
FRET
A
$E = 1 - \frac{F_{DA}}{F_D}$
$\propto \frac{1}{(\text{distance})^6}$
B
D = CY3
A = CY5
Absorbance/ Fluorescence (A.U.)
J(λ)
Wavelength (nm)
C
Excitation
Emission
Dark State
32% FRET
+hυ
38% FRET
+hυ 30 min.
46% FRET
Dark State
+hυ
+hυ 30 min.
Fluorescence Intensity (x10-4 cps)
Wavelength (nm)

Figure 4. 4: FRET Signal As a Function of Receptor Density. (A) Experimentally determined FRET efficiencies for Rh in the dark-state (DS), and after illumination (+hυ), at different predicted receptor densities (Rh/liposome). The FRET signals are well above the non-specific or "background FRET" predicted to occur due to molecular crowding with increasing receptor density (dotted lines) [263]. **(B)** Isopycnic centrifugation at the lowest receptor concentration (10,000x lipid/Rh). Open circles indicate the Rh-CY5 fluorescence and filled circles indicate the NBD-labeled lipid fluorescence. The data indicate ≈ 90% of Rh incorporates into ≈ 11% of the total liposomes. Thus, Rh-containing vesicles have ≈ 200 Rh per liposome, yielding a predicted background FRET signal of ≈ 8% in the dark state and ≈ 11% after light activation (note these values are still well below the measured FRET signals in panel A above).

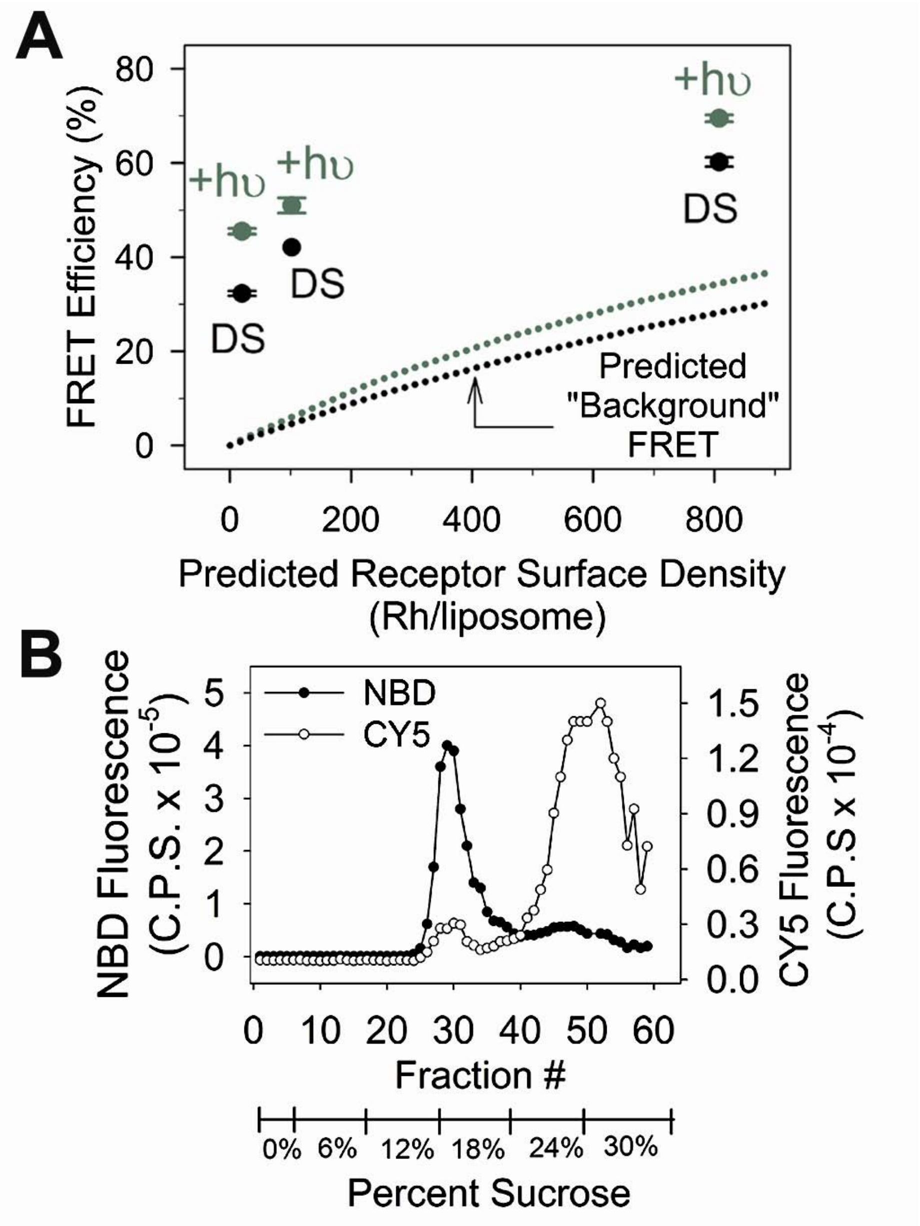

A
FRET Efficiency (%)
80
60
40
20
0
+hυ
+hυ
+hυ
DS
DS
DS
Predicted
"Background"
FRET
0
200
400
600
800
Predicted Receptor Surface Density
(Rh/liposome)
B
NBD Fluorescence
(C.P.S. x 10^{-5})
5
4
3
2
1
0
NBD
CY5
CY5 Fluorescence
(C.P.S x 10^{-4})
1.5
1.2
0.9
0.6
0.3
0.0
0
10
20
30
40
50
60
Fraction #
0%
6%
12%
18%
24%
30%
Percent Sucrose

Figure 4. 5: Rh Samples Show Near Quantitative Self-Association in Liposomes. (A) Cartoon illustrating how only half of the mixed samples can form donor, D, and acceptor, A, FRET pairs. **(B)** Plot of energy transfer efficiency as a function of distance between the Rh-CY3 and Rh-CY5 pairs. The predicted FRET efficiency for Rh-CY3:Rh-CY5 is ≈ 56 % at the ≈ 50 Å dark-state Rh-Rh distance measured by LRET. The maximum FRET for an equimolar mixture Rh-CY3 and Rh-CY5 in the dark-state is ≈ 28% (half of 56%). For light-activated Rh, the maximum possible FRET signal at the LRET distance of 47 Å is ≈ 37% (half of 74%). **(C)** The theoretical maximum and measured FRET efficiencies are nearly identical, indicating that essentially all of the Rh samples are close enough to participate in a dimeric (or other higher order) interaction. The theoretical maximum FRET efficiencies are shown in the blue bars, and the experimentally determined FRET efficiencies (corrected for the background FRET predicted in Figure 4. 4) are shown by the gray bars.

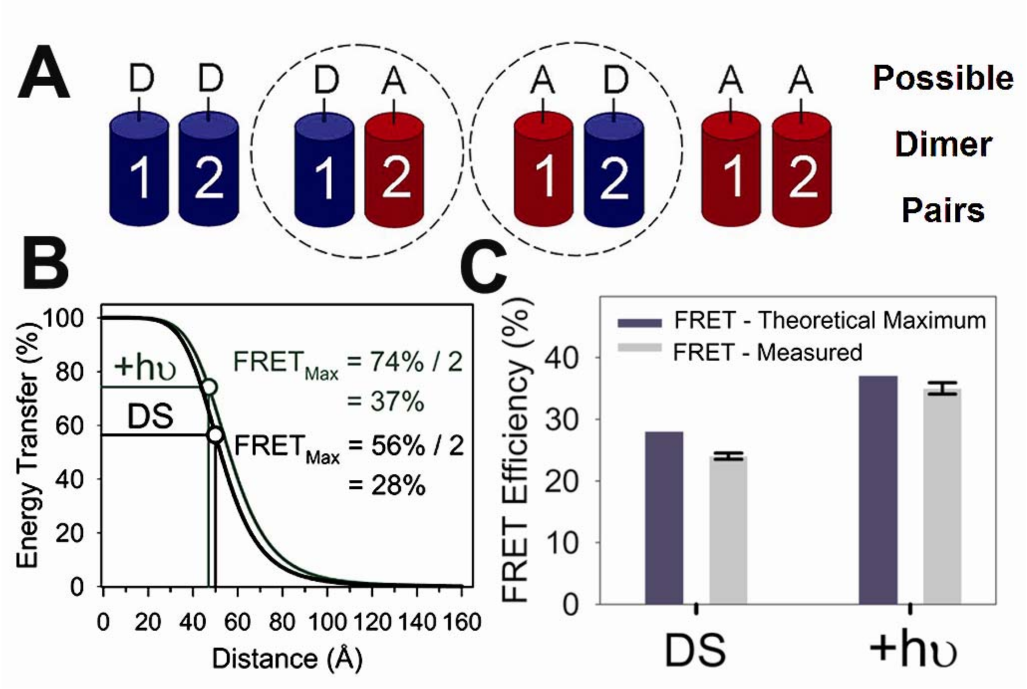
A
D
D
D
A
A
D
A
A
1
2
1
2
1
2
1
2
Possible
Dimer
Pairs
B
Energy Transfer (%)
+hυ
DS
FRET$_{Max}$ = 74% / 2
= 37%
FRET$_{Max}$ = 56% / 2
= 28%
0
20
40
60
80
100
0 20 40 60 80 100 120 140 160
Distance (Å)
C
FRET Efficiency (%)
FRET - Theoretical Maximum
FRET - Measured
0
10
20
30
40
DS
+hυ

4. 7: SUPPLEMENTAL MATERIAL

4. 7. 1: Materials.

CY3-maleimide and CY5-maleimide were purchased from Amersham Biochemicals. The Tb^{3+} chelate, CS124-DTPA-EMCH•Tb^{3+}, was purchased from Panvera. Asolectin soybean lipid was purchased from Fluka. Sephadex G15 size-exclusion beads were purchased from Sigma and 10,000 MW cut-off concentrators were purchased from Millipore. NBD-labeled Phosphatidyl Serine (NBD-PS) was purchased from Avanti Polar Lipids.

4. 7. 2: Purification of Rh.

Rod outer segment (ROS) membranes were prepared from bovine retina, as described in [42], and then 1 mL of ~ 1.0 – 2.0 mg/mL Rh in the membranes was solubilized in 10 mL of buffer B by nutating at 4 ºC in the dark for 90 min. After solubilization, the sample was centrifuged at 30,000 × *g* for 30 min. The supernatant was then removed and added to Con A beads previously equilibrated with buffer B and allowed to bind at 4 ºC for 90-120 min. Next, the binding slurry was added to a small, disposable polystyrene column. The beads, bound with protein, were then washed with 30 mL of buffer C before being eluted in buffer D (350 – 400 μL elution fractions collected after 20- to 30-min incubations). The concentration of protein in each elution fraction was determined using a Shimadzu 1601 UV/VIS spectrophotometer and an extinction coefficient for Rh of $\varepsilon_{500} = 40{,}600\ \mathrm{L{\cdot}cm^{-1}{\cdot}mol^{-1}}$ [287].

4. 7. 3: Fluorescent Labeling of Purified Rh.

Immediately after purification, Rh in buffer D was labeled overnight (~ 16 h) at 4 ºC with either CY3-maleimide or CY5-maleimide (at a 7-fold molar excess) or the CS-

124-DTPA-EMCH•Tb^{3+} (at a 1.5-fold molar excess). Free label was removed by concentrating the solutions to 100 μL using a Millipore 10,000 molecular weight cut-off concentrator and then passing the solutions over a Sephadex G15 size-exclusion column previously equilibrated with buffer C. This procedure was repeated three to four times on each sample to ensure complete removal of free label. The fluorophore labeling efficiency for each sample was determined by diluting an aliquot of sample into buffer C containing 50 mM hydroxylamine and then taking the absorption spectrum before and after photo-bleaching using a 150-watt light source from a Techni-Quip Corporation filtered through a > 500-nm long pass filter. The Rh concentration was determined by subtracting the dark state spectrum from the light-activated spectrum to give a difference spectrum. Fluorophore concentrations were calculated from the bleached spectrum using extinction coefficients of $\varepsilon_{554} = 150{,}000\ L\cdot cm^{-1}\cdot mol^{-1}$ for CY3-maleimide, $\varepsilon_{652} = 250{,}000\ L\cdot cm^{-1}\cdot mol^{-1}$ for CY5-maleimide, and $\varepsilon_{343} = 10{,}560\ L\cdot cm^{-1}\cdot mol^{-1}$ for CS-124-DTPA-EMCH.

4. 7. 4: V8 Proteolysis of Fluorescently Labeled Rh to Assess Labeling Stoichiometry.

Fluorescently labeled Rh was incubated in the dark at room temperature with V8 protease at a V8:Rh molar ratio of 1:30. After incubating for 1.5 h, additional V8 was added to bring the V8:Rh ratio to 1:15 and the reaction was allowed to proceed for an additional 1.5 h. Following incubation, the reactions were analyzed by SDS-PAGE. The fluorescent fragments, F1 (~27 kDa containing Cysteine 140) and F2 (~13 kDa containing Cysteine 316) [41], were visualized using an Alpha Innotech FluorChem 5500 imaging system.

4. 7. 5: Reconstitution of Labeled, Purified Rh.

Reconstitution of Rh into asolectin liposomes was performed in the dark under dim red light, following a previously published protocol [259] Reconstitution was carried out by first incubating together equal moles of protein samples for ~ 16 h at 4 °C in buffer C according to the following scheme: (1) donor-labeled Rh with equimolar unlabeled Rh, (2) acceptor-labeled Rh with equimolar unlabeled Rh, (3) donor-labeled Rh with equimolar acceptor-labeled Rh, and (4) buffer only – reconstituted lipid but no protein. Importantly, all the reconstitutions were set up such that equal molar total protein was used in each of the above conditions.

After 16 h, the reconstitution procedure was continued by the addition of a defined amount of asolectin lipid. This involved adding the appropriate volume of buffer A containing 1 mg/ml asolectin lipids (MW ~ 760 g/mol) plus 1.46% OG such that the molar ratio of asolectin/Rh was 250:1, 2000:1, or 10,000:1. These lipid/protein ratios should theoretically produce ~ 800, 100 and 20 total Rh proteins per liposome, or dark-state reduced acceptor surface density (C_A) values of 0.156, 0.020, and 0.0039, and light activated C_A values of 0.180, 0.023, and 0.0045, respectively. By keeping the amount of lipid at 1 mg/ml in 1.46% OG and altering the volume of this lipid/detergent solution added to the protein, the lipid/protein ratio was altered without changing the lipid/detergent ratio during the reconstitution procedure. The samples were then dialyzed for 36-48 h against buffer A (~1, 000 fold volume excess) at 4 ºC in the dark with buffer exchanges every 6-8 h. The proteoliposome suspensions were then pelleted at 140,000 ×

g for 60 min at 4 ºC and resuspended in buffer A for experiments and storage in the dark at 4 ºC.

4. 7. 6: Electron Microscopy of Asolectin Proteoliposomes.

Proteoliposomes were lifted onto carbon-coated copper grids for 1 minute, wicked, rinsed in water for 1 minute, wicked, stained 1 min in 1.33% uranyl acetate, wicked and dried. Samples were imaged at 100 kV on a Philips CM120/Biotwin transmission electron microscope (EM) at magnifications of ×11,000 to ×37,000 and photographed on a Gatan 794 charge-coupled device (CCD) multiscan camera at 0.524-1.76 nm/pixel. Images in Gatan DM3 format were converted to TIFF format with GATAN DIGITAL MICROGRAPH software.

4. 7. 7: Orientation of Rhodopsin in Liposomes as Determined by Proteolysis.

The orientation of the receptor in the liposome was determined using the endoprotease Asp-N [259], which specifically cleaves between Gly-329 and Asp-330 in the C-terminus of rhodopsin [278]. Briefly, 1.5 μgram of each rhodopsin sample in 10 μL was combined with Asp-N at a molar ratio of 1:4 (Asp-N/rhodopsin) in the dark at room temperature for 4 h. The reaction was stopped by the addition of SDS/PAGE loading buffer and the samples then subjected to SDS/PAGE. The resultant fragments were analyzed both by fluorescence imaging of the CY3 label and by Coomassie stain using an Alpha Innotech FluorChem 5500 imager. Unfortunately, the FluorChem 5500 was unable to image CY5 fluorescence.

4. 7. 8: Determination of the Quantum Yield of Rh-CY3 Donor and R$_0$ Value for CY3-CY5 FRET Pair.

The quantum yield for reconstituted Rh-CY3 in the dark state and following light-activation was measured using the following relation [64,288]:

$$\Phi_x = \Phi_{st} \times \frac{F_x}{F_{st}} \times \frac{OD_{st}}{OD_x} \qquad \text{[Eq. 4. S1]}$$

where subscripts *st* and *x* refer to the standard and unknown solutions, respectively, Φ is the quantum yield, F is the relative integrated fluorescence intensity, and OD is the optical density at the exciting wavelength. Rhodamine-6-G (quantum yield equal to 0.94 in ethanol; ref [69]) was chosen as the standard. Emission spectra were performed at 22 °C using 520 nm excitation (1/4 nm bandpass) while collecting from 529-800 nm (8 nm bandpass). The buffer intensity was subtracted from each sample and from the standard before integration.

The R$_0$ value for the CY3-CY5 FRET pair was calculated using the relationship:

$$R_0 = [8.8x10^{23} \times \mathrm{K}^2 \times n^{-4} \times \Phi_D \times J(\lambda)]^{1/6}\,\text{Å} \qquad \text{[Eq. 4. S2]}$$

where K^2 is the orientation factor (equal to 2/3), n is the refractive index (equal to 1.3), Φ_D is the quantum yield of the donor, and J(λ) is the spectral overlap integral between the emission spectrum of Rh-CY3 and the absorbance spectrum of Rh-CY5.

4. 7. 9: Rhodopsin Function Assessed by Transducin Activation Assays.

The final reaction mixture contained 10 mM Tris·HCl (pH 7.5), 0.1 M NaCl, 5 mM $MgCl_2$, 0.1 mM EDTA, 1 mM DTT, ~ 275 pmole transducin, 0.5 pmol of rhodopsin, and 4.5 μM $[^{35}S]GTP[\gamma S]$ (32 nCi/mol). The samples were assayed as follows. $[^{35}S]GTP[\gamma S]$ was added in the dark at room temperature, then the samples were exposed to yellow light for 30 s, and 10 μL aliquots subsequently removed at different time points, spotted onto filter paper in a modified Brandell M-24 cell harvester and washed 3 times with 4 mL of transducin assay buffer. Each filter paper was then removed and assayed for $[^{35}S]GTP[\gamma S]$ content bound to transducin. As a negative control, two dark state time points were assayed for $[^{35}S]GTP[\gamma S]$ content – one immediately before light activation and one after the last light-state time point.

4. 7. 10: Isopycnic Density Centrifugation.

Rh was analyzed by isopycnic density centrifugation using purified Rh, labeled with CY3- and CY5-, and reconstituted into asolectin liposomes which have been supplemented with NBD-labeled Phosphatidyl Serine (0.4% of the total lipid content) to enable fluorescent monitoring of the lipid fractions. After reconstitution, proteoliposomes were subjected to discontinuous flotation gradients in the absence of light, using a slight modification from a previously published protocol [261].

Briefly, this procedure involved mixing 250 μL of the proteoliposome mixture (described above) with 3.0 mL of 60% sucrose (wt/wt) in buffer A and 2.75 mL of buffer A supplemented with 0.05% Triton X-100. The resulting 6 mL solution of proteoliposomes in 30% sucrose was added to the bottom of a 35 mL centrifuge tube. Subsequently, 6 mL each of 24%, 18%, 12%, and 6% sucrose (wt/wt) in buffer A were successively layered onto the sample, followed by 3 mL of buffer A, and the discontinuous gradients were then centrifuged overnight at 110,000 × *g* in a Beckman SW 28 rotor. Fractions were collected in the dark in 550 μL aliquots from the top of the gradient down to the bottom and analyzed for rhodopsin and lipid content. Rh content was assessed by following the CY5 fluorescence emission (650 nm excitation; emission collected from 656-800 nm). Lipid content was determined following NBD fluorescence (360 nm excitation; emission measured from 366-800 nm).

4. 7. 11: Measurement of the Rate of Lanthanide Resonance Energy Transfer (LRET) Between Labeled Rh Samples in Asolectin Proteolipsomes.

LRET studies were performed on 1 μM of Rh-Tb (donor) and Rh-CY3 (acceptor) reconstituted in asolectin liposomes at 10,000 lipids per Rh. The measurements were made on a PTI LaserStrobe phosphorescence lifetime system, exciting the samples with a 337 nm laser pulse. The emission was either monitored at 545 nm (10 nm bandpass), to obtain the lifetime of the donor alone (τ_D) when Rh-Tb and unlabeled Rh were reconstituted together, or at 570 nm (10 nm bandpass), to obtain the sensitized emission lifetime (τ_{AD}) of Rh-CY3 when both Rh-Tb and Rh-CY3 were reconstituted together. To reduce light scatter from the liposomes, a 298-435 nm bandpass filter was also used on the excitation beam and three > 500 nm longpass filters were used with the emission monochromator. Measurements were performed at 22 ºC. Each data point represents two averages of five laser shots collected linearly in time over 350 total channels. To eliminate possible artifacts due to tube ringing after the laser pulse [289], the first 75 μsec of the decay after the peak channel of the instrument response function was excluded from the data analysis. This treatment only improved the quality of the fits and did not substantially affect the resulting calculated lifetimes.

4. 7. 12: Steady-State Fluorescence Measurements for FRET Measured in Asolectin Proteoliposomes.

Before FRET measurements, four samples were set up to incubate at room temperature overnight (~16 h): one containing donor-labeled Rh reconstituted with unlabeled Rh, one containing acceptor-labeled Rh reconstituted with unlabeled Rh, one containing donor-labeled Rh reconstituted with acceptor-labeled Rh, and finally a control sample containing only liposomes (no protein).

The FRET measurements, performed on 1 μM reconstituted Rh at 22 ºC, compared the individual emission and excitation spectra from separately reconstituted Rh-CY3 and Rh-CY5 to the spectra where Rh-CY3 and Rh-CY5 were mixed together before reconstitution. The amount of FRET was measured for each sample in two ways. First, the emission spectrum of the acceptor was monitored while exciting the donor, and then the excitation spectrum of the donor was measured while collecting emission from the acceptor. Emission spectra were measured by exciting the donor at 520 nm (1/4 nm bandpass) while scanning the fluorescence intensity of the acceptor from 529-800 nm (8 nm bandpass). The excitation spectra were performed by collecting emission from the acceptor at 670 nm (8 nm bandpass) while scanning the excitation spectrum of the donor from 400-661 nm (1/4 nm bandpass). All measurements were performed in the dark state, immediately after light activation, and 30 min after light activation using a step size of 1 nm, 0.2 second integration time, and 2 averages. Under these conditions, Rh was found to undergo less than 5% bleaching (as measured by following the loss of absorbance at 500 nm).

4. 7. 13: Fluorescence Lifetime Measurements of FRET Efficiency Measured in Asolectin Liposomes.

Fluorescence lifetimes of the fluorescently labeled Rh samples reconstituted at the lowest receptor density were measured using a PTI LaserStrobe fluorescence lifetime instrument. Measurements used magic angle conditions (vertically polarized excitation and an emission polarizer oriented 54.7° from the vertical [69]), and 520 nm excitation pulses (fwhm ~ 1.5 ns), while monitoring the emission with a monochromator at 580 nm (20 nm bandpass) and 3 longpass filters (> 550 nm). Measurements used 100 μL of 1 μM reconstituted samples and represent two averages of five laser shots per channel, collected in an arithmetic progression over 100 channels. The instrument response function (IRF) was determined by measuring scatter from a solution of Ludox. The measurements were performed at 22 ºC in the dark state, immediately after light activation, and 30 min after light activation. Under these conditions, Rh was found to undergo less than 15% bleaching (as measured by following the loss of absorbance at 500 nm).

4. 7. 14: Steady-State Anisotropy Measurements.

The steady-state fluorescence anisotropy (r) of the labeled Rh samples reconstituted into liposomes was measured using the PTI steady-state fluorometer, and the data analyzed as:

$$r = \frac{I\| - GI_{\perp}}{I\| + 2\mathrm{GI}_{\perp}} \qquad \text{[Eq. 4. S3]}$$

where $I_{\parallel}$ and $I_{\perp}$ refer to the intensity of fluorescence emission parallel and perpendicular to the plane of excitation light, respectively. The G-factor was determined before measuring the anisotropy of each sample to correct for any bias in the monochromator.

Anisotropy measurements of Rh-CY3 used 520 nm excitation (2 nm bandpass) and emission collected at 570 nm (8 nm bandpass). The anisotropy of Rh-CY5 used excitation at 650 nm (2 nm bandpass) and emission collected at 670 nm (8 nm bandpass). Anisotropy measurements were performed on 1 μM samples at 22 ºC in the dark state, immediately after light activation and 30 min after light activation. The measurements at each time point were done in duplicate and the average steady-state anisotropies were recorded.

4. 7. 15: Anisotropy Correction of LRET Distance Measurements.

The error in FRET and LRET measurements associated with changes in κ^2, the orientation factor, were calculated from the maximum and minimum range of κ^2 using the following equations [184,290]:

$$\kappa^2{}_{\max} = \frac{2}{3}(1 + 2.5A_d + 2.5A_a) \qquad \text{[Eq. 4. S4]}$$

$$\kappa^2{}_{\min} = \frac{2}{3}\left(1 - \frac{2.5A_d + 2.5A_a}{2}\right) \qquad \text{[Eq. 4. S5]}$$

where A_d is the anisotropy of the donor and A_a is the anisotropy of the acceptor, measured as described above. For the LRET experiments, the anisotropy of the terbium is $A_d = 0$ [184]. The complete list of anisotropy values can be found in Table 4. S1. It is important to note that because these errors are the absolute extreme values that arise only if the fluorophore dipoles are all oriented at fixed, perpendicular angles relative to one another, the actual errors are likely much less significant [184].

4. 7. 16: Determination of FRET Efficiency.

FRET efficiency was determined by assessing the extent of sensitized emission from the excitation spectra using the following equation [78,273]:

$$E = \left[\frac{G(\lambda_2)}{G(\lambda_1)} - \frac{\varepsilon_A(\lambda_2)}{\varepsilon_A(\lambda_1)} \right] \times \frac{\varepsilon_A(\lambda_1)}{\varepsilon_D(\lambda_2)} \qquad \text{[Eq. 4. S6]}$$

The acceptor excitation spectra (G) and the extinction coefficients (ε) were used to choose λ_1 (650 nm), where the donor (D) has minimal absorption, and λ_2 (554 nm), where the extinction coefficient of the donor is large relative to that of the acceptor (A) [78,273]. The extinction coefficients used for the donor and acceptor fluorophores at the chosen wavelengths were $\varepsilon_A(\lambda_2)$ = 18, 243 $\mathrm{Lcm^{-1}mol^{-1}}$, $\varepsilon_A(\lambda_1)$ = 247, 766 $\mathrm{Lcm^{-1}mol^{-1}}$, and $\varepsilon_D(\lambda_2)$ = 150, 000 $\mathrm{Lcm^{-1}mol^{-1}}$, determined from the absorbance spectra of Rh-CY3 and Rh-CY5.

The FRET efficiency was also determined from the fluorescence lifetimes of the donor (Rh-CY3) in the presence and absence of the acceptor (Rh-CY5) using the following equation:

$$E = 1 - \frac{\tau_{DA}}{\tau_D} \qquad \text{[Eq. 4. S7]}$$

where τ_D is the lifetime of the donor in the absence of the acceptor and τ_{DA} is the lifetime of the donor in the presence of the acceptor [78].

Table 4. S1: Fluorescence Lifetimes and Anisotropy Measurements of Rh-CY3 and Rh-CY5 Reconstituted into Asolectin Liposomes.[a]

Sample	**Time Point**	**Lifetime (ns) ± SEM**	**Anisotropy ± S.D.**
Rh-Cy3	Dark State	0.82 ± 0.04	0.235 ± 0.005
	+hυ, 0 min.	0.92 ± 0.03	0.241 ± 0.001
	+hυ, 30 min.	0.94 ± 0.04	0.230 ± 0.002
Rh-Cy5	Dark State	1.42 ± 0.01	0.234 ± 0.002
	+hυ, 0 min.	1.44 ± 0.03	0.240 ± 0.001
	+hυ, 30 min.	---	0.221 ± 0.001
Rh-CY3 and Rh-CY5	Dark State	0.62 ± 0.03	N/A
	+hυ, 0 min.	0.73 ± 0.02	N/A
	+hυ, 30 min.	0.63 ± 0.01	N/A

[a] Measurements were carried out as described in Supplemental Section **4. 7**.

Figure 4. S1: Outline of Experimental Approach. (A) LRET experiments are carried out to determine the distance between Rh molecules in the liposome. This distance is then used in conjunction with FRET measurements to determine the total amount of interacting Rh samples. **(B)** Structure of the donor label (terbium chelate) used for the LRET studies (CS-124-DTPA-EMCH·Tb^{+3}) **(C)** Structures of the donor and acceptor fluorophores used in the FRET studies (CY3-maleimide (donor) and CY5-maleimide (acceptor)).

A **General Scheme:**

- Purify and label rhodopsin
- Reconstitute into liposomes
- Measure:
  - LRET: distance between rhodopsins
  - FRET: fraction rhodopsin dimers

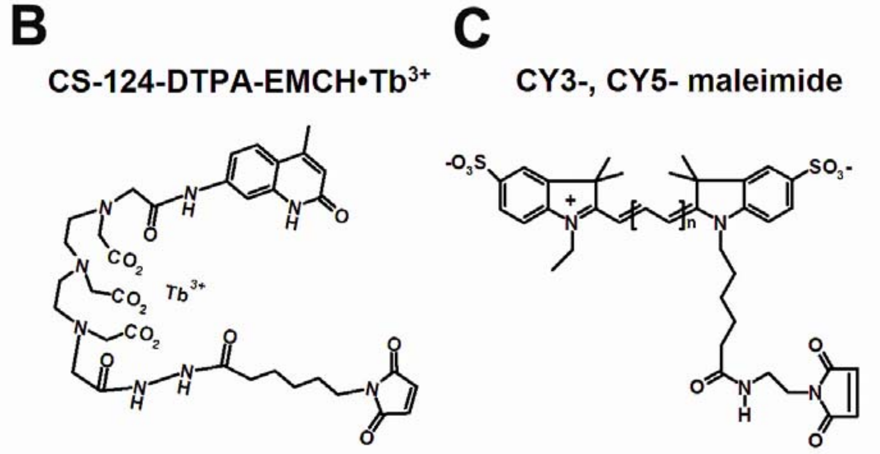

Chapter 5

Summary and Conclusions

5. 1: Overview.

In this dissertation, I have described three novel developments and applications. First, in Chapter 2, I describe how I re-discovered a fluorescence phenomenon and then developed it into a novel technique to measure short-range distances (~ 5 - 15 Å) in proteins. This method, which exploits the distance-dependent quenching of bimane fluorescence by proximal tryptophan residues, has recently been successfully used to study protein/protein interactions [45,172,173], as well as measure real-time conformational changes in membrane proteins [40,171]. Then, in Chapter 3, I determined that this approach, employing a thiol-cleavable fluorophore, PDT-Bimane, can be used to assess protein structure by site directed fluorescence labeling (SDFL). PDT-Bimane shows all of the solvent-sensitive characteristics of bimane, as well as the susceptibility to quenching by proximal Trp residues. Furthermore, the reducible nature of the PDT-Bimane linkage resolves problems often faced in SDFL experiments: ensuring specific labeling of cysteine residues, determining the extent of free label contamination, and accurately determining labeling efficiency even at low sample concentrations. Additionally, the ability to cleave PDT-Bimane off the protein enables rapid determination of these parameters, and positions it as an ideal fluorophore for automated, high-throughput SDFL structural studies. Finally, in Chapter 4, I employed a novel combination of SDFL and resonance energy transfer methodologies to assess the oligomerization state of visual rhodopsin in a membrane environment, a topic that is currently undergoing intense debate in the field. Below, I have summarized these subjects in further detail.

5. 2: Summary of Chapter 2: The Specific Quenching of Bimane Fluorescence by Proximal Tryptophan Residues Can be Used to Map Proximity Within Proteins.

My studies indicate that the fluorescence of the bimane label, even when attached to a cysteine residue in the sequence of a full-length protein, is quenched by neighboring Trp residues [170]. Of all the amino acids, only Trp (and to a lesser extent, tyrosine) affects bimane's fluorescence [192]. Specifically, a proximal Trp residue can decrease bimane fluorescence intensity by up to 500% , shorten the fluorescence lifetime (τ) of the label, and induce complicated fluorescence decay kinetics. Replacing the Trp residues with a phenylalanine substitution removes these spectral perturbations. Thus, by using the intrinsic tryptophan residues in a protein or by selectively introducing tryptophans, three-dimensional insight into the spatial organization of the protein can be determined [170].

5. 2A : Trp Quenching of Bimane Fluorescence Reports Short-Range Distances Within Proteins. The Trp/bimane quenching technique is complementary to FRET, as it reflects local, short-range distances (~ 5 – 15 Å) that are difficult to measure with the typically longer range (~ 20 – 100 Å) FRET techniques. Importantly, my studies showed that a reliable assessment of the proximity between the Trp/bimane pair could be achieved by comparing the amount of quenching in the steady-state fluorescence intensity data to the amount of quenching in the fluorescence lifetime data. In this way, distances between Trp/bimane pairs can be categorized as "not close" (> 15 Å), "close" (~ 10 - 15 Å), or "very close" (~ 5 - 10 Å). By categorizing the data in this manner, structural distance constraints can be assigned to the three-dimensional packing of the protein being studied.

5. 2B Trp Quenching of Bimane Fluorescence Can be Used to Study Protein/Protein Interactions and Measure Real-Time Conformational Changes in Membrane Proteins. The ability to monitor the fluorescent properties of a bimane label as it moves toward or away from a Trp residue provides a powerful tool to measure dynamic changes in real time. As we anticipated in our original manuscript [170], this methodology has been shown to be useful for studying protein/protein interactions and conformational changes in proteins by a number of laboratories. Four such studies are discussed below.

Using Trp/Bimane Quenching to Study Protein/Protein Interactions. In 2004, Janz and Farrens used the Trp/bimane technique to examine the light-dependent protein/protein interaction between visual rhodopsin and its G-protein, transducin [45], to determine the critical sites in rhodopsin that mediate G-protein binding upon photo-activation. They partially mapped the interaction by labeling rhodopsin mutants with the bimane probe and assessing how binding of a C-terminal peptide analog of the transducin α-subunit, $G_{T\alpha}$, affects fluorescence. They introduced a Trp residue into the peptide analog enabling them to ascertain which bimane-labeled sites on rhodopsin were within contact distance to the Trp residue in the peptide, and thus would display quenching upon peptide binding. This methodology demonstrated that the key interaction occurs between the C-terminus of $G_{T\alpha}$ and a hydrophobic cleft formed on the inner face of TM VI of rhodopsin, exposed during receptor activation. Their strategy is shown in Figure 5. 1A.

Tapley and Vickery used site-directed fluorescence labeling and Trp/bimane quenching to examine the interaction of HscA, a specialized bacterial hsp70-class chaperone protein, with an iron-sulfur cluster assembly protein, IscU [172]. Of interest was whether recognition of and binding to a conserved LPPVK sequence motif in the target occurs in a preferred orientation. HscA was selectively labeled with bimane on opposite ends of its substrate binding domain and the degree of quenching achieved with LPPVK-containing peptides having a tryptophan introduced at the N- or C-terminus was measured. Their results showed quenching was highly dependent on the position of tryptophan in the peptide and the location of bimane on HscA, implying a strong directional preference for peptide binding. The same technique was also used to study the preferential binding of DnaK to its targets [173].

Using Trp/Bimane Quenching to Measure Conformational Changes Within a Protein. Recently, Islas and Zagotta investigated the dynamic structural changes in the cyclic nucleotide-gated ion channel (CNGA1) upon activation. To do this, they simultaneously monitored channel function and Trp/bimane quenching, thus enabling them to correlate dynamic short-range changes in structure that occur upon nucleotide binding and channel activation. Their results show that the allosteric transition that leads to opening of the channel, induced by binding of cyclic nucleotide, involved a movement of the carboxy terminus of the channel. The motion was detected via a decrease in fluorescence intensity of a bimane label at C481 in the C-terminus of the channel as it moved toward a tryptophan residue at A461C. Their manuscript concludes with the following statement, "…tryptophan quenching of bimane fluorescence offers great hope for elucidating the rearrangements and dynamics of gating conformational changes in ion channels. This approach should prove generally useful for probing short-range interactions in proteins…"[171].

The Kobilka laboratory recently used the Trp/bimane quenching approach to investigate a key conformational change thought to be involved in GPCR activation. Specifically, they assessed if disruption of an “ionic lock” formed between residues at the cytoplasmic ends of TM VI and TM III is required for full receptor activation [40]. [See section **1. 1. 5** of Chapter 1 for a description of the “ionic lock”]. The goal of these studies was to assess the effects that different classes of ligands have on the stability of the “ionic lock” in the β_2-andrenergic receptor. To do this, a modified receptor with a bimane covalently attached to a residue in TM VI and a Trp residue in TM III was generated, using sites strategically chosen to monitor potential movements between the ends of these helices.

As can be seen in Figure 5. 1B (left), A271C and I135W are separated by the “ionic lock” in a model of the inactive β_2-adrenergic receptor. Because the “ionic lock” residues physically separate the fluorophore (bimane at site A271C) from the quencher (Trp at site I135W) in the inactive state, no quenching of bimane fluorescence can occur in the inactive receptor. Their studies show that activation of the β_2-adrenergic receptor results in a decrease in bimane quenching, consistent with movement of TM VI relative to TM III and breaking of the “ionic lock” (see Figure 5.1B, right). This movement is also consistent with previous studies of rhodopsin [41,42,52]. No quenching was observed upon antagonist binding (as their model predicted). Interestingly, quenching of the same magnitude was observed for <u>partial</u> agonists as for <u>full</u> agonists, suggesting that partial agonists are just as effective as full agonists at disrupting the “ionic lock”. From these results, it was postulated that disruption of the “ionic lock” is necessary, but not sufficient, for full activation of the β_2-adrenergic receptor, and thus, additional conformational changes in the receptor must occur to confer full activation over partial activation. Further understanding these changes in receptor structure may prove key to improve rational drug design of GPCR targets, allowing for better control of both ligand potency and efficacy.

5. 2C: Proposed Mechanism of Trp/Bimane Quenching. Kosower (who first synthesized bimane in the 1980s) showed bimane is sensitive to quenching by electron-donating groups (including Trp residues) both free in solution and when attached to small peptides [208,212]. Based on Kosower's earlier work, the likely mechanism by which Trp residues quench bimane fluorescence is through photo-induced electron transfer (PET). A PET mechanism would suggest quenching occurs when an electron transfers from the Trp residue to a proximal excited-state bimane fluorophore, producing a transient radical ion pair: Trp (+ ·):Bim(− ·). Reverse electron transfer back to the Trp residue subsequently returns bimane to the ground state (S_0) in a radiationless manner. When the two molecules are close together, the electron transfer rates start to approach the fluorescence lifetime rates, and the net effect is fluorescence quenching.

Note that electron transfer induced fluorescence quenching is not unique to the bimane fluorophore. Photo-induced electron transfer (PET) is a general phenomenon. The theory for PET was developed in the 1950s by Dr. Rudolph Marcus (for which he was awarded the 1992 Nobel Prize in Chemistry). Subsequent to our initial demonstration that Trp quenching of bimane fluorescence can be used to study protein structure, a number of other reports have observed similar electron transfer events from a Trp residue to various organic dyes [291-293]. These studies are primarily interested in using this phenomenon for probing molecular recognition and conformational dynamics of biopolymers such as

DNA. Appendix I reports calibration studies I have performed on T4 lysozyme using a number of additional fluorophores, each with spectral or physical properties unique from bimane.

Although my work has primarily focused on the use of bimane quenching by proximal Trp residues, it is the general phenomenon of photo-induced electron transfer (using Trp residues as the quencher) that will prove useful for protein structural studies, regardless of which fluorophore is used. However, for protein studies, it will be important to calibrate each Trp/fluorophore pair before making conclusions that correlate the amount of quenching observed to distances between the two molecules. Although photo-induced electron transfer requires close proximity and perhaps even van der Waals contact between dye and quencher, the rates (and thus the amounts of quenching observed) are known to be dependent on variables such as solvent polarity of protein surfaces [216], steric and stereochemical factors [217], and shape and relative orientation of the two molecule pairs [218]. Thus, properties of the fluorophore (such as size, shape, and conformational flexibility) can alter the relationship between quenching and distance. At this time, only the bimane fluorophore has been extensively calibrated and published on a protein of known structure [170,294], although Appendix 1 describes my work calibrating several other fluorophores.

5. 3: Summary of Chapter 3: PDT-Bimane is Ideal for High-Throughput Protein Structure Determination.

In Chapter 3 of this dissertation, I performed a complete SDFL calibration on T4 lysozyme using the thiol-cleavable fluorophore, PDT-Bimane. My studies showed that, similar to monobromobimane, PDT-Bimane can be used as a labeling reagent to map both protein secondary and tertiary structural information. Specifically, solvent accessibility and local regions of protein secondary structure can be assessed by monitoring shifts in the probe's emission λ_{max} values and changes in the steady-state anisotropy values. A plot of these data as a function of residue number reflects the periodic nature of the helix-turn-helix motif studied. Further, the fluorescence of PDT-Bimane is dramatically quenched by proximal tryptophan residues, as with monobromobimane, in a distance-dependent manner, allowing the study of tertiary structure. Most importantly, the nature of PDT-Bimane's disulfide bond attachment to the protein provides it a number of advantages that position it as an ideal fluorophore for use in automated, high-throughput protein structural analyses. These advantages are briefly described below.

PDT-Bimane Ensures Specific Labeling of Cysteine Residues. Because PDT-Bimane reacts with proteins through formation of a disulfide bond, it only reacts with cysteine residues. This ensures that the fluorophore does not attach to any other reactive residues in the protein which can happen to non-thiol specific probes (including monobromobimane) under unusual circumstances (see reference [250] for an example).

PDT-Bimane Allows for Accurate Determination of Labeling Efficiency and Quantitation of Free Label Contamination Even at Low Sample Concentrations. I found the ability of PDT-Bimane to be reduced off the protein can be exploited to determine both the total amount of bimane label and the amount of free, unattached label present in the sample. Both of these pieces of information are important to ensure high quality data in any SDFL study.

The Reducible Nature of PDT-Bimane Allows Automation of SDFL Procedures. The ability to reduce PDT-Bimane off the sample affords one critically important advantage: it offers a universal reference state to which all the data can be compared. Essentially, each sample has its own built-in control - one can simply compare the fluorescence signal of each labeled sample to the fluorescence signal after the label has been reduced off the protein. Because these comparisons can be fully automated, we propose that PDT-Bimane is ideal for high-throughput SDFL structural studies.

5. 4: Summary of Chapter 4: Site-Directed Fluorescence Labeling Studies Indicate Visual Rhodopsin Can Exist in a Membrane Environment as an Oligomer.

As discussed in the Introduction, a major question in G-protein coupled receptor signaling concerns the quaternary structure required for signal transduction and whether these transmembrane receptors function as monomers or dimers. Although it is now generally assumed many ligand-binding GPCRs exist as higher order oligomers, the amount of unassailable, physical data upon which this conclusion is based are limited. Further, the conclusions about self-association of visual rhodopsin, the most studied and best structurally characterized GPCR, have been questioned [129,155]. Thus, as described in Chapter 4, I investigated whether visual rhodopsin associates into higher order oligomers by purifying rhodopsin from its native membrane environment, attaching combinations of fluorophores to specific residues in the protein, reconstituting the labeled protein into liposomes at low receptor densities, and assessing whether the receptor prefers to associate into higher order oligomers using energy transfer approaches [295].

My luminescence resonance energy transfer (LRET) measurements revealed that the reconstituted receptors were within 47 - 50 Å of each other, consistent with the diameter of rhodopsin. By comparing the average distance measured by these LRET experiments to the size of the signal obtained by subsequent FRET studies, I calculated that > 90% of the proteins were associated as oligomers. This was true both in the dark state and following light activation. Importantly, my work included a number of controls to assure the apparent association was not due to trivial reasons, such as molecular crowding or inverted dimers.

Implications of Rhodopsin/Rhodopsin Interactions. With a concentration as high as 3 mM in the membrane, rhodopsin constitutes the majority of volume of the rod outer segment [118]. Further, only ~ 65 phospholipids solvate each rhodopsin molecule [118]. Thus, a complete absence of any rhodopsin/rhodopsin interactions at such high receptor concentrations would necessarily require an extremely low affinity between rhodopsin molecules, a possibility that is not supported by our results or the results of an earlier reconstitution study performed by Borochov-Neori *et al.* in the early 1980s [296].

Various models have been proposed in which rhodopsin functions as a dimer. For example, the cytoplasmic surface area of rhodopsin is too small to cover all the regions of transducin known to be critical for interaction with the receptor. In fact, one transducin molecule is large enough to accommodate the docking of four rhodopsin molecules [118]. Additionally, a dimer of rhodopsin can provide a platform that can anchor both the α- and β/γ-subunits of transducin (see Figure 5. 2A), which might help explain the cooperativity reported for this interaction (Hill coefficient of ~ 2) [128].

Similarly, arrestin, a protein involved in attenuating rhodopsin signaling by binding to activated rhodopsin and physically preventing its association with transducin, also has a structure compatible with a rhodopsin dimer. Crystal structures of arrestin show a bilobed protein with two concave surfaces [284,285], both surfaces of which have been demonstrated to be involved in the rhodopsin/arrestin interaction [286]. Strikingly, the two concave grooves can physically accommodate two molecules of rhodopsin, as shown in Figure 5. 2B. Although such docking/modeling studies certainly do not prove a dimeric nature of rhodopsin, they highlight the potential importance of the results described in Chapter 4.

The specific reasons for why rhodopsin may function as a dimer have not been addressed in this dissertation, as they are still speculative. However, as has been discussed elsewhere [118,253], it is clear a dimeric state may have a profound impact on the kinetics of activation, signaling through transducin, and desensitization through arrestin.

5. 5: Future Studies.

Site-Directed Fluorescence Labeling. My results leave room for a number of follow-up experiments. While my studies first identified bimane as an excellent fluorescent probe for SDFL studies, other fluorescent probes may be better suited for different experimental reasons. Some of these are discussed in Appendix 1. For example, it may be advantageous to use a fluorescent label with a positive or negative charge in a protein in order to preserve protein function and structural integrity. Alternatively, a bigger fluorescent probe that has a longer, more flexible linker attachment to the protein would display a broader range of Trp quenching than bimane at any given distance. Although this might not be ideal for measuring short-range distances within a protein or for studying conformational changes, it would be better suited for studying interactions between two proteins where a strong, binary quenching signal would suffice. It would be worthwhile to have a whole set of fluorophores calibrated on T4 lysozyme so that any one of them can be chosen for use in the appropriate SDFL study. I have calibrated a number of additional fluorophores, the results of which are outlined in Appendix 1.

Additionally, we have demonstrated through our calibration studies on T4 lysozyme that SDFL is a valid tool for identifying protein secondary and tertiary structure in proteins. Prior to my work, the most prominent SDFL studies to date have been performed by London's laboratory, which primarily focused on studying membrane protein insertion and identifying membrane/water interfaces [74,76,297]. It seems likely that the next logical step will be the application of SDFL techniques to address secondary and tertiary structural questions for proteins that are refractory to X-ray Crystallography and NMR spectroscopy, since similar site-directed spin labeling (SDSL) studies have had success in this type of *de novo* structure determination [188,252,298-301]. Based on the promising results of my calibration studies described here, it seems likely SDFL will succeed in this area as well.

GPCR Oligomerization. Although the results from this dissertation clearly indicate that rhodopsin can self-associate in a membrane environment, it still leaves a major question unanswered. What is the stoichiometry of the rhodopsin interaction – is it a *dimer*? An energy transfer approach can be used to investigate the stoichiometry. My experiments employed equimolar donor-labeled sample and acceptor-labeled sample to maximize the energy transfer signal. However, it is possible to assess stoichiometry by systematically decreasing the amount of acceptor relative to a fixed amount of donor. In such studies, the manner in which the FRET signal changes will reflect the stoichiometry of the donor/acceptor interaction [302,303]. For example, a rhodopsin dimer would result in the relative quantum yield of the donor decreasing linearly as the mole fraction of the acceptor decreases. The experiments outlined in Chapter 4 can be repeated by systemically reconstituting a fixed amount of donor-labeled rhodopsin with decreasing amounts of acceptor-labeled rhodopsin. However, this type of experiment is very difficult to perform in the reconstituted liposome system. The stoichiometry experiments would be more feasible in a detergent solubilized system because of the higher accuracy by which levels of donor-labeled rhodopsin and acceptor-labeled rhodopsin can be controlled and quantified in detergent.

Finally, the validity of the rhodopsin oligomerization models suggested in the literature (see Figure 1. 11 for an example) can be tested using my Trp/bimane quenching technique. Most models predict specific residues in TM IV and TM V to be involved in the intradimeric interface. This could be tested by incubating together samples that contain a cysteine residue labeled with bimane in TM IV or TM V with samples that contain a tryptophan residue at a site in TM IV or TM V (predicted to be involved in the interface). An observed quenching of the bimane’s fluorescence would support the model, whereas no quenching would be observed if the two residues are not involved in the dimer interface. Because Trp/bimane quenching occurs at distances less than ~ 15 Å, in this way, systematic and strategic bimane labeling and tryptophan mutagenesis could be used to identify the sites intimately involved in the rhodopsin dimer interface.

5. 6: Concluding Statements.

The results from the first two chapters of this dissertation demonstrate a novel technique that is actively being used to study protein/protein interactions as well as dynamic conformational changes in protein structure [40,45,171-173,299]. The motivation to develop this technique originated from a desire to study the mechanisms involved in GPCR activation, for which it has all ready shown great promise [40]. Additionally, this dissertation provides compelling evidence that visual rhodopsin, the model GPCR for structural studies, has a propensity to self-associate in a membrane environment. The continued development of new methodologies to elucidate the structural mechanisms of receptor activation and oligomerization are essential for the design of new pharmaceutical therapeutics as well as a fundamental understanding of cellular signal transduction.

Figure 5. 1: Trp/bimane quenching has been used to study protein/protein interactions and measure conformational changes in GPCRs. **(A)** Proposed model of the hydrophobic cleft formed by rhodopsin activation. The peptide corresponding to the C-terminus of transducin was engineered to contain a Trp residue. Binding of the peptide resulted in quenching of rhodopsin in which bimane was attached to sites C140 and K141, identifying these residues as being involved in the binding interface. This effect was further used to identify a "hydrophobic patch", involving residues L226, T229 and V230, that is critical for the affinity of this interaction. In the figure, the rhodopsin extracellular domain and a portion of cytoplasmic loop i3 have been removed for clarity. Figure taken from Janz, J.M. and Farrens, D.L. (2004) *J. Biol. Chem.* 279: 29767 – 29773. **(B)** Model of the inactive state of the β_2-adrenergic receptor. In the inactive state, the "ionic lock" interaction (shown as yellow dots) between residues in TM III (Asp-130, Arg-131) and TM VI (Glu-268) physically prevents direct contact between a bimane label attached at residue Cys-271 in helix VI and a tryptophan residue in helix III (Trp-135). No fluorescence quenching is observed in the inactive state of the receptor. Following activation, however, the "ionic lock" interaction is broken and the resultant conformational change moves bimane attached at Cys-271 toward Trp-135, resulting in significant quenching of bimane fluorescence. The size of the quenching signal was the same for partial agonists as for full agonists, indicating that breaking the "ionic lock" is necessary, but not sufficient, for full receptor activation. Figure taken from Yao, X. *et al.* (2006) *Nat. Chem. Biol.* 2: 417 – 422.

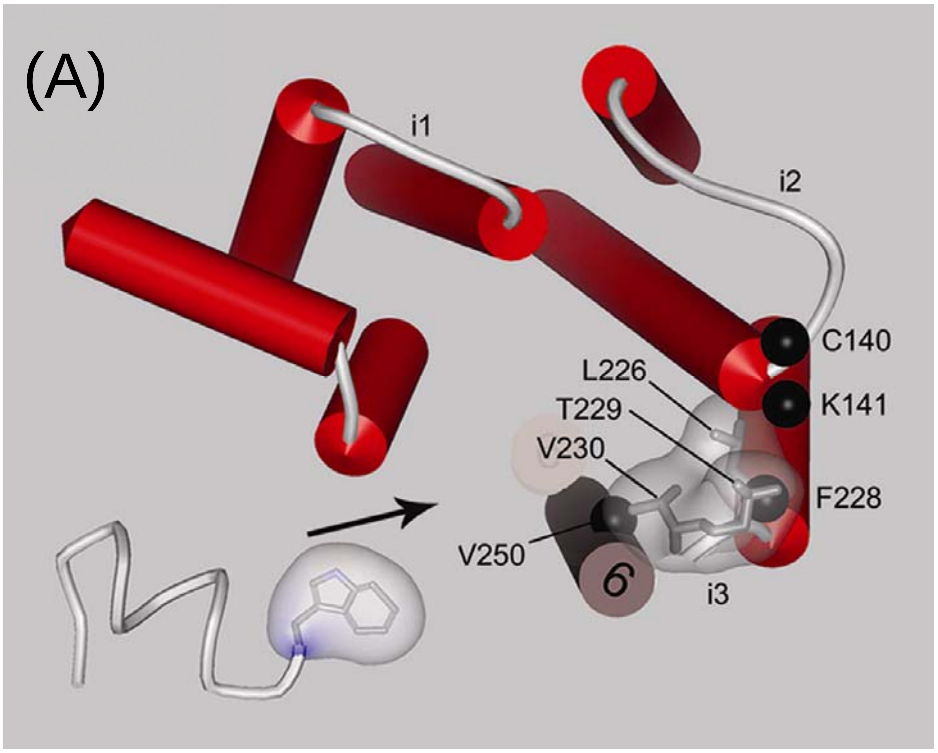
(A)
i1
i2
C140
K141
L226
T229
V230
F228
V250
6
i3

(B)

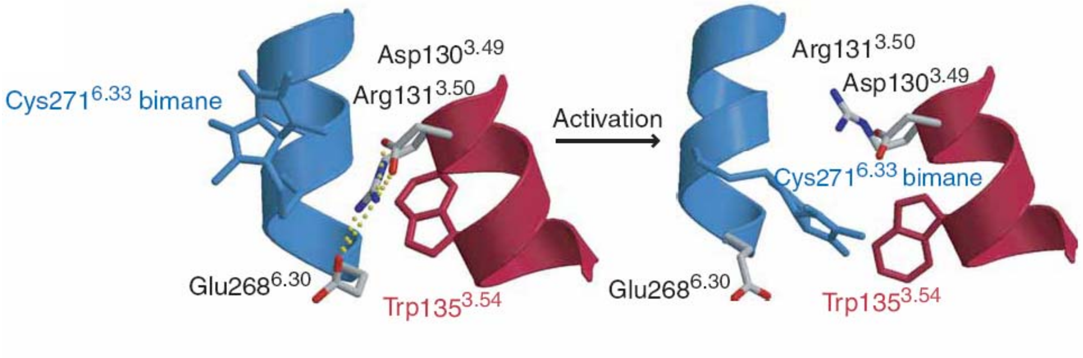
Cys271$^{6.33}$ bimane
Asp130$^{3.49}$
Arg131$^{3.50}$
Glu268$^{6.30}$
Trp135$^{3.54}$
Activation
Arg131$^{3.50}$
Asp130$^{3.49}$
Cys271$^{6.33}$ bimane
Glu268$^{6.30}$
Trp135$^{3.54}$

Figure 5. 2: Model of a rhodopsin dimer with downstream signaling components of the visual system. (A) A theoretical model of the rhodopsin/transducin complex demonstrating how a dimer of rhodopsin provides a platform that can anchor both the α- and β/γ-subunits of the G-protein, transducin. Helices of rhodopsin are colored as shown: helix I in blue, helix II in light blue, helix III in green, helix IV in light green, helix V in yellow, helix VI in orange, and helix VII and cytoplasmic helix VIII in red. Transducin is represented in a yellow space-filled background for the α-subunit, in red for the β-subunit, and in green for the γ-subunit. Figure taken from Liang, Y. *et al.* (2003) *J. Biol. Chem*. 278: 21655 – 21662. **(B)** A theoretical model shown from a side view reflecting how the two concave surfaces of arrestin, both of which are known to be important for the rhodopsin/arrestin interaction [286], can accommodate the cytoplasmic surfaces of a rhodopsin dimer. The rhodopsin dimer is shown in yellow and arrestin is shown in purple. Figure taken from Park, P.S.-H. *et al.* (2004) *Biochemistry* 43: 15643 – 15656.

(A)

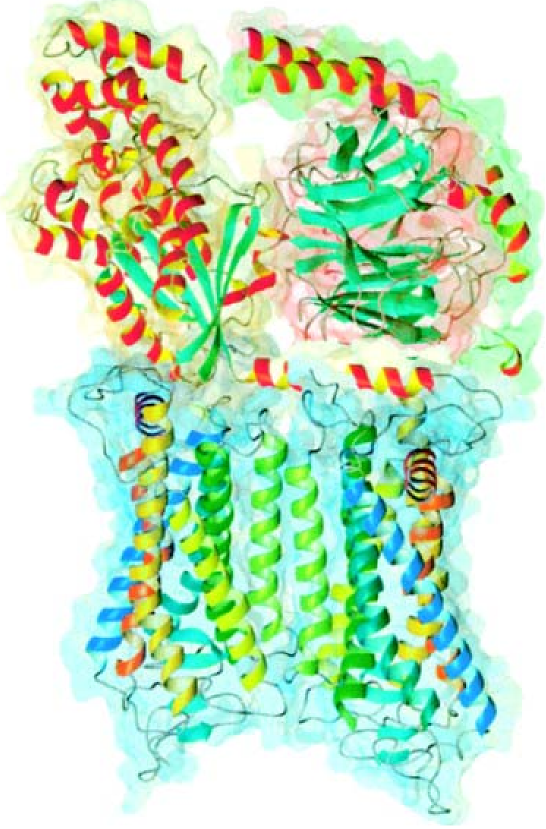

(B)

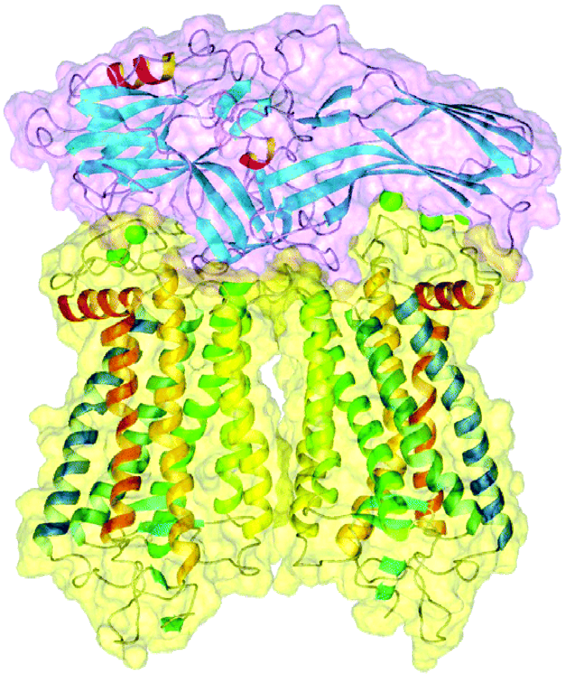

REFERENCES

1. Salom D, Lodowski DT, Stenkamp RE, Le Trong I, Golczak M, Jastrzebska B, Harris T, Ballesteros JA, Palczewski K: **Crystal structure of a photoactivated deprotonated intermediate of rhodopsin**. *Proc Natl Acad Sci U S A* 2006, **103**:16123-16128.
2. Okada T, Palczewski K: **Crystal structure of rhodopsin: implications for vision and beyond**. *Curr Opin Struct Biol* 2001, **11**:420-426.
3. Palczewski K, Kumasaka T, Hori T, Behnke CA, Motoshima H, Fox BA, Le Trong I, Teller DC, Okada T, Stenkamp RE, et al.: **Crystal structure of rhodopsin: A G protein-coupled receptor**. *Science* 2000, **289**:739-745.
4. Fredriksson R, Schioth HB: **The repertoire of G-protein-coupled receptors in fully sequenced genomes**. *Mol Pharmacol* 2005, **67**:1414-1425.
5. Fredriksson R, Lagerstrom MC, Lundin LG, Schioth HB: **The G-protein-coupled receptors in the human genome form five main families. Phylogenetic analysis, paralogon groups, and fingerprints**. *Mol Pharmacol* 2003, **63**:1256-1272.
6. Palczewski K: **G protein-coupled receptor rhodopsin**. *Annu Rev Biochem* 2006, **75**:743-767.
7. Dahl SG, Sylte I: **Molecular modelling of drug targets: the past, the present and the future**. *Basic Clin Pharmacol Toxicol* 2005, **96**:151-155.
8. Doggrell SA: **New drugs and new targets**. *Drug News Perspect* 2004, **17**:615-632.

9. Bjenning C, Al-Shamma H, Thomsen W, Leonard J, Behan D: **G protein-coupled receptors as therapeutic targets for obesity and type 2 diabetes**. *Curr Opin Investig Drugs* 2004, **5**:1051-1062.

10. Howard AD, McAllister G, Feighner SD, Liu Q, Nargund RP, Van der Ploeg LH, Patchett AA: **Orphan G-protein-coupled receptors and natural ligand discovery**. *Trends Pharmacol Sci* 2001, **22**:132-140.

11. Lundstrom K: **Latest development in drug discovery on G protein-coupled receptors**. *Curr Protein Pept Sci* 2006, **7**:465-470.

12. Gilman AG: **Nobel Lecture. G proteins and regulation of adenylyl cyclase**. *Biosci Rep* 1995, **15**:65-97.

13. Rodbell M: **Nobel Lecture. Signal transduction: evolution of an idea**. *Biosci Rep* 1995, **15**:117-133.

14. Sutherland EW: **Studies on the mechanism of hormone action**. *Science* 1972, **177**:401-408.

15. Albert AD, Yeagle PL: **Structural studies on rhodopsin**. *Biochim Biophys Acta* 2002, **1565**:183-195.

16. Stubbs GW, Smith HG, Jr., Litman BJ: **Alkyl glucosides as effective solubilizing agents for bovine rhodopsin. A comparison with several commonly used detergents**. *Biochim Biophys Acta* 1976, **426**:46-56.

17. Caron MG, Srinivasan Y, Pitha J, Kociolek K, Lefkowitz RJ: **Affinity chromatography of the beta-adrenergic receptor**. *J Biol Chem* 1979, **254**:2923-2927.

18. Fung BK, Hurley JB, Stryer L: **Flow of information in the light-triggered cyclic nucleotide cascade of vision**. *Proc Natl Acad Sci U S A* 1981, **78**:152-156.

19. Stryer L: **Cyclic GMP cascade of vision**. *Annu Rev Neurosci* 1986, **9**:87-119.

20. Abood ME, Hurley JB, Pappone MC, Bourne HR, Stryer L: **Functional homology between signal-coupling proteins. Cholera toxin inactivates the GTPase activity of transducin**. *J Biol Chem* 1982, **257**:10540-10543.

21. Gether U, Kobilka BK: **G protein-coupled receptors. II. Mechanism of agonist activation**. *J Biol Chem* 1998, **273**:17979-17982.

22. Bockaert J, Pin JP: **Molecular tinkering of G protein-coupled receptors: an evolutionary success**. *Embo J* 1999, **18**:1723-1729.

23. Karnik SS, Gogonea C, Patil S, Saad Y, Takezako T: **Activation of G-protein-coupled receptors: a common molecular mechanism**. *Trends Endocrinol Metab* 2003, **14**:431-437.

24. Wess J: **Molecular basis of receptor/G-protein-coupling selectivity**. *Pharmacol Ther* 1998, **80**:231-264.

25. Milligan G, Kostenis E: **Heterotrimeric G-proteins: a short history**. *Br J Pharmacol* 2006, **147 Suppl 1**:S46-55.

26. Pierce KL, Premont RT, Lefkowitz RJ: **Seven-transmembrane receptors**. *Nat Rev Mol Cell Biol* 2002, **3**:639-650.

27. Hamm HE: **The many faces of G protein signaling**. *J Biol Chem* 1998, **273**:669-672.

28. Wettschureck N, Offermanns S: **Mammalian G proteins and their cell type specific functions**. *Physiol Rev* 2005, **85**:1159-1204.

29. Sprang SR: **G protein mechanisms: insights from structural analysis**. *Annu Rev Biochem* 1997, **66**:639-678.

30. Bourne HR, Sanders DA, McCormick F: **The GTPase superfamily: a conserved switch for diverse cell functions**. *Nature* 1990, **348**:125-132.

31. Bourne HR, Sanders DA, McCormick F: **The GTPase superfamily: conserved structure and molecular mechanism**. *Nature* 1991, **349**:117-127.

32. Gilman AG: **G proteins: transducers of receptor-generated signals**. *Annu Rev Biochem* 1987, **56**:615-649.

33. Baylor DA, Lamb TD, Yau KW: **Responses of retinal rods to single photons**. *J Physiol* 1979, **288**:613-634.

34. Sampath AP, Rieke F: **Selective transmission of single photon responses by saturation at the rod-to-rod bipolar synapse**. *Neuron* 2004, **41**:431-443.

35. Perry SJ, Lefkowitz RJ: **Arresting developments in heptahelical receptor signaling and regulation**. *Trends Cell Biol* 2002, **12**:130-138.

36. Freedman NJ, Lefkowitz RJ: **Desensitization of G protein-coupled receptors**. *Recent Prog Horm Res* 1996, **51**:319-351; discussion 352-313.

37. Claing A, Laporte SA, Caron MG, Lefkowitz RJ: **Endocytosis of G protein-coupled receptors: roles of G protein-coupled receptor kinases and beta-arrestin proteins**. *Prog Neurobiol* 2002, **66**:61-79.

38. Luttrell LM, Lefkowitz RJ: **The role of beta-arrestins in the termination and transduction of G-protein-coupled receptor signals**. *J Cell Sci* 2002, **115**:455-465.

39. Robinson PR, Cohen GB, Zhukovsky EA, Oprian DD: **Constitutively active mutants of rhodopsin**. *Neuron* 1992, **9**:719-725.
40. Yao X, Parnot C, Deupi X, Ratnala VR, Swaminath G, Farrens D, Kobilka B: **Coupling ligand structure to specific conformational switches in the beta2-adrenoceptor**. *Nat Chem Biol* 2006, **2**:417-422.
41. Farrens DL, Altenbach C, Yang K, Hubbell WL, Khorana HG: **Requirement of rigid-body motion of transmembrane helices for light activation of rhodopsin**. *Science* 1996, **274**:768-770.
42. Dunham TD, Farrens DL: **Conformational changes in rhodopsin. Movement of helix f detected by site-specific chemical labeling and fluorescence spectroscopy**. *J Biol Chem* 1999, **274**:1683-1690.
43. Hamm HE: **How activated receptors couple to G proteins**. *Proc Natl Acad Sci U S A* 2001, **98**:4819-4821.
44. Wess J: **G-protein-coupled receptors: molecular mechanisms involved in receptor activation and selectivity of G-protein recognition**. *Faseb J* 1997, **11**:346-354.
45. Janz JM, Farrens DL: **Rhodopsin activation exposes a key hydrophobic binding site for the transducin alpha-subunit C terminus**. *J Biol Chem* 2004, **279**:29767-29773.
46. Shapiro DA, Kristiansen K, Weiner DM, Kroeze WK, Roth BL: **Evidence for a model of agonist-induced activation of 5-hydroxytryptamine 2A serotonin receptors that involves the disruption of a strong ionic interaction between helices 3 and 6**. *J Biol Chem* 2002, **277**:11441-11449.

47. Greasley PJ, Fanelli F, Rossier O, Abuin L, Cotecchia S: **Mutagenesis and modelling of the alpha(1b)-adrenergic receptor highlight the role of the helix 3/helix 6 interface in receptor activation**. *Mol Pharmacol* 2002, **61**:1025-1032.

48. Ballesteros JA, Jensen AD, Liapakis G, Rasmussen SG, Shi L, Gether U, Javitch JA: **Activation of the beta 2-adrenergic receptor involves disruption of an ionic lock between the cytoplasmic ends of transmembrane segments 3 and 6**. *J Biol Chem* 2001, **276**:29171-29177.

49. Ghanouni P, Gryczynski Z, Steenhuis JJ, Lee TW, Farrens DL, Lakowicz JR, Kobilka BK: **Functionally different agonists induce distinct conformations in the G protein coupling domain of the beta 2 adrenergic receptor**. *J Biol Chem* 2001, **276**:24433-24436.

50. Swaminath G, Deupi X, Lee TW, Zhu W, Thian FS, Kobilka TS, Kobilka B: **Probing the beta2 adrenoceptor binding site with catechol reveals differences in binding and activation by agonists and partial agonists**. *J Biol Chem* 2005, **280**:22165-22171.

51. Swaminath G, Xiang Y, Lee TW, Steenhuis J, Parnot C, Kobilka BK: **Sequential binding of agonists to the beta2 adrenoceptor. Kinetic evidence for intermediate conformational states**. *J Biol Chem* 2004, **279**:686-691.

52. Janz JM: **Structural Dynamics of Rhodopsin: Relationships Between Retinal Schiff Base Integrity and Receptor Signaling States**. Portland: Oregon Health and Science University: 2004.

53. Lundstrom K: **Structural genomics for membrane proteins**. *Cell Mol Life Sci* 2006, **63**:2597-2607.

54. Mittermaier A, Kay LE: **New tools provide new insights in NMR studies of protein dynamics**. *Science* 2006, **312**:224-228.

55. Ratnala VR: **New tools for G-protein coupled receptor (GPCR) drug discovery: combination of baculoviral expression system and solid state NMR**. *Biotechnol Lett* 2006, **28**:767-778.

56. Yu H: **Extending the size limit of protein nuclear magnetic resonance**. *Proc Natl Acad Sci U S A* 1999, **96**:332-334.

57. Wider G, Wuthrich K: **NMR spectroscopy of large molecules and multimolecular assemblies in solution**. *Curr Opin Struct Biol* 1999, **9**:594-601.

58. Sanders CR, Oxenoid K: **Customizing model membranes and samples for NMR spectroscopic studies of complex membrane proteins**. *Biochim Biophys Acta* 2000, **1508**:129-145.

59. Loewen MC, Klein-Seetharaman J, Getmanova EV, Reeves PJ, Schwalbe H, Khorana HG: **Solution 19F nuclear Overhauser effects in structural studies of the cytoplasmic domain of mammalian rhodopsin**. *Proc Natl Acad Sci U S A* 2001, **98**:4888-4892.

60. Klein-Seetharaman J, Getmanova EV, Loewen MC, Reeves PJ, Khorana HG: **NMR spectroscopy in studies of light-induced structural changes in mammalian rhodopsin: applicability of solution (19)F NMR**. *Proc Natl Acad Sci U S A* 1999, **96**:13744-13749.

61. Klein-Seetharaman J, Reeves PJ, Loewen MC, Getmanova EV, Chung J, Schwalbe H, Wright PE, Khorana HG: **Solution NMR spectroscopy of [alpha - 15N]lysine-labeled rhodopsin: The single peak observed in both conventional**

and TROSY-type HSQC spectra is ascribed to Lys-339 in the carboxyl-terminal peptide sequence. *Proc Natl Acad Sci U S A* 2002, **99**:3452-3457.

62. Klein-Seetharaman J, Yanamala NV, Javeed F, Reeves PJ, Getmanova EV, Loewen MC, Schwalbe H, Khorana HG: **Differential dynamics in the G protein-coupled receptor rhodopsin revealed by solution NMR**. *Proc Natl Acad Sci U S A* 2004, **101**:3409-3413.
63. Hubbell WL, Altenbach C: **Investigation of structure and dynamics in membrane proteins using site-directed spin labeling**. *Curr Opin Struct Biol* 1994, **4**:566-573.
64. Mansoor SE, McHaourab HS, Farrens DL: **Determination of protein secondary structure and solvent accessibility using site-directed fluorescence labeling. Studies of T4 lysozyme using the fluorescent probe monobromobimane**. *Biochemistry* 1999, **38**:16383-16393.
65. Hubbell WL, McHaourab HS, Altenbach C, Lietzow MA: **Watching proteins move using site-directed spin labeling**. *Structure* 1996, **4**:779-783.
66. Hubbell WL, Gross A, Langen R, Lietzow MA: **Recent advances in site-directed spin labeling of proteins**. *Curr Opin Struct Biol* 1998, **8**:649-656.
67. Hubbell WL, Cafiso DS, Altenbach C: **Identifying conformational changes with site-directed spin labeling**. *Nat Struct Biol* 2000, **7**:735-739.
68. Farrens DL: **Site-directed spin-labeling (SDSL) studies of the G protein-coupled receptor rhodopsin.** In *Structure-Function Analysis of G Protein-Coupled Receptors.* Edited by Wess J: Wiley-Liss, Inc.; 1999:289-314.

69. Lakowicz JR: *Principles of fluorescence spectroscopy* edn 2nd. New York: Kluwer Academic/Plenum; 1999.

70. Lakowicz JR, Weber G: **Quenching of protein fluorescence by oxygen. Detection of structural fluctuations in proteins on the nanosecond time scale**. *Biochemistry* 1973, **12**:4171-4179.

71. Eftink MR, Ghiron CA: **Fluorescence quenching studies with proteins**. *Anal Biochem* 1981, **114**:199-227.

72. Stryer L: **Fluorescence spectroscopy of proteins**. *Science* 1968, **162**:526-533.

73. O'Neil KT, Wolfe HR, Jr., Erickson-Viitanen S, DeGrado WF: **Fluorescence properties of calmodulin-binding peptides reflect alpha-helical periodicity**. *Science* 1987, **236**:1454-1456.

74. Kachel K, Ren J, Collier RJ, London E: **Identifying transmembrane states and defining the membrane insertion boundaries of hydrophobic helices in membrane-inserted diphtheria toxin T domain**. *J Biol Chem* 1998, **273**:22950-22956.

75. Malenbaum SE, Collier RJ, London E: **Membrane topography of the T domain of diphtheria toxin probed with single tryptophan mutants**. *Biochemistry* 1998, **37**:17915-17922.

76. Wang Y, Kachel K, Pablo L, London E: **Use of Trp mutations to evaluate the conformational behavior and membrane insertion of A and B chains in whole diphtheria toxin**. *Biochemistry* 1997, **36**:16300-16308.

77. Stryer L, Haugland RP: **Energy transfer: a spectroscopic ruler**. *Proc Natl Acad Sci U S A* 1967, **58**:719-726.

78. Stryer L: **Fluorescence energy transfer as a spectroscopic ruler**. *Annu Rev Biochem* 1978, **47**:819-846.

79. Roda A, Pasini P, Mirasoli M, Michelini E, Guardigli M: **Biotechnological applications of bioluminescence and chemiluminescence**. *Trends Biotechnol* 2004, **22**:295-303.

80. Pfleger KD, Eidne KA: **Illuminating insights into protein-protein interactions using bioluminescence resonance energy transfer (BRET)**. *Nat Methods* 2006, **3**:165-174.

81. Heyduk T: **Measuring protein conformational changes by FRET/LRET**. *Curr Opin Biotechnol* 2002, **13**:292-296.

82. Zou P, Surendhran K, McHaourab HS: **Distance measurements by fluorescence energy homotransfer: evaluation in T4 lysozyme and correlation with dipolar coupling between spin labels**. *Biophys J* 2007, **92**:L27-29.

83. Limbird LE, Meyts PD, Lefkowitz RJ: **Beta-adrenergic receptors: evidence for negative cooperativity**. *Biochem Biophys Res Commun* 1975, **64**:1160-1168.

84. Limbird LE, Lefkowitz RJ: **Negative cooperativity among beta-adrenergic receptors in frog erythrocyte membranes**. *J Biol Chem* 1976, **251**:5007-5014.

85. Potter LT, Ballesteros LA, Bichajian LH, Ferrendelli CA, Fisher A, Hanchett HE, Zhang R: **Evidence of paired M2 muscarinic receptors**. *Mol Pharmacol* 1991, **39**:211-221.

86. Maggio R, Vogel Z, Wess J: **Reconstitution of functional muscarinic receptors by co-expression of amino- and carboxyl-terminal receptor fragments**. *FEBS Lett* 1993, **319**:195-200.

87. Maggio R, Vogel Z, Wess J: **Coexpression studies with mutant muscarinic/adrenergic receptors provide evidence for intermolecular "cross-talk" between G-protein-linked receptors**. *Proc Natl Acad Sci U S A* 1993, **90**:3103-3107.

88. Jones KA, Borowsky B, Tamm JA, Craig DA, Durkin MM, Dai M, Yao WJ, Johnson M, Gunwaldsen C, Huang LY, et al.: **GABA(B) receptors function as a heteromeric assembly of the subunits GABA(B)R1 and GABA(B)R2**. *Nature* 1998, **396**:674-679.

89. Kaupmann K, Malitschek B, Schuler V, Heid J, Froestl W, Beck P, Mosbacher J, Bischoff S, Kulik A, Shigemoto R, et al.: **GABA(B)-receptor subtypes assemble into functional heteromeric complexes**. *Nature* 1998, **396**:683-687.

90. White JH, Wise A, Main MJ, Green A, Fraser NJ, Disney GH, Barnes AA, Emson P, Foord SM, Marshall FH: **Heterodimerization is required for the formation of a functional GABA(B) receptor**. *Nature* 1998, **396**:679-682.

91. Romano C, Yang WL, O'Malley KL: **Metabotropic glutamate receptor 5 is a disulfide-linked dimer**. *J Biol Chem* 1996, **271**:28612-28616.

92. Jordan BA, Devi LA: **G-protein-coupled receptor heterodimerization modulates receptor function**. *Nature* 1999, **399**:697-700.

93. Bai M, Trivedi S, Brown EM: **Dimerization of the extracellular calcium-sensing receptor (CaR) on the cell surface of CaR-transfected HEK293 cells**. *J Biol Chem* 1998, **273**:23605-23610.

94. Zeng FY, Wess J: **Identification and molecular characterization of m3 muscarinic receptor dimers**. *J Biol Chem* 1999, **274**:19487-19497.

95. Xie Z, Lee SP, O'Dowd BF, George SR: **Serotonin 5-HT1B and 5-HT1D receptors form homodimers when expressed alone and heterodimers when co-expressed**. *FEBS Lett* 1999, **456**:63-67.

96. Bouvier M: **Oligomerization of G-protein-coupled transmitter receptors**. *Nat Rev Neurosci* 2001, **2**:274-286.

97. Devi LA: **Heterodimerization of G-protein-coupled receptors: pharmacology, signaling and trafficking**. *Trends Pharmacol Sci* 2001, **22**:532-537.

98. Marshall FH, Jones KA, Kaupmann K, Bettler B: **GABAB receptors - the first 7TM heterodimers**. *Trends Pharmacol Sci* 1999, **20**:396-399.

99. Prinster SC, Hague C, Hall RA: **Heterodimerization of g protein-coupled receptors: specificity and functional significance**. *Pharmacol Rev* 2005, **57**:289-298.

100. Kaupmann K, Huggel K, Heid J, Flor PJ, Bischoff S, Mickel SJ, McMaster G, Angst C, Bittiger H, Froestl W, et al.: **Expression cloning of GABA(B) receptors uncovers similarity to metabotropic glutamate receptors**. *Nature* 1997, **386**:239-246.

101. Ng GY, Clark J, Coulombe N, Ethier N, Hebert TE, Sullivan R, Kargman S, Chateauneuf A, Tsukamoto N, McDonald T, et al.: **Identification of a GABAB receptor subunit, gb2, required for functional GABAB receptor activity**. *J Biol Chem* 1999, **274**:7607-7610.

102. Martin SC, Russek SJ, Farb DH: **Molecular identification of the human GABABR2: cell surface expression and coupling to adenylyl cyclase in the absence of GABABR1**. *Mol Cell Neurosci* 1999, **13**:180-191.

103. Kuner R, Kohr G, Grunewald S, Eisenhardt G, Bach A, Kornau HC: **Role of heteromer formation in GABAB receptor function**. *Science* 1999, **283**:74-77.

104. Couve A, Filippov AK, Connolly CN, Bettler B, Brown DA, Moss SJ: **Intracellular retention of recombinant GABAB receptors**. *J Biol Chem* 1998, **273**:26361-26367.

105. Carrillo JJ, Pediani J, Milligan G: **Dimers of class A G protein-coupled receptors function via agonist-mediated trans-activation of associated G proteins**. *J Biol Chem* 2003, **278**:42578-42587.

106. Milligan G: **Construction and analysis of function of G protein-coupled receptor-G protein fusion proteins**. *Methods Enzymol* 2002, **343**:260-273.

107. Milligan G: **Insights into ligand pharmacology using receptor-G-protein fusion proteins**. *Trends Pharmacol Sci* 2000, **21**:24-28.

108. Mercier JF, Salahpour A, Angers S, Breit A, Bouvier M: **Quantitative assessment of beta 1- and beta 2-adrenergic receptor homo- and heterodimerization by bioluminescence resonance energy transfer**. *J Biol Chem* 2002, **277**:44925-44931.

109. Ramsay D, Kellett E, McVey M, Rees S, Milligan G: **Homo- and hetero-oligomeric interactions between G-protein-coupled receptors in living cells monitored by two variants of bioluminescence resonance energy transfer (BRET): hetero-oligomers between receptor subtypes form more efficiently than between less closely related sequences**. *Biochem J* 2002, **365**:429-440.

110. Angers S, Salahpour A, Joly E, Hilairet S, Chelsky D, Dennis M, Bouvier M: **Detection of beta 2-adrenergic receptor dimerization in living cells using**

bioluminescence resonance energy transfer (BRET). *Proc Natl Acad Sci U S A* 2000, **97**:3684-3689.

111. Cornea A, Janovick JA, Maya-Nunez G, Conn PM: **Gonadotropin-releasing hormone receptor microaggregation. Rate monitored by fluorescence resonance energy transfer**. *J Biol Chem* 2001, **276**:2153-2158.
112. Overton MC, Blumer KJ: **G-protein-coupled receptors function as oligomers in vivo**. *Curr Biol* 2000, **10**:341-344.
113. McVey M, Ramsay D, Kellett E, Rees S, Wilson S, Pope AJ, Milligan G: **Monitoring receptor oligomerization using time-resolved fluorescence resonance energy transfer and bioluminescence resonance energy transfer. The human delta -opioid receptor displays constitutive oligomerization at the cell surface, which is not regulated by receptor occupancy**. *J Biol Chem* 2001, **276**:14092-14099.
114. Rocheville M, Lange DC, Kumar U, Sasi R, Patel RC, Patel YC: **Subtypes of the somatostatin receptor assemble as functional homo- and heterodimers**. *J Biol Chem* 2000, **275**:7862-7869.
115. Rocheville M, Lange DC, Kumar U, Patel SC, Patel RC, Patel YC: **Receptors for dopamine and somatostatin: formation of hetero-oligomers with enhanced functional activity**. *Science* 2000, **288**:154-157.
116. Roess DA, Horvat RD, Munnelly H, Barisas BG: **Luteinizing hormone receptors are self-associated in the plasma membrane**. *Endocrinology* 2000, **141**:4518-4523.

117. James JR, Oliveira MI, Carmo AM, Iaboni A, Davis SJ: **A rigorous experimental framework for detecting protein oligomerization using bioluminescence resonance energy transfer**. *Nat Methods* 2006, **3**:1001-1006.

118. Filipek S, Krzysko KA, Fotiadis D, Liang Y, Saperstein DA, Engel A, Palczewski K: **A concept for G protein activation by G protein-coupled receptor dimers: the transducin/rhodopsin interface**. *Photochem Photobiol Sci* 2004, **3**:628-638.

119. George SR, O'Dowd BF, Lee SP: **G-protein-coupled receptor oligomerization and its potential for drug discovery**. *Nat Rev Drug Discov* 2002, **1**:808-820.

120. Benkirane M, Jin DY, Chun RF, Koup RA, Jeang KT: **Mechanism of transdominant inhibition of CCR5-mediated HIV-1 infection by ccr5delta32**. *J Biol Chem* 1997, **272**:30603-30606.

121. Zhu X, Wess J: **Truncated V2 vasopressin receptors as negative regulators of wild-type V2 receptor function**. *Biochemistry* 1998, **37**:15773-15784.

122. Werry TD, Wilkinson GF, Willars GB: **Mechanisms of cross-talk between G-protein-coupled receptors resulting in enhanced release of intracellular Ca2+**. *Biochem J* 2003, **374**:281-296.

123. Vazquez-Prado J, Casas-Gonzalez P, Garcia-Sainz JA: **G protein-coupled receptor cross-talk: pivotal roles of protein phosphorylation and protein-protein interactions**. *Cell Signal* 2003, **15**:549-557.

124. Hur EM, Kim KT: **G protein-coupled receptor signalling and cross-talk: achieving rapidity and specificity**. *Cell Signal* 2002, **14**:397-405.

125. Teller DC, Okada T, Behnke CA, Palczewski K, Stenkamp RE: **Advances in determination of a high-resolution three-dimensional structure of rhodopsin,**

a model of G-protein-coupled receptors (GPCRs). *Biochemistry* 2001, **40**:7761-7772.

126. Okada T, Fujiyoshi Y, Silow M, Navarro J, Landau EM, Shichida Y: **Functional role of internal water molecules in rhodopsin revealed by X-ray crystallography**. *Proc Natl Acad Sci U S A* 2002, **99**:5982-5987.
127. Fotiadis D, Liang Y, Filipek S, Saperstein DA, Engel A, Palczewski K: **Atomic-force microscopy: Rhodopsin dimers in native disc membranes**. *Nature* 2003, **421**:127-128.
128. Liang Y, Fotiadis D, Filipek S, Saperstein DA, Palczewski K, Engel A: **Organization of the G protein-coupled receptors rhodopsin and opsin in native membranes**. *J Biol Chem* 2003, **278**:21655-21662.
129. Chabre M, Cone R, Saibil H: **Biophysics: is rhodopsin dimeric in native retinal rods?** *Nature* 2003, **426**:30-31; discussion 31.
130. Filipek S, Teller DC, Palczewski K, Stenkamp R: **The crystallographic model of rhodopsin and its use in studies of other G protein-coupled receptors**. *Annu Rev Biophys Biomol Struct* 2003, **32**:375-397.
131. Hargrave PA, McDowell JH, Curtis DR, Wang JK, Juszczak E, Fong SL, Rao JK, Argos P: **The structure of bovine rhodopsin**. *Biophys Struct Mech* 1983, **9**:235-244.
132. Sakmar TP: **Rhodopsin: a prototypical G protein-coupled receptor**. *Prog Nucleic Acid Res Mol Biol* 1998, **59**:1-34.
133. Sakmar TP, Menon ST, Marin EP, Awad ES: **Rhodopsin: insights from recent structural studies**. *Annu Rev Biophys Biomol Struct* 2002, **31**:443-484.

134. Cha K, Reeves PJ, Khorana HG: **Structure and function in rhodopsin: destabilization of rhodopsin by the binding of an antibody at the N-terminal segment provides support for involvement of the latter in an intradiscal tertiary structure**. *Proc Natl Acad Sci U S A* 2000, **97**:3016-3021.

135. Liu X, Garriga P, Khorana HG: **Structure and function in rhodopsin: correct folding and misfolding in two point mutants in the intradiscal domain of rhodopsin identified in retinitis pigmentosa**. *Proc Natl Acad Sci U S A* 1996, **93**:4554-4559.

136. Kaushal S, Khorana HG: **Structure and function in rhodopsin. 7. Point mutations associated with autosomal dominant retinitis pigmentosa**. *Biochemistry* 1994, **33**:6121-6128.

137. Doi T, Molday RS, Khorana HG: **Role of the intradiscal domain in rhodopsin assembly and function**. *Proc Natl Acad Sci U S A* 1990, **87**:4991-4995.

138. Karnik SS, Sakmar TP, Chen HB, Khorana HG: **Cysteine residues 110 and 187 are essential for the formation of correct structure in bovine rhodopsin**. *Proc Natl Acad Sci U S A* 1988, **85**:8459-8463.

139. Meng EC, Bourne HR: **Receptor activation: what does the rhodopsin structure tell us?** *Trends Pharmacol Sci* 2001, **22**:587-593.

140. Bourne HR, Meng EC: **Structure. Rhodopsin sees the light**. *Science* 2000, **289**:733-734.

141. Janz JM, Fay JF, Farrens DL: **Stability of dark state rhodopsin is mediated by a conserved ion pair in intradiscal loop E-2**. *J Biol Chem* 2003, **278**:16982-16991.

142. Visiers I, Braunheim BB, Weinstein H: **Prokink: a protocol for numerical evaluation of helix distortions by proline**. *Protein Eng* 2000, **13**:603-606.

143. Sansom MS, Weinstein H: **Hinges, swivels and switches: the role of prolines in signalling via transmembrane alpha-helices**. *Trends Pharmacol Sci* 2000, **21**:445-451.

144. Shi L, Liapakis G, Xu R, Guarnieri F, Ballesteros JA, Javitch JA: **Beta2 adrenergic receptor activation. Modulation of the proline kink in transmembrane 6 by a rotamer toggle switch**. *J Biol Chem* 2002, **277**:40989-40996.

145. Sakmar TP, Franke RR, Khorana HG: **Glutamic acid-113 serves as the retinylidene Schiff base counterion in bovine rhodopsin**. *Proc Natl Acad Sci U S A* 1989, **86**:8309-8313.

146. Strader CD, Sigal IS, Candelore MR, Rands E, Hill WS, Dixon RA: **Conserved aspartic acid residues 79 and 113 of the beta-adrenergic receptor have different roles in receptor function**. *J Biol Chem* 1988, **263**:10267-10271.

147. Osborne HB, Sardet C, Helenius A: **Bovine rhodopsin: characterization of the complex formed with Triton X-100**. *Eur J Biochem* 1974, **44**:383-390.

148. Osborne HB, Sardet C, Michel-Villaz M, Chabre M: **Structural study of rhodopsin in detergent micelles by small-angle neutron scattering**. *J Mol Biol* 1978, **123**:177-206.

149. Saibil H, Chabre M, Worcester D: **Neutron diffraction studies of retinal rod outer segment membranes**. *Nature* 1976, **262**:266-270.

150. Cone RA: **Rotational diffusion of rhodopsin in the visual receptor membrane**. *Nat New Biol* 1972, **236**:39-43.

151. Liebman PA, Entine G: **Lateral diffusion of visual pigment in photorecptor disk membranes**. *Science* 1974, **185**:457-459.

152. Poo M, Cone RA: **Lateral diffusion of rhodopsin in the photoreceptor membrane**. *Nature* 1974, **247**:438-441.

153. Wey CL, Cone RA, Edidin MA: **Lateral diffusion of rhodopsin in photoreceptor cells measured by fluorescence photobleaching and recovery**. *Biophys J* 1981, **33**:225-232.

154. Kuhn H, Bennett N, Michel-Villaz M, Chabre M: **Interactions between photoexcited rhodopsin and GTP-binding protein: kinetic and stoichiometric analyses from light-scattering changes**. *Proc Natl Acad Sci U S A* 1981, **78**:6873-6877.

155. Chabre M, le Maire M: **Monomeric G-protein-coupled receptor as a functional unit**. *Biochemistry* 2005, **44**:9395-9403.

156. Lamb TD, Pugh EN, Jr.: **Dark adaptation and the retinoid cycle of vision**. *Prog Retin Eye Res* 2004, **23**:307-380.

157. Medina R, Perdomo D, Bubis J: **The hydrodynamic properties of dark- and light-activated states of n-dodecyl beta-D-maltoside-solubilized bovine rhodopsin support the dimeric structure of both conformations**. *J Biol Chem* 2004, **279**:39565-39573.

158. Le Maire M, Aggerbeck LP, Monteilhet C, Andersen JP, Moller JV: **The use of high-performance liquid chromatography for the determination of size and molecular weight of proteins: a caution and a list of membrane proteins suitable as standards**. *Anal Biochem* 1986, **154**:525-535.

159. Tanford C, Nozaki Y, Reynolds JA, Makino S: **Molecular characterization of proteins in detergent solutions**. *Biochemistry* 1974, **13**:2369-2376.

160. le Maire M, Champeil P, Moller JV: **Interaction of membrane proteins and lipids with solubilizing detergents**. *Biochim Biophys Acta* 2000, **1508**:86-111.

161. Moller JV, le Maire M: **Detergent binding as a measure of hydrophobic surface area of integral membrane proteins**. *J Biol Chem* 1993, **268**:18659-18672.

162. Jastrzebska B, Maeda T, Zhu L, Fotiadis D, Filipek S, Engel A, Stenkamp RE, Palczewski K: **Functional characterization of rhodopsin monomers and dimers in detergents**. *J Biol Chem* 2004, **279**:54663-54675.

163. Aveldano MI: **Phospholipid solubilization during detergent extraction of rhodopsin from photoreceptor disk membranes**. *Arch Biochem Biophys* 1995, **324**:331-343.

164. Jastrzebska B, Fotiadis D, Jang GF, Stenkamp RE, Engel A, Palczewski K: **Functional and structural characterization of rhodopsin oligomers**. *J Biol Chem* 2006, **281**:11917-11922.

165. Fotiadis D, Jastrzebska B, Philippsen A, Muller DJ, Palczewski K, Engel A: **Structure of the rhodopsin dimer: a working model for G-protein-coupled receptors**. *Curr Opin Struct Biol* 2006, **16**:252-259.

166. Suda K, Filipek S, Palczewski K, Engel A, Fotiadis D: **The supramolecular structure of the GPCR rhodopsin in solution and native disc membranes**. *Mol Membr Biol* 2004, **21**:435-446.

167. Kota P, Reeves PJ, Rajbhandary UL, Khorana HG: **Opsin is present as dimers in COS1 cells: identification of amino acids at the dimeric interface**. *Proc Natl Acad Sci U S A* 2006, **103**:3054-3059.

168. Guo W, Shi L, Javitch JA: **The fourth transmembrane segment forms the interface of the dopamine D2 receptor homodimer**. *J Biol Chem* 2003, **278**:4385-4388.

169. Guo W, Shi L, Filizola M, Weinstein H, Javitch JA: **Crosstalk in G protein-coupled receptors: changes at the transmembrane homodimer interface determine activation**. *Proc Natl Acad Sci U S A* 2005, **102**:17495-17500.

170. Mansoor SE, McHaourab HS, Farrens DL: **Mapping proximity within proteins using fluorescence spectroscopy. A study of T4 lysozyme showing that tryptophan residues quench bimane fluorescence**. *Biochemistry* 2002, **41**:2475-2484.

171. Islas LD, Zagotta WN: **Short-range molecular rearrangements in ion channels detected by tryptophan quenching of bimane fluorescence**. *J Gen Physiol* 2006, **128**:337-346.

172. Tapley TL, Vickery LE: **Preferential substrate binding orientation by the molecular chaperone HscA**. *J Biol Chem* 2004, **279**:28435-28442.

173. Tapley TL, Cupp-Vickery JR, Vickery LE: **Sequence-dependent peptide binding orientation by the molecular chaperone DnaK**. *Biochemistry* 2005, **44**:12307-12315.

174. Lodowski DT, Pitcher JA, Capel WD, Lefkowitz RJ, Tesmer JJ: **Keeping G proteins at bay: a complex between G protein-coupled receptor kinase 2 and Gbetagamma**. *Science* 2003, **300**:1256-1262.

175. Ferguson SS, Caron MG: **G protein-coupled receptor adaptation mechanisms**. *Semin Cell Dev Biol* 1998, **9**:119-127.

176. Altenbach C, Yang K, Farrens DL, Farahbakhsh ZT, Khorana HG, Hubbell WL: **Structural features and light-dependent changes in the cytoplasmic interhelical E-F loop region of rhodopsin: a site-directed spin- labeling study**. *Biochemistry* 1996, **35**:12470-12478.

177. McHaourab HS, Lietzow MA, Hideg K, Hubbell WL: **Motion of spin-labeled side chains in T4 lysozyme. Correlation with protein structure and dynamics**. *Biochemistry* 1996, **35**:7692-7704.

178. Flitsch SL, Khorana HG: **Structural studies on transmembrane proteins. 1. Model study using bacteriorhodopsin mutants containing single cysteine residues**. *Biochemistry* 1989, **28**:7800-7805.

179. Wu J, Kaback HR: **Cysteine 148 in the lactose permease of Escherichia coli is a component of a substrate binding site. 2. Site-directed fluorescence studies**. *Biochemistry* 1994, **33**:12166-12171.

180. Barry JK, Matthews KS: **Ligand-induced conformational changes in lactose repressor: a fluorescence study of single tryptophan mutants**. *Biochemistry* 1997, **36**:15632-15642.

181. Shepard LA, Heuck AP, Hamman BD, Rossjohn J, Parker MW, Ryan KR, Johnson AE, Tweten RK: **Identification of a membrane-spanning domain of the thiol-**

activated pore-forming toxin Clostridium perfringens perfringolysin O: an alpha- helical to beta-sheet transition identified by fluorescence spectroscopy. *Biochemistry* 1998, **37**:14563-14574.

182. Sinev MA, Sineva EV, Ittah V, Haas E: **Domain closure in adenylate kinase**. *Biochemistry* 1996, **35**:6425-6437.

183. Navon A, Ittah V, Landsman P, Scheraga HA, Haas E: **Distributions of intramolecular distances in the reduced and denatured states of bovine pancreatic ribonuclease A. Folding initiation structures in the C-terminal portions of the reduced protein**. *Biochemistry* 2001, **40**:105-118.

184. Cha A, Snyder GE, Selvin PR, Bezanilla F: **Atomic scale movement of the voltage-sensing region in a potassium channel measured via spectroscopy**. *Nature* 1999, **402**:809-813.

185. Yang CS, Skiba NP, Mazzoni MR, Hamm HE: **Conformational changes at the carboxyl terminus of Galpha occur during G protein activation**. *J Biol Chem* 1999, **274**:2379-2385.

186. McHaourab HS, Oh KJ, Fang CJ, Hubbell WL: **Conformation of T4 lysozyme in solution. Hinge-bending motion and the substrate-induced conformational transition studied by site-directed spin labeling**. *Biochemistry* 1997, **36**:307-316.

187. Koteiche HA, McHaourab HS: **Folding pattern of the alpha-crystallin domain in alphaA-crystallin determined by site-directed spin labeling**. *J Mol Biol* 1999, **294**:561-577.

188. Perozo E, Cortes DM, Cuello LG: **Three-dimensional architecture and gating mechanism of a K+ channel studied by EPR spectroscopy**. *Nat Struct Biol* 1998, **5**:459-469.

189. Rabenstein MD, Shin YK: **HIV-1 gp41 tertiary structure studied by EPR spectroscopy**. *Biochemistry* 1996, **35**:13922-13928.

190. Yuan T, Weljie AM, Vogel HJ: **Tryptophan fluorescence quenching by methionine and selenomethionine residues of calmodulin: orientation of peptide and protein binding**. *Biochemistry* 1998, **37**:3187-3195.

191. Ghanouni P, Steenhuis JJ, Farrens DL, Kobilka BK: **Agonist-induced conformational changes in the G-protein-coupling domain of the beta 2 adrenergic receptor**. *Proc Natl Acad Sci U S A* 2001, **98**:5997-6002.

192. Sato E, Sakashita M, Kanaoka Y, Kosower EM: **XIV. Novel Fluorogenic Substrates for Microdetermination of Chymotrypsin and Aminopeptidase: Bimane Fluorescence Appears after Hydrolysis**. *Bioorganic Chemistry* 1988, **16**:298-306.

193. Hudson BS: *Accounts of Chemical Research* 1999, **32**:297-300.

194. Matsumura M, Matthews BW: **Control of enzyme activity by an engineered disulfide bond**. *Science* 1989, **243**:792-794.

195. Ho SN, Hunt HD, Horton RM, Pullen JK, Pease LR: **Site-directed mutagenesis by overlap extension using the polymerase chain reaction**. *Gene* 1989, **77**:51-59.

196. Sauer UH, San DP, Matthews BW: **Tolerance of T4 lysozyme to proline substitutions within the long interdomain alpha-helix illustrates the**

adaptability of proteins to potentially destabilizing lesions. *J Biol Chem* 1992, **267**:2393-2399.

197. Inoue H, Nojima H, Okayama H: **High efficiency transformation of Escherichia coli with plasmids**. *Gene* 1990, **96**:23-28.

198. Pace CN, Scholtz JM: In *Protein Structure: A Practical Approach*. Edited by Creighton TE: Oxford University Press; 1997:Chapter 12.

199. Eftink MR: **The use of fluorescence methods to monitor unfolding transitions in proteins**. *Biophys J* 1994, **66**:482-501.

200. Novokhatny V, Medved L, Mazar A, Marcotte P, Henkin J, Ingham K: **Domain structure and interactions of recombinant urokinase-type plasminogen activator**. *J Biol Chem* 1992, **267**:3878-3885.

201. Becktel WJ, Schellman JA: **Protein stability curves**. *Biopolymers* 1987, **26**:1859-1877.

202. Ware WR, Doemeny LJ, Nemzek TL: **Deconvolution of fluorescence and phosphorescence decay curves. Least-squares method**. *J. Phys. Chem.* 1973, **77**:2038-2048.

203. O'Connor D, Phillips D: *Time Correlated Single Photon Counting*. San Diego, CA: Academic Press; 1984.

204. Holzwarth AR: **Time-resolved fluorescence spectroscopy**. *Methods Enzymol* 1995, **246**:334-362.

205. Kavarnos GJ: **Fundamental Concepts of Photoinduced Electron Transfer**. In *Photoinduced Electron Transfer I*. Edited by Mattay J: Springer-Verlag; 1990:23-58. Topics in Current Chemistry, vol 156.]

206. Kavarnos GJ: *Fundamentals of Photoinduced Electron Transfer*. New York, New York: VCH Publishers, Inc.; 1993.

207. Rehm D, Weller A: *Israel Journal of Chemistry* 1970, **8**:259.

208. Kosower EM, Kanety H, Dodluk H, Hermolin J: **Bimanes. 9. Solvent and Substituent Effects on Intramolecular Charge-Transfer Quenching of the Fluorescence of syn-1,5,-Diazabicyclo[3.3.0]octadienediones (syn-9,10-Dioxabimanes).** *J. Phys. Chem.* 1982, **86**:1270-1277.

209. Jones GI, Farahat CW, Oh C: **Photoinduced Electron Transfer Involving Eosin-Tryptophan conjugates. Long-lived Radical Pair States for Systems Incorporating Aromatic Amino Acid Side Chains**. *J. Phys. Chem.* 1994, **98**:6906-6909.

210. Williams RM, Zwier, J.J., Verhoeven, J.W.: **Photoinduced Intramolecular Electron Transfer in a Bridged C60 (Acceptor)-Aniline (Donor) System. Photophysical Properties of the First "Active" Fullerene Diad.** *J. Am. Chem. Soc.* 1995, **117**:4093-4099.

211. Matthews BW: **Studies on protein stability with T4 lysozyme**. *Adv Protein Chem* 1995, **46**:249-278.

212. Kosower EM, Giniger R, Radkowsky A, Hebel D, Shusterman A: **Bimanes 22. Flexible fluorescent molecules. Solvent effects on the photophysical properties of syn-bimanes (1,5-diazabicyclo[3.3.0]octa-3,6-diene-2,8-diones)**. *J. Phys. Chem.* 1986, **90**:5552-5557.

213. Eftink MR: **Fluorescence Quenching:Theory and Applications**. In *Topics in Fluorescence Spectroscopy*. Edited by Lakowicz JR: Plenum Press; 1991:53-126. vol 2.]

214. Vanderkooi JM, Englander SW, Papp S, Wright WW, Owen CS: **Long-range electron exchange measured in proteins by quenching of tryptophan phosphorescence**. *Proc Natl Acad Sci U S A* 1990, **87**:5099-5103.

215. Chen Y, Barkley MD: **Toward understanding tryptophan fluorescence in proteins**. *Biochemistry* 1998, **37**:9976-9982.

216. Lockhart DJ, Kim PS: **Internal stark effect measurement of the electric field at the amino terminus of an alpha helix**. *Science* 1992, **257**:947-951.

217. Closs GL, Miller JR: **Intramolecular Long-Distance Electron Transfer in Organic Molecules**. *Science* 1988, **240**:440-447.

218. Siders P, Cave RJ, Marcus RA: **A model for orientation effects in electron-transfer reactions**. *J. Chem. Phys.* 1984, **81**:5613-5624.

219. Lakowicz JR, Weber G: **Quenching of fluorescence by oxygen. A probe for structural fluctuations in macromolecules**. *Biochemistry* 1973, **12**:4161-4170.

220. Webber SE: **The Role of Time-Dependent Measurements in Elucidating Static Versus Dynamic Quenching Processes**. *Photochemistry and Photobiology* 1997, **65**:33-38.

221. Zelent B, Kusba J, Gryczynski I, Johnson ML, Lakowicz JR: **Time-resolved and steady-state fluorescence quenching of N-acetyl-L- tryptophanamide by acrylamide and iodide**. *Biophys Chem* 1998, **73**:53-75.

222. Gether U, Lin S, Kobilka BK: **Fluorescent labeling of purified beta 2 adrenergic receptor. Evidence for ligand-specific conformational changes**. *J Biol Chem* 1995, **270**:28268-28275.

223. Glauner KS, Mannuzzu LM, Gandhi CS, Isacoff EY: **Spectroscopic mapping of voltage sensor movement in the Shaker potassium channel**. *Nature* 1999, **402**:813-817.

224. Imamoto Y, Kataoka M, Tokunaga F, Palczewski K: **Light-induced conformational changes of rhodopsin probed by fluorescent alexa594 immobilized on the cytoplasmic surface**. *Biochemistry* 2000, **39**:15225-15233.

225. Mielke T, Alexiev U, Glasel M, Otto H, Heyn MP: **Light-induced changes in the structure and accessibility of the cytoplasmic loops of rhodopsin in the activated MII state**. *Biochemistry* 2002, **41**:7875-7884.

226. Sathish HA, Stein RA, Yang G, McHaourab HS: **Mechanism of chaperone function in small heat-shock proteins. Fluorescence studies of the conformations of T4 lysozyme bound to alphaB-crystallin**. *J Biol Chem* 2003, **278**:44214-44221.

227. Alexiev U, Rimke I, Pohlmann T: **Elucidation of the nature of the conformational changes of the EF-interhelical loop in bacteriorhodopsin and of the helix VIII on the cytoplasmic surface of bovine rhodopsin: a time-resolved fluorescence depolarization study**. *J Mol Biol* 2003, **328**:705-719.

228. Carlsson K, Osterlund M, Persson E, Freskgard PO, Carlsson U, Svensson M: **Site-directed fluorescence probing to dissect the calcium-dependent association**

between soluble tissue factor and factor VIIa domains. *Biochim Biophys Acta* 2003, **1648**:12-16.

229. Gasymov OK, Abduragimov AR, Yusifov TN, Glasgow BJ: **Site-directed tryptophan fluorescence reveals the solution structure of tear lipocalin: evidence for features that confer promiscuity in ligand binding**. *Biochemistry* 2001, **40**:14754-14762.

230. Voss J, He MM, Hubbell WL, Kaback HR: **Site-directed spin labeling demonstrates that transmembrane domain XII in the lactose permease of Escherichia coli is an alpha-helix**. *Biochemistry* 1996, **35**:12915-12918.

231. Millhauser GL, Fiori WR, Miick SM: **Electron spin labels**. *Methods Enzymol* 1995, **246**:589-610.

232. Klug CS, Su W, Feix JB: **Mapping of the residues involved in a proposed beta-strand located in the ferric enterobactin receptor FepA using site-directed spin-labeling**. *Biochemistry* 1997, **36**:13027-13033.

233. Thomas DD, Reddy LG, Karim CB, Li M, Cornea R, Autry JM, Jones LR, Stamm J: **Direct spectroscopic detection of molecular dynamics and interactions of the calcium pump and phospholamban**. *Ann N Y Acad Sci* 1998, **853**:186-194.

234. Hustedt EJ, Beth AH: **Nitroxide spin-spin interactions: applications to protein structure and dynamics**. *Annu Rev Biophys Biomol Struct* 1999, **28**:129-153.

235. Gross A, Columbus L, Hideg K, Altenbach C, Hubbell WL: **Structure of the KcsA potassium channel from Streptomyces lividans: a site-directed spin labeling study of the second transmembrane segment**. *Biochemistry* 1999, **38**:10324-10335.

236. Lakshmi KV, Brudvig GW: **Pulsed electron paramagnetic resonance methods for macromolecular structure determination**. *Curr Opin Struct Biol* 2001, **11**:523-531.

237. Fanucci GE, Lee JY, Cafiso DS: **Spectroscopic evidence that osmolytes used in crystallization buffers inhibit a conformation change in a membrane protein**. *Biochemistry* 2003, **42**:13106-13112.

238. McHaourab HS, Kalai T, Hideg K, Hubbell WL: **Motion of spin-labeled side chains in T4 lysozyme: effect of side chain structure**. *Biochemistry* 1999, **38**:2947-2955.

239. Langen R, Oh KJ, Cascio D, Hubbell WL: **Crystal structures of spin labeled T4 lysozyme mutants: implications for the interpretation of EPR spectra in terms of structure**. *Biochemistry* 2000, **39**:8396-8405.

240. Borbat PP, McHaourab HS, Freed JH: **Protein structure determination using long-distance constraints from double-quantum coherence ESR: study of T4 lysozyme**. *J Am Chem Soc* 2002, **124**:5304-5314.

241. Hosfield D, Palan J, Hilgers M, Scheibe D, McRee DE, Stevens RC: **A fully integrated protein crystallization platform for small-molecule drug discovery**. *J Struct Biol* 2003, **142**:207-217.

242. Carlsson J, Drevin H, Axen R: **Protein thiolation and reversible protein-protein conjugation. N-Succinimidyl 3-(2-pyridyldithio)propionate, a new heterobifunctional reagent**. *Biochem J* 1978, **173**:723-737.

243. James DR, Siemiarczuk A, Ware WR: **Stroboscopic optical boxcar technique for the determination of fluorescence lifetimes**. *Rev.Sci.Instrum.* 1992, **63**:1710-1716.

244. D'Auria S, Gryczynski Z, Gryczynski I, Rossi M, Lakowicz JR: **A protein biosensor for lactate**. *Anal Biochem* 2000, **283**:83-88.

245. Hawkins ME, Pfleiderer W, Balis FM, Porter D, Knutson JR: **Fluorescence properties of pteridine nucleoside analogs as monomers and incorporated into oligonucleotides**. *Anal Biochem* 1997, **244**:86-95.

246. Maliwal BP, Malicka J, Gryczynski I, Gryczynski Z, Lakowicz JR: **Fluorescence properties of labeled proteins near silver colloid surfaces**. *Biopolymers* 2003, **70**:585-594.

247. Abagyan R, Totrov M, Kuznetsov DA: **ICM - a new method for protein modeling and design. Applications to docking and structure prediction from the distorted native conformation.** *J. Comput. Chem.* 1994, **15**:488-506.

248. Nicholson H, Anderson DE, Dao-pin S, Matthews BW: **Analysis of the interaction between charged side chains and the alpha- helix dipole using designed thermostable mutants of phage T4 lysozyme**. *Biochemistry* 1991, **30**:9816-9828.

249. Han JC, Han GY: **A procedure for quantitative determination of tris(2-carboxyethyl)phosphine, an odorless reducing agent more stable and effective than dithiothreitol**. *Anal Biochem* 1994, **220**:5-10.

250. Hu L, Colman RF: **Monobromobimane as an affinity label of the xenobiotic binding site of rat glutathione S-transferase 3-3**. *J Biol Chem* 1995, **270**:21875-21883.

251. Heyduk T, Heyduk E: **Molecular beacons for detecting DNA binding proteins**. *Nat Biotechnol* 2002, **20**:171-176.

252. Liu YS, Sompornpisut P, Perozo E: **Structure of the KcsA channel intracellular gate in the open state**. *Nat Struct Biol* 2001, **8**:883-887.

253. Park PS, Filipek S, Wells JW, Palczewski K: **Oligomerization of G Protein-Coupled Receptors: Past, Present, and Future**. *Biochemistry* 2004, **43**:15643-15656.

254. Blasie JK, Worthington CR: **Planar liquid-like arrangement of photopigment molecules in frog retinal receptor disk membranes**. *J Mol Biol* 1969, **39**:417-439.

255. Blasie JK, Worthington CR: **Molecular localization of frog retinal receptor photopigment by electron microscopy and low-angle X-ray diffraction**. *J Mol Biol* 1969, **39**:407-416.

256. Chabre M: **X-ray diffraction studies of retinal rods. I. Structure of the disc membrane, effect of illumination**. *Biochim Biophys Acta* 1975, **382**:322-335.

257. Roof DJ, Heuser JE: **Surfaces of rod photoreceptor disk membranes: integral membrane components**. *J Cell Biol* 1982, **95**:487-500.

258. Fotiadis D, Liang Y, Filipek S, Saperstein DA, Engel A, Palczewski K: **The G protein-coupled receptor rhodopsin in the native membrane**. *FEBS Lett* 2004, **564**:281-288.

259. Niu L, Kim JM, Khorana HG: **Structure and function in rhodopsin: asymmetric reconstitution of rhodopsin in liposomes**. *Proc Natl Acad Sci U S A* 2002, **99**:13409-13412.

260. Oprian DD, Molday RS, Kaufman RJ, Khorana HG: **Expression of a synthetic bovine rhodopsin gene in monkey kidney cells**. *Proc Natl Acad Sci U S A* 1987, **84**:8874-8878.

261. Rigaud JL, Paternostre MT, Bluzat A: **Mechanisms of membrane protein insertion into liposomes during reconstitution procedures involving the use of detergents. 2. Incorporation of the light-driven proton pump bacteriorhodopsin**. *Biochemistry* 1988, **27**:2677-2688.

262. Fenske DB, MacLachlan I, Cullis PR: **Stabilized plasmid-lipid particles: a systemic gene therapy vector**. *Methods Enzymol* 2002, **346**:36-71.

263. Kenworthy AK, Edidin M: **Distribution of a glycosylphosphatidylinositol-anchored protein at the apical surface of MDCK cells examined at a resolution of <100 A using imaging fluorescence resonance energy transfer**. *J Cell Biol* 1998, **142**:69-84.

264. Kenworthy AK: **Imaging protein-protein interactions using fluorescence resonance energy transfer microscopy**. *Methods* 2001, **24**:289-296.

265. Li E, You M, Hristova K: **Sodium dodecyl sulfate-polyacrylamide gel electrophoresis and forster resonance energy transfer suggest weak interactions between fibroblast growth factor receptor 3 (FGFR3) transmembrane domains in the absence of extracellular domains and ligands**. *Biochemistry* 2005, **44**:352-360.

266. Dewey TG, Hammes GG: **Calculation on fluorescence resonance energy transfer on surfaces**. *Biophys J* 1980, **32**:1023-1035.

267. Wolber PK, Hudson BS: **An analytic solution to the Forster energy transfer problem in two dimensions**. *Biophys J* 1979, **28**:197-210.

268. Yguerabide J: **Theory for establishing proximity relations in biological membranes by excitation energy transfer measurements**. *Biophys J* 1994, **66**:683-693.

269. Snyder B, Freire E: **Fluorescence energy transfer in two dimensions. A numeric solution for random and nonrandom distributions**. *Biophys J* 1982, **40**:137-148.

270. Shaklai N, Yguerabide J, Ranney HM: **Interaction of hemoglobin with red blood cell membranes as shown by a fluorescent chromophore**. *Biochemistry* 1977, **16**:5585-5592.

271. Fung BK, Stryer L: **Surface density determination in membranes by fluorescence energy transfer**. *Biochemistry* 1978, **17**:5241-5248.

272. Selvin PR: **Principles and biophysical applications of lanthanide-based probes**. *Annu Rev Biophys Biomol Struct* 2002, **31**:275-302.

273. Fisher LE, Engelman DM, Sturgis JN: **Detergents modulate dimerization, but not helicity, of the glycophorin A transmembrane domain**. *J Mol Biol* 1999, **293**:639-651.

274. Yang K, Farrens DL, Altenbach C, Farahbakhsh ZT, Hubbell WL, Khorana HG: **Structure and function in rhodopsin. Cysteines 65 and 316 are in proximity**

in a rhodopsin mutant as indicated by disulfide formation and interactions between attached spin labels. *Biochemistry* 1996, **35**:14040-14046.

275. Yu H, Kono M, Oprian DD: **State-dependent disulfide cross-linking in rhodopsin**. *Biochemistry* 1999, **38**:12028-12032.

276. Gelasco A, Crouch RK, Knapp DR: **Intrahelical arrangement in the integral membrane protein rhodopsin investigated by site-specific chemical cleavage and mass spectrometry**. *Biochemistry* 2000, **39**:4907-4914.

277. Cai K, Klein-Seetharaman J, Hwa J, Hubbell WL, Khorana HG: **Structure and function in rhodopsin: effects of disulfide cross-links in the cytoplasmic face of rhodopsin on transducin activation and phosphorylation by rhodopsin kinase**. *Biochemistry* 1999, **38**:12893-12898.

278. Palczewski K, Buczylko J, Kaplan MW, Polans AS, Crabb JW: **Mechanism of rhodopsin kinase activation**. *J Biol Chem* 1991, **266**:12949-12955.

279. Heyduk T, Heyduk E: **Luminescence energy transfer with lanthanide chelates: interpretation of sensitized acceptor decay amplitudes**. *Anal Biochem* 2001, **289**:60-67.

280. Heyduk E, Heyduk T: **Thiol-reactive, luminescent Europium chelates: luminescence probes for resonance energy transfer distance measurements in biomolecules**. *Anal Biochem* 1997, **248**:216-227.

281. Selvin PR, Hearst JE: **Luminescence energy transfer using a terbium chelate: improvements on fluorescence energy transfer**. *Proc Natl Acad Sci U S A* 1994, **91**:10024-10028.

282. Selvin PR, Rana TM, Hearst JE: **Luminescence Resonance Energy Transfer**. *J. Am. Chem. Soc.* 1994, **116**:6029-6030.

283. Hofmann KP, Pulvermuller A, Buczylko J, Van Hooser P, Palczewski K: **The role of arrestin and retinoids in the regeneration pathway of rhodopsin**. *J Biol Chem* 1992, **267**:15701-15706.

284. Han M, Gurevich VV, Vishnivetskiy SA, Sigler PB, Schubert C: **Crystal structure of beta-arrestin at 1.9 A: possible mechanism of receptor binding and membrane Translocation**. *Structure (Camb)* 2001, **9**:869-880.

285. Granzin J, Wilden U, Choe HW, Labahn J, Krafft B, Buldt G: **X-ray crystal structure of arrestin from bovine rod outer segments**. *Nature* 1998, **391**:918-921.

286. Gurevich VV, Gurevich EV: **The molecular acrobatics of arrestin activation**. *Trends Pharmacol Sci* 2004, **25**:105-111.

287. Wald G, Brown PK: **The molar extinction of rhodopsin**. *J Gen Physiol.* 1953, **20**:189-200.

288. Chen RF: **Fluorescence quantum yield measurements: vitamin B6 compounds**. *Science* 1965, **150**:1593-1595.

289. Xiao M, Selvin PR: **An improved instrument for measuring time-resolved lanthanide emission and resonance energy transfer.** *Rev.Sci.Instrum.* 1999, **70**:3877-3881.

290. Dale RE, Eisinger J, Blumberg WE: **The orientational freedom of molecular probes. The orientation factor in intramolecular energy transfer**. *Biophys J* 1979, **26**:161-193.

291. Vaiana AC, Neuweiler H, Schulz A, Wolfrum J, Sauer M, Smith JC: **Fluorescence quenching of dyes by tryptophan: interactions at atomic detail from combination of experiment and computer simulation**. *J Am Chem Soc* 2003, **125**:14564-14572.

292. Marme N, Knemeyer JP, Sauer M, Wolfrum J: **Inter- and intramolecular fluorescence quenching of organic dyes by tryptophan**. *Bioconjug Chem* 2003, **14**:1133-1139.

293. Neuweiler H, Sauer M: **Using photoinduced charge transfer reactions to study conformational dynamics of biopolymers at the single-molecule level**. *Curr Pharm Biotechnol* 2004, **5**:285-298.

294. Mansoor SE, Farrens DL: **High-throughput protein structural analysis using site-directed fluorescence labeling and the bimane derivative (2-pyridyl)dithiobimane**. *Biochemistry* 2004, **43**:9426-9438.

295. Mansoor SE, Palczewski K, Farrens DL: **Rhodopsin self-associates in asolectin liposomes**. *Proc Natl Acad Sci U S A* 2006, **103**:3060-3065.

296. Borochov-Neori H, Fortes PA, Montal M: **Rhodopsin in reconstituted phospholipid vesicles. 2. Rhodopsin-rhodopsin interactions detected by resonance energy transfer**. *Biochemistry* 1983, **22**:206-213.

297. Donnelly D, Overington JP, Blundell TL: **The prediction and orientation of alpha-helices from sequence alignments: the combined use of environment-dependent substitution tables, Fourier transform methods and helix capping rules**. *Protein Eng* 1994, **7**:645-653.

298. Koteiche HA, Reeves MD, McHaourab HS: **Structure of the substrate binding pocket of the multidrug transporter EmrE: site-directed spin labeling of transmembrane segment 1**. *Biochemistry* 2003, **42**:6099-6105.

299. Cortes DM, Cuello LG, Perozo E: **Molecular architecture of full-length KcsA: role of cytoplasmic domains in ion permeation and activation gating**. *J Gen Physiol* 2001, **117**:165-180.

300. Kaplan RS, Mayor JA, Kotaria R, Walters DE, McHaourab HS: **The yeast mitochondrial citrate transport protein: determination of secondary structure and solvent accessibility of transmembrane domain IV using site-directed spin labeling**. *Biochemistry* 2000, **39**:9157-9163.

301. Perozo E, Kloda A, Cortes DM, Martinac B: **Site-directed spin-labeling analysis of reconstituted Mscl in the closed state**. *J Gen Physiol* 2001, **118**:193-206.

302. Li M, Reddy LG, Bennett R, Silva ND, Jr., Jones LR, Thomas DD: **A fluorescence energy transfer method for analyzing protein oligomeric structure: application to phospholamban**. *Biophys J* 1999, **76**:2587-2599.

303. Veatch W, Stryer L: **The dimeric nature of the gramicidin A transmembrane channel: conductance and fluorescence energy transfer studies of hybrid channels**. *J Mol Biol* 1977, **113**:89-102.

304. McHaourab HS, Berengian AR, Koteiche HA: **Site-directed spin-labeling study of the structure and subunit interactions along a conserved sequence in the alpha-crystallin domain of heat-shock protein 27. Evidence of a conserved subunit interface**. *Biochemistry* 1997, **36**:14627-14634.

305. Selvin PR: **The renaissance of fluorescence resonance energy transfer**. *Nat Struct Biol* 2000, **7**:730-734.

306. Vereb G, Jares-Erijman E, Selvin PR, Jovin TM: **Temporally and spectrally resolved imaging microscopy of lanthanide chelates**. *Biophys J* 1998, **74**:2210-2222.

307. Chen J, Selvin PR: **Thiol-reactive luminescent chelates of terbium and europium**. *Bioconjug Chem* 1999, **10**:311-315.

Appendix 1

Tryptophan Fluorescence Quenching of Four Different Fluorophores: A Calibration Study

Steven E. Mansoor[‡], Mark A. DeWitt[‡] and David L. Farrens[‡]

[‡] Department of Biochemistry and Molecular Biology, Oregon Health and Science
University, Portland, Oregon 97239-3098, USA

A1. 1: SUMMARY

In this appendix, I assessed the ability of several fluorescent probes, qBBr, lucifer yellow, bodipy 507/535 and Atto-655, to be quenched by proximal tryptophan residues. The goal of this work was to calibrate the effect of tryptophan residues on these fluorophores while bound to a protein of known structure. Such a calibration is essential in order to use these fluorophores as structural probes in SDFL studies. Using the same T4 lysozyme system for these fluorophores as used for bimane (see Chapter 2 and Chapter 3) enables direct comparisons to be made across the set of fluorophores. Although all four fluorophores were quenched by proximal Trp residues, the amount of quenching differed for each probe when attached to the same sites on T4 lysozyme. This suggests that each fluorophore has a different "sphere of quenching", reflected by its size and the rotational flexibility of its attachment to the protein. Thus, the best fluorophore for determining distances by Trp quenching in an SDFL study will depend on the application. Fluorophores with smaller "spheres of quenching" (identified as bimanes or bodipy in this study) will be more useful for measuring short-range distances in proteins or for detecting conformational changes in a protein. Probes with a larger "sphere of quenching" (such as lucifer yellow or Atto-655) will be more useful for protein/protein studies where detection of a robust, binary signal is desired.

All experiments performed with qBBr, all data analysis, and all writing of this appendix were performed by the author of this dissertation. The experiments performed using all other fluorophores were performed by Mark A. DeWitt under the direction of the author of this dissertation. The DNA plasmid constructs used to express the protein samples were supplied by Dr. Hassane S. Mchaourab.

A1. 2: INTRODUCTION

Site-directed labeling (SDL) methods are emerging as powerful tools for assessing protein structure and conformational dynamics [49,64,73-76,170,191,222,294]. These approaches can provide invaluable structural information even in protein systems that are not easily amenable to NMR spectroscopy and X-ray crystallography [40,45,171]. Unlike these other techniques, SDL studies may be undertaken in dilute aqueous solutions, at physiological temperature and pH. The SDL techniques involve engineering cysteine residues into strategic locations in a protein to which either a spin-label or a fluorescent-label reporter probe is subsequently attached. The characteristics of the reporter probe can reveal the mobility or the solvent accessibility of the site of attachment. Determination of how these parameters change in a scan through a sequence can provide protein secondary structural information in a full-length protein [64,170,186,238,294,304] or in a short peptide [73].

The above scanning approach works well for assessing secondary structure but knowledge about tertiary structure requires distance constraints. Traditionally, fluorescence spectroscopy methods to measure distance has employed fluorescence energy transfer methodologies (FRET) [77,78]. Although powerful, FRET methods are complicated by the need to label with two different, spectrally overlapping probes at or near 100% labeling efficiency. In addition, FRET measurements are also limited to longer-range distances (~ 20 – 100 Å), often too large for determining close packing between sites in a protein. Since the sizes of many traditional fluorescent probes are usually larger than 10 Å, local conformational changes in protein structure upon activation may go undetected using FRET based approaches.

As described in Chapter 2 and 3, I recently helped develop a fluorescent approach complementary to FRET, which enables measurement of short-range distances (~ 5 – 15 Å) in proteins [170,294]. This technique exploits the fact that tryptophan (Trp) residues in a protein will specifically quench the fluorescence of a proximal bimane fluorophore. In contrast to FRET, this effect only works at short distances, as it requires close proximity (or van der Waal's contact) between dye and quencher for fast and efficient quenching. Because the quenching effect is distance-dependent and orientation specific, the amount and type of quenching observed reliably reflects the distance between the Trp residue and the bimane label.

Recently, Trp quenching of bimane fluorescence has been used to identify key sites for the interaction between visual rhodopsin and its G-protein transducin [45], to orient the interaction between molecular chaperone proteins and their targets [172,173], to investigate the dynamic structural changes in a cyclic nucleotide-gated ion channel upon activation [171], and to investigate a key conformational change involved in GPCR activation [40]. Together, these studies demonstrate the broad applicability of the Trp/bimane quenching methodology.

Quenching of fluorescence by proximal Trp residues is not unique to bimane. Since our original manuscript on the use of Trp/bimane quenching for protein structural studies [170], a number of other reports have used Trp quenching of various organic dyes such as Atto-655 and Bodipy [291-293] to probe molecular recognition and conformational dynamics of biopolymers such as DNA.

To date, our bimane studies are the only published manuscripts which have standardized the Trp quenching effect on a fluorescent probe attached to a protein of known structure (T4 lysozyme). Thus, in this Appendix, we have assessed the ability of several other fluorescent probes to be quenched by proximal tryptophan residues. Such a study is a required step toward using these other fluorophores as structural probes since the physical and spectroscopic properties of the fluorophore (such as size, shape, and conformational flexibility) can alter the relationship between quenching and distance. We decided to assay each Trp/fluorophore pair (to correlate the amount of quenching observed to distances between the two molecules) using the same T4 lysozyme system as was used for bimane (see Chapter 2 and Chapter 3). Thus, the data reported in this appendix can be directly compared with our previous work.

The fluorescent probes studied here were chosen because (1) their different spectral properties should prove useful under various experimental conditions and (2) they have been previously reported to be sensitive to Trp induced quenching [291-293]. These probes are: monobromotrimethylammoniobimane (qBBr), lucifer yellow, bodipy 507/535, and Atto-655. The structures of these probes are shown Figure A1. 1A. Note that these fluorophores span a wide range of absorbance and emission wavelengths (see Figure A1. 1B). The exact Atto-655 structure is not known to the public (USPTO # 2006/0179585 A1)

A1. 3: EXPERIMENTAL PROCEDURES

A1. 3. 1: Materials.

Unless otherwise mentioned, all reagents and biochemical supplies (buffers, salts, concentrators, plastic-ware, etc) were purchased from Fisher or Sigma and their affiliates, except Tris base and ultrapure guanidine HCl, which were purchased from Invitrogen

(Carlsbad, CA). qBBr was purchased from Toronto Research Chemicals (North York, Ontario, Canada). BODIPY 507/535 iodoacetamide and Lucifer Yellow iodoacetamide were purchased from Molecular Probes (Eugene, OR). Cy5-maleimide was purchased from GE Healthcare. Atto-655 maleimide was purchased from Atto-tec (Siegen, Germany).

A1. 3. 2: Buffers.

The buffers used were as follows: buffer A, 50 mM MOPS, 50 mM Tris, and 1 mM EDTA, pH 7.6; buffer B, 20 mM Tris, 20 mM MOPS, 0.02% sodium azide, 1 mM EDTA, and 1 mM DTT, pH 7.6; buffer C, 20 mM KH_2PO4 and 25 mM KCl, pH 3.0; buffer D, 50 mM MOPS, 50 mM Tris, 1 mM EDTA, pH 7.6, and 3 M guanidine hydrochloride; Buffer E, 250 mM MOPS, 250 mM Tris, 1 mM EDTA, pH 7.6; buffer F, 12 g tryptone digest, 5 g yeast extract, 10 g NaCl, 1 g glucose, 1 mL 100 mg/mL ampicillin per liter of medium.

A1. 3. 3: Construction, Expression and Purification of T4 Lysozyme Mutants.

The construction of the cysteine mutants used in the present work has been previously described in detail (refer to section **2. 3. 3)**. For expression, K38 *Escherichia coli* cells were transformed with the T4L cysteine-mutant plasmid and inoculated into 25 mL of buffer F and grown overnight with shaking. The next morning, 10-15 mL of overnight growth was added to 500 mL of buffer F in a 2.8 L flask, and grown with ≥ 250 rpm shaking at 37ºC. Protein production was induced in log phase cultures (OD_{600} of ~1.2) by the addition of IPTG to a final concentration of 1 mM. The induced cultures were allowed to express for 1.5 - 2 hours until harvesting by centrifugation. Pelleted cultures were stored at -80 ºC for later use.

Purification of mutant T4L was performed using a slight modification of a previously described protocol (refer to section **2. 3. 5**). Briefly, thawed pellets containing expressed mutant lysozyme (see above) were resuspended manually in 30 - 35 mL Buffer B, lysed, and cleared by centrifugation at 10,000 *g* for 30 minutes. DTT was added to ~20 mM, and the lysate was filtered (0.45 μm filter) and loaded onto a cation exchange column (GE Healthcare HiTrap, 1 mL SP Sepharose) pre-equilibrated with buffer A. The samples were eluted with a salt gradient in buffer A (ramped from 0 to 1 M NaCl). T4 lysozyme, eluted at around 200 - 300 mM NaCl, was collected in multiple fractions, snap-frozen in liquid nitrogen, and stored at -80 ºC. The purity of the fractions was assessed by SDS-PAGE and judged to be at least 90% pure for all samples studied.

A1. 3. 4: Fluorescence Labeling of T4L Mutants.

Because the fluorophores used in this appendix possess a variety of reactive groups and solubilities, the method used to label the T4 lysozyme mutants with each fluorophore was slightly different. In general, labeling of ~10 nanomoles of each lysozyme mutant (~100 µM T4L concentration) was carried out using ~ 5 – 10x molar excess of fluorescent label, taken from stock solutions made in DMSO. Labeling was carried out in buffer D at 4 °C overnight (5x for BODIPY and Lucifer Yellow, 7x for Cy5 maleimide, 10x for Atto-655 maleimide and qBBr). Care was taken to ensure that DMSO concentrations were always ≤ 10% of final reaction volume.

For the fluorophores using a maleimide attachment (Atto-655 and CY5), 1M MOPS was added to lower the pH to ~ 6.5 to avoid amine reactivity and maleimide ring opening. For the BODIPY 507/535 reactions, DMSO was added to a final concentration of 10% to help improve solubility of the relatively insoluble free label. The reactions were then incubated overnight with rocking at 4ºC in the dark. For qBBr, unreacted free label was separated from the labeled protein by gel filtration on a desalting column (Pharmacia Biotech HiTrap, 5 mL) equilibrated with buffer A. For all other labels, free label was removed from the reaction solution using G-15 Sephadex in a small desalting column (1.25 cm x 3 cm) with buffer A and gravity flow. Absorbance spectra (measured using a Shimadzu UV 1601) were used to calculate the labeling efficiency for each mutant.

Concentrations were calculated using extinction coefficients of ε_{280} = 23327 L cm^{-1} mol^{-1} for T4 lysozyme. To correct for mutants in which a Trp residue was either introduced or removed, an extinction coefficient value of ε_{280} = 5600 L cm^{-1} mol^{-1} was either added or subtracted to the WT T4 lysozyme extinction coefficient. (Note that a mutation from a tryptophan to a phenylalanine resulted in an extinction coefficient of ε_{280} = 18027 L cm^{-1} mol^{-1}.) Concentrations of label were approximated using the appropriate extinction coefficient for each label (ε_{508} = 64000 L cm^{-1} M^{-1} for BODIPY; ε_{427} = 11,000 L cm^{-1} M^{-1} for Lucifer Yellow, ε_{655} = 125, 000 L cm^{-1} M^{-1} for Atto-655, ε_{650} = 250,000 L cm^{-1} M^{-1} for Cy5, and ε_{380} = 5,000 L cm^{-1} M^{-1} for qBBr). The contribution from each label at 280 nm was subtracted before calculating the protein concentrations.

All reacted T4 lysozyme mutants were analyzed by SDS-PAGE for purity and determined to be > 90% pure. Levels of unreacted free label in the samples for all labels except Atto-655 were determined using a TCA precipitation protocol, as described previously (see section **3. 3. 16**). Note, this approach could not be used for Atto-655 as it was not fluorescent in acid. The amount of fluorescence retained following acid precipitation was taken to be due to unreacted free label, which was < 3% for all samples tested, except for the Cy5-labeled negative controls.

A1. 3. 5: Nomenclature.

Throughout this appendix, mutants are named by specifying the original residue, the number of the residue, and the new residue, in that order. For example, the code N132C indicates that the native asparagine residue at the 132nd amino acid position was mutated to a cysteine. Similarly, N116W indicates the native asparagine was mutated to a tryptophan. For labeled mutant samples, the given protein is described by specifying the original residue, the number of the residue, and then an abbreviation for the label. Each fluorophore has its own suffix: B_3 for monobromotrimethylammoniobimane (qBBr), -LY for lucifer yellow, –By for Bodipy, -Atto for Atto-655, and -Cy5 for Cyanine-5. Thus, for example, the code $N132B_3$ indicates that the native lysine residue at the 132nd amino acid position has been mutated to a cysteine and reacted with the qBBr label. References made to the general sample set, and not a specific mutant, for a particular fluorophore will be called T4L-suffix (suffix as above).

A1. 3. 6: Assessment of Fluorophore Quenching by Free Amino Acids.

All measurements were performed using a PTI steady-state fluorimeter, with 1 nm excitation slits (3 nm for QBBr), and 3 nm emission slits. Amino acids were made up to 60 mM stock concentrations in Buffer E. Note - since tyrosine is only minimally soluble in this buffer, the tyrosine methyl ester derivative was used. For the quenching experiments, fluorophores were used at a range of concentrations between 1 – 10 μM in buffer E. Unquenched intensity was taken as the buffer-subtracted integrated fluorescence of the fluorophore stock diluted 1:1 with buffer E. Quenched intensity was taken as the buffer-subtracted integrated fluorescence of the same fluorophore stock diluted 1:1 with 60 mM amino acid stock (50 mM for Tryptophan diluted to 30 mM final concentration) in Buffer E. The ratio of the fluorescence intensities in the presence of quencher to the fluorescence intensity in the absence of quencher (30 mM amino acid) is reported as a relative quantum yield.

A1. 3. 7: Thermodynamic Stability.

Analysis of thermal unfolding properties was used to assess the stability of a subset of the labeled mutants. Since the unfolding measurements are carried out at pH 3, the samples (originally in Buffer A) were thawed and dialyzed at 4 °C overnight against buffer C (pH 3) with at least three changes of reservoir. The pH of the reservoir was monitored before and after each change to ensure it was around 3.00 +/- 0.03. The CD melts were performed by monitoring the helical signal at 222 nm on ~ 350 μL of each sample at concentrations between 3.5 μM - 6 μM. Slit widths were 1 nm. The melts involved ramping the temperature from 5 to 85 °C, after which the samples were cooled to 5 °C to determine the extent of protein refolding. The labeled samples exhibited greater than 75% refolding, as judged by the extent to which the CD signal returned to its starting value.

A1. 3. 8: Steady-State Fluorescence and Anisotropy Measurements.

All steady-state fluorescence excitation, emission, and anisotropy measurements were carried out using a PTI fluorescence spectrometer in a T-format at 22 °C. The parameters of the fluorescence emission spectra for each fluorophore labeled sample were measured as follows. T4L-B_3: 380 nm excitation, 395 – 600 nm emission, 2 μM sample, 1 nm exc. slits, 10 nm emission slits; T4L-LY: 427 nm excitation, 432 - 750 nm emission, 2-3 µM sample, 1 nm excitation slits, 3 nm emission slits; T4L-By: 490 nm excitation, 495 - 750 nm emission, 1.5-2.5 µM sample, 1 nm excitation slits, 3 nm emission slits; T4L-Atto: 620 nm excitation, 625 - 900 nm emission, 0.7-1 µM labeled sample, 1 nm excitation slits, 3 nm emission slits; T4L-Cy5: 615 nm excitation, 620 - 850 nm emission, 0.3-0.5 µM sample, 1 nm excitation slits, 3 nm emission slits.

Anisotropy measurements were carried out at 22ºC using each labeled T4L sample at above concentrations in buffer A. Excitation/emission for each set of labeled samples taken at the maxima for each fluorophore: 381/475 for T4L-B_3; 506/530 for T4L-By; 427/525 for T4L-LY; 664/678 for T4L-Atto, and 650/665 for T4L-Cy5. For all samples, excitation slits were set at 3 nm and emission slits were 5 nm. The measurements were performed in duplicate and the average steady-state anisotropy was obtained using buffer subtraction of individual intensities and real-time emission and excitation correction.

A1. 3. 9: Quantum Yield Measurements.

The quantum yield of each mutant labeled with qBBr, lucifer yellow and bodipy were measured using quinine sulfate as the standard (quantum yield of 0.55 in 1 N H_2SO_4). For mutants labeled with Atto-655 and Cy5, rhodamine 6G was used as the standard (quantum yield of 0.94 in ethanol). For the red-shifted fluorophores (BODIPY, Atto 655, and Cy5), emission correction was used to account for drop-off of photomultiplier tube sensitivity at longer wavelengths. Measurements were made by matching the absorbance maximum of the standard to each of the labeled T4 lysozyme samples and measuring integrated fluorescence emission intensity under identical optical conditions (350 nm excitation, 355-750 nm emission for quinine sulfate; 500 nm excitation, 505-750 nm emission for rhodamine). In all cases, the buffer intensity was subtracted before integrating the fluorescence intensity.

A1. 3. 10: Fluorescence Lifetime Measurements.

Fluorescence lifetimes for all the samples (except the Bodipy labeled samples) were measured at 22ºC using a PTI Laserstrobe fluorescence lifetime instrument at sample concentrations identical to those used for the steady-state measurements (see section **A1. 3. 8**). The lifetimes for the Bodipy-labeled samples were measured at 22ºC using the PTI EasyLife system, with excitation from a 505 nm LED and emission collected using longpass filters. The instrument response function (IRF ~ 1.5 ns) was determined using a solution of Ludox. Measurements were set up to ensure < 5% measured intensity due to scattered light using the following parameters for each fluorophore set. T4L-qBBr: measurements used 381 nm excitation passed through a 298-435 nm band-pass filter, and emission was monitored through two long-pass filters (> 470 nm). Each lifetime decay was measured using two averages of five shots per point, collected randomly in time over 150 channels; T4L-By: Measurements used a 500 nm interference filter on excitation from a 505 nm LED, and emission was collected using two > 520 nm plus one > 550 nm longpass filters on emission. Each lifetime decay was measured using three averages of 150 data points collected randomly in time; T4L-LY: Measurements used 427 nm excitation and emission collected on a monochromator at 527 nm (6 nm slits) plus two > 500 nm longpass filters. Each decay was measured using two averages of 400 data points collected randomly in time; T4L-Atto: Measurements used 640 nm excitation and emission was collected at 676 nm emission (6 nm slits). Each lifetime decay was measured using two averages of 300 data points collected randomly in time using PTI software.

A1. 4: RESULTS

Overview. The goals in this appendix are to: (1) identify new fluorophores that are susceptible to Trp induced quenching, and (2) calibrate the extent of Trp induced quenching of these probes attached to T4 lysozyme, thus establishing an expanded set of probes that researchers can use to measure short-range distances in proteins by SDFL.

To do this, I first searched the literature and identified four other probes reported to show susceptibility to Trp quenching. These probes are: monobromotrimethylammoniobimane (qBBr), lucifer yellow, Bodipy 507/535, and Atto-655 (Cy5 was used as a negative control). Each of these probes was then used to label mutants of T4 lysozyme and each sample was then subjected to an array of fluorescence measurements with and without a proximal Trp residue at position 116 near the site of attachment. A subset of the labeled mutants was further characterized thermodynamically to assess the extent of destabilization caused by introduction of each of the fluorescent labels. The results are discussed below.

A1. 4. 1: Measurement of Amino Acid Quenching of the Fluorophores in Solution.

Table A1. 1 shows the results of measuring the relative effect on fluorescence intensity of several different amino acids known to cause fluorescence quenching [69]. As expected, we observed significant Trp induced quenching for qBBr, lucifer yellow, bodipy, and atto-655. In some cases, tyrosine also caused some quenching. As expected, the negative control, Cy5, was not significantly quenched by any of the amino acids.

Importantly, the other amino acids often shown to cause fluorescence quenching did not substantially affect the fluorescence of any of the probes. The effect of Trp on these probes was next studied further while attached to T4 lysozyme (discussed below).

A1. 4. 2: Thermodynamic Analysis of a Subset of Labeled Lysozyme Mutants.

The labeling efficiencies for the complete set of mutants are shown in Table A1. 2. As seen from the Table A1. 2, the labeling efficiencies ranged from 50% to 100%. It is important to note that the extent of quenching is not sensitive to labeling efficiency, since a Trp residue is always present in the sequence.

A subset of the labeled mutants were also subjected to a thermodynamic analysis (Table A1. 3). The thermodynamic stability assays were performed on labeled samples E128C and N116W/E128C, as addition of mBBr and PDT-Bimane to these sites were previously shown to cause minimal perturbation [170,294]. Thus, the effect of qBBr, lucifer yellow, bodipy, and atto-655 on protein stability can be compared to both mBBr and PDT-Bimane (see Chapter 2 and Chapter 3).

The thermodynamic stability was measured by following the CD signal at 222 nm with increasing temperature [198]. These measurements were used to calculate the T_m and ΔΔG values reported in Table A1. 3. The measurements indicate that protein stability, as assessed by ΔΔG values, is not any more impaired for qBBr, lucifer yellow, or bodipy than it is for samples labeled with mBBr or PDT-Bimane (ΔΔG values ~ - 0. 7 kcal/mole). The impairment was more substantial for Atto-655 (ΔΔG value ~ - 1. 6 kcal/mole), although this might be expected since it is the largest of the probes (Figure A1. 1).

A1. 4. 3: Spectral Properties of mBBr-Labeled Mutants.

Table A1. 2 reports the stead-state fluorescence parameters for all the labeled mutants studied: absorbance λ_{max}, emission λ_{max}, quantum yields, and steady-state anisotropy values. The table clearly demonstrates how the quantum yields for some of the fluorescently labeled samples are dramatically affected by the Trp residue at site 116.

Table A1. 2 reports the absorbance λ_{max} and emission λ_{max} values for each labeled mutant. Generally, these parameters are not affected for most of the fluorophores. However, a trend in the absorbance λ_{max} values is evident for the lucifer yellow samples. Specifically, there appear to be shifts in the absorbance λ_{max} values between E128-LY and N116W/E128-LY and between N132-LY and N116W/N132-LY. In comparison, no shifts in the excitation λ_{max} values between the same sets of mutants are observed. A possible interpretation of these results is presented in the Discussion section **A1. 5. 4**.

A1. 4. 4: The Fluorophores Show Differential Amounts of Quenching from the Trp at Site 116.

Figure A1. 2 demonstrates that Trp quenching of qBBr fluorescence is distance-dependent. Labels at sites 132 and 128 show the most quenching and labels at site 135 show the least. The quenching pattern observed for qBBr is comparable to that observed for both mBBr (see Chapter 2) and PDT-Bimane (see Chapter 3).

The steady-state quenching patterns for each of the samples labeled with lucifer yellow, bodipy, and Atto are shown in Figure A1. 3. Notice that, in general, the relative pattern of quenching is the same: sites 132 and 128 for each label show more quenching than sites 123 and 135, consistent with the relative distance of each of these residues to the Trp residue at site 116. However, the relative amount of quenching <u>between</u>

fluorophores on the same samples varies substantially. For example, bodipy shows absolutely no quenching at site 135 while Atto shows significant quenching at site 135. The significance of this result is covered in the Discussion of this Appendix.

A1. 4. 5: Fluorescence Lifetimes for each Labeled Sample.

The fluorescence lifetimes of the each of the labeled T4L mutants were measured and analyzed using either a mono-exponential or two-exponential fit. The results for the qBBr labeled samples can be seen in Table A1. 4 and the results for the lucifer yellow, bodipy, and atto-labeled samples are in Table A1. 5. In the case of two-exponential fits, the amplitude-weighted average lifetime, $<\tau>$, is reported. The amplitude-weighted average lifetime is proportional to the steady-state fluorescence intensity [69].

A1. 5: DISCUSSION

Overview. My goal in this appendix was to test and calibrate the extent of Trp quenching on the fluorescence of four fluorophores. As discussed below, the results clearly show that although the relative quenching pattern observed for each fluorophore at the labeled sites in T4 lysozyme is consistent with the distance from the Trp residue, the absolute value in the amount of quenching for each fluorophore is different. This is a very important point for trying to correlate the size of the quenching signal to distances.

Probable Mechanism of Trp-Induced Fluorescence Quenching. Based on earlier observations by Kosower, the likely mechanism for the Trp induced quenching of bimane fluorescence involves a photo-induced electron transfer (PET) mechanism [208,212] in which an electron is transferred from the Trp residue to a proximal excited-state bimane fluorophore, producing a transient radical ion pair: Trp $(+\cdot)$:Bim$(-\cdot)$. This is discussed in further detail in Chapter 2. If the other fluorophores studied here are also quenched through a PET mechanism, as suggested by several authors [291-293], it is crucial to calibrate their extent of quenching on a protein of known structure for the following reasons. First, although PET-induced quenching requires close proximity between dye and quencher, the rates (and thus the amounts of quenching observed) are known to be dependent on variables such as solvent polarity of protein surfaces [216], steric and stereochemical factors [217], and shape and relative orientation of the two molecule pairs [218]. Furthermore, the probes have different modes of attachment and linker lengths which further complicate *a priori* assumptions.

A1. 5. 1: Unique Properties of Each Fluorescent Probe.

Each fluorescent probe in this study was chosen because of its unique set of properties that make it desirable for an SDFL study. The advantages and disadvantages of each probe are discussed below.

qBBr. The qBBr fluorophore absorbs in the UV and is a small, positively charged fluorophore that should not penetrate a biological membrane. Because it is small, like the other bimanes, it should be less perturbing to the overall fold of a protein when attached. The charged nature of qBBr can be used to preserve protein function and structural integrity in situations where a charged residue must be maintained. The positive charge on qBBr also allows it to be useful to label on extracellular cysteine residue on a receptor, for example, in whole cell studies, as it does not penetrate the membrane. However, because qBBr absorbs in the UV and only has an extinction coefficient of about 5000 L cm^{-1} M^{-1}, use of this probe for whole cell studies may result in low signal to noise ratios due to high background absorbance.

Bodipy. Bodipy has many of the advantages of bimane – it too is very small, and it shows great distance selectivity. It is better than bimane in that it is more highly absorbant (ε_{508} = 64000 L cm^{-1} M^{-1} for bodipy and ε_{380} = 5000 L cm^{-1} M^{-1} for bimane), and it is significantly red-shifted, allowing its use in biological tissue with less background absorbance. However, we found bodipy to be more difficult to work with than other probes, often causing a small amount of protein aggregation following repeated pipetting.

Lucifer Yellow LY is larger than both qBBr and bodipy. However, it exhibits a larger extinction coefficient (ε_{427} = 11,000 L cm^{-1} M^{-1} for Lucifer Yellow) and is red-shifted from the bimane fluorophores, moving its absorbance out of the UV.

Atto-655. Atto-655 is significantly red-shifted and its use would be ideal for cell microscopy studies. However, its selectivity for quenching by tryptophan residues is very broad (see below). It is also very costly.

A1. 5. 2: The Fluorophores Demonstrate Different "Spheres of Quenching".

The data from Figure A1. 2 and Figure A1. 3 demonstrate that even when attached to the same sites on a protein, the fluorescence of each probe is affected by proximal Trp residues to differing extents. For example, in Figure A1. 3, the steady-state quenching on each sample observed for bodipy is quite different from that observed for either lucifer yellow or atto-655. There is absolutely no quenching observed for N116W/K135-By, compared to K135-By. In contrast, there is roughly 3x quenching observed for N116W/K135-LY and N116W/K135-Atto compared to K135-Ly and K135-Atto, respectively. This means that at any given fluorophore/Trp distance, less quenching is observed for a bodipy label than for either lucifer yellow or atto-655 because it has a smaller “sphere of quenching”.

Bodipy may display a smaller or more selective “sphere of quenching” for several reasons. First, bodipy is substantially smaller than either lucifer yellow or atto-655 (Figure A1. 1A). Because PET quenching mechanisms require very close proximity (or even van der Waal’s contact), the smaller bodipy probe would have less opportunity to collide with a proximal Trp residue. In simple terms, it cannot reach the Trp residue as easily as a bigger, bulkier fluorophore. Additionally, bodipy has a shorter linkage to the cysteine residue than either lucifer yellow or atto-655. This may limit its rotational freedom and thus lower its ability to contact the Trp residue. Consistent with this interpretation, the steady-state anisotropies for bodipy are significantly higher than the anisotropies for lucifer yellow, supporting this assertion (Table A1. 2). The anisotropies for bodipy are only marginally higher than for Atto-655 (Table A1. 2).

A1. 5. 3: Each Fluorophore is Useful for Unique SDFL Experiments in Different Ways.

Along with the inherent spectroscopic advantages of one probe versus another, depending on the situation, different SDFL experiments will warrant probes with different “spheres of quenching.” For example, for experiments designed to measure short-range distances in proteins or to detect local, small-scale conformational changes in proteins, probes with a smaller “sphere of quenching” are preferable. This allows subtle protein movements directing the fluorophore either toward or away from a Trp residue to be discriminated. For such experiments, our studies presented here indicate either bodipy or qBBr (or mBBr or PDT-Bimane) are preferable.

However, for experiments hoping to assess a larger distance, our results show either lucifer yellow or atto-655 is preferable. These probes are larger than the other probes and have longer, more flexible linker attachments to the protein. Because of this, they clearly display a broader range of Trp quenching (versus bimane) at any given distance (compare Figure A1. 2 and Figure A1. 3). Thus, these probes might not be ideal for measuring short-range distances. However, they appear well suited for studying interactions between two proteins where a strong, binary quenching signal (ie., positive indication of binding) is desired.

A1. 5. 4: The Absorbance Spectra of Lucifer Yellow Provide Extra Information About Fluorophore/Trp Distances.

Although the “sphere of quenching” for lucifer yellow is larger than for bodipy or the bimanes and comparable to that of Atto-655, its absorbance spectra may provide additional information reflecting the distance between the fluorophore and the proximal Trp residue. Figure A1. 4 demonstrates that there is a sizeable shift in absorbance λ_{max} values for E128-LY compared to N116W/E128-LY and for N132-LY compared to N116W/N132-LY. No absorbance shift is measurable for Q123-Ly compared to N116W/Q123-Ly or K135-Ly compared to N116W/K135-Ly. Further, the excitation spectra (while monitoring emission at ~ 530 nm) for each of the lucifer yellow-labeled samples demonstrates absolutely no shifts in excitation λ_{max} values for any of the mutant pairs.

The absorbance λ_{max} shifts suggest the formation of a ground state complex between the Trp and lucifer yellow fluorophore mutants N116W/E128-LY and N116W/N132-LY. This was seen before for both mBBr and PDT-Bimane (see Chapter 2 and Chapter 3) when static quenching was observed and its also observed for qBBr (Table A1. 2). Thus, the shifts in absorbance λ_{max} values for lucifer yellow may suggest an additional piece of data to discriminate “close” fluorophore/Trp distances (~ 10 – 15 Å) from “very close” distances (~ 5 – 10 Å) where a static, ground state, non-fluorescent complex can be formed.

A1. 5. 5: Conclusions.

In summary, in this appendix, the Trp quenching effect for four fluorophores has been calibrated on a protein of known structure, T4 lysozyme. As is demonstrated, each fluorophore brings its own set of unique properties to an SDFL experiment, thus the decision of which probe to use will be governed by the goal of the experiment. For experiments that require the highest resolution discrimination of distances or local conformational changes in a protein, a probe with a small “sphere of quenching” like mBBr, PDT-Bimane, qBBr, or bodipy should be chosen. For experiments that do not require subtle discrimination of distances but rather a robust “binary” signal is better (for example, assessing protein/protein interactions), a fluorophore with a larger “sphere of quenching” such as lucifer yellow or atto-655 should be chosen. For each new Trp-sensitive probe identified, calibrations like those described here will need to be performed to establish which probes are the very best for each experimental paradigm.

Table A1. 1: Relative Quantum Yields[a] of Fluorophores in the Presence of 30 mM Selected Amino Acids.

Fluorophore	Trp	Tyr-ME	His	Phe	Met	Asp	Arg
qBBr	0.66	0.87	0.93	1.00	0.94	1.03	0.97
Lucifer Yellow	0.27	0.51	0.99	1.05	0.97	0.99	1.00
BODIPY 507	0.74	0.86	0.99	1.02	1.00	0.99	0.96
Atto-655	0.26	0.68	0.96	1.09	1.06	0.87	0.94
Cy5	0.93	1.02	0.98	1.01	0.99	0.97	1.01

[a] Relative quantum yields are calculated as the integrated fluorescence emission in the presence of 30 mM of the indicated amino acid divided by integrated emission intensity in buffer alone, as described in section **A1. 3. 6**. Amino acids used are indicated by their three-letter abbreviation, except “Tyr-ME” which is the methyl ester derivative of tyrosine. Results are an average of two independent assays.

Table A1. 2: Spectral Characterization of Labeled T4 Lysozyme Samples.

Mutant	**mol of label/mol of T4L**	**Abs. λ_{max} (nm)**	**Emm. λ_{max} (nm)**	**Quantum Yield (Φ)**	**Steady-State Anisotropy (r)**
Q123B$_3$	0.93	379	470	0.065	---
N116W/Q123B$_3$	0.98	379	469	0.037	---
E128B$_3$	0.95	385	467	0.093	---
N116W/E128B$_3$	0.89	380	467	0.018	---
N132B$_3$	0.76	375	468	0.088	---
N116W/N132B$_3$	0.97	396	467	0.014	---
K135B$_3$	0.90	375	471	0.061	---
N116W/K135B$_3$	1.02	375	471	0.048	---
Q123-LY	0.90	425	526	0.16	0.09
N116W/Q123-LY	0.90	429	526	0.04	0.05
E128-LY	0.90	426	526	0.17	0.11
N116W/E128-LY	0.90	433	526	0.01	0.05
N132-LY	0.90	428	524	0.18	0.14
N116W/N132-LY	0.90	435	527	0.02	0.10
K135-LY	1.00	427.5	523	0.18	0.14
N116W/K135-LY	0.80	428.5	521	0.04	0.15
Q123-By	0.90	508	529	0.40	0.21
N116W/Q123-By	1.00	508.5	528	0.33	0.24
E128-By	0.90	508.7	534	0.37	0.21
N116W/E128-By	0.90	509.2	537	0.16	0.24
N132-By	1.00	507.5	534	0.38	0.22
N116W/N132-By	0.80	509.5	533	0.10	0.25
K135-By	0.90	509	534	0.48	0.24
N116W/K135-By	0.90	508.5	534	0.47	0.24
Q123-Atto	0.70	664	679	0.17	0.22
N116W/Q123-Atto	0.70	665	678.5	0.09	0.24
E128-Atto	0.50	663.5	680	0.21	0.21
N116W/E128-Atto	0.70	666	677.5	0.04	0.23
N132-Atto	0.50	663	677	0.22	0.21
N116W/N132-Atto	0.80	664.5	677	0.06	0.21
K135-Atto	0.70	660	676.5	0.20	0.24
N116W/K135-Atto	0.70	664.5	677.5	0.08	0.24
Q123-Cy5	0.80	651.5	666	0.28	0.22
N116W/Q123-Cy5	0.70	651.5	669	0.25	0.24
E128-Cy5	0.90	650.5	668.5	0.28	0.21
N116W/E128-Cy5	1.00	651	668.5	0.25	0.23
N132-Cy5	0.90	650.5	669.5	0.32	0.21
N116W/N132-Cy5	0.80	650.5	668.5	0.29	0.21
K135-Cy5	0.90	651.5	670	0.283	0.24
N116W/K135-Cy5	1.10	651	669	0.208	0.24

Table A1. 3: **Thermodynamic Characterization of a Subset of Labeled T4 Lysozyme Samples.**

Labeled Mutant	**T_m (ºC)**	**ΔT_m (ºC)**	**$\Delta\Delta G$ (kcal/mol)[a]**
Wild-Type	52.1	---	---
E128B_3	49.7	- 2. 4	- 0.7
N116W/E128B_3	49.5	- 2. 6	- 0.8
E128-LY	49.8	- 2. 3	- 0.7
N116W/E128-LY	53.7	+ 1. 8	+ 0.5
E128-By	49.2	- 2. 9	- 0.8
N116W/E128-By	49.2	- 2. 9	- 0.8
E128-Atto	46.7	- 5. 4	- 1.6
N116W/E128-Atto	49.2	- 2. 9	- 0.8

[a] $\Delta\Delta G$ calculated using the approximation that $\Delta\Delta G = \Delta T_m * \Delta S_{WT}$

Table A1. 4: Two-Exponential Lifetime Analysis of the Fluorescence Decay Measurements of qBBr-labeled Lysozyme Samples.[a]

Mutant	τ_1 (ns)	α_1	τ_2 (ns)	α_2	χ^2	$\langle\tau\rangle$ (ns)[b]
Q123B$_3$	4.8	0.5	1.9	0.6	0.9	3.1 ± 0.1
	5.0	0.4	1.9	0.6	1.1	
N116W/Q123B$_3$	3.9	0.4	1.0	0.6	0.8	2.2 ± 0.1
	4.0	0.4	1.1	0.6	0.9	
E128B$_3$	6.8	0.5	2.9	0.5	0.8	4.9 ± 0.1
	6.3	0.6	2.7	0.4	0.9	
N116W/E128B$_3$	4.1	0.4	0.7	0.6	1.3	1.9 ± 0.1
	3.7	0.4	0.6	0.6	1.1	
N132B$_3$	7.4	0.5	2.2	0.5	0.8	4.9 ± 0.2
	7.8	0.5	2.5	0.5	1.0	
N116W/N132B$_3$	4.3	0.6	1.3	0.4	0.7	3.0 ± 0.2
	4.4	0.5	1.1	0.5	0.8	
K135B$_3$	4.6	0.4	1.7	0.6	0.7	2.7 ± 0.1
	4.3	0.4	1.6	0.6	1.1	
N116W/K135B$_3$	3.4	0.4	1.2	0.6	0.8	2.1 ± 0.1
	3.5	0.4	1.2	0.6	0.8	

[a] Excitation wavelength 381 nm; emission collected using two > 470 nm longpass filters. Two sets of the lifetime data are reported for comparison purposes.

Abbreviations: τ_1, τ_2, fluorescence lifetimes in nanoseconds; α_1, α_2, normalized pre-exponential factors such that $\alpha_1 + \alpha_2 = 1.0$; χ^2, chi-squared value of the fit.

[b] $\langle\tau\rangle = \alpha_1\tau_1 + \alpha_2\tau_2$, the amplitude-weighted average fluorescence lifetime. The $\langle\tau\rangle$ values reported in this table represent the average of the two sets of lifetimes ± the standard error of the mean.

Table A1. 5: One and Two-Exponential Lifetime Analysis of the Fluorescence Decay Measurements of Lucifer Yellow-, Bodipy-, and Atto-Labeled Lysozyme Samples.[a]

Mutant	τ_1 (ns)	α_1 (ns)	τ_2 (ns)	α_2	χ^2	<τ> (ns)[b]
Q123-LY	7.32 ± 0.03	1.00	---	---	0.99 ± 0.03	7.32 ± 0.04
N116W/Q123-LY	1.78 ± 0.17	0.26 ± 0.01	5.77 ± 0.05	0.74 ± 0.01	1.04 ± 0.05	4.74 ± 0.06
E128-LY	7.27 ± 0.09	1.00			1.00 ± 0.05	7.27 ± 0.09
N116W/E128-LY	1.36 ± 0.13	0.15 ± 0.01	6.75 ± 0.06	0.85 ± 0.01	0.99 ± 0.07	5.98 ± 0.04
N132-LY	7.63 ± 0.03	1.00			0.97 ± 0.02	7.63 ± 0.03
N116W/N132-LY	1.49 ± 0.19	0.19 ± 0.01	6.96 ± 0.06	0.81 ± 0.01	1.01 ± 0.09	5.92 ± 0.04
K135-LY	7.49 ±0 .05	1.00			1.04 ± 0.02	7.49 ± 0.05
N116W/K135-LY	1.59 ± 0.29	0.16 ± 0.02	6.48 ± 0.06	0.84 ± 0.03	0.98 ± 0.05	5.70 ± 0.11
Q123-By	3.39 ± 0.01	0.91 ± 0.01	8.85 ± 0.54	0.09 ± 0.01	1.01 ± 0.02	3.75 ± 0.14
N116W/Q123-By	2.62 ± 0.20	0.81 ± 0.08	7.11 ± 1.19	0.19 ± 0.08	1.02 ± 0.05	3.13 ± 0.11
E128-By	3.28 ± 0.03	1.00			1.16 ± 0.02	3.41 ± 0.01
N116W/E128-By	1.73 ± 0.03	0.73 ± 0.02	4.32 ± 0.14	0.27 ± 0.02	1.03 ± 0.10	2.42 ± 0.02
N132-By	2.97 ± 0.02	0.95 ± 0.01	11.01 ± 0.78	0.05 ± 0.01	0.99 ± 0.06	3.35 ± 0.03
N116W/N132-By	1.17 ± 0.07	0.52 ± 0.02	3.15 ± 0.06	0.48 ± 0.02	0.84 ± 0.01	2.11 ± 0.06
K135-By	1.62 ± 0.81	0.33 ± 0.11	4.86 ± 0.66	0.67 ± 0.11	1.03 ± 0.09	3.87 ± 0.26
N116W/K135-By	2.24 ± 0.59	0.42 ± 0.16	5.19 ± 0.57	0.57 ± 0.16	1.01 ± 0.03	3.94 ± 0.12
Q123-Atto	2.23 ± 0.01	1.00	---	---	1.13 ± 0.02	2.23 ± 0.01
N116W/Q123-Atto	2.12 ± 0.01	1.00	---	---	1.10 ± 0.09	2.12 ± 0.01
E128-Atto	2.14 ± 0.01	1.00	---	---	1.08 ± 0.06	2.14 ± 0.01
N116W/E128-Atto	2.01 ± 0.01	1.00	---	---	1.08 ± 0.04	2.01 ± 0.01
N132-Atto	2.07 ± 0.03	1.00	---	---	1.09 ± 0.09	2.07 ± 0.03
N116W/N132-Atto	1.82 ± 0.02	1.00	---	---	1.07 ± 0.03	1.82 ± 0.02
K135-Atto	2.41 ± 0.02	1.00	---	---	1.05 ± 0.07	2.41 ± 0.02
N116W/K135-Atto	1.97 ± 0.01	1.00	---	---	1.13 ± 0.03	1.97 ± 0.01

[a] Excitation and emission as reported in **A1. 3. 10**. The average of three sets of lifetime data are reported ± the SEM.

Abbreviations: τ_1, τ_2, fluorescence lifetimes in nanoseconds; α_1, α_2, normalized pre-exponential factors such that $\alpha_1 + \alpha_2 = 1.0$; χ^2, chi-squared value of the fit.

[b] $\langle\tau\rangle = \alpha_1\tau_1 + \alpha_2\tau_2$, the amplitude-weighted average fluorescence lifetime. The $\langle\tau\rangle$ values reported in this table represent the average of the three sets of lifetimes ± the standard error of the mean.

Figure A1. 1: Structure, absorbance, and fluorescence emission spectra of each fluorophore used in this calibration study. (A) The reaction scheme of each fluorophore used in the study demonstrating how the probes attach to the protein. **(B)** The four probes used in the calibration study cover nearly the entire range of wavelengths in the visible spectrum. The bimane derivative, qBBr, is the most blue-shifted (hypsochromic) of the probes, with an absorbance maximum around 380 nm and emission around 475 nm. Lucifer Yellow absorbs around 420 nm and emits around 520 nm. Bodipy absorbs around 510 nm and emits around 540 nm. Finally, the most red-shifted (bathochromic) fluorophore is Atto-655, which absorbs around 650 nm and emits at around 685 nm.

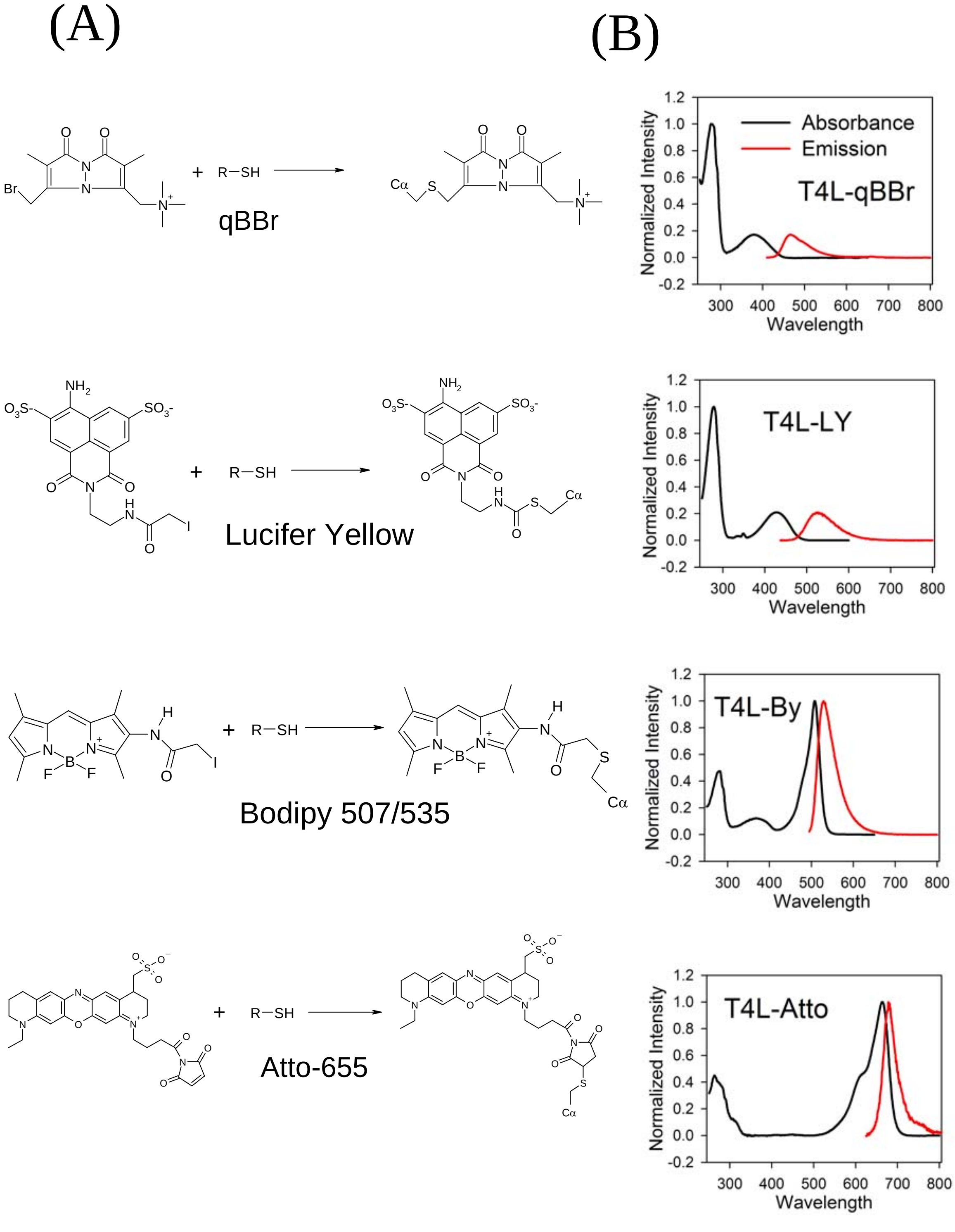
(A)
(B)
qBBr
Lucifer Yellow
Bodipy 507/535
Atto-655
R—SH
Cα
Absorbance
Emission
T4L-qBBr
T4L-LY
T4L-By
T4L-Atto
Normalized Intensity
Wavelength
-0.2
0.0
0.2
0.4
0.6
0.8
1.0
1.2
300
400
500
600
700
800

Figure A1. 2: Trp quenching of qBBr fluorescence is distance-dependent. (A) Model of T4 lysozyme indicating the α-carbon site for each cysteine substitution and the location of the tryptophan residue introduced in this region (N116W). **(B)** Steady-state fluorescence intensity measurements of qBBr-labeled cysteine mutants with and without the Trp residue introduced at site 116. Notice the decrease in fluorescence intensity, especially at sites 128 and 132, upon introduction of the Trp residue.

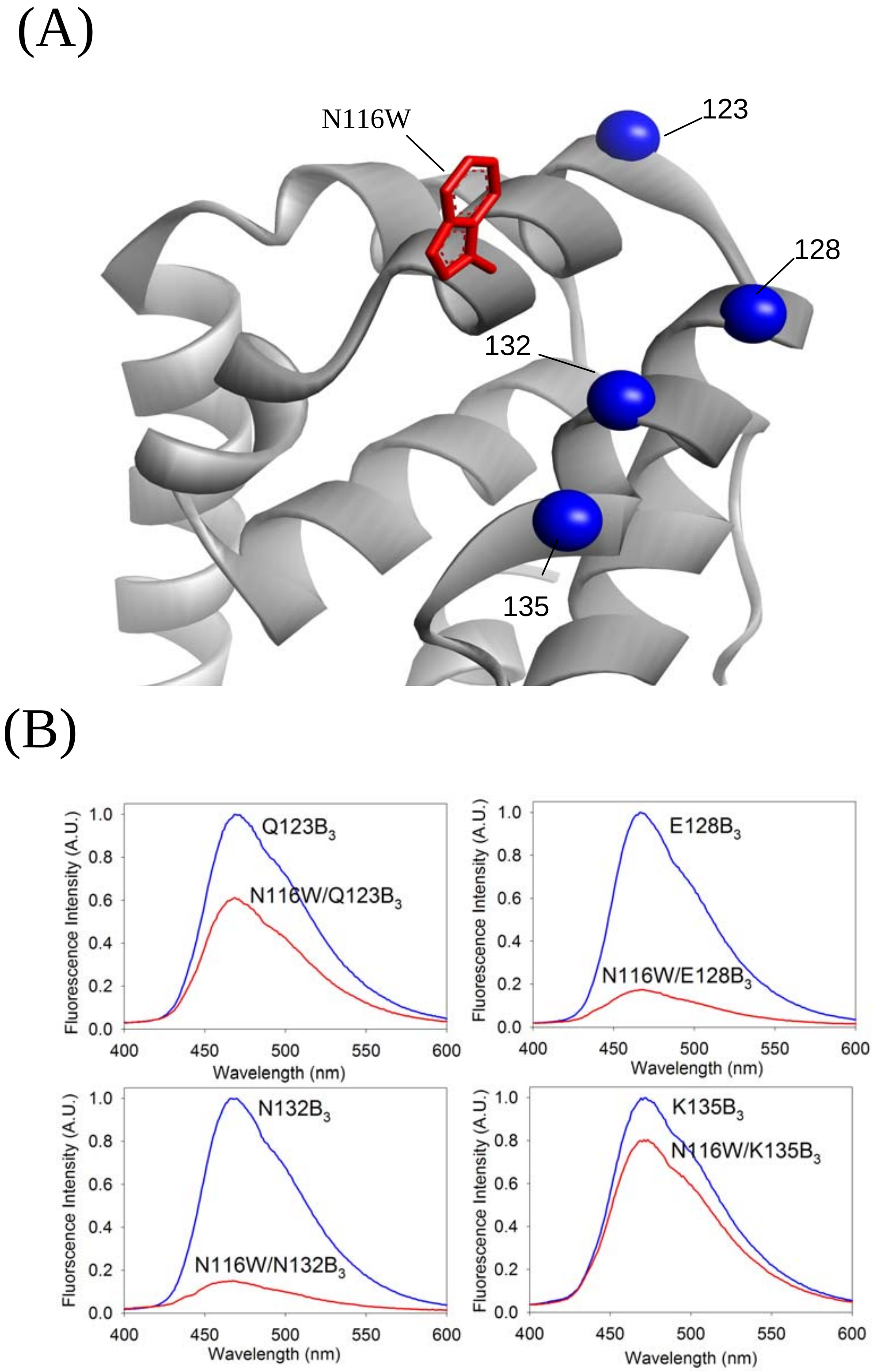
(A)
N116W
123
128
132
135
(B)
Q123B3
N116W/Q123B3
E128B3
N116W/E128B3
N132B3
N116W/N132B3
K135B3
N116W/K135B3
Fluorescence Intensity (A.U.)
Wavelength (nm)
0.0
0.2
0.4
0.6
0.8
1.0
400
450
500
550
600

Figure A1. 3. Steady-state fluorescence quenching of lucifer yellow-, bodipy-, and atto-labeled lysozyme samples due to trp residue at site 116. (A) Model of T4 lysozyme indicating the α-carbon site for each cysteine substitution and the location of the tryptophan residue introduced in this region (N116W). **(B)** Steady-state fluorescence intensity measurements of lucifer yellow-labeled cysteine mutants (left), bodipy-labeled cysteine mutants (middle), and atto-labeled cysteine mutants (right) with and without the Trp residue introduced at site 116. Notice the quenching effects of the Trp residue for bodipy discriminate very well: the closest sites, 128 and 132, demonstrate significant quenching while the sites where Trp is further away, 123 and 135, show almost zero quenching. Contrast this to lucifer yellow and atto-655. For these fluorophores, sites 128 and 132 show the most quenching but sites 123 and 135 still have substantial amounts of quenching. This suggests that bodipy has a smaller "sphere of quenching" than either lucifer yellow or atto-655.

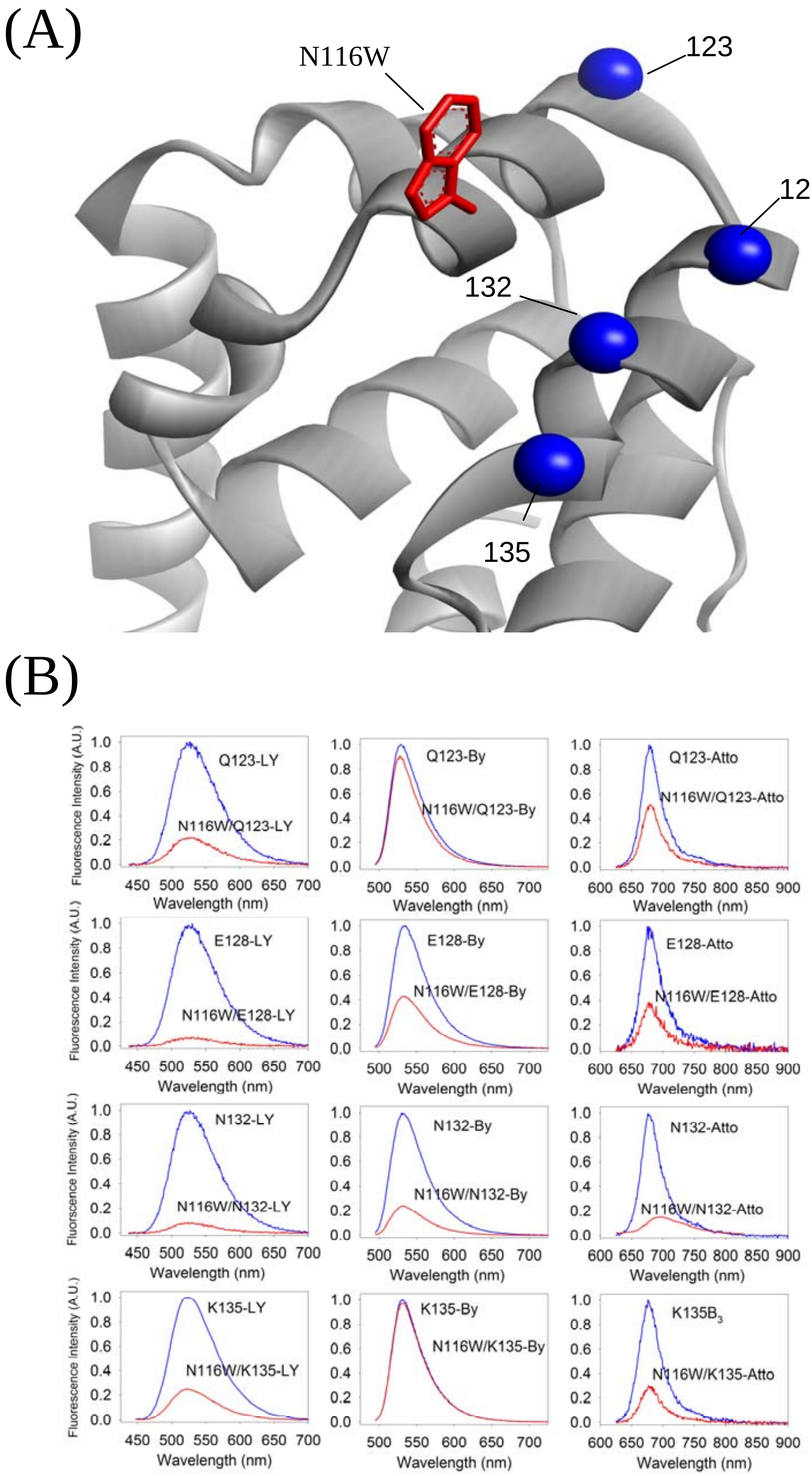
(A)
N116W
123
128
132
135
(B)
Fluorescence Intensity (A.U.)
Wavelength (nm)
Q123-LY
N116W/Q123-LY
Q123-By
N116W/Q123-By
Q123-Atto
N116W/Q123-Atto
E128-LY
N116W/E128-LY
E128-By
N116W/E128-By
E128-Atto
N116W/E128-Atto
N132-LY
N116W/N132-LY
N132-By
N116W/N132-By
N132-Atto
N116W/N132-Atto
K135-LY
N116W/K135-LY
K135-By
N116W/K135-By
K135B$_3$
N116W/K135-Atto
0.0
0.2
0.4
0.6
0.8
1.0
450
500
550
600
650
700
750
800
850
900

Figure A1. 4. Shifts in absorbance λ_{max} values for lucifer yellow labeled lysozyme samples indicate some samples show static quenching. (A) Absorbance spectra for each of the lucifer yellow-labeled samples exhibit a shift in absorbance λ_{max} values for E128-LY compared to N116W/E128-LY and for N132-LY compared to N116W/N132-LY. (B) Excitation spectra (while monitoring emission at ~ 530 nm) for each of the lucifer yellow-labeled samples demonstrates absolutely no shifts in excitation λ_{max} values for any of the mutant pairs. The absorbance λ_{max} shifts suggest the formation of a ground state complex between the Trp and lucifer yellow fluorophore mutants N116W/E128-LY and N116W/N132-LY. This type of data can be used to further quantitate distance constraints for Trp/lucifer yellow quenching in protein studies – shifts in the absorbance λ_{max} values will only occur when the Trp residue and lucifer yellow fluorophore are “very close” in the overall three-dimensional fold of the protein structure, such that a ground-state complex is formed.

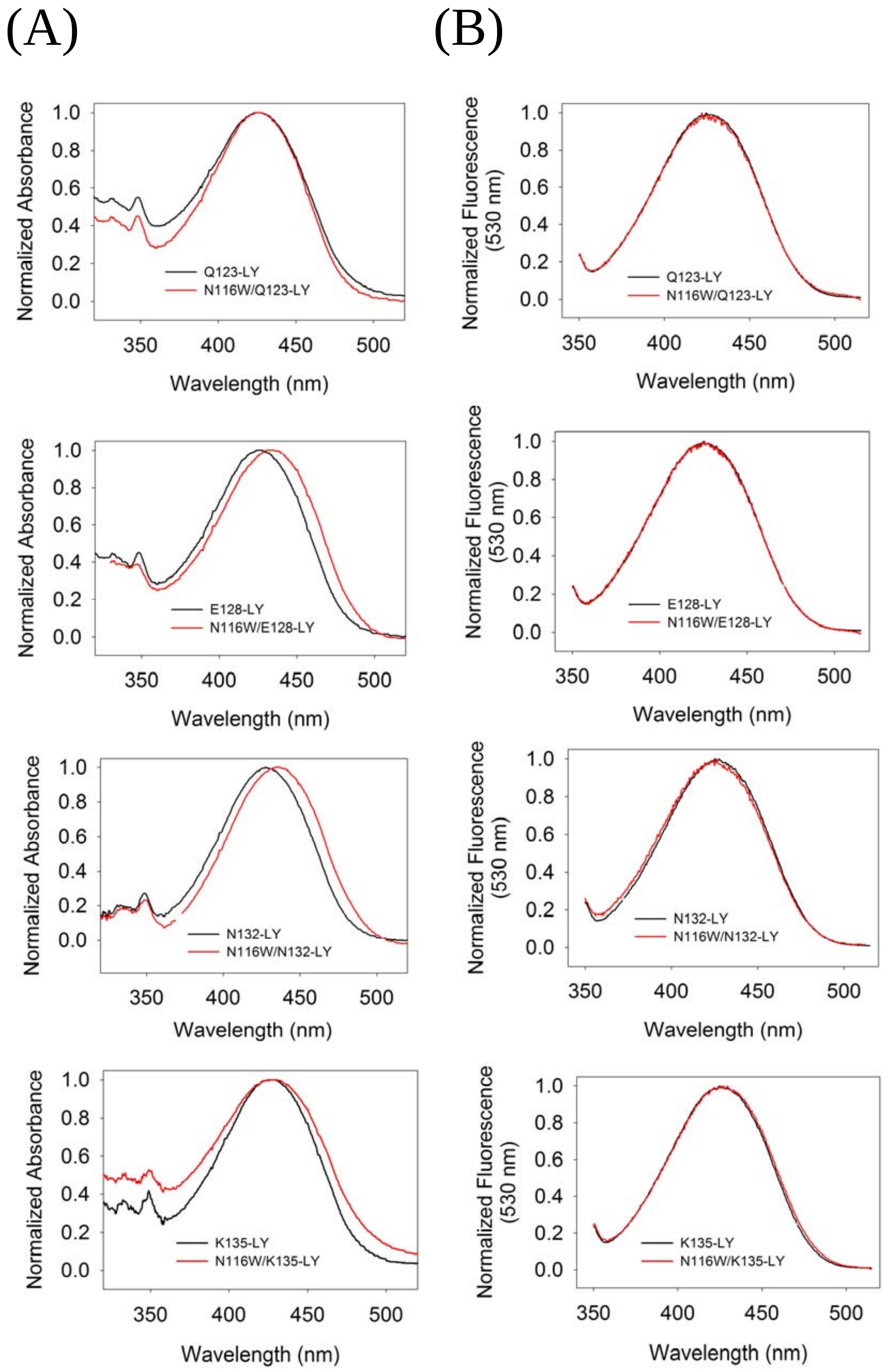
(A)
(B)
Normalized Absorbance
Normalized Fluorescence (530 nm)
Wavelength (nm)
1.0
0.8
0.6
0.4
0.2
0.0
350
400
450
500
Q123-LY
N116W/Q123-LY
E128-LY
N116W/E128-LY
N132-LY
N116W/N132-LY
K135-LY
N116W/K135-LY

Appendix 2

Luminescence Resonance Energy Transfer: A Distance Calibration Using Double Cysteine Mutants in T4 Lysozyme

Steven E. Mansoor[‡], Hassane S. Mchaourab[§] and David L. Farrens[‡]

[‡] Department of Biochemistry and Molecular Biology, Oregon Health and Science
University, Portland, Oregon 97239-3098, USA

[§] Department of Molecular Physiology and Biophysics, Vanderbilt University,
Nashville, Tennessee 37232, USA

Running Title: LRET: A Distance Calibration in T4 Lysozyme

A2. 1: SUMMARY

In this appendix, I report the results of a luminescence resonance energy transfer (LRET) calibration study I carried out to determine how accurately LRET can measure the intramolecular β-carbon to β-carbon distance between pairs of cysteine residues. The study was performed on a pair of double cysteine mutants in T4 lysozyme and the results were compared to the actual distances obtained from the crystal structure of T4 lysozyme. The two pairs of double cysteine mutants generated were K65C/K135C and K65C/R80C with crystal structure β-carbon distances of 37 Å and 22 Å, respectively. For these studies, the donor was the terbium chelate, CS-124-DTPA-EMCH·Tb^{+3} and two different acceptors were used, fluorescein and rhodamine. Unfortunately, the sensitized emission lifetimes, τ_{AD}, for the K65C/R80C pair were too short to be accurately measured by our phosphorescence system. However, the sensitized lifetimes for the K65C/K135C mutant pair predicted distances of 37 Å using the fluorescein acceptor and 42 Å using the rhodamine acceptor, and the methods used to obtain and calculate these values are reported. The data suggest that although LRET may not be measureable at < 20 Å due to instrumental limitations, it can accurately predict distances of ~ 40 Å. This is consistent with the literature claiming LRET can measure distances between ~ 20 – 100 Å.

All experiments and data analysis reported in this appendix were performed by the author of this dissertation. The DNA plasmid constructs used to express the protein samples were supplied by Dr. Hassane S. Mchaourab. The data presented in this chapter has been previously presented as a poster at the 49th Annual Biophysical Society Meeting, Long Beach, CA, 2005, for which the abstract received a Biophysical Society Student Travel Award.

A2. 2: INTRODUCTION

Fluorescence resonance energy transfer (FRET) is an optical technique where a donor fluorophore is excited and transfers energy to an acceptor fluorophore in a distant-dependent fashion. The distance-dependent transfer of energy enables the measuring of interatomic distances on the order of ~ 20 – 100 Å [77,78,81,282]. These distances are comparable with the diameters of many biological molecules, making FRET techniques useful for assessing intramolecular distances in protein, for studying protein/protein interactions, and for detecting dynamic conformational changes in proteins. For more details on FRET, see Chapter 1, section **1. 2. 2**.

A2. 2. 1: LRET Provides Multiple Advantages Over FRET.

Recently, luminescence from lanthanide atoms has been demonstrated to provide a number of advantages as donors in luminescence resonance energy transfer (LRET) experiments. In this approach, long-lived donor probes (typically lanthanide chelates) and short-lived acceptor probes are used as the donor/acceptor pair. Advantages provided by LRET over FRET include greatly improved accuracy and signal/background noise ratios for distance measurements [305]. The advantages arise because of the unique spectroscopic properties of the lanthanides, especially when placed in a coordinated chelate cage to avoid solvent interactions (Figure A2. 1). While in this cage, 337 nm pulsed light will excite the antenna which then transfers energy to the caged lanthanide. When protected from quenching by water molecules while in the cage, the lanthanide luminescence emission has three sharp emission lines (Figure A2. 2A) with a long lifetime on the millisecond time scale (Figure A2. 2B). This provides two different ways to ensure collection of the energy transfer signal while discarding unwanted emission from directly excited acceptor or from the donor itself.

First, the significantly longer luminescence lifetime allows any contaminating emission from directly excited acceptor (not emission from energy transfer) to be easily eliminated by time gating the detection electronics (ie., directly excited acceptors decay to zero on a nanosecond time scale, which is insignificantly short compared to the lifetime of the donor). Further, because of the narrow emission wavelength of the lanthanide, donor emission can be completely eliminated by selection of a wavelength where the acceptor emits but the donor is silent. This concept is visualized in Figure A2. 2A and is reviewed in [272,305]. As shown in Figure A2. 2A, similar to FRET, LRET requires one of the emission lines from the lanthanide donor to overlap with the absorbance spectrum of the acceptor, in this case fluorescein. Further note the emission maximum of fluorescein occurs at 520 nm, a wavelength where the lanthanide is spectrally silent. Thus, if one time gates to exclude emission from direct acceptor excitation while simultaneously monitoring acceptor emission at 520 nm, it is possible to obtain a measured signal which can only have come from energy transfer. Such a signal is referred to as sensitized emission.

An additional advantage of LRET over FRET is an increased ease of sample preparation. Because sensitized emission is independent of absolute concentration, and because the delayed sensitized emission only arises from donor-acceptor pairs, a completely labeled donor-acceptor sample is not necessary for LRET. The approach only requires that some fraction of labeled proteins contains both donor and acceptor probes.

Any incomplete labeling (donor-labeled samples with no acceptor partner or acceptor-labeled samples with no donor partner) does not contribute to or contaminate the signal.

Finally, it is well-known that the accuracy of traditional FRET experiments depends on the relative orientation of the donor and acceptor. This is because the electric field of the donor may be polarized and anisotropic [272]. However, because the lanthanide donors have millisecond lifetimes, the acceptor will likely rotate during this time, and additionally, emission from lanthanides in solution is almost always unpolarized [184] due to the degeneracy of the high-spin energy states and the spherical symmetry of the isolated atom [306]. Thus, the error in distances measured due to the orientation factor is essentially negligible. This in turn makes the distance determination via LRET generally more accurate than FRET because the orientation factor in FRET is often poorly known.

A2. 2. 2: The Sensitized Emission Lifetime (τ_{AD}) Reflects the Donor/Acceptor Distance.

In an LRET experiment, the distance between the lanthanide donor and the acceptor is reflected in the lifetime of the sensitized emission (τ_{AD}). The closer the donor/acceptor pair, the shorter the value of τ_{AD}, while the further apart the donor/acceptor pair, the longer the value of τ_{AD}. This concept is demonstrated in Figure A2. 3. The relationship between distance and τ_{AD} arises because the probability of energy transfer is dependent on the distance between the donor and acceptor according to [272]:

$$E = \frac{R_0^6}{R_0^6 + r^6} \qquad \text{[Eq. A2. 1]}$$

where E is the efficiency of energy transfer, R_0 is a constant that depends on the spectral properties of the donor and acceptor representing the distance at which 50% energy transfer is expected, and r is the distance between the donor and acceptor. Figure A2. 3 indicates that fluorescence from the acceptor is almost instantaneous relative to luminescence from the donor. Therefore, any process that increases the probability of transfer from donor to acceptor will result in faster emission rates and a subsequently shorter sensitized emission, τ_{AD}. Equation A2. 1 indicates that donor/acceptor proximity increases the probability of transfer and so it follows that the closer the donor/acceptor pair, the shorter the value of τ_{AD}.

The efficiency of energy transfer (E) can also be expressed by:

$$E = 1 - \frac{\tau_{AD}}{\tau_D} \qquad \text{[Eq. A2. 2]}$$

where τ_{AD} is the sensitized emission lifetime from the acceptor and τ_D is the luminescence lifetime of the donor. Combining Eq. A2. 1 and Eq. A2. 2 produces a theoretical expression that reflects predicted sensitized lifetimes (τ_{AD}) as a function of distance. This type of theoretical function can be generated for any lanthanide/acceptor pair. Experimentally measured τ_{AD} values can then be compared to this theoretical function to determine any experimentally observed lanthanide/acceptor distance (the steps required to calculate these functions are demonstrated in **A2. 4. 4)**. Although the theory behind this approach has been discussed [81,272,279,280,282], to my knowledge, no extensive study has actually been carried out to demonstrate it accurately reflects intramolecular distances between residues in a protein.

Thus, I carried out such an LRET calibration study. This appendix reports LRET experiments on T4 lysozyme designed to assess how accurately LRET can predict intramolecular β-carbon to β-carbon distances in proteins. Two double cysteine mutants in T4 lysozyme were used, K65C/K135C and K65C/R80C, with crystal structure β-carbon distances of 37 Å and 22 Å, respectively (Figure A2. 4). Although the K65C/R80C sample resulted in τ_{AD} values that were too short to be measured by our phosphorescence system, the K65C/K13C mutant resulted in τ_{AD} values of 485 μsec using fluorescein as the acceptor and 154 μsec using rhodamine as the acceptor. Comparison of theses values to the theoretical τ_{AD} vs. distance curves generated for fluorescein and rhodamine resulted in predicted distances of 37 Å and 42 Å, respectively. Taken together, these results suggest that LRET measurements on a standard phosphorescence lifetime system can be used to accurately measure distances in a protein structure.

A2. 3: EXPERIMENTAL PROCEDURES

A2. 3. 1: Materials.

Fluorescein-5-maleimide and rhodamine were purchased from Biotium. The Tb^{3+} chelate, CS124-DTPA-EMCH•Tb^{3+}, was purchased from Panvera. Neutral density filters, long-pass filters, and interference filters were from Oriel Corp. All cuvettes were from Uvonics. All buffer components were purchased from Fisher-Biotech.

A2. 3. 2: Buffers.

The buffers used were as follows: buffer A, 50 mM MOPS, 50 mM Tris, and 1 mM EDTA, pH 7.6; buffer B, 20 mM Tris, 20 mM MOPS, 0.02% sodium azide, 1 mM

EDTA, and 1 mM DTT, pH 7.6; buffer C, 20 mM KH_2PO4 and 25 mM KCl, pH 3.0; buffer D, 50 mM MOPS, 50 mM Tris, 1 mM EDTA, pH 7.6, and 3 M guanidine hydrochloride.

A2. 3. 3: Construction, expression and purification of T4 lysozyme Mutants.

For construction, expression and purification of T4 lysozyme double cysteine mutants, K65C/K135C and K65C/R80C, please refer to section **2. 3. 3** and **2. 3. 5** in chapter 2.

A2. 3. 4: Fluorescence and Luminescence Labeling of T4 Lysozyme Double Cysteine Mutants.

Labeling of each lysozyme mutant was carried out by mixing both the lanthanide donor and the fluorescence acceptor (either fluorescein or rhodamine) together using ~ 1.0× donor and ~ 1.0× acceptor. Thus, 50 μL of 100 μM total protein was incubated with ~ 100 μM donor and ~ 100 μM acceptor in buffer A at 4 °C overnight. Label that did not react with the protein was removed by passing the solutions over a Sephadex G15 500 μL capacity size-exclusion column previously equilibrated with buffer A. Each sample was passed over the column only once. Absorption spectra (measured using a Shimadzu UV 1601) were used to calculate the labeling efficiency for each mutant with both the lanthanide/fluorescein as well as the lanthanide/rhodamine combination. Concentrations were calculated using extinction coefficients of $\varepsilon_{280} = 23,327\ \text{L cm}^{-1}\ \text{mol}^{-1}$ for T4 lysozyme, $\varepsilon_{343} = 10,560\ \text{L cm}^{-1}\ \text{mol}^{-1}$ for CS124-DTPA-EMCH•Tb^{3+}, $\varepsilon_{495} = 83,000\ \text{L cm}^{-1}\ \text{mol}^{-1}$ for fluorescein, and $\varepsilon_{570} = 100,000\ \text{L cm}^{-1}\ \text{mol}^{-1}$ for rhodamine. The contribution from fluorescein and rhodamine at 280 nm was subtracted before the protein concentrations were calculated.

A2. 3. 5: Nomenclature.

Throughout this appendix, mutants are named by specifying the original residue, the number of the residue, and the new residue, in that order. For example, the code K65C/K135C indicates that the native lysine residues at the 65th and 135th amino acid positions were mutated to cysteine residues. Double mutants labeled with the lanthanide donor and fluorescein acceptor are named by specifying the original residue, the number of the residue, and the suffix TbF, indicating the terbium/fluorescein donor/acceptor combination. Similarly, mutants labeled with both the lanthanide donor and rhodamine acceptor are named by specifying the original residue, the number of the residue, and the suffix TbR. For example, the code K65/K135TbF indicates that the native lysine residues at the 65th and 135th amino acid positions have been mutated to cysteine residues and reacted with both the lanthanide donor and the fluorescein acceptor.

A2. 3. 6: Luminescence Resonance Energy Transfer Measurements.

Phosphorescence experiments to measure the sensitized emission lifetimes (τ_{AD}) were performed at ~7. 5 °C using a PTI Laserstrobe phosphorescence lifetime system on 250 μL of a 5 – 10 μM sample (total protein concentration) placed in a 4 mm black-jacketed cuvette. The samples were excited at 337 nm using a nitrogen pumped dye laser while emission was collected using a monochromator at 520 nm when fluorescein was used as the acceptor and 590 nm when rhodamine was used as the acceptor. Each data point on the sensitized emission decay curve represents 3 averages of five laser flashes, and each decay represents 200 of these data points spaced out linearly over the collection time interval. The lifetime of the lanthanide donor in the absence of acceptor (τ_D) was measured on a 1 μM peptide excited at 337 nm while collecting emission collection at 545 nm.

A2. 4: RESULTS

A2. 4. 1: Rationale for Choice of Mutants Generated.

To investigate whether LRET can accurately measure intramolecular β-carbon to β-carbon distances in proteins, we employed site-directed labeling strategies in double cysteine mutants of T4 lysozyme. Although LRET is often reported to be accurate for measuring distances between 20 – 100 Å in proteins [81,272,279,282], no systematic calibration study has been published to date. An ideal calibration study would generate a number of double cysteine mutants in a protein of known structure, with β-carbon distances systematically increasing by ~ 10 Å from 20 Å to 100 Å. LRET distances measured should be performed on each of these double cysteine mutants to determine how closely the measured distances are to the crystal structure β-carbon distances across the entire range of 20 Å to 100 Å.

In this appendix, we generated two sets of double cysteine mutants in T4 lysozyme, K65C/K135C and K65C/R80C with crystal structure β-carbon distances of 37 Å and 22 Å, respectively (Figure A2. 4). These β-carbon distances cover the low-end of distances typically measured by LRET. Both sets of double cysteine mutants were labeled with CS-124-DTPA-EMCH·Tb^{+3} as the LRET donor while two different acceptors were used, fluorescein and rhodamine.

A2. 4. 2: Characterization of Labeled Lysozyme Mutants.

The labeling efficiencies for the two double cysteine mutants are shown in Table A2. 1. As seen from the table, the acceptor labeling efficiencies ranged from 28% to 50%. The donor labeling efficiencies ranged from 41% to 55%. The less than quantitative labeling efficiencies are not unexpected because of the labeling protocol where protein was simply incubated with ~ 1.0× donor and ~ 1.0× acceptor. Also note that this labeling protocol does not control which of the cysteine residues label with donor and which label with acceptor. These issues do not affect the quality of the LRET data, as discussed below in Section **A2. 5. 1.**

A2. 4. 3: Sensitized Emission Lifetimes.

Both the lifetime of the lanthanide donor in the absence of acceptor (τ_D) and the sensitized lifetimes (τ_{AD}) of each of the donor/acceptor labeled T4L mutants were measured and analyzed using a monoexponential fit. The resulting lifetime values from the fits can be seen in Table A2. 2.

The lifetime (τ_D) of the CS-124-DTPA-EMCH·Tb^{+3} lanthanide donor attached to a short peptide was measured to be 2. 2 ms, consistent with previously published reports [272,307]. When the labeled T4L samples were measured, a strong energy transfer signal was detected for both samples K65/K135TbF and K65/K135TbR, resulting in monoexponential decay curves (Figure A2. 5). The sensitized fluorescence lifetimes (τ_{AD}) were measured to be 485 μsec for K65C/K135TbF and 154 μsec for K65C/K135TbR. These values are significantly shorter than the τ_D value of 2. 2 msec, as expected for successful LRET.

Although time-resolved emission scans (data not shown) demonstrated evidence of successful energy transfer for samples K65/R80TbF and K65/R80TbR, a sensitized lifetime was not measureable for either sample. The β-carbon distance of ~ 22 Å for these samples predicts a sensitized lifetime of ~ 4 μs for K65/R80TbR and ~ 30 μs for K65/R80TbF which are significantly shorter than the response time of our instrument (~ 60 μs). This is demonstrated by the width of the instrument response function of Figure A2. 5B. Thus, the sensitized lifetimes for these samples are simply too short to be measured using the PTI phosphorescence lifetime system.

A2. 4. 4: Sensitized Lifetimes (τ_{AD}) Versus Distance for Fluorescein and Rhodamine.

Eq. A2. 1 and Eq. A2. 2 combined with the R_0 values for CS-124-DTPA-EMCH·Tb^{+3} and fluorescein (45 Å; [272]) and CS-124-DTPA-EMCH·Tb^{+3} and rhodamine (65 Å; [281]) were used to generate functions predicting the expected sensitized fluorescence lifetimes versus distance for each donor/acceptor pair.

A demonstration of how to calculate the function predicting the expected sensitized lifetime versus distance for CS-124-DTPA-EMCH·Tb^{+3} and fluorescein, using R_0 = 45 Å and τ_D = 2. 2 ms, is performed here. The first step is to set Eq. A2. 1 and Eq. A2. 2 equal to each other:

$$E = \frac{R_0^6}{R_0^6 + r^6} = 1 - \frac{\tau_{AD}}{\tau_D}$$

Rearrange: $$\frac{\tau_{AD}}{\tau_D} = 1 - \frac{R_0^6}{R_0^6 + r^6}$$

Solve for τ_{AD}: $$\tau_{AD} = \tau_D - \frac{\tau_D * R_0^6}{R_0^6 + r^6}$$

Substitute $\tau_D = 2.2e^{-3}$ seconds and $R_0 = 45$ Å:

$$\tau_{AD} = 0.0022\,\text{sec} - \frac{0.0022\,\text{sec} * (45\text{Å})^6}{(45\text{Å})^6 + r^6}$$

In this example, for a β-carbon distance of 37 Å between K65C/K135C, the sensitized lifetime, τ_{AD}, would be predicted, when using the fluorescein acceptor, to be:

$$\tau_{AD} = 0.0022\,\text{sec} - \frac{0.0022\,\text{sec} * (45\text{Å})^6}{(45\text{Å})^6 + (37\text{Å})^6}$$

$$\tau_{AD} = 519\,\mu\text{sec}$$

In this manner, the expected sensitized lifetime (τ_{AD}) for any donor/acceptor pair at any given distance (r) can be calculated.

The top half of Figure A2. 6 shows the functions for both the CS-124-DTPA-EMCH·Tb^{+3}/fluorescein and CS-124-DTPA-EMCH·Tb^{+3}/rhodamine pair. Note that because the R_0 for rhodamine (65 Å) is larger than the R_0 for fluorescein (45 Å), the amount of energy transfer for rhodamine is expected to be greater than for fluorescein at any given distance, and thus, the predicted τ_{AD} value for a rhodamine labeled sample will always be shorter.

A2. 5: DISCUSSION

In this appendix, I wanted to assess how accurately luminescence resonance energy transfer (LRET) can measure β-carbon to β-carbon distances in proteins. To do this, I labeled two pairs of double cysteine mutants in T4 lysozyme, K65C/K135C (β-carbon distance of ~ 37 Å) and K65C/R80C (β-carbon distance of ~ 22 Å) with CS-124-DTPA-EMCH·Tb^{+3} lanthanide donor and with either fluorescein or rhodamine as the energy transfer acceptor. The sensitized fluorescence lifetime (τ_{AD}) of each sample was measured and used to predict the donor/acceptor distance. The experimental distances were then compared to the β-carbon distances determined from the crystal structure of T4 lysozyme.

A2. 5. 1: Sample Labeling Efficiency Does not Affect the Quality of the Data.

Table A2. 1 shows that, for a number of the samples, the efficiency of labeling was not quantitative. Ideally, in these experiments, the donor and acceptor labeling efficiencies would each be 100% based on protein concentration since each protein has two reactive cysteine residues, ie., within each protein, one cysteine would be labeled with the lanthanide donor while the other is labeled with the acceptor. This was not the case; in most instances, the labeling efficiency was below 50% for both the donor and the acceptor. However, it is important to note that with LRET, non-quantitative labeling does not lower the quality of the data. Only donor/acceptor pairs contribute to the sensitized lifetime signal. Neither a donor without an acceptor partner nor an acceptor without a donor partner contribute to the signal. This is one of the main advantages of LRET since, in biological fluorophores, it is not always possible to prepare a sample labeled with donor and acceptor fluorophores in a clean stoichiometric fashion [279]. In fact, sample preparation for specific labeling with donor and acceptor molecules is often the most difficult and time-consuming part of an energy transfer experiment.

A2. 5. 2: The Sensitized Emission Lifetimes Accurately Measure the β-carbon Distance between K65C/K135C in T4 Lysozyme.

The sensitized lifetimes measured for K65/K135TbF and K65/K135TbR from Table A2. 2 were compared to the theoretical functions describing sensitized lifetime versus distance (top half of Figure A2. 6) for each donor/acceptor pair to arrive at an experimental donor/acceptor distance. The value of τ_{AD} = 485 μsec for K65/K135TbF corresponds to a distance of 37 Å and the value of τ_{AD} = 154 μsec for K65/K135TbR corresponds to a distance of 42 Å (bottom half of Figure A2. 6 and Table A2. 2). Thus, using fluorescein as the acceptor exactly measures the β-carbon distance between residues 65 and 135 in T4 lysozyme. Meanwhile, the rhodamine acceptor measures a distance that is within 5 Å of the actual distance (37 Å) between these two residues determined from the crystal structure of T4 lysozyme. It is clear that, for the K65C/K135C double cysteine mutant pair of T4 lysozyme, LRET could accurately predict the β-carbon distance to within 5 Å.

It is not surprising that the distance determined using fluorescein as the acceptor fluorophore is more accurate than the distance determined using rhodamine for the K65C/K135C mutant pair. Determination of distances based on energy transfer studies will be most accurate when the measured distance is near the R_0 for the donor/acceptor pair. This is the linear portion the functions plotted in Figure A2. 6. In the case of K65C/K135C, the crystal structure β-carbon distance of 37 Å is nearer the lanthanide/fluorescein R_0 value of 45 Å, compared to the lanthanide/rhodamine R_0 value of 65 Å. It is likely that fluorescein will be the better choice as an acceptor in LRET experiments for shorter distances (20 – 55 Å) while rhodamine will be better suited for the longer range distance experiments (55 – 100 Å).

A2. 5. 3: The Sensitized Emission Lifetimes for Mutant K65C/R80C Were Too Short to Be Successfully Measured.

Unfortunately, I was unable to measure the sensitized lifetimes for K65/R80TbF and K65/R80TbR. The β-carbon distance for this double cysteine mutant pair is ~ 22 Å. From Figure A2. 6, this distance predicts sensitized lifetimes of τ_{AD} = 33 μsec for K65/R80TbF and τ_{AD} = 4 μsec for K65/R80TbR. For the standard phosphorescence lifetime system used in these measurements, these lifetime values are too short to accurately obtain a decay signal.

One of the current limitations in phosphorescence decay measurements is a spectral artifact that occurs in the data due to detector tube ringing following the laser pulse [289]. To ensure this instrumental artifact is excluded from data analysis, the first ~ 75 μsec of the decay is sometimes eliminated. For example, a sensitized lifetime of τ_{AD} = 4 μsec would be completely masked by the spectral artifact. After 75 μsec, a decay with a lifetime of τ_{AD} = 33 μsec has decayed to nearly 10% of the starting signal intensity and thus, it is not surprising that a sensitized lifetime was not measureable for this sample. It is possible to substantially reduce the tube ringing using a fast bipolar pre-amplifier and a constant discriminator [289] and the need to measure distances that have sensitized lifetimes below about 50 – 60 μsec will require these electronic components.

A2. 5. 4: Conclusions.

In summary, LRET accurately predicted the β-carbon distance between the residues in the K65C/K135C double mutant of T4 lysozyme. The measured distance of

37 Å using fluorescein as the acceptor and 42 Å using rhodamine as the acceptor are remarkably close to the actual distance of 37 Å from the crystal structure of T4 lysozyme. Although it is theoretically possible to measure distances around ~ 20 Å using LRET, it requires modification of standard phosphorescence systems to eliminate spectral artifacts resulting from tube ringing in the detector. I estimate that sensitized lifetimes beneath ~ 50 – 60 μsec will require this modification. As exciting as the results for the experiments on K65C/K135C are, additional calibration studies need to be performed to determine whether LRET can be as accurate at longer distances (~ 50 – 100 Å).

A2. 6: ACKNOWLEDGEMENTS

We thank Dr. T. Heyduk and Dr. K. Palczewski for providing the lanthanide reagents for the LRET experiments.

Table A2. 1: **Labeling Efficiencies for Double Cysteine Mutants of T4 Lysozyme.**

Sample	**Mole Donor/Mole T4L**	**Mole Acceptor/Mole T4L**
K65/K135TbF	0.55	0.50
K65/K135TbR	0.41	0.28
K65/R80TbF	0.50	0.41
K65/R80TbR	0.44	0.34

Table A2. 2: **Sensitized Lifetimes (τ_{AD}) Accurately Predict Donor/Acceptor Distances.**

Sample	**β-carbon Distance (Å)**	**Expected τ_{AD} (μsec)**	**Measured τ_{AD} (μsec)**	**Experimental Distance (Å)**	**ΔDistance (Å)**
K65/K135TbF	37	519	485	37	0
K65/K135TbR	37	72	154	42	+ 5
K65/R80TbF	22	33	--	--	--
K65/R80TbR	22	4	--	--	--

Figure A2. 1: Structure of the lanthanide chelate, CS-124-DTPA-EMCH·Tb^{+3}. Excitation of the lanthanide chelate is a two-step process. The antenna (CS-124) acts to first absorb a photon (excited with 337 nm light) and then due to their very close proximity, passes this energy onto the lanthanide. The DTPA chelates the terbium, protecting it from quenching by water, enabling the lanthanide to emit the light with a millisecond lifetime. The EMCH group allows modification to a cysteine residue on a protein. Following emission from the lanthanide, the energy can be transferred to an appropriate acceptor, shown as fluorescein, and the resulting lifetime of the sensitized emission (τ_{AD}) can be measured to determine the distance between the donor and the acceptor. Figure adapted from Selvin, P.R. (2002) *Annu. Rev. Biophys. Biomol. Struct*. 31: 275 – 302.

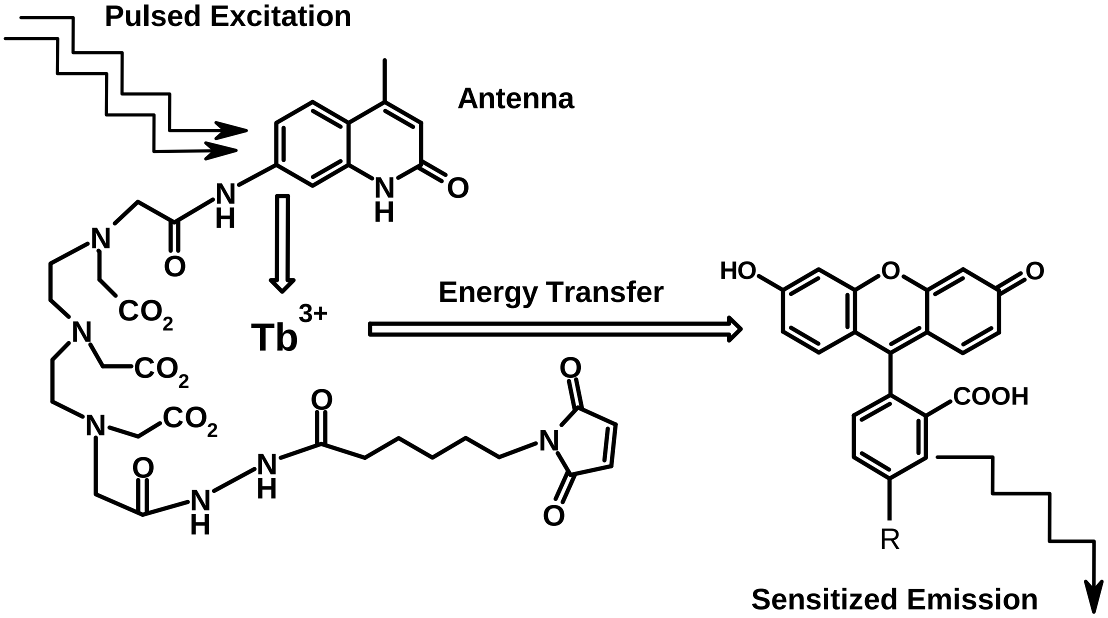
Pulsed Excitation
Antenna
N
H
O
N
H
N
O
CO2
N
CO2
N
CO2
Tb3+
Energy Transfer
O
O
N
H
N
H
O
O
N
HO
O
O
COOH
R
Sensitized Emission

Figure A2. 2: Spectral properties of lanthanide donor and fluorescein acceptor guarantees a positive signal can only originate from energy transfer. (A) The emission spectrum of the lanthanide donor (shown in red) is composed of three sharp peaks. The first major peak in lanthanide emission, centered around 475 nm, overlaps with the absorbance spectrum of the fluorescein acceptor (shown in blue), satisfying the primary criterion for a successful donor/acceptor energy transfer pair. The emission spectrum of fluorescein (shown in green) is maximal around 520 nm, a wavelength where the lanthanide donor is spectrally silent. **(B)** The luminescence decay of 1 μM lanthanide donor, CS-124-DTPA-EMCH·Tb^{+3}, attached to a peptide. Notice that the lifetime of the lanthanide donor (τ_D), in the absence of any acceptor, is significantly longer (τ_D = 2.2 ms) than the typical fluorescence lifetimes of the acceptor (τ_A) when it is directly excited (fluorescein τ_A = 4 ns). Thus, by gating the detector to a point in time where directly excited acceptor has decayed to zero, while simultaneously monitoring acceptor emission at 520 nm (where lanthanide donor does not emit), it guarantees that a positive signal can only have come from successful energy transfer.

(A)

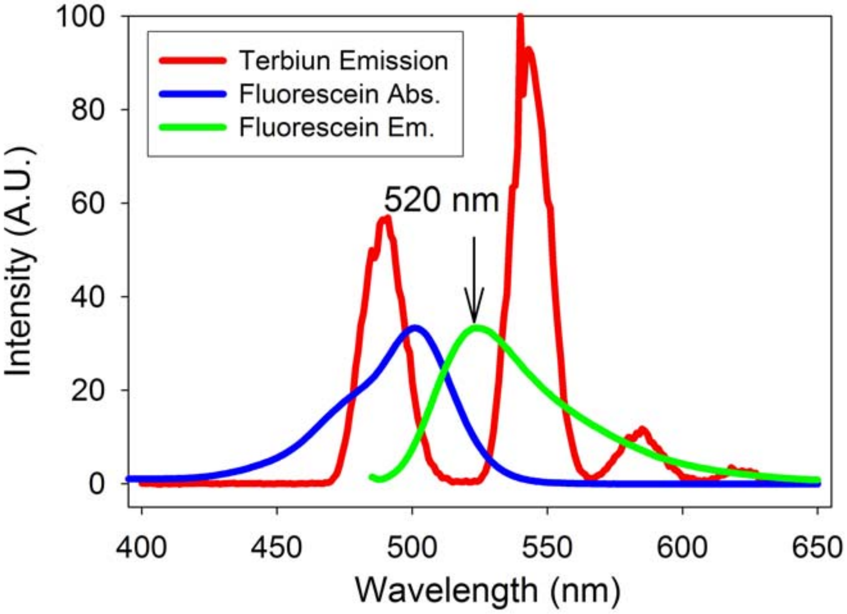
Terbiun Emission
Fluorescein Abs.
Fluorescein Em.
520 nm
Intensity (A.U.)
100
80
60
40
20
0
400
450
500
550
600
650
Wavelength (nm)

(B)

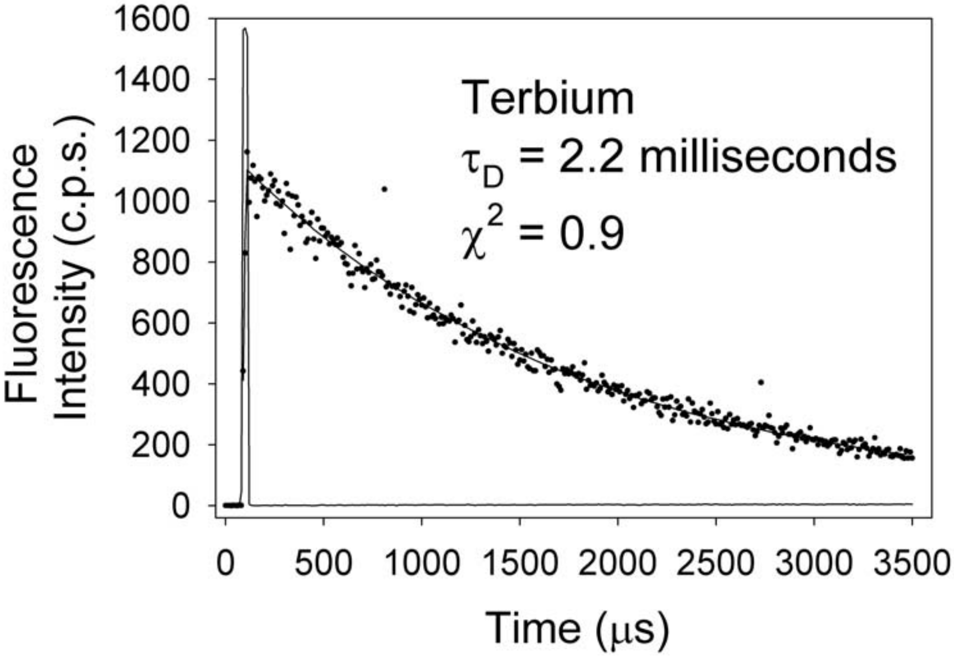
Terbium
τ_D = 2.2 milliseconds
χ^2 = 0.9
Fluorescence Intensity (c.p.s.)
1600
1400
1200
1000
800
600
400
200
0
0
500
1000
1500
2000
2500
3000
3500
Time (μs)

Figure A2. 3: The sensitized lifetimes (τ_{AD}) in an LRET experiment can be used to calculate the donor/acceptor distance. The luminescence lifetime (τ_D ~ milliseconds) of the lanthanide donor is significantly longer than the fluorescence lifetime (τ_A ~ nanoseconds) of the acceptor (directly excited acceptor). Thus, emission from the acceptor is instantaneous on the time-scale of the donor. Efficiency of energy transfer is dependent on the distance between the donor/acceptor (see Eq. A2. 1). Therefore, any process that increases the probability of transfer from donor to acceptor will result in faster emission rates and a subsequently shorter sensitized emission, τ_{AD}. **(A)** The donor/acceptor proximity increases the probability of transfer and so it follows that the closer the donor/acceptor pair, the shorter the value of τ_{AD}. **(B)** Conversely, the further the donor/acceptor pair, the lower the probability of energy transfer and thus the higher the τ_{AD} value.

(A)

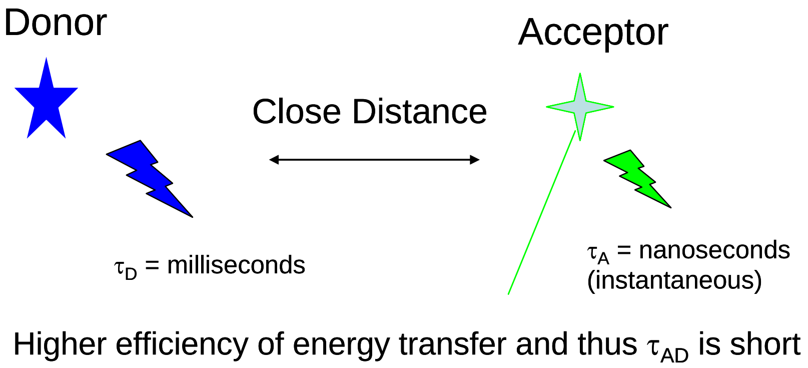
Donor
Acceptor
Close Distance
τ_D = milliseconds
τ_A = nanoseconds
(instantaneous)
Higher efficiency of energy transfer and thus τ_{AD} is short

(B)

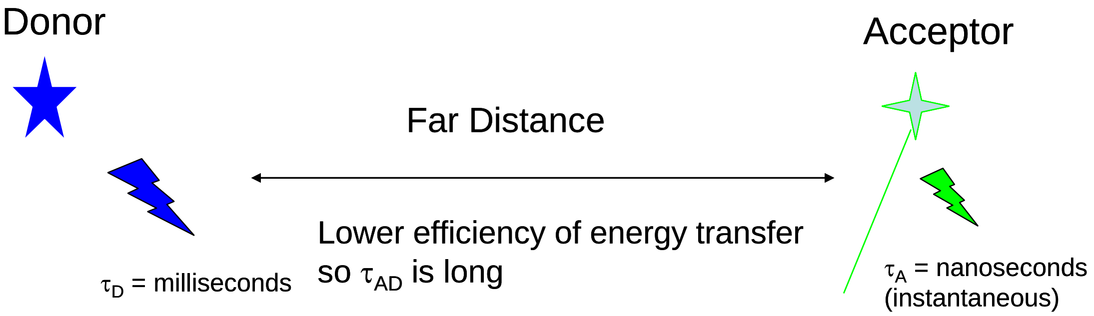
Donor
Acceptor
Far Distance
Lower efficiency of energy transfer
so τ_{AD} is long
τ_D = milliseconds
τ_A = nanoseconds
(instantaneous)

Figure A2. 4. Crystal structure of T4 lysozyme showing the positions of residues 65, 80, and 135. The two double cysteine mutants generated, K65C/K135C and K65C/R80C, have β-carbon to β-carbon distances of 37 Å and 22 Å, respectively. The figure was made using WebLab Viewer Pro and the coordinates of the crystal structure of cysteine-less T4 lysozyme in PDB file 1L63 from Nicholson, H., *et al.* (1991) *Biochemistry 30*, 9816 - 9828.

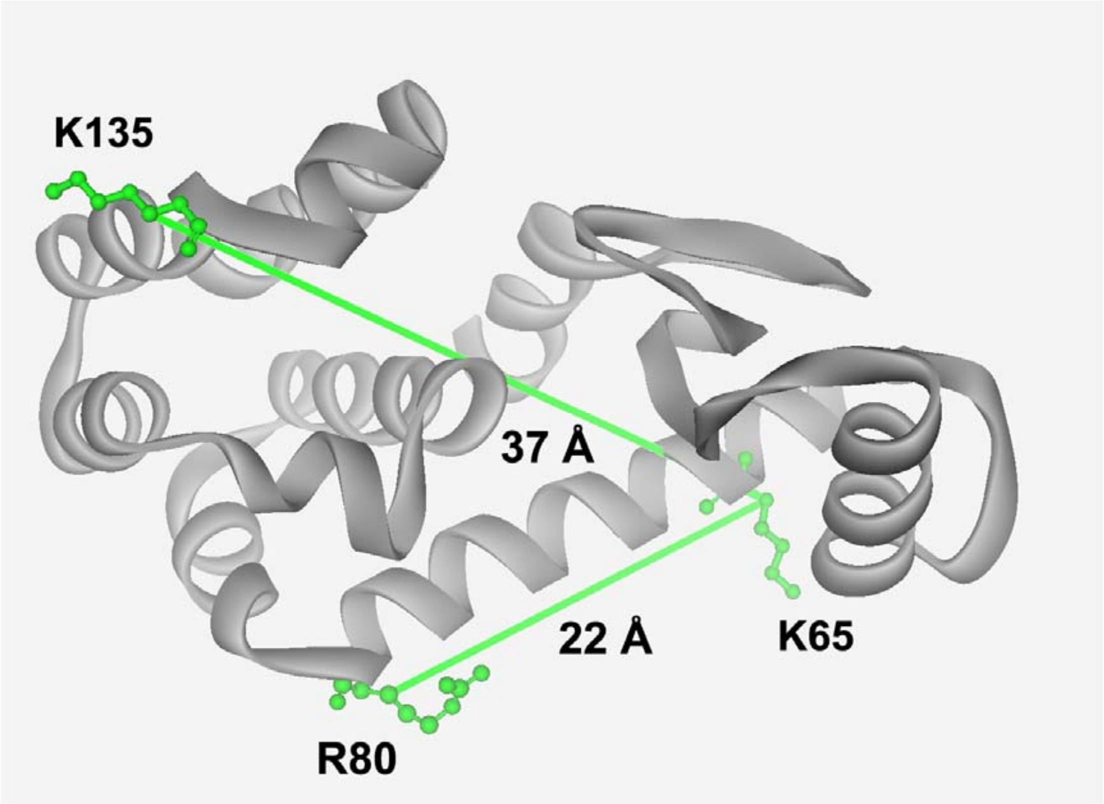
K135
37 Å
22 Å
K65
R80

Figure A2. 5. Sensitized lifetimes of K65/K135TbF and K65/K135TbR. (A) The phosphorescence decay from energy transfer in K65/K135TbF resulted in a monoexponential sensitized lifetime of τ_{AD} = 485 μsec. Emission was monitored at 520 nm. **(B)** The phosphorescence decay from energy transfer in K65/K135TbR resulted in a monoexponential sensitized lifetime of τ_{AD} = 154 μsec. Emission was monitored at 590 nm.

(A)

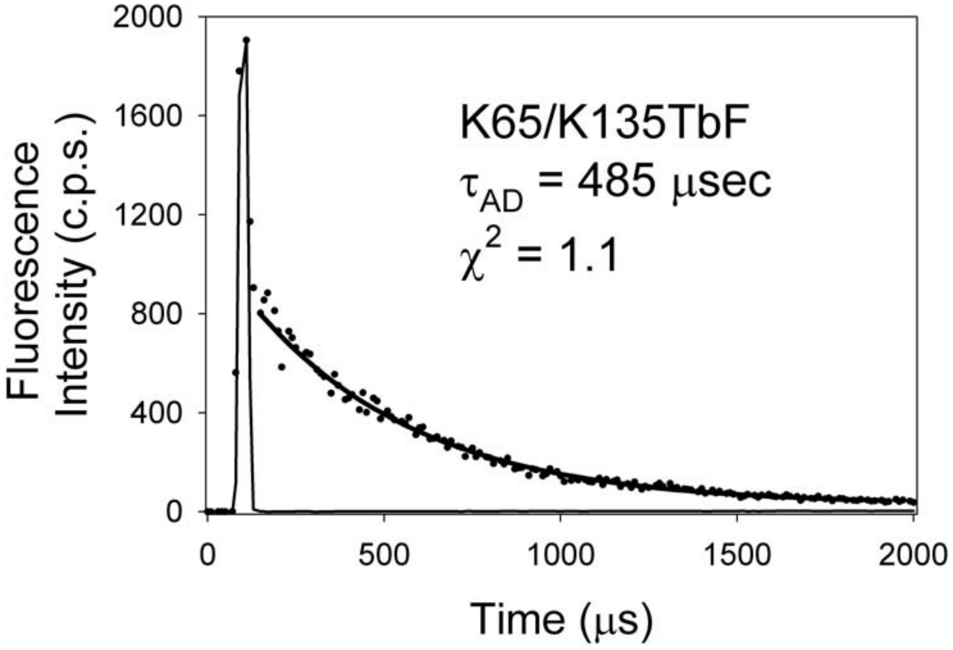
K65/K135TbF
τ_{AD} = 485 μsec
χ^2 = 1.1
Fluorescence Intensity (c.p.s.)
0
400
800
1200
1600
2000
Time (μs)
0
500
1000
1500
2000

(B)

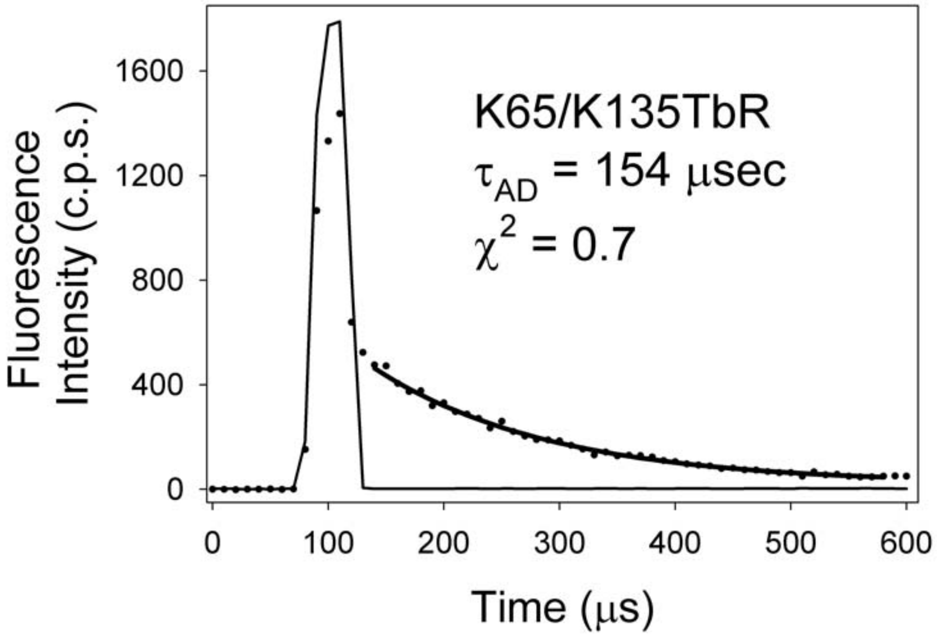
K65/K135TbR
τ_{AD} = 154 μsec
χ^2 = 0.7
Fluorescence Intensity (c.p.s.)
0
400
800
1200
1600
Time (μs)
0
100
200
300
400
500
600

Figure A2. 6: Measured sensitized fluorescence lifetimes can be compared to theoretical functions to predict donor/acceptor distances. Theoretical functions that reveal the expected sensitized fluorescence lifetime (τ_{AD}) at any given distance between a terbium lanthanide donor and **(top half of A)** fluorescein and **(top half of B)** rhodamine. These functions are dependent on the R_0 value between the donor and the acceptor. **(bottom half of A)** When compared to the lanthanide/fluorescein function, the τ_{AD} = 485 μsec for K65/K135TbF measures the distance between residues 65 and 135 in T4 lysozyme as 37 Å. **(bottom half of B)** The τ_{AD} = 154 μsec for K65/K135TbR measures the distance between residues 65 and 135 in T4 lysozyme as 42 Å.

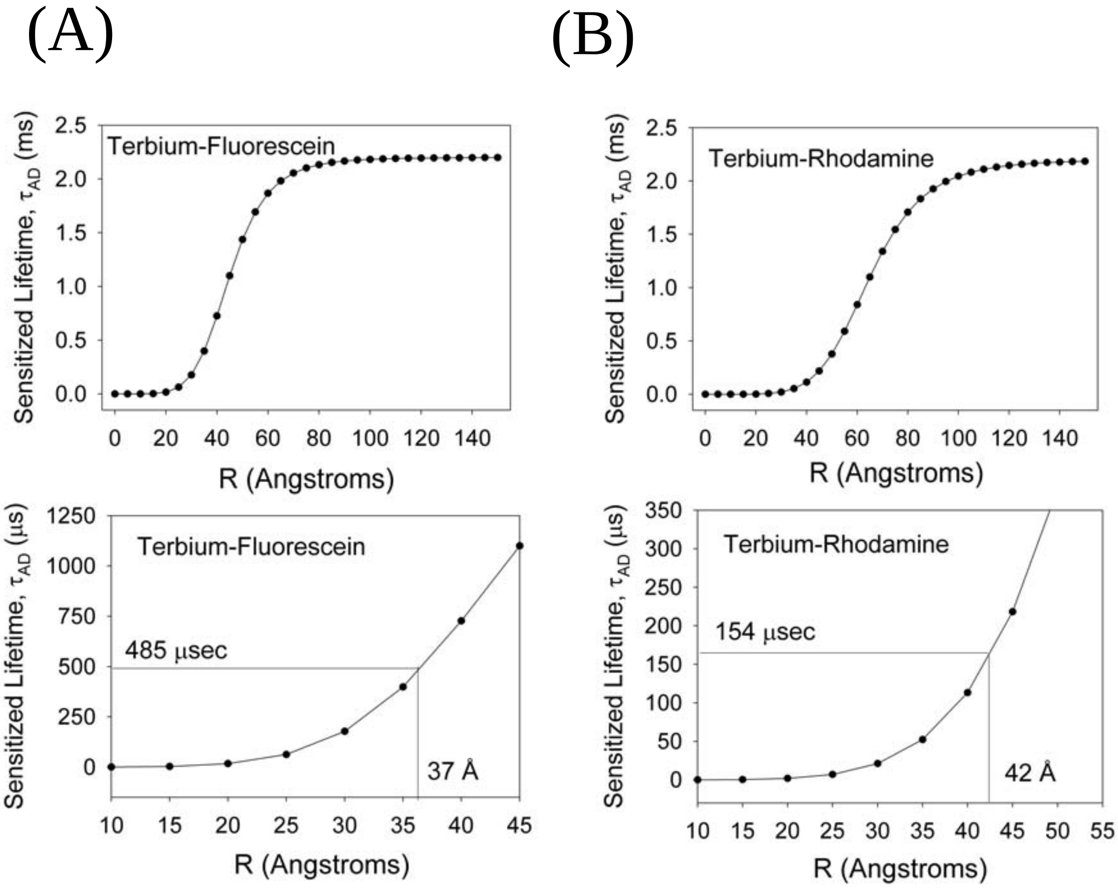
(A)
(B)
Terbium-Fluorescein
Sensitized Lifetime, τ_{AD} (ms)
2.5
2.0
1.5
1.0
0.5
0.0
0
20
40
60
80
100
120
140
R (Angstroms)
Terbium-Rhodamine
Sensitized Lifetime, τ_{AD} (ms)
R (Angstroms)
Terbium-Fluorescein
Sensitized Lifetime, τ_{AD} (µs)
1250
1000
750
500
250
0
485 µsec
37 Å
10
15
20
25
30
35
40
45
R (Angstroms)
Terbium-Rhodamine
Sensitized Lifetime, τ_{AD} (µs)
350
300
250
200
150
100
50
0
154 µsec
42 Å
10
15
20
25
30
35
40
45
50
55
R (Angstroms)